Host-Guest Systems and Their Derivatives Based on Metal-Organic Frameworks

Tiesheng Wang

Darwin College

Department of Materials Science and Metallurgy

University of Cambridge

EPSRC Centre for Doctoral Training in Sensor Technologies and Applications

University of Cambridge

This dissertation is submitted for the degree of *Doctor of Philosophy*.

November 2018

Declaration

This dissertation is the result of my own work and includes nothing which is the outcome of work done in collaboration except as declared in the Preface and specified in the text. It is not substantially the same as any that I have submitted, or, is being concurrently submitted for a degree or diploma or other qualification at the University of Cambridge or any other University or similar institution except as declared in the Preface and specified in the text. I further state that no substantial part of my dissertation has already been submitted, or, is being concurrently submitted for any such degree, diploma or other qualification at the University of Cambridge or any other University or similar institution except as declared in the Preface and specified in the text. It does not exceed the prescribed word limit for the relevant Degree Committee (no more than 60,000 words).

This dissertation is submitted for the degree of Doctor of Philosophy at the University of Cambridge, United Kingdom. The study is a part of the MRes + PhD programme in EPSRC Centre for Doctoral Training in Sensor Technologies and Applications.

The research described herein was carried out by me under the supervision of Professor R. Vasant Kumar (Professor in Materials Chemistry, University of Cambridge) and Dr Stoyan K. Smoukov (Reader in Chemical Engineering, Queen Mary University of London). The research was co-advised by Professor Anthony K. Cheetham, FRS (Distinguished Professor, University of Cambridge).

Tiesheng Wang (王铁胜)

Cambridge, United Kingdom

Submitted on November 2018

Revised on May 2019

Host-Guest Systems and Their Derivatives Based on Metal-Organic Frameworks

Tiesheng Wang

Abstract

Including guest compounds inside the pores of nanoporous crystalline hosts (*e.g.* zeolite) is a key strategy to post-synthetically functionalise these nanoporous materials over past half a century. It yields highly active and stable heterogeneous catalysts as well as robust materials with tuneable photoluminescence properties due to geometric/quantum confinement. More recently, metal-organic frameworks (MOFs), which are hybrid hosts assembled with metal centres and organic ligands, start to be considered for creating host-guest composites. Apart from the aforementioned confinement effects, MOFs with diverse chemistries as hosts can give rise to a variety of host-guest interactions in these composite systems. It is, however, challenging to investigate these MOF-guest systems due to small MOF pore dimensions, MOF instability, poor guest loading control and limitations in guest characterisations.

The thesis explores three different MOF-guest systems covering their preparation, characterisation as well as some unusual behaviour owing to MOF-guest interactions and/or confinement effects. The first system is incorporating electrically conducting poly(3,4-ethylenedioxythiophene) (PEDOT) into a $Zn_2(1,4\text{-ndc})_2(dabco)$ (1,4-ndc = 1,4-naphthalenedicarboxylate, dabco = 1,4-diazabicyclo[2.2.2]octane) [$PEDOT@Zn_2(1,4\text{-ndc})_2(dabco)$], which turned the electrically insulating MOF into a semiconducting composite. The formation of nanostructured PEDOT by removing the MOF from the $PEDOT@Zn_2(1,4\text{-ndc})_2(dabco)$ is also demonstrated.

The success in MOF-PEDOT system preparation is the motivation to expand the synthesis to forming inorganic guests (the second system). Thermodynamically favourable solid/solution phases of inorganic compounds, which relate to electrochemical potential and pH, are considered to choose reaction agents and conditions to form desired guests. The application of the concept to the synthesis of MOF-RuO_2 catalysts (RuO_2@MOF-808-P), where the confined RuO_2@MOF-808-P has exceptionally high activity for CO oxidation compared to unconfined RuO_2 with poor activity at low temperatures ($\leq$150 °C) is demonstrated.

In the final system, guest-induced metamorphosis by carbonising the MOF-guest composites made of HKUST-1-type MOFs and thiomolybdates is unveiled. With implications for the transformation mechanisms, MOF- and guest-dependent morphology of the carbonised products are shown. The carbonised product based upon HKUST-1(Cu) and thiomolybdate was also demonstrated as lithium-ion battery anode.

For my parents, Mr Yongjun Wang and Ms Chong Han,

and for my wife, Ms Yifan Wang,

to whom I love and owe a great deal

There's Plenty of Room at the Bottom.

- Richard P. Feynman

American Physical Society Meeting

Pasadena, California, U.S.A., 1959

成功的花，人们只惊羡她现时的明艳！

然而当初她的芽儿，浸透了奋斗的泪泉，洒遍了牺牲的血雨。

The flower of success is only adored for her beauty when blooming!

However, her sprouts were immersed in streams of tears and sprinkled by the blood rain of sacrifice.

- 冰心 Bing Xin (谢婉莹 Wanying Xie)

《繁星》(A Maze of Stars), 1921

Translated by 叶织文 Zhiwen Ye, 2003

Acknowledgement

My PhD study (2015-2018) would have not been possible with the guidance and suggestions from my supervisors and advisers, financial supports from funding agencies, generous helps from collaborators and colleagues, and understanding and tolerance from my family and girlfriend.

First and foremost, my heartfelt thanks go to China Scholarship Council (CSC), who covered my tuition fee, my college fee and a part of my living cost. I am appreciated for the assistance provided by Education Section, Embassy of the People's Republic of China.

I would like to express my sincere gratitude to Dr Stoyan K. Smoukov, who supervised me and funded my research through his European Research Council (ERC) grant (grant number: EMATTER 280078). It was a pleasant experience working with Stoyan. He mentored me as a future scientist, who is prepared to do both independent and collaborative research. While providing me with sufficient guidance and feedback, Stoyan also encouraged me to explore the true beauty of science use my own 'eyes'. I will remember the time we spent together to exchange the ideas and to write the scientific papers.

Meanwhile, I count myself very lucky to have been co-supervised and co-advised by Professor R. Vasant Kumar and Professor Anthony K. Cheetham FRS. I would like to thank Professor R. Vasant Kumar, who kindly supported my research and hosted me to complete my PhD study. I benefit hugely from his suggestions and networks in energy-related applications. I wish to acknowledge Professor Anthony K. Cheetham FRS, who provided insights in materials chemistry and built my confidence in research. The meetings with Tony and Stoyan were always enjoyable, insightful and productive.

Priceless collaborative and daily supports were provided by my current and previous colleagues in Cambridge: Professor Judith L. MacManus-Driscoll FREng, Dr Rosie E.M. Ward, Ms Claire Thrower, Ms Rebecca Stamford, Mr Anthony P. Fox, Mr Nathan Cliff, Mr Anthony J. Gledhill, Professor Xianbo Jin, Professor Kelvin H. L. Zhang, Professor Lijun Wang, Professor Tong Wei, Dr Sohini Kar-Narayan, Dr Sen Zhang, Dr Xin Min, Dr Jean E. Marshall, Dr Feng-hua Zhang, Mr I-Ting Lin, Mr Tianheng Zhao, Ms Kara D. Fong, Mr Noel M. Thompson, Dr Sneha R. Bajpe, Dr Shijing Sun, Dr Yue Wu, Dr Jingwei Hou, Dr Hyun-Kyung Kim, Dr Yingjun Liu, Dr Teng Zhao, Mr Cheng-Yen Lao, Dr Weiwei Li, Dr

Rui Wu, Dr Qingshen Jing, Mr Yisong Lin, Mr ChaoYun, Mr Zeyu Deng, Mr Tianwei Wang, Mr Yeon Sik Choi, Dr Jonathan S. Barnard, Dr Tongtong Zhu, Dr James T. Griffiths, Mr Boning Ding, Dr Suman-Lata Sahonta, Mr Giovanni Orlando, Mr David Nicol, Mr Simon J. Griggs, Ms Sue Gymer, Mr Robert Cornell, Mr Chris Dolan, Dr Mary Vickers, Mr Andrew Moss, Mr James Goodchild, Ms Lori Richardson, Ms Anya Howe, and Ms Fiona Morgan.

I would like to extend my gratitude to other collaborators in the world: Professor Mary P. Ryan FREng, Dr Fang Xie, Professor Xinhe Bao, Professor Qiang Fu, Dr Lijun Gao, Mr Jinhu Dong, Professor John D. W. Madden**,** Dr Meisam Farajollahi, Professor Bettina V. Lotsch, Dr Sourav Laha, Mr Filip Podjaski, Professor Sebastian Henke, Professor Maria-Magdalena Titirici, Mr Servann J. A. Herou, Professor Jiaqi Zhang, and Ms Song Gao.

I would like to thank the administration team for Engineering and Physical Sciences Research Council (EPSRC) Centre for Doctoral Training in Sensor Technologies and Applications (2014-2018, EP/L015889/1 and 1566990): Professor Clemens Kaminski, Dr Oliver Hadeler, Dr Tanya Hutter, Dr Fernando da Cruz Vasconcellos, Ms Caroline Yan-Man-Shing, Dr Nathan Curry, Ms Zizi Hollander, and Ms Karen Scrivener. As a cohort member of EPSRC Centre for Doctoral Training in Sensor Technologies and Applications, I was supported by them throughout my study. I am also grateful to Professor Daping Chu who kindly supported my CSC scholarship application.

Dr Margaret Wilkinson, Mr Ting Ben, and Dr Callum Benson from Cambridge Enterprise are acknowledged here for their kind assistance in exploring the commercial aspects of the inventions from my PhD study.

Phenom-World is acknowledged for the free use of the Phenom Pro X SEM. DoITPoMS is acknowledged for the use of its online materials.

I am not sure if my wife, Ms Yifan Wang, is going to read this, but I want to say a heartfelt thank you to her for her trust and tolerance. I only spent approx. a month with her in the past three years, but she kept the relation without complaining. Even though we were 5,000 miles apart, her accompany and encouragement over distance helped me get through the hard times.

Last but not the least, I would like to express my deepest gratitude to my parents, Mr Yongjun Wang and Ms Chong Han, who brought me to the world and continuously support me to pursue my dream. I have been in the UK since 2010 and I miss them.

Supervision and Collaborations for the Thesis

Department of Materials Science and Metallurgy, University of Cambridge, United Kingdom:

Active and Intelligent Materials Lab:

Dr Stoyan K. Smoukov, Ms Kara D. Fong, Mr June Sang Lee

Materials Chemistry Group:

Professor R. Vasant Kumar, Dr Hyun-Kyung Kim, Dr Yingjun Liu

Functional Inorganic and Hybrid Materials Group:

Professor Anthony K. Cheetham FRS, Dr Sneha R. Bajpe, Dr Shijing Sun, Dr Yue Wu, Dr Jingwei Hou

Device Materials Group:

Dr Weiwei Li, Mr ChaoYun

Cambridge Centre for Gallium Nitride:

Dr Tongtong Zhu, Dr James T. Griffiths

Electron Microscopy Group:

Dr Jonathan S. Barnard

Advanced Materials and Process Engineering Laboratory, University of British Columbia, Canada:

Professor John D. W. Madden**,** Dr Meisam Farajollahi

Inorganic Chemistry 2, Ruhr University Bochum, Germany:

Professor Sebastian Henke

State Key Laboratory of Catalysis, Dalian Institute of Chemical Physics， Chinese Academy of Sciences, China:

Professor Xinhe Bao, Professor Qiang Fu, Dr Lijun Gao, Mr Jinhu Dong

School of Engineering and Materials Science, Queen Mary University of London, United Kingdom:

Professor Maria-Magdalena Titirici, Mr Servann J. A. Herou

School of Chemical Engineering, University of New South Wales, Australia:

Ms Song Gao

Max Planck Institute for Solid State Research, Germany:

Professor Bettina V. Lotsch, Dr Sourav Laha, Mr Filip Podjaski

List of Publications and Patents

Publications and filed patents covered in the thesis:

1. Tiesheng Wang, Meisam Farajollahi, Sebastian Henke, Tongtong Zhu, Sneha R. Bajpe, Shijing Sun, Jonathan S. Barnard, June Sang Lee, John D.W. Madden, Anthony K. Cheetham, Stoyan K. Smoukov*, ***Functional Conductive Nanomaterials via Polymerisation in Nano-channels: PEDOT in a MOF***, doi: 10.1039/C6MH00230G, **Materials Horizons**, 2017, 4 (1), pp 64–71
2. Tiesheng Wang, Hyun-Kyung Kim, Yingjun Liu, Weiwei Li, James T. Griffiths, Yue Wu, Sourav Laha, Kara D. Fong, Filip Podjaski, Chao Yun, R. Vasant Kumar, Bettina V. Lotsch, Anthony K. Cheetham, Stoyan K. Smoukov*, ***Bottom-up Formation of Carbon-based Structures with Multilevel Hierarchy from MOF-guest Polyhedra***, doi: 10.1021/jacs.8b02411, **Journal of the American Chemical Society**, 2018, 140(19), pp 6130-6136
3. Tiesheng Wang#, Lijun Gao#, Jingwei Hou, Servann J. A. Herou, James T. Griffiths, Weiwei Li, Jinhu Dong, Song Gao, Maria-Magdalena Titirici, R. Vasant Kumar, Anthony K. Cheetham, Xinhe Bao, Qiang Fu*, Stoyan K. Smoukov*, ***Rational Approach to Guest Confinement inside MOF Cavities for Low-Temperature Catalysis***, doi: 10.1038/s41467-019-08972-x, **Nature Communications**, 2019, 10, Article number: 1340 (# co-first author)
4. Tiesheng Wang, Stoyan K. Smoukov, Hyun-Kyung Kim, **GB1801331.8**: ***Porous Carbonaceous Materials and Methods for Their Manufacture*** (patent filed on 26 January 2018)
5. Tiesheng Wang, Stoyan K. Smoukov, Qiang Fu, Lijun Gao, **GB1813334.8**: ***Nanocomposite Materials and Methods of Manufacture Thereof*** (patent filed on 15 August 2018)

Other Publications and Patents (October 2015 - November 2018):

6. Tiesheng Wang, Meisam Farajollahi, Yeon Sik Choi, I-Ting Lin, Jean E. Marshall, Noel M. Thompson, Sohini Kar-Narayan, John D. W. Madden, Stoyan K. Smoukov*, ***Electroactive Polymers for Sensing***, doi: 10.1098/rsfs.2016.0026, **Interface Focus**, 2016, 6 (4), 20160026
7. Kara D. Fong#, Tiesheng Wang#, Hyun-Kyung Kim, R. Vasant Kumar, Stoyan K. Smoukov*, ***Semi-Interpenetrating Polymer Networks for Enhanced***

Supercapacitor Electrodes, doi: 10.1021/acsenergylett.7b00466, **ACS Energy Letters**, 2017, 2 (9), pp 2014–2020 (# co-first author)

8. Kara D. Fong, Tiesheng Wang, Stoyan K. Smoukov*, ***Multidimensional Performance Optimization of Conducting Polymer-based Supercapacitor Electrodes***, doi: 10.1039/C7SE00339K, **Sustainable Energy & Fuels**, 2017, 1 (9), pp 1857-1874
9. I-Ting Lin, Tiesheng Wang, Fenghua Zhang, Stoyan K. Smoukov*, ***Fault-Tolerant Electro-Responsive Surfaces for Dynamic Micropattern Molds and Tunable Optics***, doi: 10.1038/s41598-017-12899-y, **Scientific Report**, 2017, 7, 12481
10. Tiesheng Wang, Anthony Centeno, Daniel Darvill, Jing S. Pang, Mary P. Ryan and Fang Xie*, ***Tuneable Fluorescence Enhancement over Nanostructured ZnO Arrays with Controlled Morphology***, doi: 10.1039/C8CP01493K, **Physical Chemistry Chemical Physics**, 2018, 20(21), pp 14828-14834
11. Can He, Haipeng Ji, Zhaohui Huang*, Tiesheng Wang, Xiaoguang Zhang, Yangai Liu, Minghao Fang, Xiaowen Wu, Jiaqi Zhang, Xin Min*, ***Red-Shifted Emission in Y3MgSiAl3O12:Ce3+ Garnet Phosphor for Blue Light-Pumped White Light-Emitting Diodes***, doi: 10.1021/acs.jpcc.8b03940, **The Journal of Physical Chemistry C**, 2018, 122 (27), pp 15659–15665
12. Stoyan K. Smoukov, Tiesheng Wang, Kara D. Fong, Hyun-Kyung Kim, **GB1712274.8**: ***Polymer-based energy storage device*** (patent filed on 31 July 2017, PCT on 31 July 2018)

Contents

List of Abbreviations/Acronyms (Alphabetically Sorted)

ADF: annular dark field

AFM: atomic force microscope

ALD: atomic layer deposition

ATM: ammonium tetrathiomolybdate [$(NH_4)_2MoS_4$]

ATT: ammonium tetrathiotungstate [$(NH_4)_2WS_4$]

BET: Brunauer-Emmett-Teller

BF: bright field

BHT: butylated hydroxytoluene

BJH: Barrett-Joyner-Halenda

BSE: backscattered electron

BTC: 1,3,5-benzenetricarboxylate

CL: cathodoluminescence

COF: covalent organic framework

CO-TPR: CO temperature-programmed reduction

CSD: Cambridge structural database

CV: cyclic voltammetry

CVD: chemical vapour deposition

dabco: 1,4-diazabicyclo[2.2.2]octane

DE: diethyl ether

DF: dark field

DFT: density function theory

DMF: N,N-dimethylformamide

DRIFT: diffuse reflectance infrared Fourier transform spectroscopy

E_a: activation energy

EC/DMC: ethylene carbonate/dimethyl carbonate

EDOT: 3,4-ethylenedioxythiophene

EDS: energy-dispersive X-ray spectroscopy

EELS: electron energy loss spectroscopy

EXAFS: Extended X-ray absorption fine structure

FTIR: Fourier-transform infrared spectroscopy

H_2ndc: 1,4-naphthalenedicarboxylic acid

H_2tdc: 2,5-thiophenedicarboxylic acid

H_3BTC: 1,3,5-benzenetricarboxylic acid

HOMO-LUMO: highest occupied molecular orbital - lowest unoccupied molecular orbital

HR-TGA: high-resolution thermogravimetric analysis

ICP-OES: inductively coupled plasma optical emission spectrometry

I-V: current-voltage

LC-MS: liquid chromatography – mass spectrometry

LiB: lithium-ion battery

MOF: metal-organic framework

MOP: metal-organic polyhedral

ndc: 1,4-naphthalenedicarboxylate

NMR: nuclear magnetic resonance

PCP: porous coordination polymer

PEDOT: Poly(3,4-ethylenedioxythiophene)

PEGS: Pourbaix enabled guest synthesis

POM: polyoxometalate

PPy: polypyrrole

PSD: pore size distribution

PVDF: polyvinylidene fluoride

PXRD: powder X-ray diffraction

QSDFT: quenched solid state functional theory

SBU: secondary building units

SE: secondary electron

SEM: scanning electron microscopy

SSRF: Shanghai Synchrotron Radiation Facility

STEM: scanning transmission electron microscopy

STP: standard temperature and pressure

tBMP: 2-tert-butyl-4-methylphenol

TCD: thermal conductivity detector

TCNQ: 7,7,8,8-tetracyanoquinododimethane

TEM: transmission electron microscopy

TGA: thermogravimetric analysis

TGA-FTIR: thermogravimetric analysis with Fourier-transform infrared spectroscopy

TOF: turnover frequency

TPR: temperature programmed reduction

WHSV: weight hourly space velocity

XANES: X-ray absorption near edge structure

XAS: X-ray absorption spectroscopy

XPS: X-ray photoelectron spectroscopy

XRD: X-ray diffraction

Chapter 1

Scope and Outline

Chapter 1: Scope and Outline

The term "host-guest chemistry" is often used to describe the supramolecular complexes with guest molecules included.[1] In porous materials, host-guest systems are also very common, where the porous materials serve as the hosts to accommodate a range of guest moieties in the pore (*i.e.* inclusion chemistry).[2–5] The as-formed host-guest systems can be vividly described as "ship in a bottle" systems (Figure 1.1), where the bottle represents a pore in the porous host and the ship refers to a guest entity within the pore.[4–9] In this thesis, metal-organic frameworks (MOFs),[10–16] as an important family of nanoporous materials, is focused as the host for the host-guest system (*i.e.* MOF-guest system). For simplicity, the expression "guest@MOF" will be used to denote a specific MOF-guest system, where "@" means "within the pore of".

Figure 1.1 Personal work based on the ship Black Pearl in Davy Jones' bottle in *Pirates of the Caribbean*. Reprinted from ref. 17 made by Conflig (Copyright 2017 blenderartists.org) under a Creative Commons Attribution-NonCommercial-ShareAlike 3.0 Unported License (CC BY-NC-SA 3.0).

Nanoporous materials are porous materials with typical pore dimension from sub-nm to sub-micron. Host-guest systems based on nanoporous materials can yield highly active and stable heterogeneous catalysts[3,4,24,25,8,9,18–23] as well as robust photo/electro-luminescence materials[3,26–28]. These are contributed by encapsulation-enabled guest stabilization and confinement-induced guest property change. Although inorganic nanoporous crystals and MOFs share some key features (*i.e.* 3-directional framework and controlled pore structure), MOFs have a much broader selection of building blocks. MOFs' diverse chemistries enable tuneable pore microenvironments, controllable pore sizes (for both cavity and aperture) and further framework functionalization.[8] Therefore, further interactions between MOFs and guests in the MOF-guest systems become even more attractive. This is the major driving force of this PhD research. As brief summary, key motivations to explore host-guest systems based on MOFs are:

(i) geometric confinement, *i.e.* guest materials could be kept small (sub-nm to nm regime);
(ii) quantum confinement, *i.e.* the insulating MOF hosts could effectively act as finite potential wells to confine the electron structure of the guests, which could be potential experimental platforms to study "particle in finite-walled box".[28]
(iii) above-mentioned MOF-guest interactions;
(iv) pushing the synthesis and characterisation limits in nanoscience.

Note that although the behaviours of small molecules inside MOF are also considered by applications such as MOF-based gas storage[29–31], separation[31,32], sensing[33,34] and drug delivery[35–38], there is a conceptual difference between these applications and study about MOF-guest systems. The major research object of the above-mentioned applications is MOF whereas that of the host-guest research is the MOF-guest composites which can be regarded as a new category of materials derived from MOF.

Apart from the overall backgrounds and concepts of MOFs and host-guest systems based on the MOFs, the Introduction (Chapter 2) also mentions several important points covering the pore and stability of the MOFs as well as the preparation methods and challenges of the MOF-guest systems. Chapter 3 covers general methodology for the experiments. Chapters 4-6 focuses on three case studies of MOF-guest systems: a polymer@MOF and its MOF-templated derivative (Chapter 4), oxides@MOFs design and preparation (Chapter 5), and carbonized thiomolybdates@MOFs (Chapter 6). In Chapter 5, CO oxidation catalysis performances of oxides@MOFs are evaluated; some carbonized products in Chapter 6 are tested as anodes for lithium-ion battery.

Chapter 2

Introduction

Chapter 2: Introduction

2.1 Host-Guest Systems with Nanoporous Crystalline Hosts: Before the Age of MOF

The study about host-guest systems using nanoporous materials as the hosts was initiated as a consequence of the accidental discovery of zeolite in 1756 by the Swedish mineralogist and chemist, Baron Axel Fredrik Cronstedt.[2] He used the term "zeolite" based on Greek ("ζέω-λίθος" meaning "boil-stone") to describe the rock (stilbite) which can produce a large amount of water steam after heating. In fact, the water is the "guest" resided in the zeolite "host". Zeolite was later used to describe a family of nanoporous silica (*a.k.a.* zeotypes) which are constructed by Si/Al-O building blocks. The typical dimension of the nanoporosity for zeolite is 3-20 Å.[2]

Since the late 1960s, nanoporous silica materials have experienced a significant development.[2] After the late 1980s, the entire category of open-framework inorganic materials expanded rapidly covering aluminosilicates, phosphates, chalcogenides, halides, nitrides, and oxides.[39] One major driving force is that they usually have a high porosity as well as high specific surface area (*i.e.* surface area per unit mass).[2] Such features make them particularly attractive as an adsorbent for small chemical species (*e.g.* gas molecules) and catalysts for hydrocracking in petroleum refining.[2,40]

Guest immobilization in the nanoporous hosts was initially introduced in the 1970s for heterogeneous catalysis with improved high-activity retention (*e.g.* Pt in zeolite for hydroisomerization)[41] and selectivity. Since the 1990s, forming guest entities inside tridirectional, open-porous hosts have become a popular topic. These hosts can keep the catalyst highly dispersed, minimise thermal sintering and screen out large unwanted reagents for small-molecule reactions.[2,18] The electronic and photoluminescent aspects of host-guest nanocomposites were also investigated by solid-state physicists later in the 20th century, due to the realisation of quantum confinement. Nanoporous crystalline hosts were chosen not only to provide the confinement to the guests, typically inorganic semiconducting compounds and organic conductors/dyes but also to influence the guest surface states, inter-guest interaction, and effective charge carrier behaviours.[3,28]

2.2 Brief Introduction to MOF

The concept of MOF is quite self-explanatory – a framework built by metal-based and organic moieties. To achieve the structural periodicity (*i.e.* crystallinity), metal-containing clusters (*a.k.a.* nodes) are interconnected by organic/inorganic ligands (*a.k.a.* linker) as briefly illustrated in the embedded schematic diagram in Figure 2.1. Both clusters and ligands are so-called secondary building units (SBUs). So far, several leading MOF groups have summarized many aspects of MOFs into literature.[10–16]

Although the construction of metal-organic crystals (or coordination polymers) can be traced back by more than half a century [when Kinoshita and Saito *et al.*[42] reported the periodic covalent structure of bis(adiponitrilo)copper(I) nitrate in 1959], it is actually until early 1990s scientists start to seriously explore/design MOFs.[12,43–48] A part of the reasons for such "renaissance" owes to the better understanding in metal-organic coordination chemistry (*e.g.* metallo-catenanes[49] and metal-organic polyhedra[50], MOP, *a.k.a.* metal-organic cages) and reticular chemistry[12,16]. In fact, some of the early MOFs were built to construct the periodically ordered networks of MOPs.[43,47] More recently, many MOFs with complicated structures can be understood and categorised using MOPs as more basic building units.[11,51] Another significant driving force for the development of MOFs, similar to their aforementioned inorganic analogue, is the intrinsic open porosity found in many MOFs, which contributes to the high specific surface area (area per unit mass) and enables the impregnation of guest species.[10,12] The porous nature of many MOFs is revealed by a complimentary name of MOF, "porous coordination polymer (PCP)"[14], which emphasizes the significance of porosity and coordination nature rather than the crystallinity. In fact, as raised by Férey[15], the development of MOF can be regarded as the progress towards the hybridization of the inorganic crystalline porous materials.

Due to the broad selection of chemistries for MOFs, a large variety of MOFs have been discovered or predicted with diverse topologies and pore architectures.[12,16,52] In 2016, the estimated number of MOFs exceeded 70,000 (Figure 2.1).[52] Meanwhile, the pore dimension (*i.e.* pore aperture size, detailed in Section 2.3) of MOFs can be bigger than inorganic nanoporous materials in general and approaches 100 Å.[12] Amongst the synthesized MOFs, there are a number of them have been widely known and extensively investigated, such as MOF-5[53], ZIF-8[54], HKUST-1[55], UiO-66[56] and NU-1000[57], owing to various reasons, such as low cost and easiness of preparation. MOFs constructed with light organic molecules can have much larger specific surface area than their inorganic analogues. Meanwhile, the well-controlled MOF frameworks can be superior to many activated porous carbons with random pores, particularly for applications requiring high pore regularity, such as gas separation.[12,14] With outstanding features as a category of porous materials, MOFs have been developed for numerous applications, such as gas storage and separation[31,32,58], catalysis[9,59,60], sensing[34,61] and drug delivery[38,62].

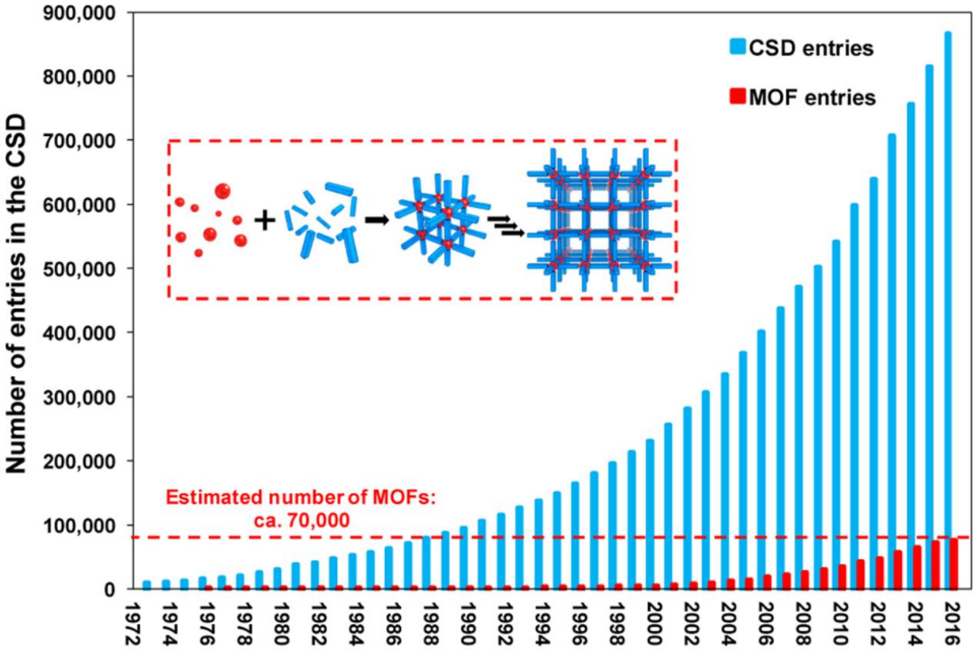

Figure 2.1 A roadmap of MOF entries in the Cambridge structural database (CSD). The schematic illustration in the middle shows how a MOF is assembled by an SBU and organic linker. The figure is reproduced from the work by Moghadam and Fairen-Jimenez *et al.* with permission from ref. 52 (Copyright 2017 American Chemistry Society).

Unlike inorganic frameworks usually with high rigidity, the frameworks for MOFs can be more flexible and dynamic. Many organic linkers can have some degree of bending and/or rotation flexibility; the interpenetrating or layered networks can exhibit mutual displacements.[63] Those degrees of freedom bring MOFs with three outcomes as summaries by Kitagawa *et al.*[14,63]: frameworks undergoing irreversible collapse or deformation after guest removal (1st generation), rigid and robust frameworks (2nd generation) and frameworks experiencing revisable structural transformation/alteration upon external stimuli (*e.g.* guest impregnation) (3rd generation). MOF's structural flexibility enables guest species with similar or even larger dimensions than the aperture of MOF's pore (detailed in Section 2.3) to be incorporated into the preformed MOF. In parallel, some known guest-induced structural responses can be used to verify the inclusion of guests.

The presence of pores that are accessible is essential for guest formation. Therefore, in the following two sections, two concepts, namely pore, and stability with regards to MOF are introduced.

2.3 MOF's Pores

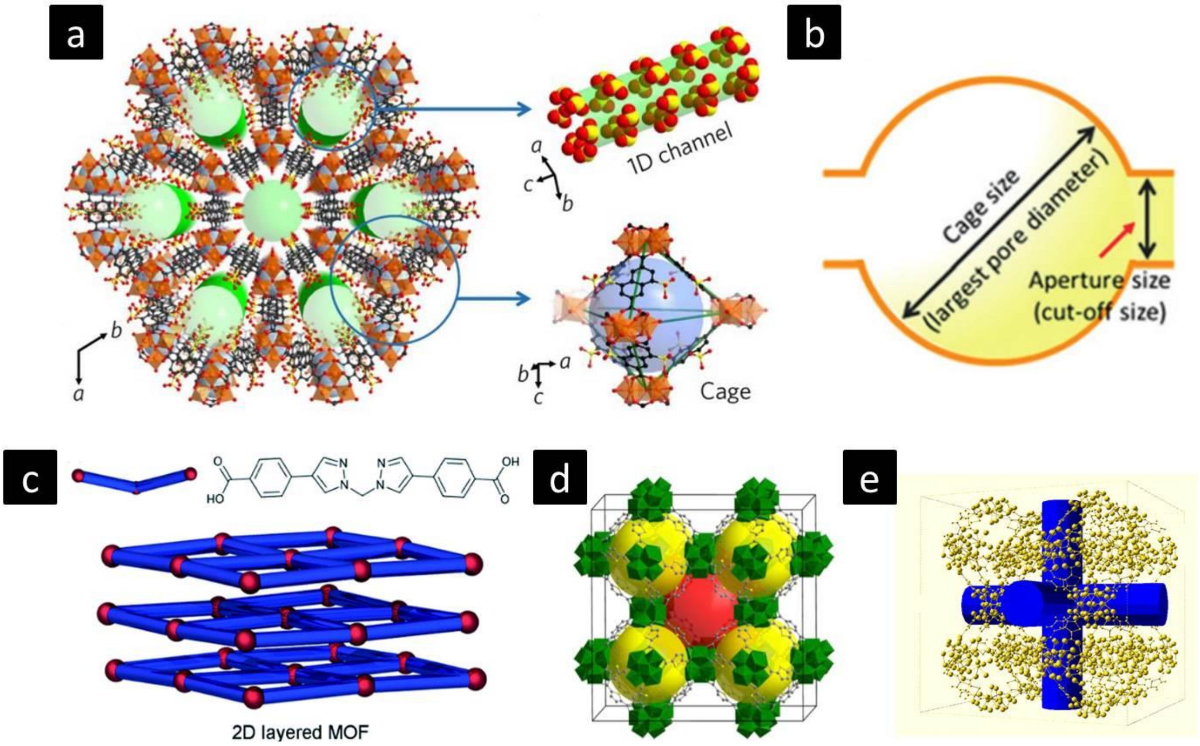

Figure 2.2 MOFs with different pore geometries: (a) BUT-8(M) contains the 0D cavity (light blue) and paralleled 1D channel (light green). The figure is reproduced from the work by Chen *et al.* with permission from ref. 64 (Copyright 2017 Nature Publishing Group). (b) A schematic illustration for the 0D cavity showing the cavity diameter (*i.e.* cage size) and opening aperture size (*i.e.* window size). The figure is reproduced from the work by Yang *et al.* with permission from ref. 65 (Copyright 2015 John Wiley and Sons). (c) A schematic diagram for 2D layered MOF showing interlayer spaces. The figure is reproduced from the work by Doonan *et al.* with permission from ref. 66 (Copyright 2014 The Royal Society of Chemistry). (d) Two types of cavity (red and yellow) contained in a DUT-67 unit cell. The figure is reproduced from the work by Senkovska *et al.* with permission from ref. 67 (Copyright 2013 American Chemical Society). (e) Intersecting channels (blue) along <100> in a DUT-67 unit cell.

MOF's pore generally refers to the vacant space inside the MOF. Similar to inorganic zeolites, the MOFs (excluding MOF glass) are crystalline thus have well-controlled pore with respects to both size and location within the crystal.[12,14] Common basic geometries of the pore are zero-dimensional (0D) cavity (*a.k.a.* cage, Figure 2.2a, bottom) and one-dimensional (1D) channel (Figure 2.2a, bottom). As a less frequent case, layered MOFs made with two-dimensional (2D) metal-organic network stacking are sometimes regarded as MOFs with 2D layered pores (Figure 2.2c).[14,66]

There are two critical dimensions for a 0D cavity in an open-porous MOF, namely cavity diameter (*a.k.a.* cage size) and opening aperture size (*a.k.a.* window size) as shown in Figure 2.2b. For a guest moiety inside the MOF' cavity, the cavity diameter (assuming the cavity is spherical) limits the maximum size of the guest that can be accommodated; the aperture size restricts the maximum size of a compound that can migrate in and out the cavity. Similarly, for the 1D channel, guest species that are smaller than its diameter is allowed to be loaded in the channel. Nonetheless, the cross-sectional diameter along the channel's length may not be the same. In many cases, the channel originates from the periodically formed cavities interconnecting each other, *e.g.* the channel along <100> (in blue, Figure 2.2e) in DUT-67[67] comes from the connection of opening primary cavities (in red, Figure 2.2d). Therefore, two typical cross-sectional diameters similar to the case of a 0D cavity should be considered. Furthermore, channels constructed by 0D cavities with apertures along multiple directions are likely to intersect other channels (Figure 2.2e) forming three-dimensional (3D) channels.[14]

2.4 MOF's Stability

MOFs are metastable. Hence, MOF's stability is one of the primary concerns for MOF-based applications and MOF's post-synthetic modifications.[12,13,68–71] Although MOFs may suffer from all kinds of external stimuli, four aspects of stability are mostly considered: chemical stability, thermal stability, mechanical stability, and hydrothermal stability. Generally, a MOF is considered stable if it remains its structure [through *e.g.* X-ray diffraction (XRD)], porosity (through *e.g.* N_2 adsorption) and chemistry [through *e.g.* Fourier-transform infrared spectroscopy (FTIR), Raman spectroscopy and energy-dispersive X-ray spectroscopy (EDS)]. Note that the results from the above-mentioned characterisations focus on the qualitative determination of MOF's stability. Therefore, MOFs with only slight degradation is often indistinguishable from the perfectly stabilized MOFs.

MOF’s chemical stability refers to its endurance in the external chemical environment, *e.g.* solvents. It is often related to the bonding stability between the metal-containing cluster and the organic linker. Water (in liquid or gas form) stability is one of the most crucial subsets of the chemical stability, as water is commonly presented in most of the MOF-related applications. MOF degradation in aqueous systems (*e.g.* hydrolysis) can be accelerated by a change in pH. At low pH (in acid), the organic linkers can leave the structure by reprotonation; at high pH (in base), the metal-containing cluster can also detach from the framework by forming more stable hydroxide or hydrate. Numerous commonly used MOFs with known water stability are summarized by Howarth *et al.*[13] (Figure 2.3).

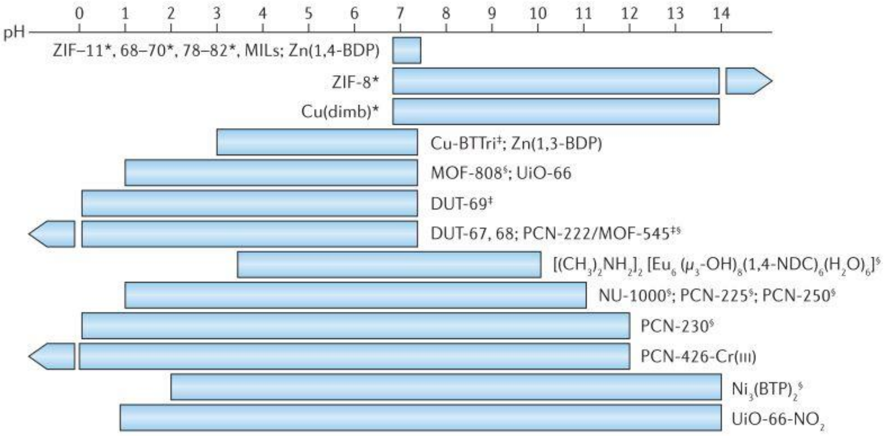

Figure 2.3 Stability of a selection of MOFs against acid or base in aqueous system summarized by Howarth *et al.*[13]. The figure is reproduced from their recent review on MOF’s stability with permission from ref. 13 (Copyright 2016 Nature Publishing Group). Please refer to the original article for further details.

The strength of chemical bonds between the building units is also very critical for MOF’s thermal stability.[71] In parallel, the bonding strength within the metal-containing cluster and the organic linker is equally important. At sufficiently high temperatures, a MOF can suffer both node-linker bond breaking/rearrangement (e.g. phase transformation[72], amorphization[73] or melting[74]) and chemical degradation within the building units (dehydration, dehydrogenation, calcination or carbonization[75–84]).

Since inorganic-organic hybridized MOF is generally softer than the inorganic nanoporous materials, MOF is more vulnerable to the external pressure.[85–87] The excess amount of applied loading may cause irreversible phase change, pore collapse, and even amorphization to a MOF.[13] Unlike above-mentioned stabilities related to a single external stimulus, hydrothermal stability is assessed under a more complicated environment combining the presences of water, high temperature and, sometimes, high pressure. Such condition is often closer to that for real applications and post-synthetic modifications.

2.5 MOF-Guest Systems and Derivatives

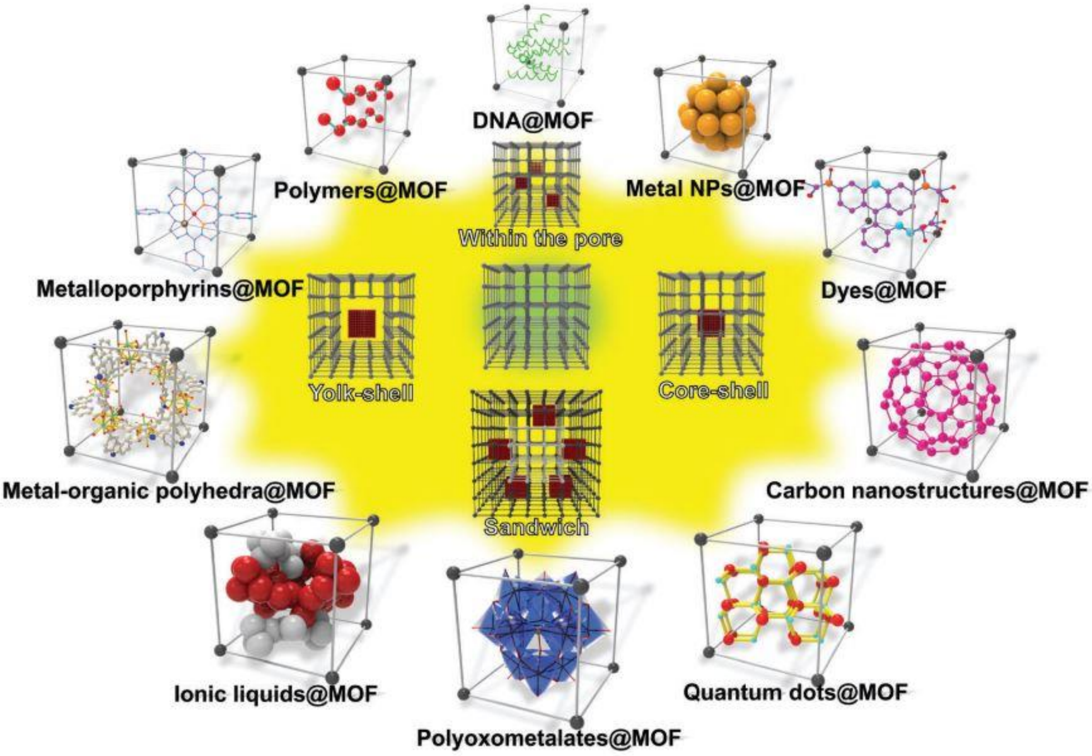

Figure 2.4 The state-of-the-art of MOF-based Composites: materials being incorporated and their distributions in the MOF matrix. Host-guest systems based on MOFs is shown as "within the pore" arrangement in the figure. The figure is reproduced from the recent review written by Li *et al.* with permission from ref. 8 (Copyright 2017 The Royal Society of Chemistry).

Incorporating materials in MOF matrix to form MOF-based composites has been extensively developed (Figure 2.4). For further details about the state-of-the-art of MOF-based composites, numerous reviews are available.[8,9,88–93] Loading guest entities inside MOF's pore (*e.g.* cavity and/or channel) to form **host-guest systems (*i.e.* MOF-guest systems or MOF-guest composites)**, which is shown as "within the pore" structure arrangement, is one major subset of MOF-based composites. The concept is transferred from the host-guest systems based on inorganic nanoporous crystals (*e.g.* zeolites) due to the parallelism between the inorganic and metal-organic porous frameworks, *e.g.* tridirectional and open porous.[8,9,21,22,27]

In general, materials with high surface energy are thermodynamically unfavourable. Therefore, the instability of MOFs is inevitably contributed by their ultra-high surface area. Guests incorporation (*e.g.* solvents in the as-synthesized MOFs) can effectively stabilise the MOFs by mitigating the surface energy penalty, particularly for the 1st generation MOF (categorized by Kitagawa *et al.*[14,63]). In order to synthesize MOF-guest systems that are energetically feasible, the change in surface/interface energy should be briefly considered.[94] This includes any significant non-bonding interactions (*e.g.* hydrophobicity), hydrogen bonding and chemical bonding between MOFs and guests. Furthermore, if the driving force for the growth of guests exceeds the bonding strength within the MOFs, the oversize guests can impinge the MOF pores leading to structure partial collapse.

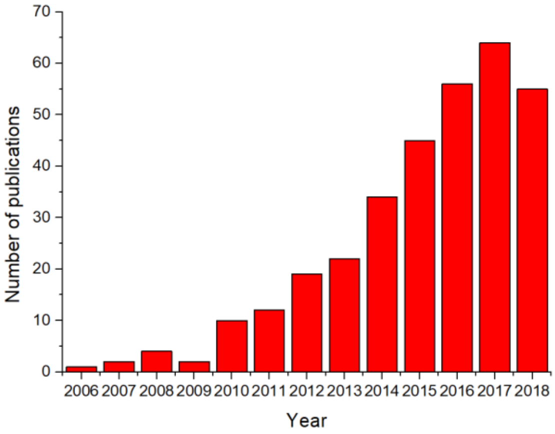

Figure 2.5 Publication statistics about "host guest MOF" provided by Web of Science in September 2018.[95]

At the beginning of the 21st century, development of MOF-guest systems started soon after the extensive research about MOFs. The publication about "host guest MOF" is experiencing a steady growth since 2006 (Figure 2.5). As an early stage exploration, organometallic compounds were directly incorporated in MOF by Fisher *et al.*[96–98] via solvent-assisted or solvent-free vapour-phase impregnation. These organometallic compounds then serve as the precursors to form metals and metal oxides in MOF to form metal@MOF and oxide@MOF composites.[9,21,22,99,100] Similar to guest@zelite systems, the MOF matrix can effectively immobilize the guest compounds and prevent agglomeration/fusion.[8,22] Such metal/oxide nanostructure stabilization is found to be useful for heterogeneous catalysis where the high active surface is favoured.[8,9,21,22] Apart from metal and oxide guests, GaN@MOF has also been prepared.[99]

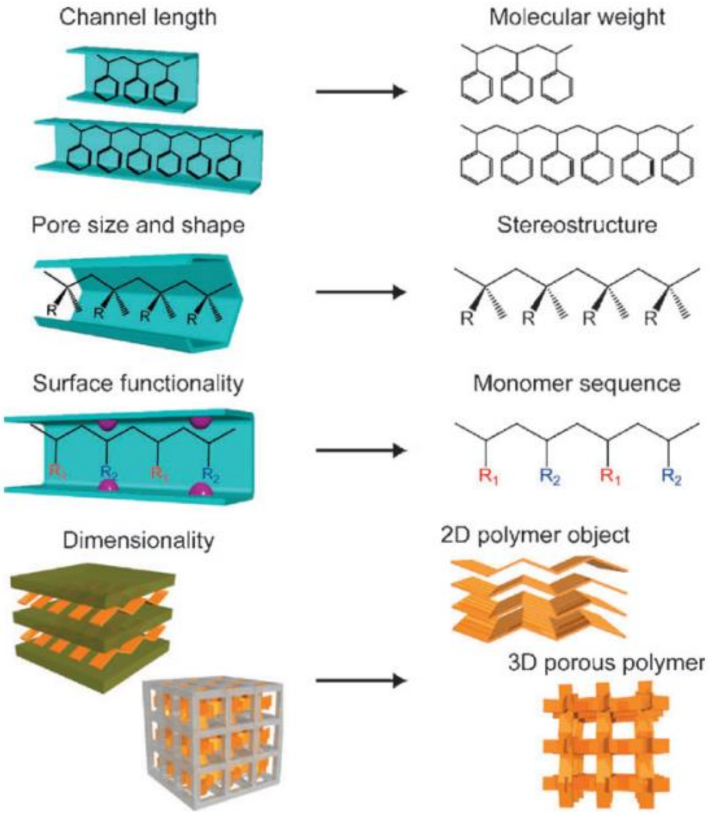

Figure 2.6 Controllable polymeric guests in polymer@MOF systems. The figure is reproduced from the review contributed by Uemura and Kitagawa *et al.* with permission from ref. 101 (Copyright 2009 The Royal Society of Chemistry).

In parallel to the impregnation of organometallics for guest@MOF synthesis, other catalytically active moieties such as metallorganic molecules[9,22] and polyoxometalates (POMs)[102] have been loaded in MOF as a way to heterogenize the homogeneous catalysts, *e.g.* Eddaoudi *et al.* encapsulated a porphyrin in a zeolite-like MOF to catalyse cyclohexane oxidation.[103] The MOF hosts have been found not only to stabilise the active guests but sometimes also enhance the catalytic activity.[8,22] For more comprehensive overviews about MOF-guest systems for catalysis, the author recommends numerous reviews covering this topic.[7,22,59,60,89,1049] Besides catalysis, the impregnation of large organic molecules in MOFs has drawn a substantial amount of attention by groups interested in tuneable optics/photoluminescence[27,105–107]. The photo-stability, non-linear properties and luminescent properties of MOFs, therefore, become important. The tuneable luminescent properties in MOF-guest composites have also been explored for guests made with quantum dots.[8,88,89,100,108] Additionally, development of MOF-polymer systems (*i.e.* polymer@MOF) led by Uemura and Kitagawa *et al.*[92,101,109] are towards the controlled polymerization inside MOFs. So far, using MOF's nanochannel to control molecular weight, stereostructure, and monomer sequence have been either proposed and/or realised (Figure 2.6).[92,101,109–111]

MOFs can also serve as removable templates to form free guest nanostructures after recovery, as some MOFs can be removed (*e.g.* via dissolution) under mild conditions. Such template-assisted guest nanostructure formation has been used in oxide@MOF[112,113] (*a.k.a.* nano-casting) and polymer@MOF systems[114–116]. Meanwhile, the metal-organic nature of MOFs enables the formation of oxides (via calcination) or carbon-based (via carbonisation) derivatives at elevate temperatures.[80–84,117–121] Although MOFs' calcined or carbonised derivatives have been extensively developed for energy storage and catalysis, fewer examples can be found for MOF-guest composites.[122]

2.6 MOF-Guest Systems Preparation

If the guest materials were predetermined, to experimentally prepare MOF-guest systems, several factors should be considered, including MOF stability (*e.g.* thermally and chemically), MOF pore size (particularly aperture size), functional group on MOF ligand, guest stability, guest size (particularly the longest dimension), functional group on guest and other physical properties of guest (*e.g.* boiling point). Several reviews have covered the general strategies to prepare the MOF-guest systems.[8,9,91,123]

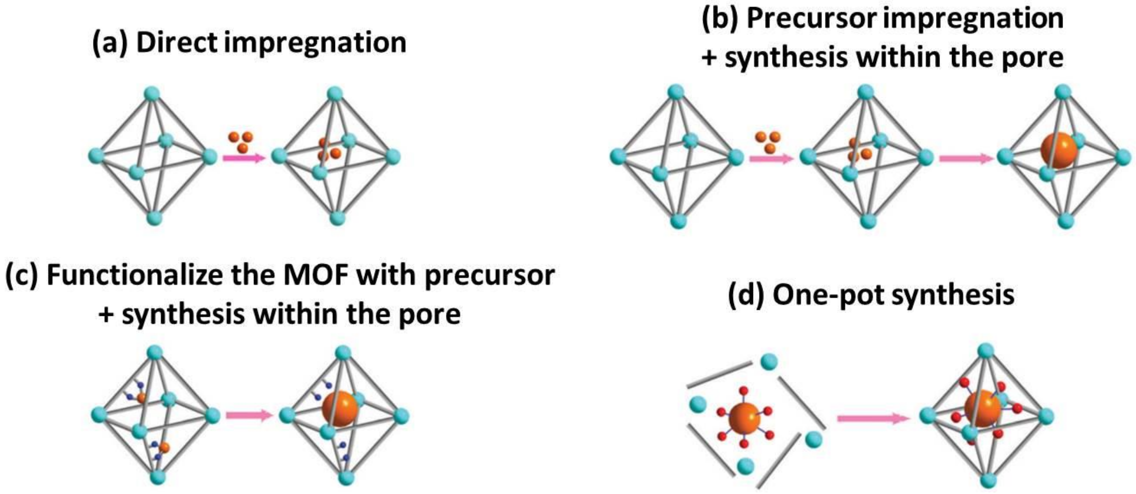

Figure 2.7 Common approaches to obtain MOF-guest composites. The figure is modified from the work contributed by Li *et al.* with permissions from ref. 8,124 (Copyright 2014 and 2017 The Royal Society of Chemistry).

If guests were smaller or similar to the MOF aperture size, direct impregnation (Figure 2.7a) is a preferable approach due to its simplicity. Guests that are mobile (large diffusion, *e.g.* liquid or gas) can be adsorbed by MOFs. For the gaseous guests, several well-established vapour-phase deposition methods [e.g. chemical vapour deposition (CVD)[91,94] and atomic layer deposition (ALD)[125]] have been adopted. To achieve the mobile states of guests, heating up the guests are often necessary during the direct impregnation. Therefore, reasonable thermal and high-temperature chemical stability are required for MOFs. If (i) the melting or boiling points of guests were higher than the highest temperature MOFs can endure or (ii) guests can decompose easily by heating, then alternative direct impregnation methods (*e.g.* solid grinding or solvent assisting) should be considered.[91] However, mechanical mixing can damage the MOF structure leading to amorphization;[85–87] solvent-assisting impregnation is often restricted by the guest solubility and influenced by different MOF-guest (*i.e.* solute) and MOF-solvent interactions thus yielding low and less controlled loading concentration.[9] More recently, direct impregnation was also reported for guests much larger than the MOF's apertures. This was achieved by opening the aperture via temporary linker detachment to allow the guest migration and restoring the MOF structure after guest impregnation.[126,127]

Nonetheless, the most preferred strategy to incorporate large guests is precursor impregnation followed by the guest formation inside the MOF pore (Figure 2.7b).[8,9,21,22,91,123,124] It is also known as "ship-in-a-bottle synthesis"[9] due to its significance for the ship-in-a-bottle system preparation. Since precursors are also effectively small guests, precursor impregnation is essentially the same as the aforementioned direct guest impregnation. Metal or oxide guests can be formed via decomposition, photochemical and redox reactions; polymer guests are synthesized through polymerization reactions.[8,9] To improve the guest placement in MOFs (*i.e.* more uniform distribution), precursors can be immobilized on the MOFs by chemical grafting[124,128,129] or electrostatic interactions[130,131] (Figure 2.7c). Functionalizing MOFs with precursors, however, only work for a small fraction of MOFs with *special chemistries* (*e.g.*, building blocks with functional groups or electrical charge).

Besides post-synthetic modifications, where MOFs are formed prior to guest loading, MOF-guest systems can also be prepared by one-pot synthesis (Figure 2.7d).[132,133] During this synthesis, MOFs can lock the guests within its framework during the growth. However, since guests can agglomerate particularly for those without physical hindrance (*e.g.* steric or electrostatic), they usually cannot be accommodated inside MOF pores. Instead, MOFs will grow around the guest moieties forming yolk-shell or core-shell MOF-based composites (Figure 2.4).[8]

2.7 Current Challenges for MOF-Guest Research

Although several general strategies to prepare MOF-guest systems have been established, experimental research about the MOF-guest systems is still considered to be challenging.[8,9,21,27] Therefore, the field maintains its attractiveness with large publication proportion (> 20%) in top chemistry and materials science journals as analysed by Web of Science in September 2018 on the topic "host guest MOF"[95] (6.17% in Journal of the American Chemical Society, 4.87% in Angewandte Chemie, 2.92% in Chemical Communications, 2.60% in Chemistry of Materials, 2.27% in Chemical Science and 1.62% in Journal of Physical Chemistry Letters).

According to Corma *et al.*[9] and Li *et al.*[8], there are four major challenges in MOF-guest preparation, namely pore size, MOF stability, control of loading and characterisation of guests inside MOFs.

Pore size: MOFs have small apertures. The typical aperture diameter of MOF (without MOF-MOF interpenetration[8,12]) is 5-20 Å (though some MOF can have aperture as large as ~ 100 Å). The small aperture inevitably restricts the guest size for direct impregnation and the precursor size for ship-in-a-bottle synthesis. Therefore, chemicals that are used for bulk synthesis and particle synthesis in free systems often cannot work for the guests.

MOF stability: As mentioned in Section 2.3, MOFs are generally considered to have poor stability. Therefore, chemicals (*e.g.* precursor, solvent and redox reagent) and conditions (*e.g.* temperature and pressure) applied to prepare MOF-guest systems are likely to damage the framework.[8,12] To minimize the risk of MOF degradation during guest incorporation, the MOF candidate should be carefully selected based available stability data from the literature and/or simple experiments. Furthermore, characterizations (*e.g.* XRD) are necessary to confirm the presence of MOFs after the MOF-guest formation. Additionally, MOF stability will also influence further exploration on MOF-guest application. For a MOF-guest with poor MOF stability, the derivative of the MOF-guest (via *e.g.* carbonization) is considered for applications.

Control of loading: Here, the control refers to location/distribution (relative to the MOF), precise composition (i.e. identity and purity), structure (e.g. crystalline or amorphous) and morphology of the as-formed guests.[4,8,12] At this stage, there are two major challenges to control the guest location/distribution: (i) to achieve homogeneous distribution and (ii) to ensure the guests can only form inside the MOF rather than depositing a significant fraction on the MOF surface. Although chemically grafting the MOF with guests or precursors (mentioned in Section 2.5) can effectively solve the distribution dilemma, the strategy only applicable to the MOFs with additional functionality.

MOF-guest characterisation: Although there are numerous techniques known to find out the chemistry and structure information for host-guest systems based on nanoporous materials,[4,9] it is still a challenge to characterise MOF-guest systems owing to (i) small guest size (*e.g.* 2 nm in diameter), (ii) poor MOF host stability, and (iii) signal interference from the MOF host. Powder XRD is a common tool to check the presence of a crystalline compound but it often fails to find the guests, which has been attributed to the small cluster/particle size.[9] Transmission electron microscopy (TEM) is capable to directly visualise the guest clusters/nanoparticles.[134] The electron beam from TEM, however, may damage the MOFs which can be revealed by the coarsened guests.[9] Furthermore, spectroscopy techniques (e.g. FTIR, Raman, nuclear magnetic resonance (NMR) and terahertz) can provide some indirect evidences about the guests, significant signal interference sometimes occurs which increase the uncertainty of the measurements.

2.8 Vision and Objectives of the Thesis

Motivated by the aforementioned geometric confinement, quantum confinement, MOF-guest interaction, and recent advancement in synthesis and characterisation in nanoscience and MOFs, there are three major objectives for each project covered in the thesis:

(i) To improve the existing MOF-guest preparation methods or to develop novel approaches for this challenging area.

(ii) To explore the novel aspects about influence of MOF or guest on each other, which is associated with nanoconfinement and MOF-guest interaction.

(iii) To develop novel functional materials based on MOF-guest systems for several applications including energy storage and heterogeneous catalysis.

These objectives are built into the recent development of host-guest chemistry (or inclusion chemistry). The host, however, is shifting from pure inorganic to metal-organic hybrid systems. With more diverse chemistries for both host and guest, novel physics, chemistry and materials science are expected. Hence, the ultimate goal is to provide an experimental and theoretical foundation for MOF-based host-guest systems potentially for a range of discoveries and applications.

Chapter 3

General Methodology

Chapter 3: General Methodology

3.1 MOF Synthesis

Stock and Biswas have provided a fairly comprehensive review about the synthesis of MOFs.[135] The most popular approach involves the mixing of reaction reagents (*i.e.* metal salts and organic linkers) with controlled temperatures. Solvents, such as DMF, ethanol, methanol and water, are usually added for the synthesis.[135] Additionally, structure-directing agents (*e.g.* benzene[136] and organic amines[137]) and additives (or modulators)[138,139] have been used to control the pore structure and crystal morphology respectively.[140–142] Although numerous MOFs have been successfully prepared at room temperature, elevated temperatures (typically between 50 °C and 150 °C) are often applied. To provide additional pressure to assist the MOF formation, the reaction can take place in sealed containers such as Teflon-lined autoclaves (for a typical solvothermal reaction) and borosilicate reaction bottles with screw caps. As complementary methods, microwave radiation, electrochemistry, mechanochemistry and ultrasonication have been reported to prepare MOFs.[135]

Activation is an important process for open-porous MOFs to achieve high pore volume by removing the entrapped solvent molecules.[143] Apart from the conventional activation method, which involves either direct heating or solvent exchange followed by the thermal treatment under vacuum or inert gas, supercritical CO_2 exchange, freeze-drying and chemical treatment (*e.g.* acid wash) are also used.

In this thesis, MOFs were prepared in solvents (*e.g.* DMF, water or ethanol) at controlled temperatures. Additives (*e.g.* formic acid) are sometimes added to achieve the desired structure. The reactions took place either in sealed containers (*i.e.* Teflon-lined autoclaves or borosilicate reaction bottles) or in the round-bottom flask under reflux. The as-synthesized MOFs were activated by solvent exchange and a sequential thermal treatment under vacuum or inert gas.

3.2 X-Ray Diffraction (XRD)

X-ray refers to the electromagnetic radiation with wavelength roughly between 0.1 Å and 100 Å, which falls into the similar spatial range to the interatomic distance of materials.[144] When the X-ray enters into a material, it can be scattered by the electrons of the atoms within the material. X-ray diffraction occurs when the scattered X-rays from coherent source (no change in wavelength) form constructive interferences, *i.e.* amplitudes of X-rays add together due to the phase separation of integer numbers of the wavelength.[144,145] Taking the scattering from two adjacent lattice planes as an example (shown in Figure 3.1a), constructive interference takes place when:

$$n\lambda = 2d\sin\theta \qquad \text{Equation (3.1)}$$

where, n is an integer number, λ is the wavelength, d is the interplanar space and θ corresponds to an angle between the incident beam and the diffracted beam which is indicated in Figure 3.1a. The diffraction due to constructive interference can therefore be summarised by Bragg’s Law:

$$n\lambda = 2d_{hkl}\sin\theta_{hkl} \qquad \text{Equation (3.2)}$$

where, h, k and l are the integer numbers to describe a family of lattice planes (*a.k.a.* Miller indices).[145]

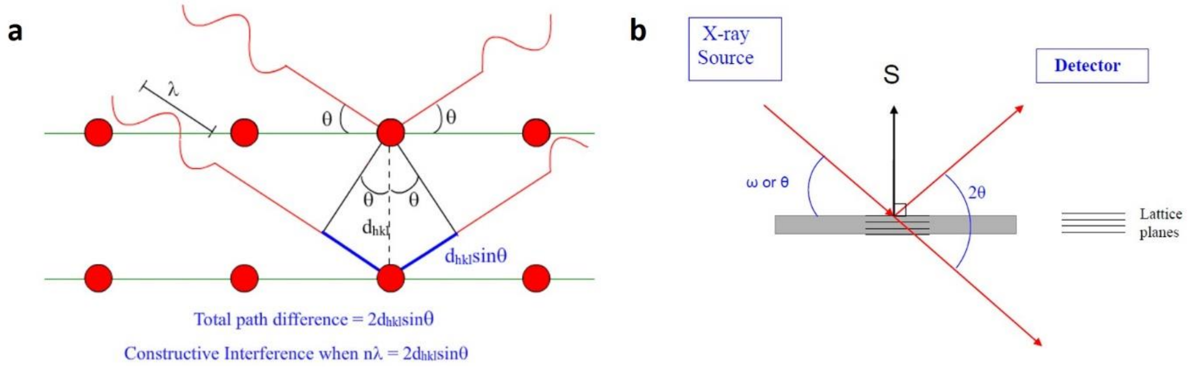

Figure 3.1 Basics for X-ray diffraction: (a) constructive interference from two adjacent lattice planes and (b) schematic powder X-ray diffractometer set-up in reflection mode. The figure is reproduced with permissions from DoITPoMS[144] and Dr M. E. Vickers[146] respectively.

X-rays for diffraction can be generated by bombarding a metal target with accelerating electrons produced from a heated tungsten filament. The as-produced X-rays contain both a continuous spectrum of X-rays (*a.k.a.* Bremsstrahlung radiation) and intense characteristic radiations with well-defined wavelengths. Cu and Mo are common targets for X-ray generation with average wavelengths of 1.5418 Å (Cu Kα) and 0.7107 Å (Mo Kα). To achieve a single characteristic X-ray wavelength for diffraction (*i.e.* minimising wavelength-induced information duplication) a filter (screening by radiation adsorption) or a monochromator (screening by diffraction) is added. Other methods to achieve monochromatisation include placing Si/W mirrors to enhance the characteristic radiation and using detectors with energy discrimination function.[146]

The majority X-ray diffraction experiments included in the thesis are powder X-ray diffraction (PXRD). The powder form of a crystalline material consists crystals with all possible orientations. The X-rays scattered from the same family of lattice plane of different crystals can therefore point to different directions. As a result, unlike single-crystal diffraction that forms diffraction spots in 2 dimensions, the diffraction pattern for PXRD consists rings in 2 dimensions. The continuous diffraction rings are revealed as peaks in 1 dimension corresponding to the 2θ angles defined by the Bragg's Law.[144] The PXRD patterns can be obtained by the diffractometer in reflection mode as shown in Figure 3.1b.

Since X-rays can penetrate deeper into the samples at higher 2θ angles, controls are made to maintain the constant X-ray interaction volume at various 2θ angles during the measurements: (i) to prepare sufficiently thin sample on the single-crystal silicon flat-plate support and (ii) to keep illumination area unaltered. Samples are also rotated (*e.g.* 30 revolutions per minute) to optimise the sampling uniformity.[146]

The collected PXRD pattern can be further analysed with refinement methods, namely Le Bail, Pawley and Rietveld. The key difference amongst these refinement methods are the peak intensity fitting. In Le Bail method, all the peak intensities are pre-set to an arbitrary value; as for Pawley refinement, simple mathematical fitting strategies (*e.g.* least-squares fitting) are applied to fit the peak intensities. The Rietveld refinement, however, fitting the peak intensities based on the structure factor, F_{hkl}, which is calculated based on i atoms in a unit cell:[146]

$$\mathrm{F}_{hkl} = \sum_i N_i f_i e^{[2\pi i(hx_i + ky_i + lz_i)]} e^{-M_i} \qquad \text{Equation (3.3)}$$

where, N_i is site occupancy factor, f_i is scattering factor, M_i is thermal parameter. x_i, y_i and z_i are coordinates; h, k and l are Miller indices. Essentially, a structural model is required for Rietveld refinement.[147]

3.3 Thermogravimetric Analysis (TGA)

Thermogravimetry often refers to a technique investigating the change in weight of a sample as a function of temperature.[148] In some circumstances, the change in mass of a sample versus time is also reported. The relevant thermogravimetric analysis (TGA) can be performed either isothermally (*i.e.* temperature unaltered) or dynamically (*i.e.* temperature altered). TGA can provide information about several physical and chemical events, including vaporisation, sublimation, absorption, adsorption, desorption, chemisorption, desolvation, decomposition, oxidation, etc.

To achieve reasonable TGA results, one needs to have (i) a balance with good precision; (ii) a furnace to alter and control the temperature; (iii) a temperature probe to monitor the real-time *in situ* temperature and (iv) a controlled atmosphere.[148] The results from TGA can be presented not only by weight versus temperature or time but also by rate of loss of weight versus temperature (*i.e.* differential thermogravimetric curve). Here, the rate of loss of weight is defined as the change of weight due to the incremental change of temperature.

In this thesis, TGA results were obtained by measuring the weight loss at constant heating rate (e.g. 10 ºC/min). Ar is used for thermal decomposition analysis whereas air is applied for combustion (oxidation) study. Note that since the thermogravimetry measurements are kinetic processes where the characteristic temperatures for the physical/chemical phenomena depend on the heating rate, these temperatures can deviate from the standard values in the literature.[148]

3.4 Gas Adsorption

By monitoring the amount of gas molecules loaded into open-porous materials information about pore structure/size and interior surface area can be obtained.[149] The gas adsorption characterisations often reply on the physisorption due to weak interactions (e.g. Van der Waals attraction) between the adsorbate and the material. Chemisorption may also occur during the measurement but is less common. The popular gases used for gas adsorption includes N_2, Ar, CO_2 and Kr.

In a typical gas adsorption measurement, the sample is degassed beforehand and then exposed to the gas at the critical liquid temperature of the gas. The amount of adsorbed gas is measured against incremental change in pressure (*i.e.* pressure steps) normally increasing from the lower end to P_0 (the critical pressure for free gas condensation to occur) first then dropping back to the low pressures.

The results are usually presented as an isotherm plot with the normalised quantity of gas adsorbed versus relative equilibrium pressure, P/P_0. The IUPAC report[150] covers six types of adsorption isotherms for physisorption (shown in Figure 3.2). Amongst these six types, the most common and representing types are Type I, II and IV.[149] The concave shape in Type I isotherm indicates the domination of micropores (pore dimension of less than 2 nm) where hardly any further adsorption can be achieved after the completion of monolayer adsorption. Unlike Type I isotherm, Type II isotherm has a second turning point (inflection) at high P/P_0, which corresponds to the multilayer adsorption. Type II isotherm is commonly found in non-porous or macroporous materials (pore dimension of much larger than 50 nm). The key difference between Type I & II isotherms and Type IV isotherm is the presence of hysteresis, which comes from capillary condensation of the gas molecules. Type IV isotherm are typically associated with the domination of mesopores and small macropores (i.e. pore dimension of 2-100 nm).[150]

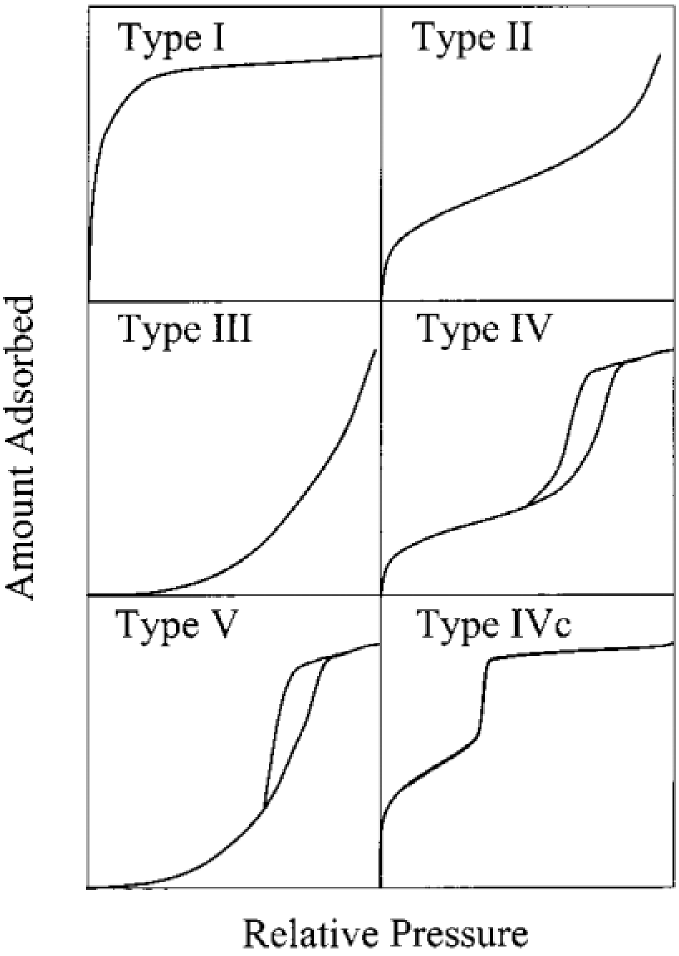

Figure 3.2 Common types for physisorption isotherms. The figure is reproduced from the review provided by Jaroniec *et al.* with permission from ref. 151 (Copyright 2001 American Chemical Society). The IUPAC standard was first published in ref 150.

The most popular method to quantify surface area of the mesoporous samples from the gas adsorption experiments is the Brunauer-Emmett-Teller (BET) approach[152], which is considering multilayer adsorption based on the monolayer adsorption model (i.e. Langmuir model). The core assumption of BET method is that both gas condensation and multi-molecular adsorption share the same forces. By equating the rate of condensation on the adsorbed layer and the rate of gasification from the layer,[149] a linear formula can be achieved by plotting $\frac{1}{Q(\frac{P_0}{P}-1)}$ as a linear function of $\frac{P}{P_0}$:

$$\frac{1}{Q(\frac{P_0}{P}-1)} = \frac{c-1}{Q_m c}\left(\frac{P}{P_0}\right) + \frac{1}{Q_m c} \qquad \text{Equation (3.4)}$$

where, Q is the specific quantity of N_2 adsorbed (cm^3/g), Q_m is the specific quantity of N_2 adsorbed to form a monolayer on the sample, P is the applied pressure, P_0 is the maximum pressure applied, and c is the BET constant. Since Q and $\frac{P}{P_0}$ were experimentally measured, Q_m can be determined from the slope, $\frac{c-1}{Q_m c}$, and the y-intercept, $\frac{1}{Q_m c}$ of the linear plot:

$$Q_m = \frac{1}{\left(\frac{c-1}{Q_m c}+\frac{1}{Q_m c}\right)} \qquad \text{Equation (3.5)}$$

The specific surface area, S (m^2/g), can then be obtained:

$$S = \frac{Q_m N_A s}{V} \qquad \text{Equation (3.6)}$$

where, N_A is Avogadro's number, s is the adsorption cross-sectional area of N_2 (0.162 nm^2)[153] and V is the molar volume of N_2, which is ~22,400 cm^3/mol under standard temperature and pressure (STP). Apart from BET model, other theories such as Barrett-Joyner-Halenda (BJH) theory[154] and density functional theory (DFT)[155] have been developed to assess the surface area and pore distribution.[149]

3.5 Some X-Ray Spectroscopy Techniques

3.5.1 X-Ray Photoelectron Spectroscopy (XPS)

When the sufficiently energetic electromagnetic waves radiate a compound, the photoelectrons can be emitted from the sample which is known as the photoelectric effect. X-ray photoelectron spectroscopy (XPS)[156] is a technique to analyse the energy distributions of the photoelectrons from X-ray-irradiated materials.[157] Similar to the X-ray source for

PXRD, the X-rays used for XPS are normally monochromatic (typically Al or Mg Kα emissions). The detector is used to collect the kinetic energy spectrum of the emitted photoelectrons, where the specific electron kinetic energy can be expressed as E_k. Based on energy conservation, the specific electron binding energy, E_b, can be derived:

$$\mathrm{E}_b = \mathrm{E}_{h\nu} - \mathrm{E}_{\phi} - \mathrm{E}_k \qquad \text{Equation (3.7)}$$

where, $\mathrm{E}_{h\nu}$ is the incident X-ray energy and E_{ϕ} is a correction constant for solid effect (*e.g.* work function). The energy of incident X-rays for XPS ranges from tens of eV to tens of keV but the lower end is commonly used due to the easier access to the less powerful X-ray sources. Since weak X-rays can only interact with the top a few layers of a compound, XPS is widely used to study the surface chemistry of materials. In most circumstances, high or ultrahigh vacuum is required to optimise the photoelectron detection, particularly for the electrons with low kinetic energy.[158]

XPS can be used to identify the presence of elements in a compound, as each element can emit photoelectrons with a set of characteristic kinetic energies which are revealed as peaks in the XPS spectrum (signal counts versus binding energy). These energies are associated with the electronic configuration of the element.[157,158] Furthermore, with the support of controlled experiments and available database, XPS can also provide some indications about the local bonding environment of the element (*i.e.* chemical shift).[157,158] Since XPS with weak X-ray sources can hardly characterise the inner part of a bulk sample, ion beam can be used to etch away the surface part of the sample thus expose the inner part to the incident X-ray. For a sample with poor electric conductivity, flood gun with low-energy charge carriers (*e.g.* electron and ion) can be employed to compensate the accumulated photoelectrons on the sample surface.

3.5.2 X-Ray Absorption Spectroscopy (XAS)

X-ray absorption occurs when a core electron receives sufficient photo-energy to be reach the ionisation level. By considering the wave-particle duality, this energetic electron can be considered as a wave which can be scattered by the neighbouring atoms. Since this ionisation process can last longer than the duration for the scattered waves to be bounced back, the superposition between the emitted electron wave and the scattered waves can take place. The related wave interferences can be either constructive or destructive, which depends on wavelength of the electron, distance between two atoms (the X-ray absorbing atom and a neighbouring atom) and number of orbital electrons in these two atoms.[158] Such interferences can further influence the X-ray absorption process (*i.e.* core electrons excited to become photoelectrons).

Since in most cases the inter-atomic distance and the electron number can be assumed to be unaltered for a solid-state sample, the interferences will be determined by the wavelength of the electron from the ionisation, which carries energy given by the incident X-ray. By changing the energy of incident X-ray, an interference-modulated absorption spectrum can therefore be produced.[158] As a result, an X-ray absorption spectroscopy (XAS) spectrum can contains both information about the absorption edge for ionisation and numerous absorption maxima and minima in the post-edge regime due to the interferences.

The relationship between the wavelength of the photoelectron, $\lambda_{electron}$, and its kinetic energy, $\mathrm{E}_{electron}$, can be expressed by a combination of Planck-Einstein relation and de Broglie hypothesis:

$$\lambda_{electron} = \frac{hc}{\mathrm{E}_{electron}} \qquad \text{Equation (3.8)}$$

where, h is the Planck constant; and c is the speed of light. There are two major techniques for XAS analysis, which focus on different $\mathrm{E}_{electron}$, namely X-ray absorption near edge structure (XANES, typically from absorption edge to less than 50 eV above the ionisation threshold) and extended X-ray absorption fine structure (EXAFS, typically more than 50 eV above the ionisation threshold).[158]

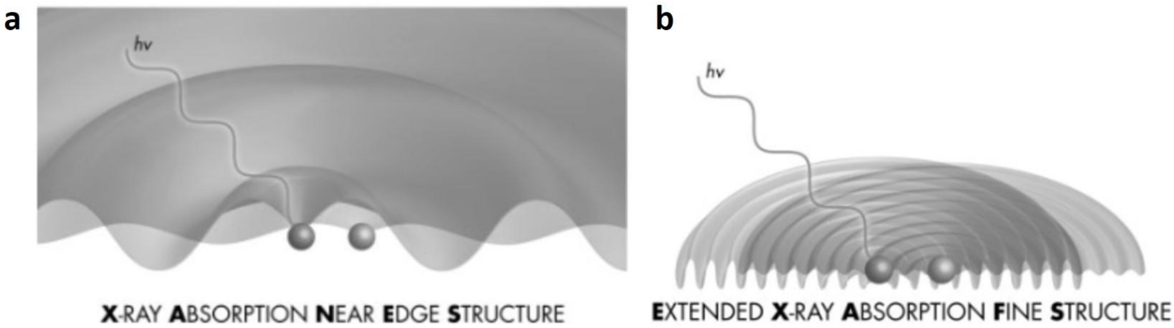

Figure 3.3 2-dimensional wave-form schematics of the photoelectrons for (a) XANES technique and (b) EXAFS technique in proximity to the X-ray absorbing atoms and the neighbouring atoms. The figure is reproduced from the review written by Guo *et al.* with permission from ref. 158 (Copyright 2009 John Wiley and Sons).

Since the XANES technique covers the incident X-rays that are less energetic, the corresponding emitted electrons have wavelength often longer than the interatomic distance (shown in Figure 3.3a).[158] The multiple scattering from neighbour atoms can occur which renders the XANES to be more sensitive to the surrounding atom arrangement (*e.g.* geometry of a molecule). Since the absorption edge is solely influenced by the X-ray absorbing atom, the XANES can reveal the electronic features (*e.g.* oxidation state) of the X-ray absorbing atom.[158] However, it is very challenging to deconvolute the information about local atom arrangement from the XANES overall results. In contrast, EXAFS considers more energetic excited electrons with wavelength often shorter than the interatomic distance (shown in Figure 3.3b).[158] This effectively obtains the information with predominantly single scattering from the neighbouring atoms, which simplifies the structure simulation. Meanwhile, EXAFS can be element specific, as it only contains information about the core-level electrons of the X-ray absorbing atom. Hence, EXAFS is a powerful technique to reveal the neighbouring atom arrangement with respect to the X-ray absorbing atom. Additionally, EXAFS results can be interpreted in real space via spline and background subtraction and Fourier transformation, which shows the interatomic distance distribution.[158]

3.6 Some Electron Microscopy Techniques

3.6.1 Scanning Electron Microscopy (SEM) and Transmission Electron Microscopy (TEM)

To overcome the diffraction limit of optical microscopy which restricts the spatial resolution for imaging, electron with short wavelengths (considering wave-particle duality) are used as the source in electron microscopy. The electron wavelengths, λ_e, can be tuned by changing the accelerating voltage of the electron, V_e with a relativistic correction:[159]

$$\lambda_e = \frac{1}{1+\frac{e\mathrm{V}_e}{2\mathrm{m}_e c^2}} \qquad \text{Equation (3.9)}$$

where, e is the electron charge and m_e is the effective electron mass. The electron from the source (*i.e.* primary electron) can be generated by either thermionic emission (heating a conducting material like tungsten) or by field emission (applying strong electric field on a conducting material to trigger electron tunnelling). The as-produced electron is accelerated under an electric field to gain additional kinetic energy (*i.e.* short electron wavelength). Its trajectory is controlled by the electromagnetic lenses under Lorentz force to achieve focus on a desired location. There are three major types of aberration that may deteriorate the image quality:[160] spherical aberration (due to the uncertainty in primary electron spatial distribution), chromatic aberration (due to the uncertainty in primary electron energy) and astigmatism (due to the instrumentation limit in lens and/or presence of floating particles). Apertures can be used to minimise the spherical aberration and chromatic aberration by block out the unwanted primary electrons. The astigmatism can be corrected by a stigmator.[159]

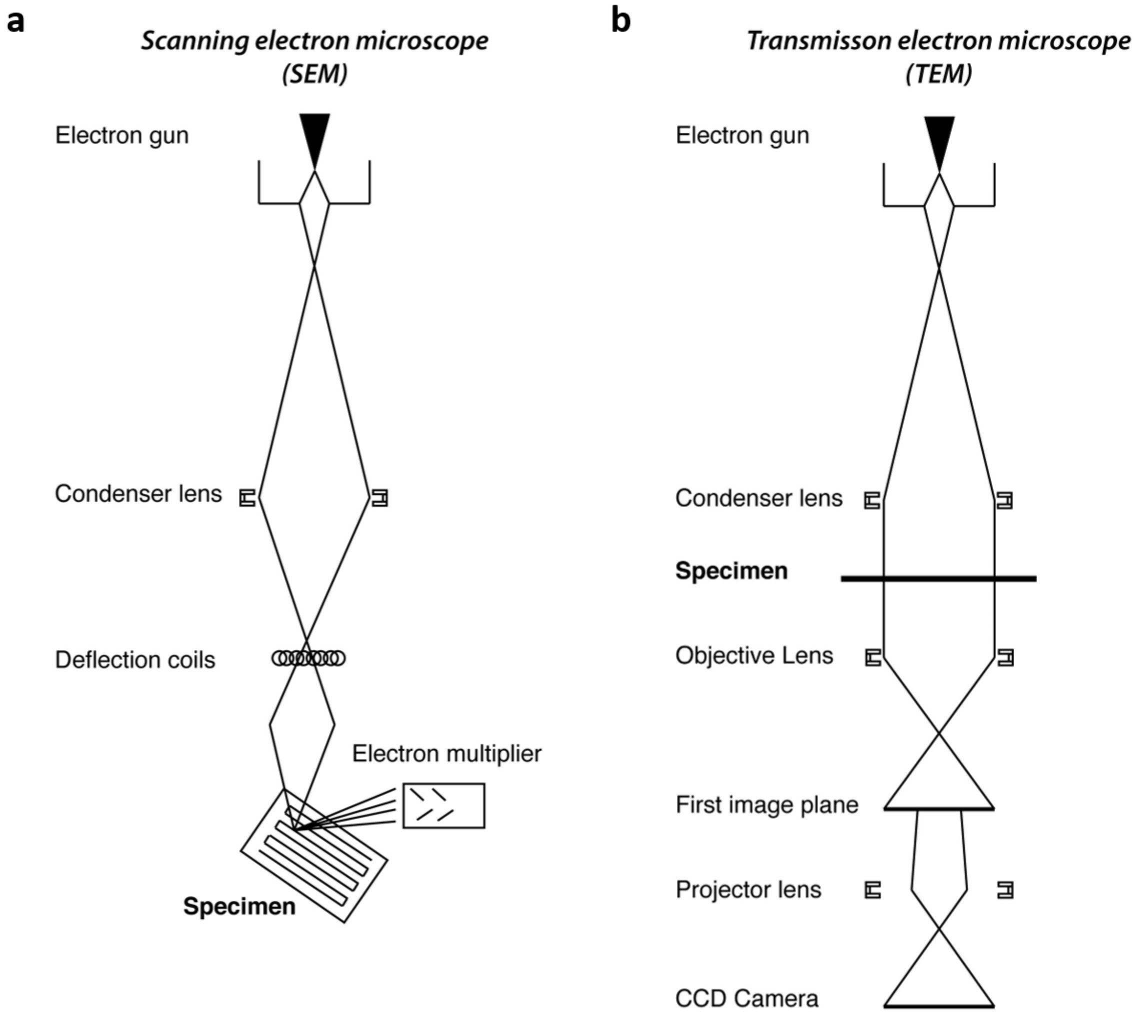

Figure 3.4 Figure 3.4 Schematics for (a) SEM and (b) TEM. The figure is reproduced with permission from Dr Harald Hagendorfer[161].

Apart from the specimens being places in different locations in SEM and TEM, another key difference between them is that SEM as a set of deflection coils (Figure 3.4a). These coils allow the SEM to perform a scanning over the sample surface. SEM mainly detect secondary electron (SE) and backscattered electron (BSE) for imaging.[159] SEs with low kinetic energy are knocked off by the more energetic primary or scattered electrons from the outer shells of the atoms.[159] Since the SEs are more easily to lose the kinetic energy for escape, only those close to the specimen surface can be detected. Therefore, imagines obtained with SEs contain information close to the surface and topography sensitive.[162] BSEs are primary electrons after numerous elastic and inelastic scattering events.[159] The energy loss during the scattering will depend on the composition of the specimen (*i.e.* element sensitive). Since BSEs are still relatively more energetic than SEs, BSEs further beneath the surface can still be detected. As a result, BSE images have information less close to the surface with compositional contrast.[162]

TEM detects the electrons passing through a sample (Figure 3.4b). Hence, the specimen is required to be sufficiently thin and transparent to the primary electrons. Since electron carries charge and mass, it can interact strongly with both nuclei and electrons in an atom. Its wavelength which is typically 10^{-12} m enables electron diffraction to occur when it goes through the sample. Therefore, the primary electron can either penetrate the specimen without being significantly scattered or be diffracted. A TEM image generated from undiffracted electrons is called bright-field (BF) image whereas a TEM image made from diffracted electrons is referred as dark-field (DF) image.[159] The contrast of a TEM image can come from mass (composition), thickness, local diffraction property and phase of electron waves (more than one beam in use, *e.g.* high-resolution TEM). Scanning transmission electron microscopy (STEM) adopts the scanning function into TEM by rearranging the components and adding the scanning coils. As for STEM imaging, apart from BF and DF (*i.e.* annular dark field, ADF) options, high-angle inelastically scattered can also be collected for imagining (*i.e.* high-angular annular dark field, HAADF).[163]

3.6.2 Energy-Dispersive X-Ray Spectroscopy (EDS), Electron Energy Loss Spectroscopy (EELS) and Cathodoluminescence (CL) Spectroscopy

EDS is a powerful microanalysis unit built into an electron microscope. It can be used to determine the presence of elements and relative quantity of the elements and to map the elemental distribution over an electron microscopy image.[159,164] EDS replies on the generation of characteristic and Bremsstrahlung X-rays from the interactions between the primary electron and the specimen, which is very similar to the mechanism of X-ray source for XRD mentioned in Section 2.2. The characteristic radiations come from the electron transitions between orbits in an atom. These electrons come from the atoms and are excited to the outer-shell orbitals by bombardments of electrons with large kinetic energy. Therefore, the energy of the generated characteristic X-ray is element dependent.[159] In contrast, Bremsstrahlung X-rays are mainly produced by the Coulomb scattering of primary electrons.[159] To detect the generated X-rays, semiconducting materials with p-i-n junction (*e.g.* lithium-doped silicon) are used to convert the received X-rays into electron-hole pairs.[159] EDS works well for heavy elements but requires sufficient kinetic energy for the incident primary electrons to produce the characteristic X-rays.[159] Since X-rays can be generated by all sorts of electrons with sufficient kinetic energy (*e.g.* primary electrons, secondary electrons and backscattered electrons), the sampling volume for EDS can be quite large even with small primary electron beam size. This significantly limits the spatial resolution for EDS mapping.

An alternative approach to obtain chemical information with an electron microscope with improved spatial resolution is EELS, which analyses energy loss of electrons passing through the specimen.[165,166] The spatial resolution of EELS depends on the electron beam size.[167,168] It is, however, only available for TEM.[169] The energy distribution of as-received electrons can be sorted by a magnetic prism which deflects the electrons under a static magnetic field. Since the electron energy loss for EELS is mainly associated with the energy required for an electron to be knocked off from its shell, the energy loss distribution has absorption edges which is also element dependent. Light elements with simpler electron energy loss mechanisms usually give rise to sharp and clear absorption edges. Hence, EELS works better for light elements.[159]

Similar to EDS, CL spectroscopy analyse the photos emitted from a specimen by injecting electrons into it. However, the photo-emission of CL replies on the electron-hole recombination, where the electrons are excited by other electrons or photos with much lower kinetic energy compared to primary electrons.[170] CL coupled with electron microscopy can provide high spatial resolution. CL can provide information about the band structure of a semiconducting materials. With good control in experiments, CL can also be used for compositional or defect mapping.[170]

Chapter 4

Poly(3,4-Ethylenedioxythiophene)@MOF (PEDOT@MOF) and Nanostructured PEDOT Derived from It

Chapter 4: Poly(3,4-Ethylenedioxythiophene)@MOF (PEDOT@MOF) and Nanostructured PEDOT Derived from It

4.1 Initiations, Collaborations, Outcomes, Research Funding

The work was carried out as a continuation of Mr June Sang Lee's MPhil project about synthesising polypyrrole@MOF (PPy@MOF) electrochemically but as an independent case study led by the author (first-author). When Mr Lee was about to finish his study in Cambridge in October 2015, the supervisor of Mr Lee and the author, Dr Stoyan K. Smoukov suggested the author to finalise his work. Some initial attempts to electrochemically polymerise PPy inside a MOF were not very successful. However, after a conversation with the visiting scholar Dr Meisam Farajollahi, the author quickly realised that chemically polymerise PEDOT in MOF could be more promising and had not been reported before. As a consequence, the project about PEDOT@MOF started after a meeting with Dr Smoukov in January 2016. The project was supervised by Dr Stoyan K. Smoukov and advised by Prof. Anthony K. Cheetham.

As close collaborations, the author worked with Dr Meisam Farajollahi from Prof. John D.W. Madden's group (The University of British Columbia) who is an expert in PEDOT synthesis and applications and with Dr Sneha R. Bajpe from Prof. Cheetham's group (University of Cambridge) on MOF synthesis. Prof. Sebastian Henke (Ruhr University Bochum) gave good advice on MOF characterisation. He also performed Pawley fittings for the powder XRD results collected. Dr Tongtong Zhu (University of Cambridge) and the author performed current-voltage measurements with an atomic force microscope (AFM) attached with an electrically conducting tip. They also performed cathodoluminescence (CL) characterisation together on the samples. Dr Shijing Sun (University of Cambridge) characterized the samples' mechanical properties using nanoindentation. Dr Jonathan S. Barnard (University of Cambridge) and the author worked on TEM characterisation of the samples. Finally, Dr Suman-Lata Sahonta, Mr David Nicol and Mr Simon J. Griggs are acknowledged here for their kind assistance in using Raman spectrometer and scanning electron microscopy (SEM). **Unless stated in the experimental and results otherwise the work was accomplished by me.**

The work covered in this chapter was published in Materials Horizons in 2016, which was also selected as the Front cover of Materials Horizons (issue 1 in 2017, Figure 4.1).

Tiesheng Wang, Meisam Farajollahi, Sebastian Henke, Tongtong Zhu, Sneha R. Bajpe, Shijing Sun, Jonathan S. Barnard, June Sang Lee, John D.W. Madden, Anthony K. Cheetham, Stoyan K. Smoukov*, ***Functional Conductive Nanomaterials via Polymerisation in Nano-channels: PEDOT in a MOF***, doi: 10.1039/C6MH00230G, **Materials Horizons**, 2017, 4 (1), pp 64–71

Note that this is an open access article published under a Creative Commons Attribution (CC-BY) License, which permits unrestricted use, distribution and reproduction in any medium, provided the author and source are cited.

Materials
Horizons

Figure 4.1 Front cover of Materials Horizons (issue 1 in 2017, doi: 10.1039/C6MH00230G) to promote the work of this chapter. The figure is reproduced with permission (Copyright 2017 The Royal Society of Chemistry)

This project was funded through the European Research Council (ERC) grant (grant number: EMATTER 280078) as well as a Discovery Grant from The Natural Sciences and Engineering Research Council of Canada (NSERC). In the period of the project, the author was funded by the China Scholarship Council (CSC) and supported by the Engineering and Physical Sciences Research Council (EPSRC) Centre for Doctoral Training in Sensor Technologies and Applications (EP/L015889/1 and 1566990). Prof. Anthony K. Cheetham was supported by the Ras Al Khaimah Centre for Advanced Materials (RAK-CAM). Prof. Sebastian Henke was funded by the Alexander von Humboldt Foundation. Dr Shijing Sun and Dr Jonathan S. Barnard were supported by the Cambridge Overseas Trust and the Isaac Newton Trust, respectively.

4.2 Introduction

MOF's nano-sized channels and diverse chemistries open the possibility to control the molecular weight, stereostructure, monomer sequence and as-polymerised nanostructure of polymeric guests (mentioned in Chapter 2.5).[101,171–174] Vinyl monomers (*e.g.* styrene, methyl methacrylate, vinyl acetate, divinylbenzene and acrylonitrile), which can form polymer simply through free radical polymerisation or co-polymerisation, have been extensively used to study the polymer@MOF systems.[111,171,175–180] These common structural polymers, however, often have no additional functionality, such as electrical conductivity and luminescent capability. Conducting polymers, which has delocalised electrons for electrical conduction, have also been incorporated in the MOF, such as polypyrrole[181,182], poly(N-vinylcarbazole)[183], polyaniline[184], polymethylpropylsilane[185] and polythiophene[174]. One of the primary interests to prepare polymer@MOF systems is to create a pathway to conduct electrons through conducting polymer guests which could improve the MOFs' conductivity. Furthermore, by using MOFs as removable templates, one could obtain nanostructured electrically conductive polymers that could be useful for sensor[186,187], redox-based supercapacitor[188] and electrocatalyst[189].

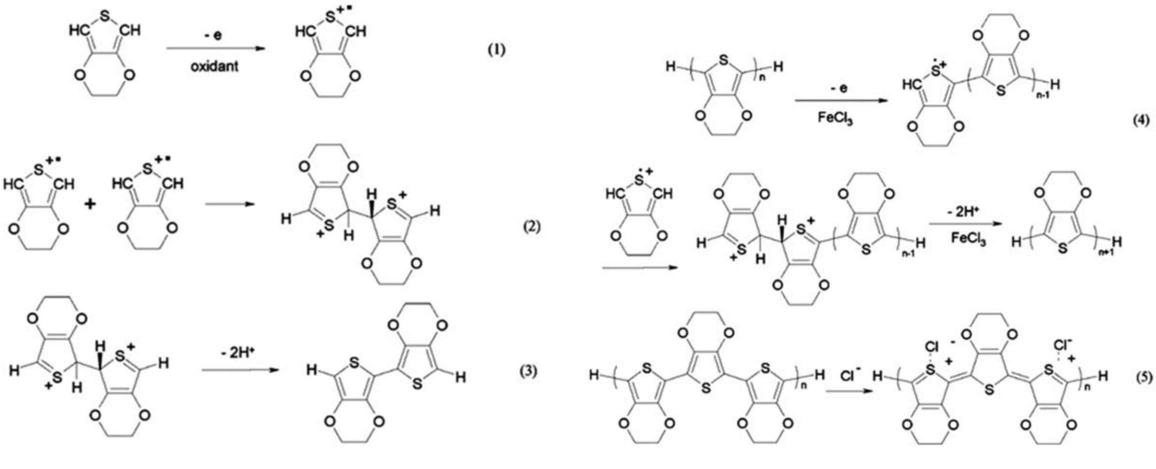

Figure 4.2 Chemical synthesis and chemical doping of PEDOT[190]: (1) EDOT is oxidised by oxidants such as Fe^{3+} forming a cation radical. (2) Two $EDOT^{+}$ cation radicals join together as a dimer cation. (3) The dimer cation is electrically neutralised via deprotonation. (4) By repeating step 1-3, a PEDOT *n*-mer becomes *(n+1)*-mer via oxidation addition and deprotonation. (5) Ions, such as Cl^{-}, can be incorporated into or detach from the polymer reversibly (*i.e.* chemical doping). Such polymer is described as pseudocapacitive polymer, which is the foundation of polymer-based pseudocapacitor.[191] The figure is reproduced with permission from ref. 189 (Copyright 2007 American Chemical Society).

In this chapter, the use of poly(3,4-ethylenedioxythiophene) (PEDOT)[192] to make the polymer@MOF system was explored. PEDOT [commonly seen as the water-processible PEDOT: polystyrene sulfonate (PSS) form] is one of the extensively investigated conducting polymers due to its high chemical/electrochemical/thermal stability, biocompatibility, electrical conductivity and optical transparency.[193,194] However, at the time when the paper was published, PEDOT had not been reported for polymer@MOF systems.[114] Note that Uemura *et al.*[195] also published the preparation for PEDOT@MOF systems almost simultaneously. PEDOT can be synthesised from its monomer, 3,4-ethylenedioxythiophene (EDOT) through oxidative polymerisation either chemically[190,196,197] or electrochemically[198,199]. As shown in Figure 4.2, there are two major steps involved in the polymerisation reaction, namely oxidation and deprotonation. Oxidizing agents such as $FeCl_3$[114] and I_2[195] are selected for the oxidation step; Solvent such as water is commonly used as the proton acceptor during the synthesis.[200] Alternatively, PEDOT can be obtained via an organometallic dehalogenation polycondensation by mixing 2,5-dichloro-3,4-ethylenedioxythiophene with bis(1,5-cyclooctadiene)nickel(0), 2,2'-bipyridyl, and 1,5-cyclooctadiene.[201] However, the monomer, 2,5-dichloro-3,4-ethylenedioxythiophene, needs to be synthesised, which brings additionaly complexity to the polymer synthesis.

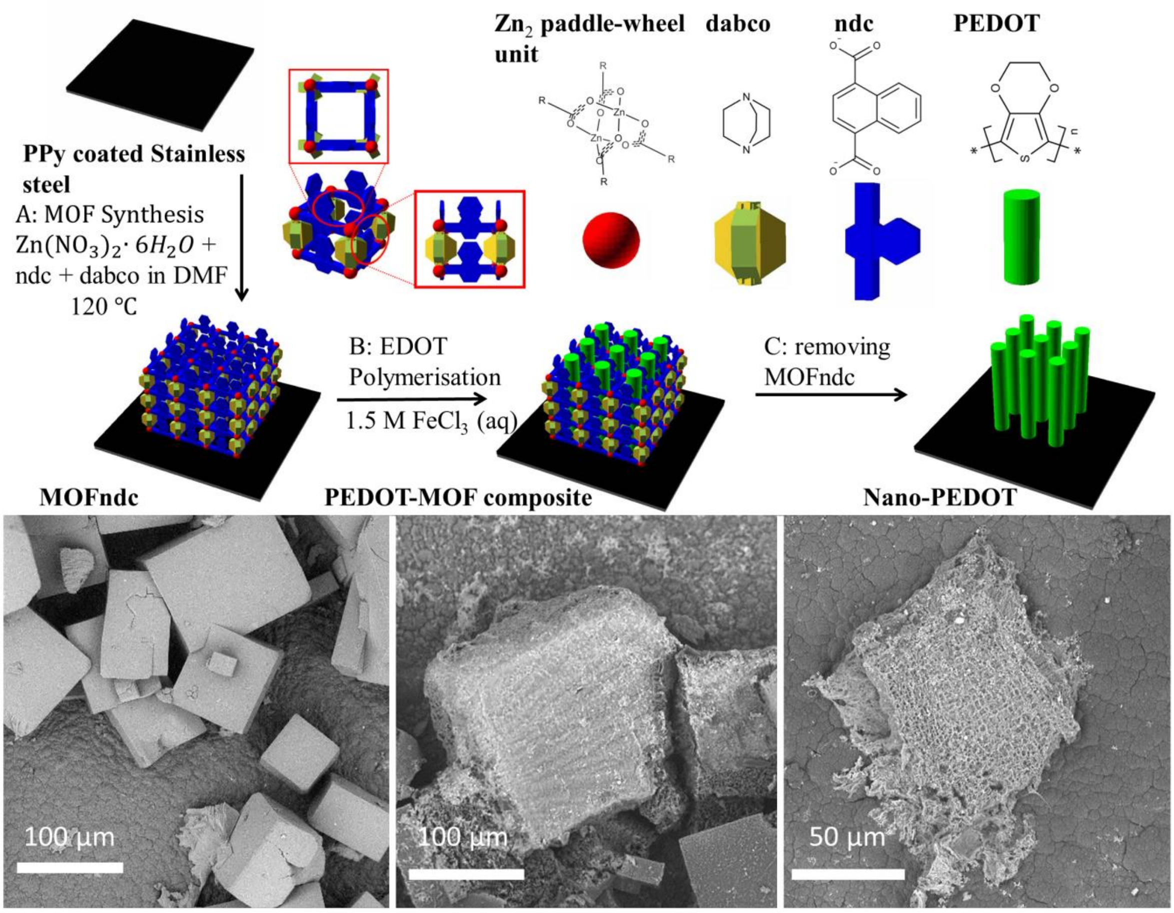

Figure 4.3 Schematic diagrams (software available from http://www.openscad.org/) to demonstrate the structure of MOFndc and the experimental steps in sequence for the work: synthesis of MOFndc on PPy coated stainless steel, chemical polymerization of EDOT in MOFndc to form PEDOT-MOF composite (*i.e.* PEDOT@MOFndc), and formation of nano-PEDOT after removing PEDOT. SEM with back-scattered electrons (SEM-BSE) images reveal the morphologies of the products at the steps A-C. The figure is reprinted under a Creative Commons Attribution 3.0 Unported Licence (CC BY 3.0) from ref. 114 (Copyright 2017 The Royal Society of Chemistry).

As for the MOF host, $Zn_2(1,4\text{-ndc})_2(dabco)$[202] (ndc = 1,4-naphthalenedicarboxylate, dabco = 1,4-diazabicyclo[2.2.2]octane), hereafter referred to as MOFndc, was used. As shown in Figure 4.3, while the dicarboxylate ligands (*i.e.* 1,4-ndc, in blue) link to Zn paddle-wheel units (in red) to form two-dimensional square grids (5.7 Å × 5.7 Å),[111,203] these layers stack on top each other connected by dabco ligands (in yellow) at the metal nodes.[202] In this way, the assembled squares form paralleled one-dimentional nanochannels. Additional, MOFndc and its homologues have been reported to have some degree of structural flexibility with regards to the pore dimensions upon taking up guest molecules.[204–206]

As a brief outline of experimental, results and discussion of this chapter, the PEDOT-MOF composite (*i.e.* PEDOT@MOFndc) was first prepared on PPy-coated steel substrate. The MOF host was then removed chemically to generate the nanostructured PEDOT (*i.e.* nano-PEDOT).

4.3 Experimental

Note that unless specified otherwise all the PEDOT@MOFndc and nano-PEDOT are on PPy-coated substrate.

4.3.1 Materials

HCl (aq, 37 wt%), NaOH (97+%), $LiClO_4$ (99+%), dabco (99+%), zinc nitrate hexahydrate [$Zn(NO_3)_2 \cdot 6H_2O$, 98+%], DMF (99.8%) and anhydrous $FeCl_3$ (98+%) were purchased from Sigma-Aldrich and used as received. PPy (98%) was also ordered from Sigma-Aldrich and distilled at ~160 °C before use. Acetonitrile (99.9%) and methanol (99.8%) were purchased from Fisher Scientific. 1,4-naphthalenedicarboxylic acid (H_2ndc, 99+%) was from Alfa Aesar. AISI 403 stainless steel was cut into 10×10 mm^2 square pieces for the substrates. EDOT (99%) was purchased from ACROS Organics™. Additionally, Milli-Q water (17 MΩ) was used.

4.3.2 Electrochemical Coating of PPy on Steel Substrate

PPy coated was achieved by Dr Meisam Farajollahi and me. PPy was polymerised on the steel substrate by electrochemical deposition (*i.e.* polymerisation). The deposition solution initially contains acetonitrile (as solvent), $LiClO_4$ (0.05 M), PPy (0.06 M) and distilled water (1 vol%). A piece of stainless-steel mesh served as a counter electrode and the AISI 403 stainless steel substrate was used as a working electrode. Deposition was performed at -20 ^{o}C by applying a constant current (0.125 mA/cm^2) for 8 hours. During the polymerisation process, PPy was deposited on the steel substrate. After deposition, the PPy film was rinsed with pure acetonitrile for 3 times followed by deionised water. The sample was dried under ambient condition. To compare the MOF grown on PPy-coated steel and on bare steel, one side of the stainless steel was masked with Kapton$^{©}$ tape during the PPy deposition. The tape was then removed to expose the bare steel surface.

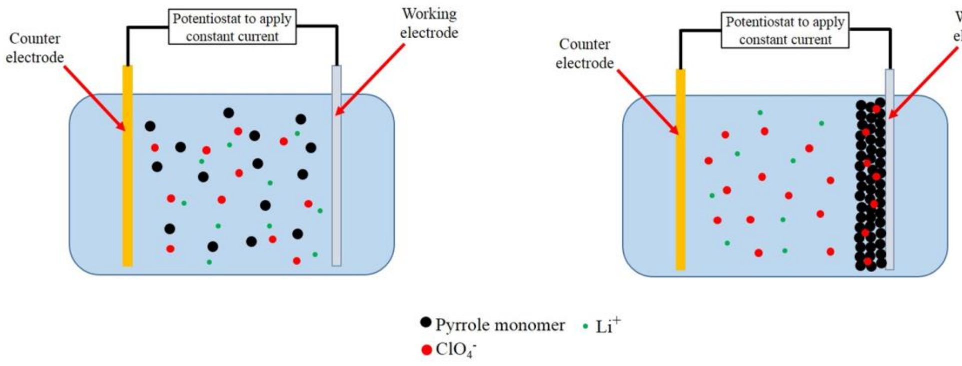

Figure 4.4 Schematic diagrams for the electrochemical deposition of PPy on the steel substrate. A two-probe setup with a working electrode (steel substrate) and a counter electrode (a piece of stainless steel mesh) was placed in an acetonitrile solution containing 1 vol% deionized water, PPy monomer and $LiClO_4$ as shown on the left. Driven by a constant voltage, electrochemical polymerisation of PPy occurred on the working electrode as shown on the right. The electrochemical polymerisation of PPy was initialised by June Sang Lee for his MPhil project. The method was adopted by Dr Meisam Farajollahi and the author for this work. The figure is reprinted under a Creative Commons Attribution 3.0 Unported Licence (CC BY 3.0) from ref. 114 (Copyright 2017 The Royal Society of Chemistry).

4.3.3 MOFndc Synthesis

The use of MOFndc was suggested by Prof. Sebastian Henke. The hydrothermal thesis was done by Dr Sneha R. Bajpe and me. MOFndc precursor solution was prepared first by mixing 0.42 mmol $Zn(NO_3)_2{\cdot}6H_2O$, 0.42 mmol ndc and 0.21 mmol dabco with 10 ml DMF. After stirring with magnetic stirrer for 10 min, the mixture was filtered. The filtrate solution was transferred to a Teflon-lined autoclave. The PPy-coated steel substrate was then immersed in the solution. The autoclave was properly sealed and kept at 120 °C for 48 hs in an oven. After the oven cooled down naturally to room temperature, the autoclave was opened to collect the MOFndc grown on the substrate. The MOF was rinsed with fresh MOF for three times and stored in fresh DMF at room temperature.

4.3.4 Preparing PEDOT@MOFndc

MOFndc was immersed for 1-2 hrs in methanol to replace DMF in the MOF with methanol. It was then dried at 150 °C under nitrogen flow for 1 h. The dried MOFndc was soaked with EDOT liquid for 4 hrs to achieve EDOT@MOFndc. To remove the excess EDOT (*i.e.* weakly adsorbed EDOT) on the MOF surface, the EDOT-MOFndc mixture was treated at 100 °C under nitrogen flow for 1 h.[195] The as-prepared EDOT@MOFndc was then immersed in the excess $FeCl_3$ (aq, 1.5 M) for 15 hrs to polymerised the EDOT to form PEDOT@MOFndc. After polymerisation the sample was rinsed with methanol for at least 3 times to remove non-polymerised EDOT, $FeCl_3$ and $FeCl_2$ (reduced from $FeCl_3$) and dried under ambient conditions.

4.3.5 Preparing Nano-PEDOT

To remove MOFndc template and to isolate nanostructured PEDOT (*i.e.* nano-PEDOT), PEDOT@MOFndc was immersed in HCl (aq, pH ~2) solution for 1 day followed by HCl (aq, pH ~4) solution for another day to prevent precipitation of $Fe(OH)_x$ as well as to gradually remove Zn_2 paddle-wheel units and dabco ligands. It was then transferred to deionised water for 2 hours followed by NaOH (aq, pH ~12) solution for more than 1 day to remove the rest of MOFndc. The sample was eventually rinsed with water and dried under ambient conditions.

4.3.6 Materials Characterisations

SEM-BSE and SEM-EDS: SEM-BSE images and SEM-EDS mappings were acquired on a Phenom ProX Desktop microscope at an accelerating voltage of 5-15 kV for BSE-SEM images and 15 kV for EDS mapping.

SEM with secondary electrons (SEM-SE): SEM-SE images were obtained using a FEI Nova NanoSEM™ with a field emission gun and a SE detector at 10 kV acceleration voltage.

SEM with focused ion beam (FIB): Sample’s cross-sections were prepared with a FEI Helios Nanolab SEM/FIB using a FIB and imaged using the in-situ SEM-SE at 10 kV acceleration voltage (field emission gun).

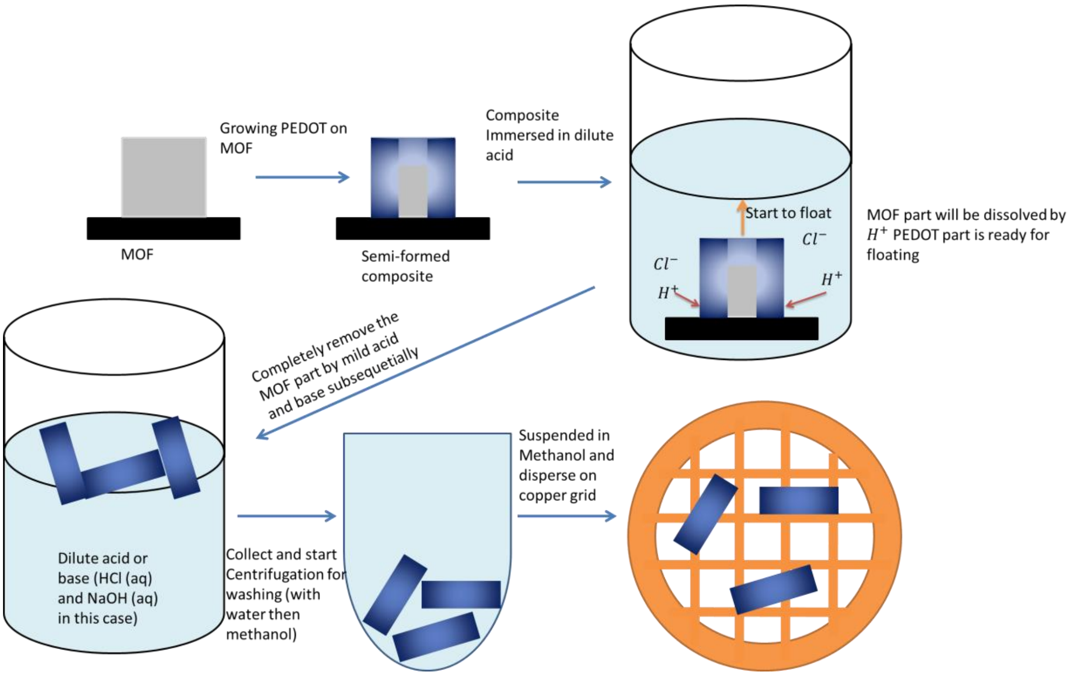

Figure 4.5 Steps for preparing the TEM sample. The figure is reprinted under a Creative Commons Attribution 3.0 Unported Licence (CC BY 3.0) from ref. 114 (Copyright 2017 The Royal Society of Chemistry).

Transmission electron microscopy (TEM) and TEM with electron energy loss spectroscopy (TEM-EELS): TEM images and TEM-EELS mappings were collected by Dr Jonathan S. Barnard and Tiesheng Wang using 200 kV FEI Tecnai™ F20 with a field emission gun. Nano-PEDOT sample was prepared in the following steps (Figure 4.5): PEDOT@MOFndc was placed in HCl (aq) followed by NaOH (aq). Those composite with PEDOT only formed in some part (mostly close to the surface) of MOF was attacked by the acid and the base gradually. Since those semi-formed composites have limited PEDOT connection to the substrate, they started to detach from the substrate after the MOF part was sufficiently dissolved. The detached material was collected by centrifugation and immersed in fresh acid and base respectively to remove the MOF. It was then rinsed with water and methanol. The prepared sample was suspended in methanol and loaded on the TEM copper grid by drop casting (100 μl).

Raman spectroscopy: Raman spectra were obtained using a silicon-calibrated Renishaw Ramascope-1000 with a 633 nm red laser source. To avoid signal interference from PPy, MOFndc, PEDOT@MOFndc and nano-PEDOT were removed from the PPy-coated steel substrate and placed on a bare glass (no Raman peaks). Background for the bare glass was subtracted for data collection.

Powder XRD: Powder X-ray diffraction patterns were collected on a Bruker D8 ADVANCE with 2θ from 4° to 55° and a step size of 0.05°.

Conductive AFM: Conductive AFM was used to measure I-V curves by Dr Tongtong Zhu and me. The conductive AFM is a Veeco Dimension 3100 with a linear current amplifier module with a range from 1 pA to 1µA. The measurement was in contact mode using Pt/Ir-coated silicon probes.

SEM-CL: Dr Tongtong Zhu and the author obtained CL spectra and images at 30 kV and room temperature in a Philips XL30 SEM equipped with a Gatan MonoCL4™ system. I-V curves were measured in the contact mode using Pt/Ir-coated silicon probes on a Veeco Dimension 3100 CAFM with a linear current amplifier module with a range from 1 pA to 1µA.

Nanoindentation: Nanoindentation was performed by Dr Shijing Sun at ambient conditions using an MTS NanoIndenter® XP. A sharp three-sided pyramidal Berkovich indenter (tip radius ~100 nm) was aligned normal the MOF. With a dynamic Continuous Stiffness Measurement (CSM) mode, as reported in previous work,[86,207] Young's moduli and hardnesses were deduced using the Oliver and Pharr method.[208]

4.4 Results and Discussion

4.4.1 Growing MOFndc on PPy-Coated Steel Substrate

Growing MOF-templated conducting polymer on a conducting substrate can be beneficial for characterisation (*e.g.* easier to handle than the powder and improving sample's electron conductivity for SEM imaging) and potential applications as electrode. The polyaniline support method reported by Lu *et al.*[184] was adopted to immobilize the MOFndc on PPy-coated steel substrate. The hypothesis about the enhanced immobilisation is that there can a stronger non-covalent interaction between PPy and organic ligands (*i.e.* dabco and/or ndc) than that between bare steel surface and the ligands. PPy was coated on the steel substrate via electrochemical deposition at -20 ^{o}C, as low temperature deposition produces films with good electrical and mechanical properties.[209,210] Acetonitrile with freezing (melting) point of -48 ^{o}C was used as the solvent for the electrolyte; $LiClO_4$ salt was used for increasing the ionic conductivity of the electrolyte. 1 vol% water was added to provide the terminating groups for the PEDOT polymer. The deposition was performed under constant current to control the deposition rate (*i.e.* amount of PPy formed on the substrate per unit time). The final PPy coating will be doped with Li^+ and ClO_4^- ions. As shown in Figure 4.6, the thickness of the film is 1 ± 0.5 μm from the cross-section of the film (Figure 4.6b). Meanwhile, the overall Raman spectra (Figure 4.6c) matches the result provided in the literature.[211]

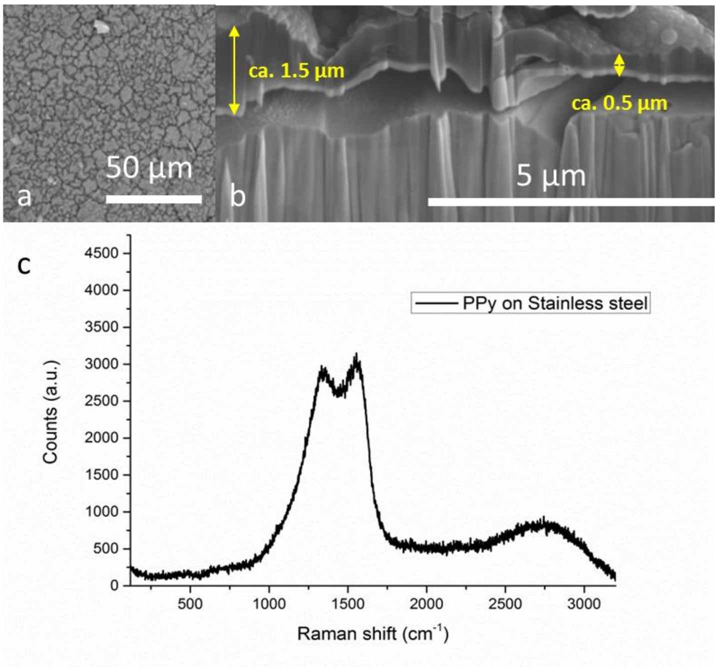

Figure 4.6 Deposited PPy: SEM images of (a) top view of the PPy film; (b) cross-sectional view of the PPy film on the steel substrate. (c) Raman spectra of PPy film. The figure is reprinted under a Creative Commons Attribution 3.0 Unported Licence (CC BY 3.0) from ref. 114 (Copyright 2017 The Royal Society of Chemistry).

Figure 4.7 Optical images of PPy-coated steel substrate (left hand side) and MOF crystals on a semi-coated substrate (right hand side). MOF crystals were immobilised on the coated part whereas tthe majority of MOF crystals on the bare steel surface disappear during the transfer. The figure is reprinted under a Creative Commons Attribution 3.0 Unported Licence (CC BY 3.0) from ref. 114 (Copyright 2017 The Royal Society of Chemistry).

After the hydrothermal growth, by simply collecting the substrate from the mother solution, the MOF crystals grown on the PPy coating was confirmed to have significantly better adhesion than those on the bare steel surface (Figure 4.7, right hand side). The PPy coating can mitigate the risk for MOFs to peel off during synthesis and transportation.

4.4.2 Structure Characterisation with Powder XRD

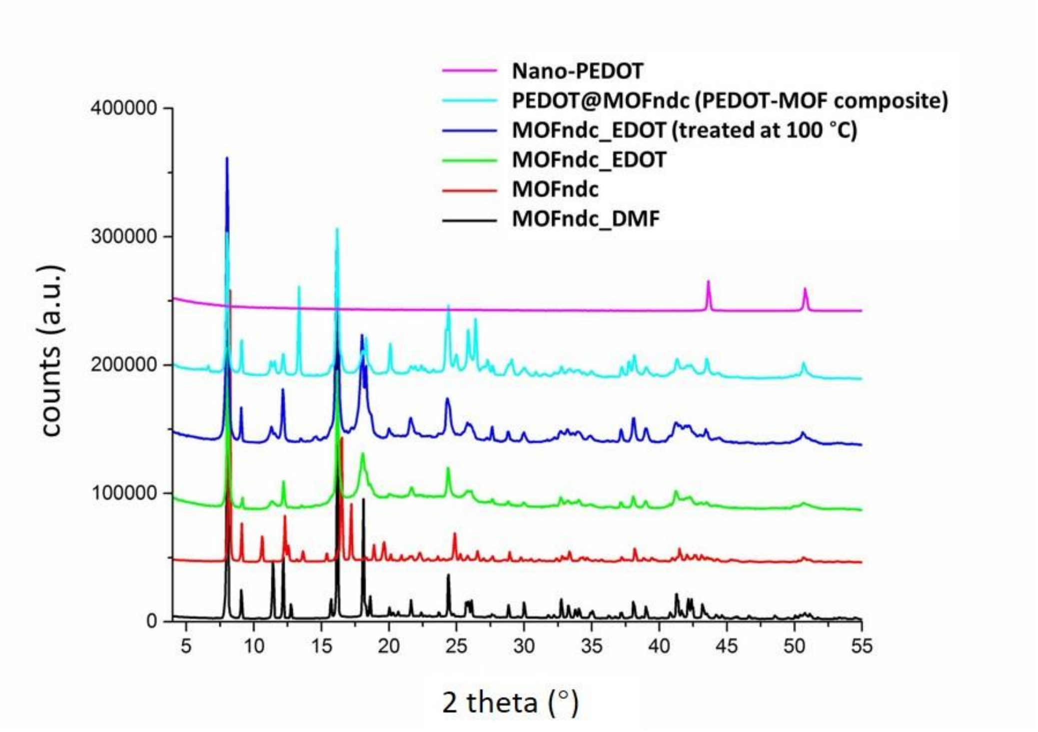

Figure 4.8 Overview about the powder XRD results for MOFndc/PEDOT-related systems. The figure is reprinted under a Creative Commons Attribution 3.0 Unported Licence (CC BY 3.0) from ref. 114 (Copyright 2017 The Royal Society of Chemistry).

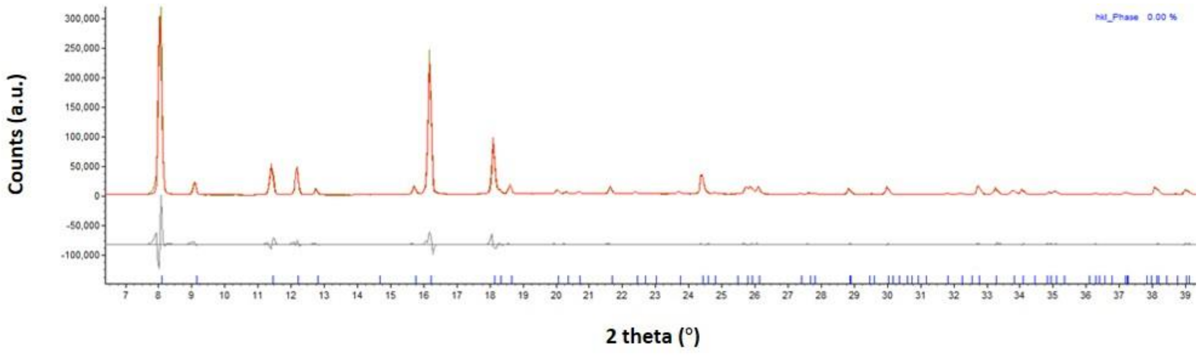

Figure 4.9 Pawley fit to the diffraction pattern of as-prepared MOFndc_DMF (space group *P4/mbm*, a = 15.4546(8) Å, c = 9.6714(9) Å; Rp = 9.28%, Rwp = 13.42%, Rexp = 1.16%). Experimental (in green), calculated (in red) and difference patterns (in grey) are shown. Positions

of allowed Bragg peaks are shown as blue tick marks. The fitting was performed by Prof. Sebastian Henke. The figure is reprinted under a Creative Commons Attribution 3.0 Unported Licence (CC BY 3.0) from ref. 114 (Copyright 2017 The Royal Society of Chemistry).

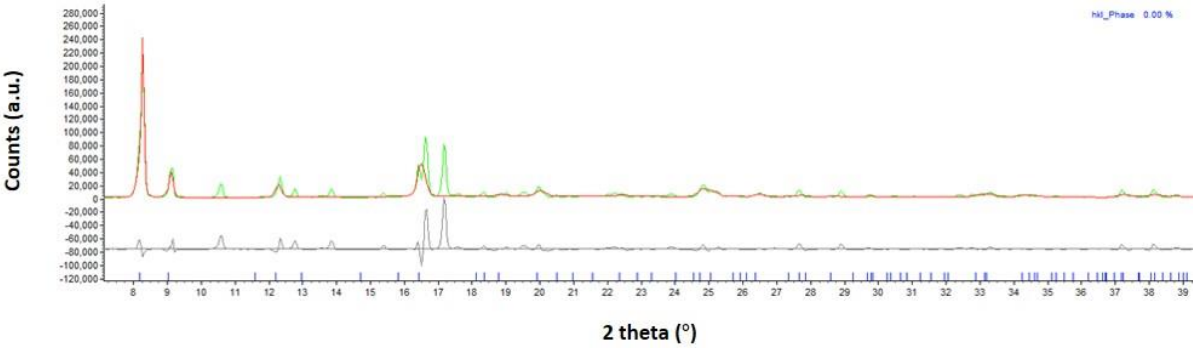

Figure 4.10 An attempt of a Pawley fit to the diffraction pattern of dried MOFndc with the *P4/mbm* space group and unit cell parameters similar to literature values. The data cannot be fitted to a satisfactory level in this space group, indicating a significant distortion of the structure as a consequence of (partial) loss of DMF upon drying. Experimental (in green), calculated (in red) and difference patterns (in grey) are shown. Guest dependent unit cell distortion has been reported for this family of MOF.[204,212] Positions of allowed Bragg peaks are shown as blue tick marks. The fitting was performed by Prof. Sebastian Henke. The figure is reprinted under a Creative Commons Attribution 3.0 Unported Licence (CC BY 3.0) from ref. 114 (Copyright 2017 The Royal Society of Chemistry).

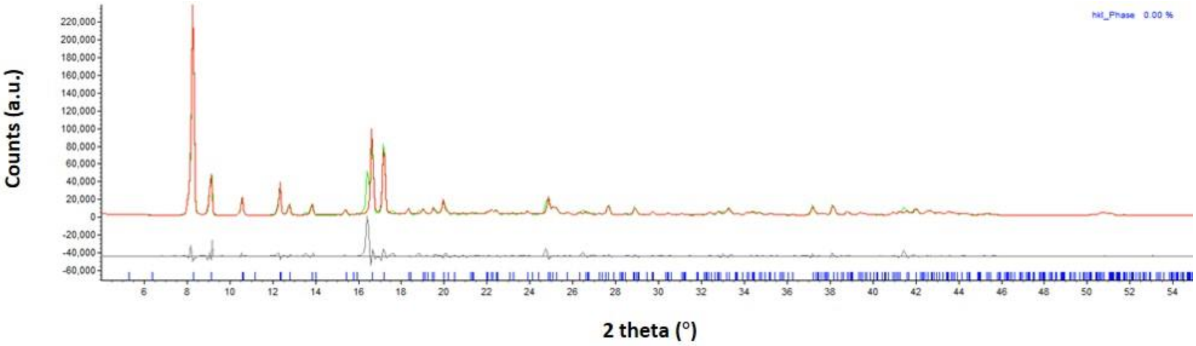

Figure 4.11 An attempt of a Pawley fit to the diffraction pattern of dried MOFndc with the orthorhombic space group *Pmmm* (*a* = 16.653(4) Å, *b* = 13.828(5) Å, *c* = 9.660(3) Å; R_p = 10.75%, R_{wp} = 18.32%, R_{exp} = 1.05%). A reflection at ~16.4º (2θ) could not be fit with the unit cell and space group which is likely due to impurities or a different phase. Experimental (in green), calculated (in red) and difference patterns (in grey) are shown. Positions of allowed Bragg peaks are shown as blue tick marks. The fitting was performed by Prof. Sebastian Henke. The figure is reprinted under a Creative Commons Attribution 3.0 Unported Licence (CC BY 3.0) from ref. 114 (Copyright 2017 The Royal Society of Chemistry).

Based on the available powder XRD results (Figure 4.8), Pawley fits were performed by Prof. Sebastian Henke with the TOPAS academic V5 program package. As mentioned in Section 3.2, Pawley fit is a method to refine the size and shape of the unit cell, the symmetry in space, and the angle-dependent peak shape by fitting the peaks with constrained peak positions. No structural mode is required for a Pawley fit.[146,147] The powder XRD pattern for as-prepared MOFndc (*i.e.* MOFndc_DMF, where DMF denotes the incorporated DMF solvent) matches well with the literature data (Figure 4.9) exhibiting the tetragonal space group *P*4/*mbm*.[206] Upon drying (*i.e.* solvents were removed from the MOF) MOFndc changes its structure as revealed by significant mismatch with the initial unit cell parameters and space group (Figure 4.10). Nonetheless, the pattern can be fit to a distorted orthorhombic unit cell in space group *Pmmm* (Figure 4.11) with TOPAS built-in function. This indicates that the square channels of MOFndc distort to rhombohedral-shaped channels upon solvent molecules removal, which has been reported for other MOFs in this family.[204,212]

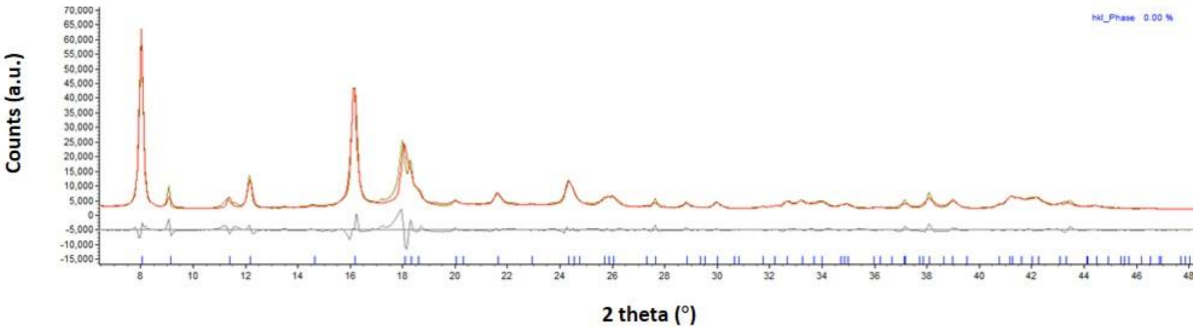

Figure 4.12 An attempt of a Pawley fit to the diffraction pattern of EDOT@ MOFndc (i.e. MOFndc_EDOT) (space group *P4/mmm*, *a* = 10.956(3) Å, *c* = 9.672(4) Å; R_p = 7.49%, R_{wp} = 11.15%, R_{exp} = 1.44%). Experimental, calculated and difference patterns are shown in dark yellow, red and grey, respectively. Positions of allowed Bragg peaks are shown as blue tick marks. The fitting was performed by Prof. Sebastian Henke. The figure is reprinted under a Creative Commons Attribution 3.0 Unported Licence (CC BY 3.0) from ref. 114 (Copyright 2017 The Royal Society of Chemistry).

The powder XRD patterns indicate significant structure change upon loss and/or exchange of the guest molecules (*e.g.* DMF and EDOT). The pattern for MOFndc_EDOT exhibits broader peaks (*i.e.* lower crystallinity) but could be still fit using a simple tetragonal unit cell in the high symmetry space group *P*4/*mmm* (Figure 4.12), which is similar to the DMF-impregnated MOFndc (Figure 4.9). The major peaks assigned to MOFndc are still retained in the pattern for PEDOT@MOFndc (Figure 4.8). This confirms that structurally intact MOFndc is still present after the polymerisation of EDOT. The diffraction pattern of the PEDOT@MOFndc, however, cannot be indexed in one of the unit cells used earlier. There are several differences in the pattern for PEDOT@MOFndc (Figures 4.8) compared to those for as-prepared MOFndc (Figures 4.9) and MOFndc_EDOT (Figure 4.12). New peaks can be seen at ~ 13.3°, ~24.2 °, and ~26.4 ° (Figures 4.8). Therefore, the PEDOT-MOF composite is likely to be a composite containing numerous phases. The additional peaks may also attribute to partially decomposed MOFndc and/or the polymer chains presented in the nanochannels. As for the nano-PEDOT sample, there are only two peaks assigned for the steel substrate owing to (i) extremely small amount of nano-PEDOT on the substrate (*i.e.* only a few on the entire substrate) and/or (ii) its disordered structure.

4.4.3 Chemistry and Morphology Characterisations

Since MOFndc has Zn but not S whereas PEDOT has S but not Zn (Figure 4.3), these two materials can be distinguished by element sensitive tools (*e.g.* EDS and EELS). EDS is sensitive to heavier elements, so it is suitable to detect the presence of S (relative atomic mass = 32.06 u) and Zn (relative atomic mass = 65.38 u). With SEM-EDS, MOFndc (Figure 4.13a) with only Zn, PEDOT@MOFndc with both Zn and S (Figure 4.13b), and nano-PEDOT (*i.e.* after MOFndc removal) with only S (Figure 4.13c) have been confirmed.

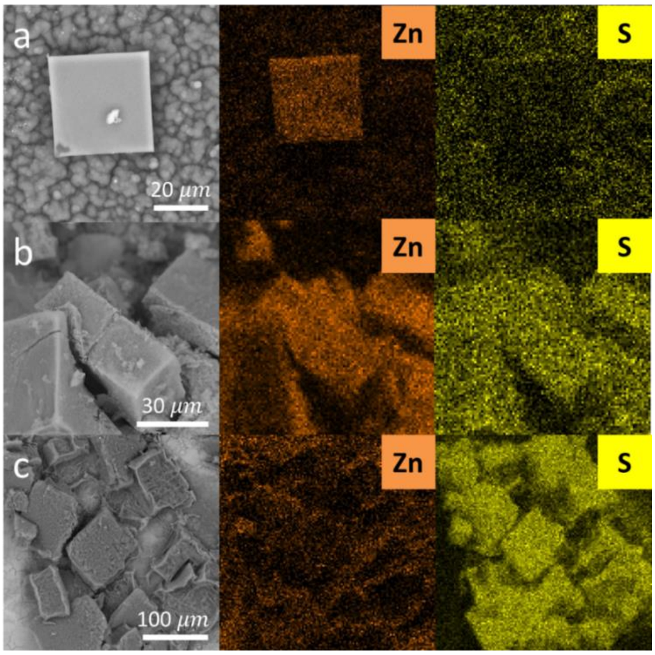

Figure 4.13 SEM-BSE images (1st column on the left hand side) and SEM-EDS mappsings of Zn and S (2nd and 3rd columns) for (a) MOFndc, (b) PEDOT-MOF composite (*i.e.* PEDOT@MOFndc) and (c) nano-PEDOT. The figure is reprinted under a Creative Commons

Attribution 3.0 Unported Licence (CC BY 3.0) from ref. 114 (Copyright 2017 The Royal Society of Chemistry).

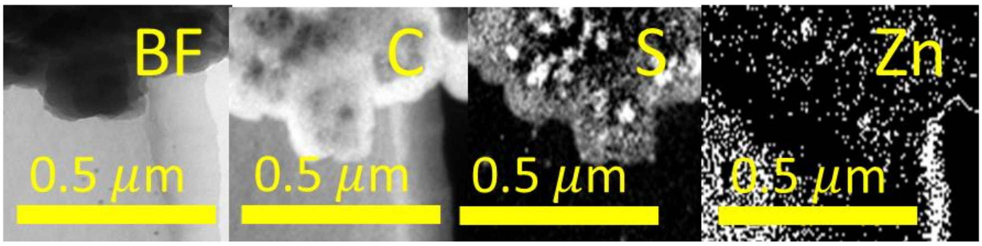

Figure 4.14 A bright-field (BF) TEM image and the corresponding TEM-EELS mappings of C (K-edge, 284 eV), S (L-edge, 165 eV) and Zn (L-edge, 1020 eV) for nano-PEDOT. Opposite to the BF image (signal marked in black), EELS mapping signals are marked in white. These TEM results were obtained by Dr Jonathan S. Barnard and the author. The figure is reprinted under a Creative Commons Attribution 3.0 Unported Licence (CC BY 3.0) from ref. 114 (Copyright 2017 The Royal Society of Chemistry).

TEM-EELS (Figure 4.14), which is more applicable to lighter elements compared with EDS, was used to successfully verify the presence of C (relative atomic mass = 12.011 u) and S in the nano-PEDOT. The nano-PEDOT samples were suspended in methanol and drop-casted on a carbon grid as described in Figure 4.5. Additionally, Zn mapping shows no appreciable Zn signal as the detectable signal level is similar to that for background noise. Since C and S are the key elements presented in the PEDOT, the EELS results further consolidate the presence of nano-PEDOT. Note that the grey part shown in the BF image is the carbon support (from copper grid) which should only contain C.

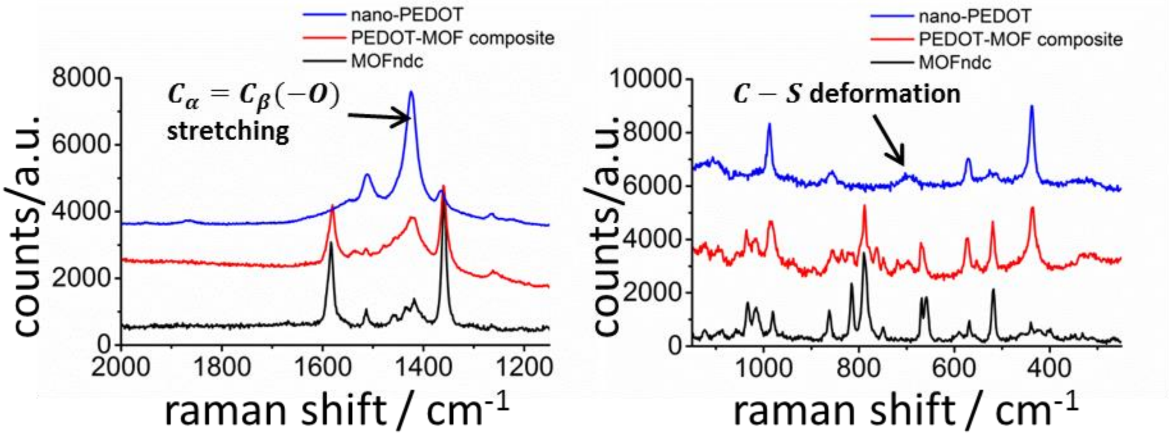

Figure 4.15 Raman spectra for MOFndc, PEDOT-MOF composite (*i.e.* PEDOT@MOFndc) and nano-PEDOT obtained from a 633 nm laser source: (a) the spectra around 1600 cm^{-1}

Raman shift and (b) the spectra around 700 cm^{-1} Raman shift. The figure is reprinted under a Creative Commons Attribution 3.0 Unported Licence (CC BY 3.0) from ref. 114 (Copyright 2017 The Royal Society of Chemistry).

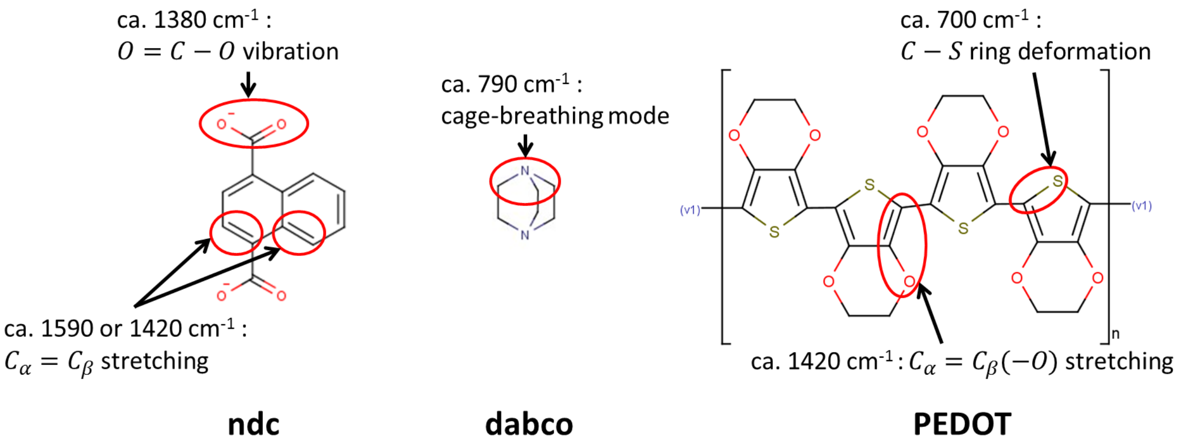

Figure 4.16 Raman peaks and their origins for ndc and dabco in MOFndc and PEDOT based on the literatures.[213–217] The figure is reprinted under a Creative Commons Attribution 3.0 Unported Licence (CC BY 3.0) from ref. 114 (Copyright 2017 The Royal Society of Chemistry).

The samples (*i.e.* MOFndc, PEDOT@MOFndc and nano-PEDOT) were further characterised with Raman spectroscopy to real some of the bonding features (Figures 4.15 and 4.16). The peaks at ~ 1380 cm^{-1} (O = C - O vibration) and ~ 1590 cm^{-1} ($C_\alpha = C_\beta$ stretching) belongs to ndc in the MOFndc;[213,214] the peak at ~ 1420 cm^{-1} [$C_\alpha = C_\beta$ or $C_\alpha = C_\beta$ (-O)stretching] is ascribed to both ndc in MOFndc and PEDOT.[215,216] Cage breathing features (at ~ 790 cm^{-1}) can be assigned to dabco in MOFndc.[217] Meanwhile, the peak at ~ 700 cm^{-1} corresponds to the C - S feature of the thiophene.[215,216]

Compared with the spectra for MOFndc, the peak at ~ 1420 cm^{-1} [$C_\alpha = C_\beta$ or $C_\alpha = C_\beta$ (- O) stretching in both ndc and PEDOT] becomes more significant in the PEDOT@MOFndc. This is likely due to the incorporation of PEDOT in the MOF. The presence of PEDOT can be further verified with a small peak at ~ 700 cm^{-1} (C – S ring deformation in PEDOT). Meanwhile, ndc (from MOFndc) can also be found in PEDOT@MOFndc with the peaks at ~ 1380 cm^{-1} and ~ 1590 cm^{-1}. Raman spectra can also confirm the bonding of nano-PEDOT with a single strong peak at ~ 1420 cm^{-1} for symmetric $C_\alpha = C_\beta$ (- O) stretching in PEDOT (Figure 4.16).[215,216] The peak at ~ 700 cm^{-1} for the C - S ring deformation in PEDOT can be noticed (Figure 4.15, right hand side). Unlike

PEDOT@MOFndc, the peaks at ~ 790 cm^{-1} for the cage-breathing mode of dabco and at ~ 1380 cm^{-1} and ~ 1590 cm^{-1} for ndc disappears supporting the removal of MOFndc.

After PEDOT polymerisation, the MOFndc turned from white to dark blue (Figures 4.17 left and middle). The blue colour matches well with the standard colour for PEDOT polymer.[192] Meanwhile, the orthorhombic shape of MOFndc can be retained after PEDOT formation inside the MOF host (Figures 4.3 and 4.17 left and middle). After the MOFndc removal, similar shape can still be found for nano-PEDOT (Figures 4.3 and 4.17 right). The shape retention upon sequential materials removal, which matches the examples reported by Uemura *et al.*[218] for a MOF-polystyrene and Poly(methyl methacrylate) system via free radical polymerization, indicates that the synthesis for MOF-templated conducting polymers works (from the MOFndc to pure nano-PEDOT).

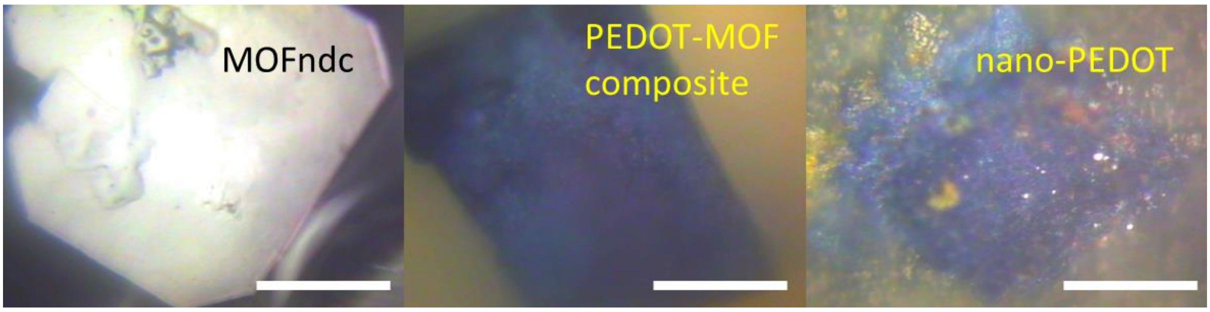

Figure 4.17 Optical photographs for MOFndc, PEDOT-MOF composite (*i.e.* PEDOT@MOF) and nano-PEDOT. All the scale bars represent 50 µm. These photos were taken by Dr Shijing Sun and the author during the nanoindentation. The figure is reprinted under a Creative Commons Attribution 3.0 Unported Licence (CC BY 3.0) from ref. 114 (Copyright 2017 The Royal Society of Chemistry).

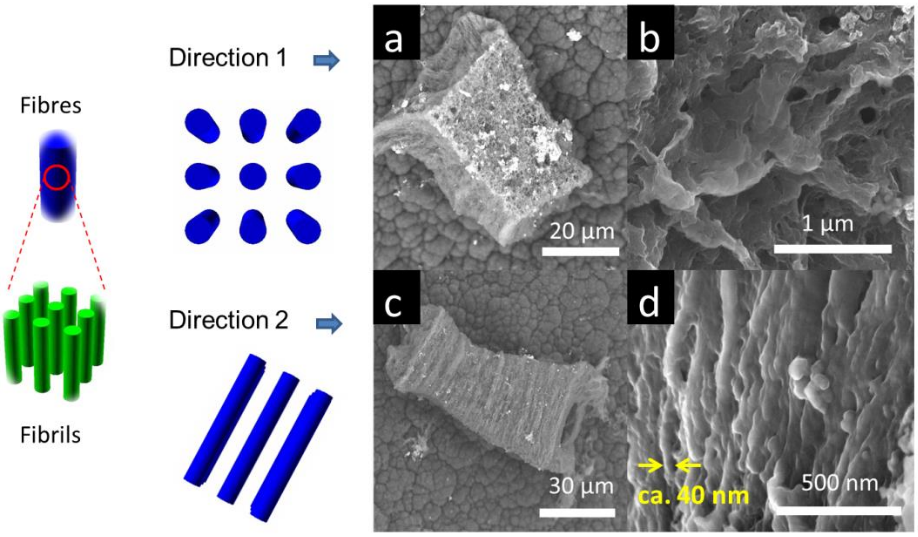

Figure 4.18 SEM-BSE images [(a) top view and (c) side view] and SEM-SE images [(b) top view and (d) side view] reveal the micro-nano morphology of nano-PEDOT. The figure is reprinted under a Creative Commons Attribution 3.0 Unported Licence (CC BY 3.0) from ref. 114 (Copyright 2017 The Royal Society of Chemistry).

Apart from the shape retention found in nano-PEDOT, the anisotropic surface morphology was also observed under SEM. On one facet of the nano-PEDOT, the images (Figures 4.18a&b) show rough surfaces with no preferred directional morphology. In contrast, on other facets, the images (Figures 4.18c&d) show highly directional fibre-like morphology with typical fibre diameter of ~ 40 nm. Such anisotropic morphological features imply that during polymerisation the growth of PEDOT was regulated in the one-dimensional MOF nanochannels forming highly aligned fibrils. After MOFndc was removed, the fibrils joined together due to inter-chain interactions and became a forest of fibres showing in Figure 4.18.

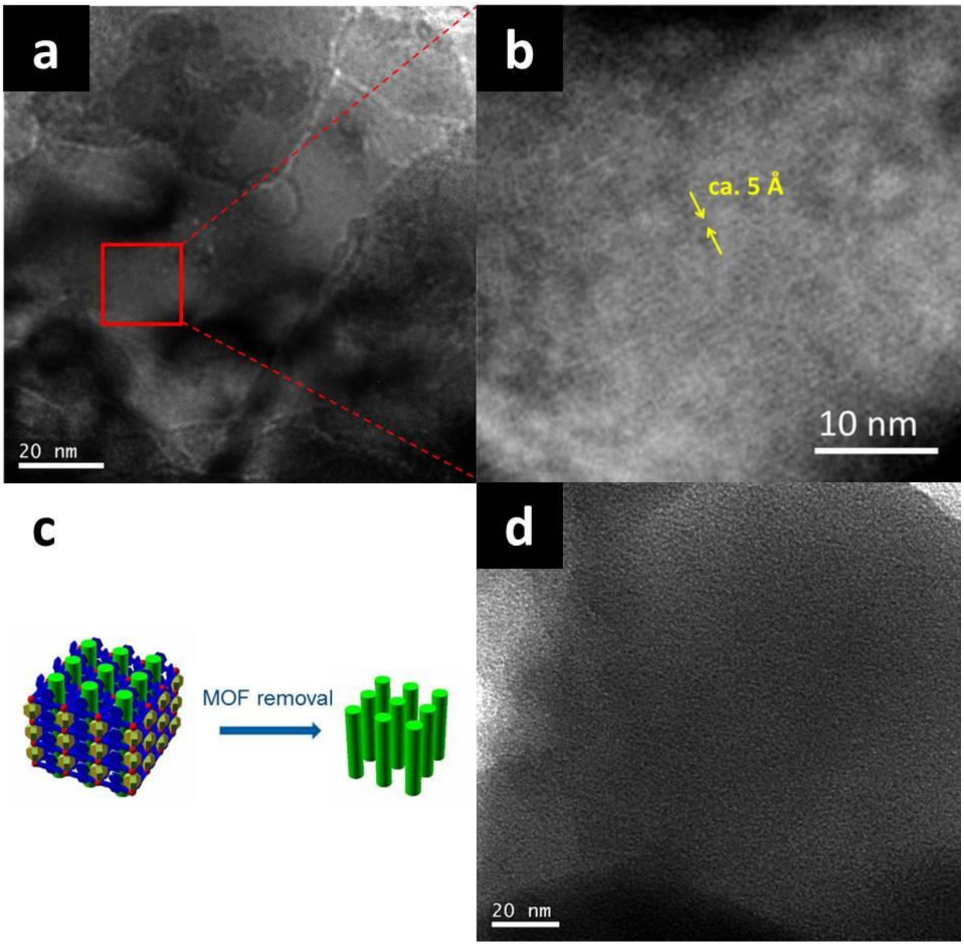

Figure 4.19 BF TEM images for (a) nano-PEDOT indicating the position taken for (b) a figure with higher magnification showing aligned chain-like structure in nano-PEDOT with inter-chain

spacing of ~ 5 Å. (c) a proposed origin for the chain-like structure. (d) standard bulk PEDOT (amorphous). The TEM results were obtained by Dr Jonathan S. Barnard and the author. The figure is reprinted under a Creative Commons Attribution 3.0 Unported Licence (CC BY 3.0) from ref. 114 (Copyright 2017 The Royal Society of Chemistry).

To further rationalise the anisotropic nature of the nano-PEDOT, it was further characterised with TEM. Although, the prepared sample mostly shows disordered nanostructures, reasonably ordered featured can still be found in some areas. At high magnifications, some highly aligned chains with ~ 5 Å inter-chain spacing can be found (Figure 4.19b), which is different from the amorphous polymer structure commonly seen in standard PEDOT (Figure 4.19d). These chains are likely to be PEDOT fibrils grown in the MOFndc nanochannels (Figure 4.19c) with 5.7 Å x 5.7 Å window formed by 4 ndc ligands. Note that similar highly aligned polymer nanostructures has been reported by Distefano *et al.*[219] for MOF-templated polystyrene, but similar alignment in a conducting polymer-based system here was shown for the first time. The local structural regularity is even comparable with the fully π-conjugated covalent organic framework (COF) reported by Guo *et al.*[220]. Although the chemistry of nano-PEDOT has been verified, the aligned feature could also come from the impurity phases (*e.g.* MOFndc and Fe-based clusters from $FeCl_3$).

Nonetheless, such these highly aligned chains correlate well with the microscale anisotropic morphology revealed under SEM (Figure 4.18). Some stability to hold a fibre forest together could be due to collapse by non-covalent interactions. This structural collapse would alter the inter-chain spacing of fibrils, and potentially increase the conductivity of nano-PEDOT. Relatively large dimensions (in sub-millimetres) of MOFndc, PEDOT@MOFndc and the nano-PEDOT make the investigation of their electrical, mechanical and CL properties possible with a few more localised techniques, such as nanoindentation, conductive AFM and SEM-CL. These characterisations will be discussed in the next section.

4.4.4 Some Characterisations in Electrical, Mechanical and Cathodoluminescent (CL) Properties of MOFndc, PEDOT@MOFndc and Nano-PEDOT

Obtaining the MOF-templated conducting polymer nanostructure is an unmet challenge so the current-voltage (I-V) curves of the samples were measured to confirm the presence of conducting material (Figure 4.20). The shapes of the curves for PEDOT@MOFndc and nano-PEDOT are influenced by the mobility of the charge carriers (*i.e.* voltage dependent).

Compared with the electrical current for MOFndc (an insulator) under the same voltage, the current for the PEDOT@MOFndc is a few orders of magnitude higher (Figure 4.20). A further two orders of magnitude increase in current was noticed on the I-V curve of nano-PEDOT, which is marginally lower than the PEDOT film prepared with a standard method.[221] Apart from some special MOFs that exhibit high intrinsic conductivity,[222,223] electrical conduction was achieved by incorporating small molecules [*e.g.* 7,7,8,8-tetracyanoquinododimethane (TCNQ)][224,225] or ions (*e.g.* K^+)[226] into the MOF. In this chapter, electrical conduction by introducing the conducting polymer guest (*i.e.* PEDOT) into the MOF host has been enabled. Additionally, an electrically conductive polymer nanostructure after removing the MOF was also achieved.

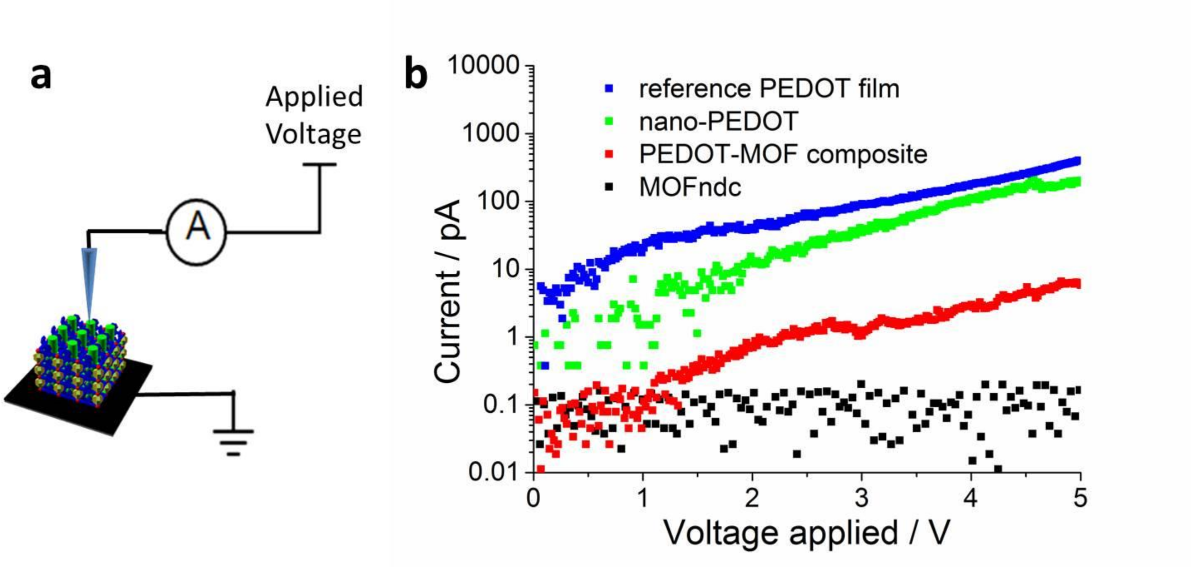

Figure 4.20 Electrical property characterisations with the conductive AFM: (a) schematic drawing about the measurement and (b) I-V relations (in log10 scale) for MOFndc, PEDOT-MOF composite (*i.e.* PEDOT@MOFndc), nano-PEDOT and standard PEDOT film (achieved via the method reported by Winther-Jensen *et al.*[221] on the steel substrate). MOFndc, PEDOT@MOFndc and nano-PEDOT were immobilized on the PPy-coated steel substrate. The measurements were performed by Dr Tongtong Zhu and the author. The figure is reprinted under a Creative Commons Attribution 3.0 Unported Licence (CC BY 3.0) from ref. 114 (Copyright 2017 The Royal Society of Chemistry).

Cathodoluminescent emissions (*i.e.* CL emissions) are triggered by injecting the high-energy electrons (30 keV) into samples to create the unstable exciting states. Photons are emitted through the electron-hole recombination.[227] The CL peaks (Figure 4.21) shows a significant red shift from ~ 410 nm (MOFndc) to ~ 470 nm (PEDOT@MOFndc) indicating a reduction in the material's highest occupied molecular orbital - lowest unoccupied molecular orbital (HOMO-LUMO) gap,[228] as the photons emitted via electron-hole recombination have lower energy (longer wavelength). The CL peak shift support the local chemistry change due to PEDOT incorporation inside the MOFndc host.

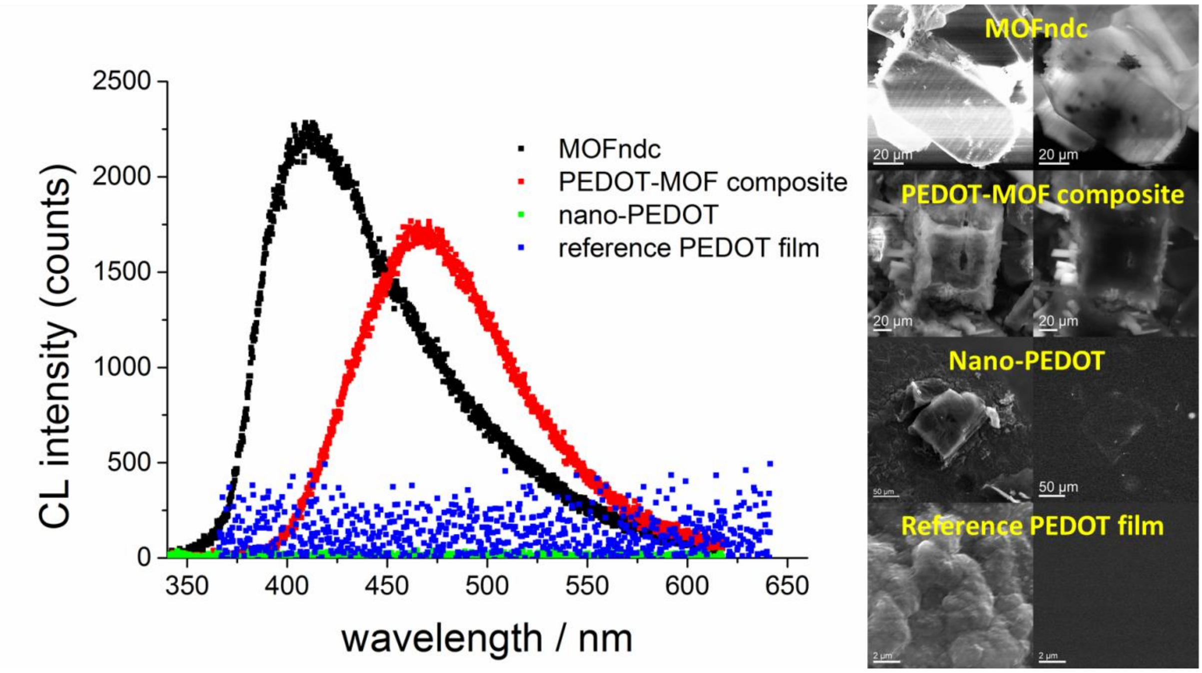

Figure 4.21 SEM-CL spectra, SEM-SEM images (left column) and 30 keV SEM-CL images (right column) for MOFndc, PEDOT-MOF composite (*i.e.* PEDOT@MOFndc), nano-PEDOT and PEDOT film. The results were collected by Dr Tongtong Zhu and the author. The figure is reprinted under a Creative Commons Attribution 3.0 Unported Licence (CC BY 3.0) from ref. 114 (Copyright 2017 The Royal Society of Chemistry).

Unlike MOFndc and PEDOT@MOFndc, nano-PEDOT shows insignificant CL emission (Figure 4.21), as the polymer suffers from electron-induced structure damage.[229] Similar effect was also observed for the PEDOT film prepared with a standard method[221]. Furthermore, though MOFs are highly susceptible to electron beam damage under TEM (200 keV),[134,230] the MOFndc and PEDOT@MOF were quite stable under CL characterization (30 keV), *i.e.* the intensity and peak position were almost unaltered within a scanning period of a few minutes. Upon PEDOT incorporation, the CL property of MOFndc changes significantly. Such PEDOT-induced luminescence alteration may provide an idea about tuning the luminescent property of MOFs in general.

The Young's modulus of MOFndc was measured as ~ 3.2GPa averaging over the indentation depths between 200 nm to 900 nm (Figure 4.22a). The mechanical anisotropy of the MOFndc (E_{110} ~ 3.2 GPa and E_{001} ~ 3.3 GPa) is within the experimental uncertainty and hence it is not obvious in this case. The lower modulus compared with that for MOFndc single crystals reported (~ 7.5 GPa[206]) may be due to a loss of guest molecules (*e.g.* DMF). Meanwhile, since the crystals grown on the substrate have random orientations, they cannot be perfectly normal to the indenter axis leading to the lower modulus. Nanoindentation identified a softer PEDOT-based material (*i.e.* nano-PEDOT) compared with literature for the bulk PEDOT. The Young's modulus of PEDOT itself was found to be ~ 0.50 GPa, which is an order of magnitude lower than the MOFndc framework, and also lower than the value reported for bulk PEDOT (~ 2 GPa[231,232]), implying that there are some empty spaces (*i.e.* pores) within the structure. However, the current synthesis method produce very limited amount of sample (*i.e.* much less than 1 mg from 5 substrates), which constrains the application of further characterization techniques such as powder XRD and gas adsorption measurements.

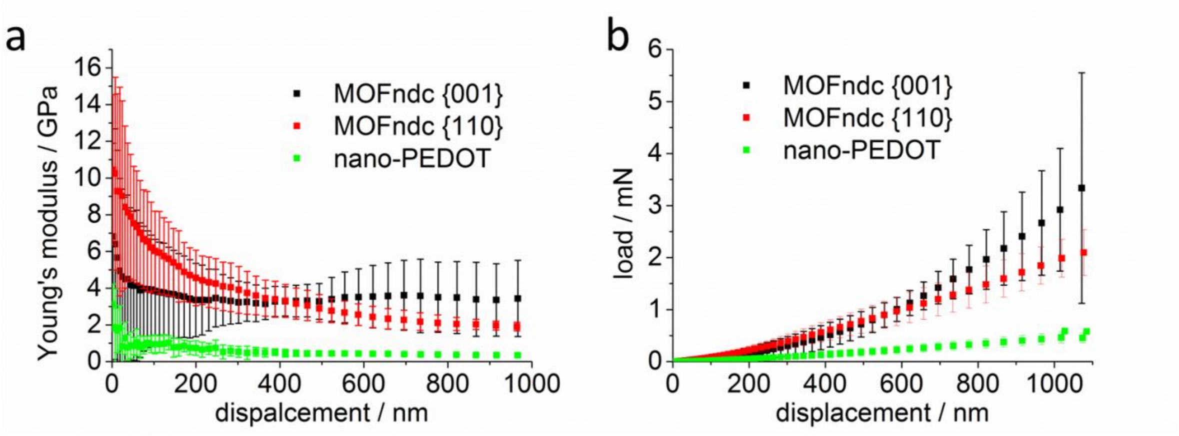

Figure 4.22 Nanoindentation experiments on {001} and {110} facets and nano-PEDOT: (a) load versus displacement and (b) Young's modulus versus displacement. The measurements were performed by Dr Shijing Sun. The figure is reprinted under a Creative Commons Attribution 3.0 Unported Licence (CC BY 3.0) from ref. 114 (Copyright 2017 The Royal Society of Chemistry).

4.5 Summary

The incorporation of an electrically conducting polymer, PEDOT, has been demonstrated in the MOFndc via chemical polymerisation (*i.e.* oxidative polymerisation). By forming the PEDOT@MOFndc composite the electrically insulating MOFndc was turned into a conducting PEDOT-MOF composite. Meanwhile, the HOMO-LUMO gap of the MOF host was altered by PEDOT incorporation leading to a red shift (from ~ 410 nm to ~ 470 nm) in

CL emission. The MOFndc was further removed and a MOF-templated electrically conducting PEDOT nanostructure (*i.e.* nano-PEDOT) was obtained. The nano-PEDOT retained the rhombohedral shape from the MOFndc was found with anisotropic morphology (*i.e.* no directional preference on the top but highly aligned fibre-like nanostructures on the side). Such anisotropy could be due to the confined PEDOT fibrils formation inside the one-dimensional MOF nanochannels. Furthermore, the nano-PEDOT was found to be significantly softer than the bulk PEDOT inferring some porosity within the nano-PEDOT.

While working on this project, the author started to realise the significance of MOF chemical stability and redox reaction (e.g. oxidative polymerisation) within MOF's pore. In the next chapter, the ideas and practical experiences gained during PEDOT@MOFndc preparation will be applied to address some more general issues in ship-in-a-bottle synthesis.

Chapter 5

Pourbaix Enabled Guest Synthesis (PEGS) Method to Prepare RuO2@MOF-808-P for Low-Temperature CO Oxidation Catalysis

Chapter 5: Pourbaix Enabled Guest Synthesis (PEGS) Method to Prepare RuO_2@MOF-808-P for Low-Temperature CO Oxidation Catalysis

5.1 Initiations, Collaborations, Outcomes, Research Funding

In October 2016, Ms Kara D. Fong joined Dr Smoukov's group as an MPhil student who was interesting in developing electrodes for electrochemical supercapacitor. She told the author that MnO_2 can be a good supercapacitor material with high capacitance. Since the author have managed to for PEDOT in a MOF via oxidative polymerisation, Dr Smoukov, Ms Fong and the author came up with the idea that $KMnO_4$ (aq) [rather than $FeCl_3$ (aq)] may work as the oxidant to polymerise the EDOT. In this way, PEDOT and MnO_x composite which could benefit supercapacitor could be achieved. While MnO_x from $KMnO_4$ (aq) was obtained the PEDOT was found to be irreversibly over-oxidised.[233] Nonetheless, a similar reaction inside a MOF (DUT-67[67]) was attempted and the deposition of MnO_x was confirmed inside the MOF. In November 2016, the author realised that the guest formation inside a MOF via redox reaction could be generalised as long as the electrochemical potential between the reducing and oxidising agents [one or both of them can be the guest precursor(s)] is sufficient to drive the redox reaction. The electrochemical conditions (as well as pH conditions) could be predicted using a well-established tool for aqueous systems, *i.e.* Pourbaix diagrams.

To prove the hypothesis, in January 2017, the author consulted Prof. Qiang Fu from Dalian Institute of Chemical Physics about an oxide@MOF system he might be interested for his research. Since the author used to work in Prof. Fu's group as a research internship, he was aware of the research capability he had for heterogeneous catalysis. One of his suggestions was RuO_2 guest for CO oxidation. During the group visit to Bulgaria in March 2017, Dr. Zahari P. Vinarov inspired the author about the use of small antioxidant lipids for reactions. Such compounds can be small, hydrophobic and ready to be oxidised (*i.e.* reducing), which are ideal for the controlled redox reactions via hydrophobic-hydrophilic interaction. In April 2017, the author started the project supervised by Dr Stoyan K. Smoukov and Prof. R. Vasant Kumar and advised by Prof. Anthony K. Cheetham.

As close collaborations, the author worked with Dr Lijun Gao from Prof. Qiang Fu's group (Dalian Institute of Chemical Physics, Chinese Academy of Sciences), which is a leading group in CO oxidation catalysis. Dr Lijun Gao used temperature programmed reduction (TPR) and diffuse reflectance infrared Fourier transform spectroscopy (DRIFT) to characterise the interaction between CO and RuO_2 inside the MOF. She tested RuO_2@MOF-808-P for CO oxidation catalysis and prepared and characterised comparison samples. She also collected X-ray absorption spectroscopy (XAS) results from Shanghai Synchrotron with Mr Jinhu Dong from the same group. Dr Jingwei Hou (University of Cambridge) and the author prepared schemes for the synthesis and the CO-RuO_2 surface interactions. Dr Jingwei Hou and Ms Song Gao (University of New South Wales) performed liquid chromatography–mass spectrometry (LC-MS). Mr Servann J. A. Herou from Prof. Maria-Magdalena Titirici's group (Queen Mary University of London) performed N_2 gas adsorption measurements for RuO_2@MOF-808-P. Dr Weiwei Li (University of Cambridge) performed X-ray photoelectron spectroscopy (XPS) characterisations. Dr James T. Griffiths (University of Cambridge) and the author worked on TEM characterisation for RuO_2@MOF-808-P. Prof. Judith L. MacManus-Driscoll, Dr Na Ta, Mr Simon J. Griggs and Mr Robert Cornell are also acknowledged here for the kind support in using XPS, dark-field scanning transmission electron microscopy (DF-STEM), SEM and high-resolution thermogravimetric analysis (HR-TGA). **Unless stated in the experimental and results otherwise the work was accomplished by me.**

A patent application related to the work covered in the chapter has been lodged (GB1813334.8). Meanwhile, the work was published in Nature Communications in 2019:

Tiesheng Wang#, Lijun Gao#, Jingwei Hou, Servann J. A. Herou, James T. Griffiths, Weiwei Li, Jinhu Dong, Song Gao, Maria-Magdalena Titirici, R. Vasant Kumar, Anthony K. Cheetham, Xinhe Bao, Qiang Fu*, Stoyan K. Smoukov*, ***Rational Approach to Guest Confinement inside MOF Cavities for Low-Temperature Catalysis***, doi: 10.1038/s41467-019-08972-x, **Nature Communications**, 2019, 10, Article number: 1340 (# co-first author)

This project is funded through the European Research Council (ERC) grant (grant number: EMATTER 280078), National Natural Science Foundation of China (No. 21688102) and Ministry of Science and Technology of China (No. 2016YFA0200200). In the period of the project, the author was funded by the China Scholarship Council (CSC) and supported by the Engineering and Physical Sciences Research Council (EPSRC) Centre for Doctoral Training in Sensor Technologies and Applications (EP/L015889/1 and 1566990). Prof. Anthony K. Cheetham was supported by the Ras Al Khaimah Centre for

Advanced Materials (RAK-CAM). Dr Weiwei Li was supported by the EPSRC grants (EP/L011700/1 and EP/N004272/1) and the Isaac Newton Trust.

5.2 Introduction

As mentioned in Section 2.6, direct impregnation of guests often fails to work for MOF-guest systems, as the guests can be too large to migrate through the aperture (typically < 2 nm). The syntheses for guests within nanoporous hosts (*i.e.* ship-in-a-bottle syntheses) are, therefore, critical to prepare the MOF-guest systems.[4,22,234] Such synthesis are, however, different from those for making bulk materials or free nanoparticles, as they must be compatible with both the stability and small pore sizes of the MOFs. The small pore aperture can restrict the size of reagents (*e.g.* precursors) for direct impregnation; the conditions (*e.g.* high temperatures) or reagents (e.g. strong redox agents) used to produce guests can also damage or destroy the host structure.[3,8] As a consequence, it remains challenging or impossible to form many guest compounds inside the pore, particularly for some oxides, hydroxides, sulfides, nitrides, phosphides.

In this chapter, the use of Pourbaix diagrams will be introduced to assist the pre-determination of conditions and precursors for ship-in-a-bottle syntheses. Pourbaix diagrams are well-known for materials scientists due to its significance in depicting the thermodynamic behaviours of corrosion processes.[235] These diagrams map the thermodynamically stable solid or solution phases against electrochemical potential and pH.[236–240] Taking the corrosion process as a general example, the Pourbaix diagrams can describe the conditions for solids to be dissolved (*i.e.* corroded). Here, rather than using the Pourbaix diagrams to understand the solid → solution processes, the author used them in a reverse fashion to predict solids formation from solutions (*i.e.* guest formation). This strategy is termed as *Pourbaix Enabled Guest Synthesis* (PEGS) (Section 5.3.1). Briefly, by checking the Pourbaix diagrams the difference in the redox potential (ΔE) and/or pH between a soluble guest precursor and a desired guest can be found. The hosts and reagents (e.g. precursors) which meet the guest formation requirements can then be shortlisted and the most appropriate candidates perhaps with other properties (i.e. desired boiling temperature and hydrophobicity) to manage the "ship-in-a-bottle" synthesis.

The current PEGS approach, however, has its own limitations particularly for guiding the reactions conditions in nano-sized space. Unlike the solution-based free system, local electrostatic field, chemical potential, pH and mass transport behaviour can be significantly influenced by the confinement of nano-sized pores.[241,242] The reaction alteration by nanoconfinement has been well-known for heterogeneous catalysis.[267–270]

The actual Pourbaix diagram for a compound can be very different from the standard one. Hence, the PEGS strategy should be used with caution. Experimental attempts are necessary to consolidation the use of PEGS method for a specific system. Nonetheless, with the development of nano-chemistry the current PEGS approach is expected to be improved significantly in the near future.

As a demonstration, Ru-based Pourbaix diagram was applied to predict the conditions and reagents to form RuO_2 guest within a MOF (*i.e.* RuO_2@MOF). RuO_2 is a well-documented catalyst for CO oxidation, which is simple but important.[243–248] From the fundamental research point of view, catalysed CO oxidation is an ideal prototypal reaction to understand the interactions between reactant molecules and catalysts. Meanwhile, CO oxidation has its practical significance in lowering automotive exhaust emissions, purifying fuel cell feed gases, and cleaning air.[244–247] The MOF used in the work is MOF-808-P [$Zr_6O_5(OH)_3(BTC)_2(HCOO)_5(H_2O)_2$, BTC = 1,3,5-benzenetricarboxylate], which is modified from MOF-808 with shorter synthesis time.[249,250] MOF-808-P is based on {Zr_6O_8} clusters with large cavity and aperture diameters (~ 18 Å and ~ 14 Å, respectively) in cubic space group $Fd\bar{3}m$. It is reported to be stable in aqueous solution over a wide pH range of 3-10.[251] The synthesized MOF- RuO_2 system is therefore RuO_2@MOF-808-P. Another reason to choose MOF-808-P is that its organic linker contains only C, O and H (no other elements which may deteriorate the potential applications).

One of the current issues for "*ship-in-a-bottle"* methods (mentioned in Section 2.6) is there is often a significant amount of guest compound deposited outside the hosts.[8,252] This inevitably creates a strong bias against investigations about confinement.[27] To address this concern solutions related to chemical grafting[129,252] and electrostatic interactions[130] have been reported. These approaches, however, only work for hosts with *special chemistries* [*e.g.* hosts with functional groups or electrical charge]. With the aid of PEGS method, a rational approach for guest synthesis and a broad selection of reagents becomes possible. To minimise guest deposition outside the host, the tBMP lipid was selected and performed a confined reaction by applying the hydrophobic-hydrophilic repulsion and temperature-controlled selective desorption (Section 5.4.1).

Although standard RuO_2 catalyses CO oxidation well at temperature above 150 °C, it is often inactive at temperatures close to room temperature.[253] Below 150 ^{o}C the catalytic CO oxidation is mostly related to the Langmuir-Hinshelwood process (reaction between two species adsorbed on the neighbouring sites).[244,254,255] Such process involves the combination of adsorbed CO with dissociated O_2 species (*i.e.* O atoms) to produce CO_2. However, the adsorption of CO and O species on RuO_2 at low temperatures can be very strong leading to the formation of densely packed CO and O domains, which limits surface desorption and diffusion of both species. As a consequence, the poor surface desorption and diffusion cause the low catalytic activity.[244,255,256] In contrast, at low temperatures, the interactions between the CO and O species and RuO_2 were found to be weaker in RuO_2@MOF-808-P. Such interaction modulation by PEGS synthesis led to highly active RuO_2-based CO oxidation catalyst even at temperatures close to room temperature. As a comparison, the commonly used mesoporous silica-supported RuO_2 catalyst (RuO_2/SiO_2) was also prepared with a conventional impregnation method.[257] In the following sections, the PEGS strategy, synthesis and characterisations of RuO_2@MOF-808-P, investigation about CO/O interactions with RuO_2 for both RuO_2@MOF-808-P and RuO_2/SiO_2, and their relevant catalytic CO oxidation tests will be detailed. **Since RuO_2/SiO_2 was prepared and characterized by Dr Lijun Gao, the experimental and results ONLY for RuO_2/SiO_2 will be detailed in the Appendix for Chapter 5.**

5.3 Experimental

5.3.1 Constructing the Ru-Based Pourbaix Diagram for Aqueous System (Ru-H_2O system)

The Pourbaix diagram for Ru-based aqueous system (Ru-H_2O system) was constructed based on the previous efforts reported.[236–238] Here, the aqueous concentration of insoluble Ru-containing compound is assumed to be negligible (effectively 0 M). Since the study is focusing on aqueous systems with pH between 5 and 10, only this pH range was considered for simplicity. At reasonably low Ru concentration (C_{Ru}^{0}) in the mixture (*e.g.* C_{Ru}^{0} = 20 mM), there are several forms of Ru-containing compounds thermodynamically stable in in pH 5-10, namely: H_2RuO_5 (solution), RuO_4^- (solution), Ru_2O_5 (insoluble solid), $RuO_2{\cdot}2H_2O$ (insoluble solid) and $Ru(OH)_3{\cdot}H_2O$ (insoluble solid).[238,258,259]

Therefore, there can be 6 different half-cell reduction reactions involved in the pH range, where E^0 denotes the standard electrode potential:

$$Ru(OH)_3{\cdot}H_2O + 3\ H^+ + 3\ e^- = Ru + 4\ H_2O,\ E_1^0 = 0.631\ V \qquad \text{Equation (5.1)}$$

$$RuO_2{\cdot}2H_2O + H^+ + e^- = Ru(OH)_3{\cdot}H_2O,\ E_2^0 = 0.777\ V \qquad \text{Equation (5.2)}$$

$$Ru_2O_5 + 3\ H_2O + 2\ H^+ + 2\ e^- = 2\ RuO_2{\cdot}2H_2O,\ E_3^0 = 1.168\ V \qquad \text{Equation (5.3)}$$

$$2\ RuO_4^- + 6\ H^+ + 4\ e^- = Ru_2O_5 + 3\ H_2O,\ E_4^0 = 1.701\ V \qquad \text{Equation (5.4)}$$

$$2\ H_2RuO_5 + 6\ H^+ + 6\ e^- = Ru_2O_5 + 5\ H_2O,\ E_5^0 = 1.466\ V \qquad \text{Equation (5.5)}$$

$$H_2RuO_5 + e^- = RuO_4^- + H_2O,\ E_6^0 = 0.996\ V \qquad \text{Equation (5.6)}$$

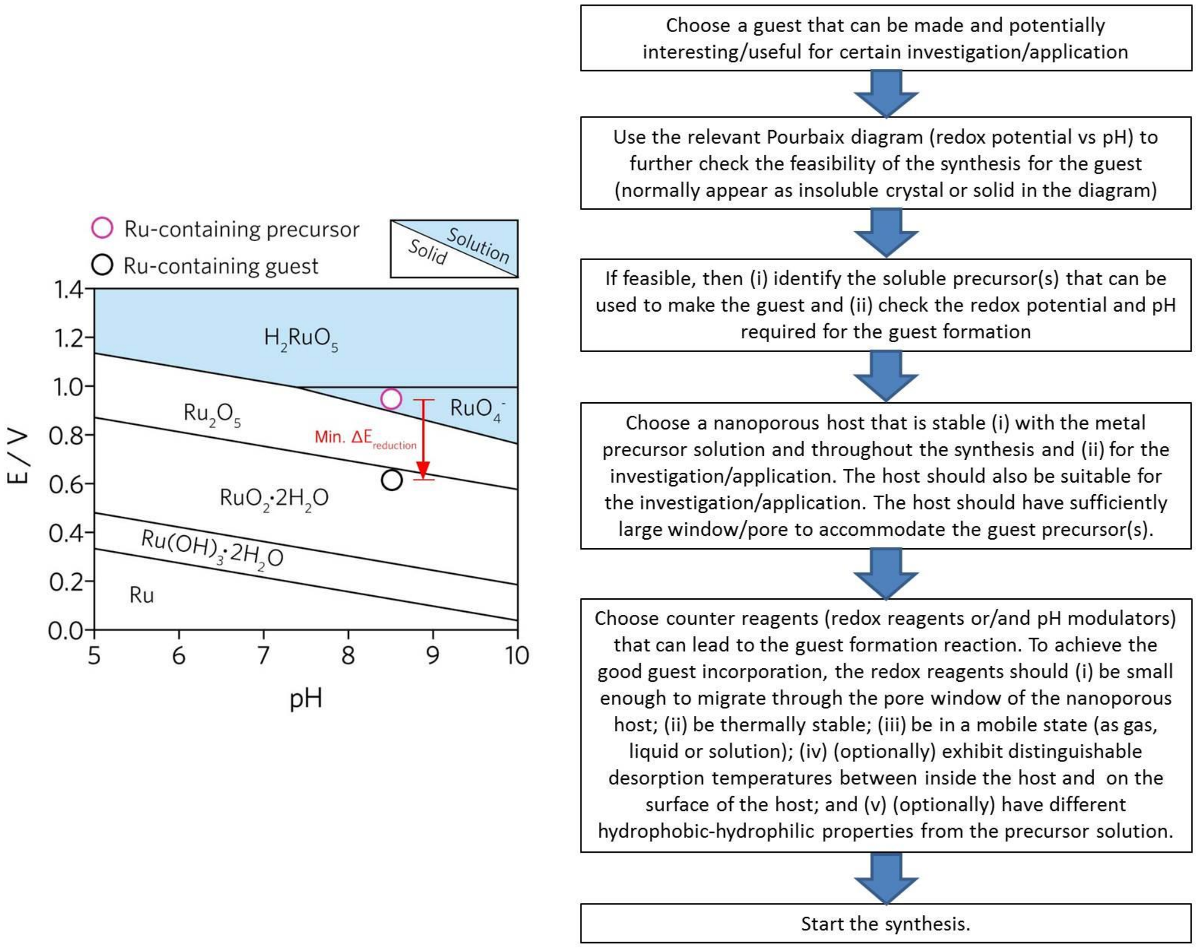

Choose a guest that can be made and potentially interesting/useful for certain investigation/application

Use the relevant Pourbaix diagram (redox potential vs pH) to further check the feasibility of the synthesis for the guest (normally appear as insoluble crystal or solid in the diagram)

If feasible, then (i) identify the soluble precursor(s) that can be used to make the guest and (ii) check the redox potential and pH required for the guest formation

Choose a nanoporous host that is stable (i) with the metal precursor solution and throughout the synthesis and (ii) for the investigation/application. The host should also be suitable for the investigation/application. The host should have sufficiently large window/pore to accommodate the guest precursor(s).

Choose counter reagents (redox reagents or/and pH modulators) that can lead to the guest formation reaction. To achieve the good guest incorporation, the redox reagents should (i) be small enough to migrate through the pore window of the nanoporous host; (ii) be thermally stable; (iii) be in a mobile state (as gas, liquid or solution); (iv) (optionally) exhibit distinguishable desorption temperatures between inside the host and on the surface of the host; and (v) (optionally) have different hydrophobic-hydrophilic properties from the precursor solution.

Start the synthesis.

Figure 5.1 The Pourbaix diagram for Ru-H_2O system (left, pH = 5-10, C_{Ru}^0 = 20 mM) indicates the formation of hydrous RuO_2 from RuO_4^- (red arrow). The diagram was constructed based on previously available data versus standard hydrogen electrode (SHE).[236–238] A flow chart (right) goes through the steps of PEGS synthesis for ship-in-a-bottle synthesis. The figure is reprinted under a Creative Commons Attribution 4.0 International Licence (CC BY 4.0) from ref. [260] (Copyright 2019 Nature Publishing Group).

According to Nernst equation for an electrochemical half-cell reduction reaction,[235] the electrical potentials, E, can be effectively written as:

$$E = E^0 - \frac{RT}{zF}\ln(\frac{concentration\ of\ ions\ on\ the\ right\ mutiplied\ together}{concentration\ of\ ions\ on\ the\ left\ mutiplied\ together})$$ Equation (5.7)

where, R is the gas constant (8.314 $J{\cdot}K^{-1}{\cdot}mol^{-1}$), T is the temperature in K, z is the number of electrons transferred in the half-cell reaction and F is the Faraday constant (96485 $C{\cdot}mol^{-1}$).

Furthermore,

$$\ln[H^+] \approx 2.303\log[H^+] = -2.303pH$$ Equation (5.8)

Therefore, the relationship between E and pH can be established for the Equation 5.1-5.6 for the given $C_{Ru}{}^0$ ($C_{Ru}{}^0$ = 20 mM here) can be established.

$$E_1 = E_1{}^0 + \frac{RT}{F}\ln[H^+] = E_1{}^0 - 2.303\frac{RT}{F}pH$$ Equation (5.9)

$$E_2 = E_2{}^0 + \frac{RT}{F}\ln[H^+] = E_2{}^0 - 2.303\frac{RT}{F}pH$$ Equation (5.10)

$$E_3 = E_3{}^0 + \frac{RT}{F}\ln[H^+] = E_3{}^0 - 2.303\frac{RT}{F}pH$$ Equation (5.11)

$$E_4 = E_4{}^0 + \frac{3RT}{2F}\ln[H^+] + \frac{RT}{2F}\ln(C_{Ru}^0) = E_3{}^0 - 3.4545\frac{RT}{F}pH + \frac{RT}{2F}\ln(C_{Ru}^0)$$ Equation (5.12)

$$E_5 = E_5{}^0 + \frac{RT}{F}\ln[H^+] + \frac{RT}{3F}\ln(C_{Ru}^0) = E_5{}^0 - 2.303\frac{RT}{F}pH + \frac{RT}{3F}\ln(C_{Ru}^0)$$ Equation (5.13)

$$E_6 = E_6{}^0$$ Equation (5.14)

Meanwhile, there is a triple junction in the diagram for a disproportionation reaction:

$$6\ RuO_4^- + H_2O + 6\ H^+ = Ru_2O_5 + 4\ H_2RuO_5$$ Equation (5.15)

A simplified Pourbaix diagram for Ru-H_2O system (pH = 5-10, $C_{Ru}{}^0$ = 20 mM) was, therefore, constructed with above-mentioned E vs pH equations in Figure 5.1.

5.3.2 Rational Design of RuO2@MOF-808-P

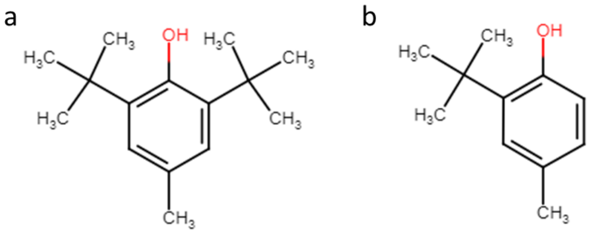

Figure 5.2 (a) butylated hydroxytoluene (BHT)[261,262] and (b) 2-tert-butyl-4-methylphenol (tBMP). The figure is reprinted under a Creative Commons Attribution 4.0 International Licence (CC BY 4.0) from ref. [260] (Copyright 2019 Nature Publishing Group).

According to the Ru-based Pourbaix diagram (Figure 5.1 left), a perruthenate salt, potassium perruthenate ($KRuO_4$), was used as the precursor. It can form hydrous RuO_2 via reduction reaction (Figure 5.1 left). Since 20 mM $KRuO_4$ (aq) is approx. at pH8.5, the minimum reduction potential required to form $RuO_2 \cdot 2H_2O$ (the preform of RuO_2) from the RuO_4^- (aq) domain, $\Delta E_{reduction}$, is 0.3 – 0.4 V (Figure 5.1 left, assuming the pH is unaltered). To trigger the reaction, 2-tert-butyl-4-methylphenol (tBMP, Figure 5.2b), an analogy to a well-known antioxidant lipid (*i.e.* hydrophobic) in food, butylated hydroxytoluene (BHT, Figure 5.2a), was chosen as the reducing agent which requires ~ 0.3 V to be partially oxidized.[261,262] tBMP is also hydrophobic (*i.e.* immiscible with water). The reason to use small tBMP lipid is that if the tBMP were pre-loaded into the MOF host it could be confined in the pore during the redox reaction with $KRuO_4$ due to its hydrophobic-hydrophilic repulsion with water (*i.e.* aqueous solution). In this way, the produced guest, hydrous RuO_2 cluster/particle, could be entrapped inside the MOF. The product can then be dehydrated at moderately high temperatures (*e.g.* 140 °C)[263] under nitrogen to achieve RuO_2@MOF-808-P. More details about the experimental procedures are provided below.

5.3.3 Materials

The following chemicals/items were used as received: 1,3,5-benzenetricarboxylic acid (H_3BTC, ACROS Organics™, 98%), zirconyl chloride octahydrate ($ZrOCl_2 \cdot 8H_2O$, ACROS Organics™, 98+%), DMF (Fisher Scientific, 99.7+%, HPLC), formic acid (HCOOH, Fisher Scientific, 98+%), ethanol absolute (C_2H_5OH, Fisher Scientific, 99.5+%, HPLC), Milli-Q water (17 MΩ), tBMP (ACROS Organics™, 99%), diethyl ether (DE, ACROS Organics™, 99+%, ACS reagent, anhydrous), $KRuO_4$ (Alfa Aesar, 97%), $KMnO_4$ (ACROS Organics™, 99+%) and Whatman® polyamide membrane filters (pore size ~0.2 µm), anhydrous $ZrCl_4$

(Sigma-Aldrich, 99.99%), 2,5-thiophenedicarboxylic acid (H_2tdc, Alfa Aesar, 97%), 1-methyl-2-pyrrolidinone (NMP, Alfa Aesar, 99+%), and zeolite Y (Alfa Aesar, Si:Al = 80:1).

5.3.4 MOF-808-P Synthesis

Zr-based MOF-808-P was synthesized based on the procedures reported by Yaghi *et al.*[249,250]. Briefly, 0.467 g H_3BTC and 2.16 g $ZrOCl_2 \cdot 8H_2O$ were dissolved in a DMF/HCOOH solvent (100 ml DMF + 100 ml HCOOH) first. The solution was kept at 130 °C for 48 hrs. The formed MOF particles were collected, washed with DMF for three times and kept in Milli-Q water for 3 days. The washed MOF particles (slurry-like) were recollected by filtration and dried gently at 50 °C to remove majority of water. It was further dried at 150 °C under dry nitrogen flow for ~ 3 hrs.

5.3.5 tBMP Impregnation and Temperature-Controlled Selective Desorption

MOF-808-P was immersed in a tBMP solution (DE as the solvent) and mixed for ~ 30 min. The guest loading amount for RuO_2@MOF-808-P depends on the tBMP added (relative to the amount of the MOF). Taking the sample for CO oxidation (~ 10 wt% Ru) as an example, 50 mg tBMP (in 1000 μl DE) was mixed with 500 mg MOF-808-P. The as-prepared tBMP/DE@MOF-808-P in this case [*i.e.* tBMP/DE@MOF-808-P (2:20), where 2:20 is the tBMP:MOF-808-P mass ratio during tBMP impregnation] was then heated under N_2 flow at 120±5 °C for ~ 1 hr to remove all the DE and the tBMP outside the MOF (*i.e.* temperature-controlled selective desorption[114,195]). The product is tBMP@MOF-808-P.

5.3.6 Preparing RuO_2@MOF-808-P

The as-prepared tBMP@MOF-808-P was collected and reweighed. An excess amount of $KRuO_4$ aqueous solution (20 mM) was then added to tBMP@MOF-808-P to form hydrous RuO_2 inside the MOF. The reaction was kept for ~ 4 hrs. In the case of tBMP:MOF-808-P=2:20, the pH was measured to be ~ pH 8.5 and ~ pH 6 before and after the reaction. The as-synthesized hydrous RuO_2@MOF-808-P was collected by filtration. The filtrate solution remained yellow indicating unreacted $KRuO_4$ left after the reaction. The hydrous RuO_2@MOF-808-P was then washed with excess amount of ethanol followed by water. It was then dehydrated at ~ 140 °C for ~ 2 hrs to obtain as-synthesized RuO_2@MOF-808-P.

5.3.7 Materials Characterisations

HR-TGA: HR-TGA was performed with a TA Instruments Q500 from room temperature to 900 ^{o}C using a dynamic mode. The HR-TGA can adjust the heating rate based on the mass loss, *i.e.* the heating rate would decrease once the mass loss starts to increase or *vice versa*. The dynamic approach can generate high-resolution mass-loss profile with more clearly-separated mass-loss steps.[264]

Nitrogen adsorption measurements: The samples were characterised by N_2 adsorption at 77 K using Autosorb and Nova Quantachrome equipment. Mr Servann J. A. Herou collected the results and analysed them. The samples were degassed at 120 ^{o}C overnight under vacuum. The pore structure and the surface area were calculated by the software Novawin (Quantachrome) using different estimations of the surface [*i.e.* Brunauer-Emmett-Teller (BET) and density function theory (DFT)]. The cumulative pore size distribution (PSD) was calculated from the isotherm adsorption line using a quenched-solid model, quenched solid state functional theory (QSDFT), assuming slit pores geometries.

Powder XRD： Powder XRD patterns were collected on a Bruker D8 ADVANCE with a Ni 0.012 filter between the X-ray source and the sample (2θ from 3.5° to 80° and a step size of 0.04°). Samples were uniformly distributed on a silicon disc supported by a round holder. The holder and the disc were rotated (30 rpm) during the measurement. The illumination slit length was fixed so that the exposure area forms a circle (16 mm in diameter) with the rotation.

SEM-SE and SEM-EDS: SEM-SE images and SEM-EDS mappings were obtained using a FEI Nova NanoSEM™ with a field emission gun, a SE detector and an EDS detector. The SEM-SE images were collected at the acceleration voltage of 5 kV; the SEM-EDS mappings were acquired at the acceleration voltage of 15 kV. Powder samples were immobilised on the carbon tapes, which were adhered to the standard aluminium stubs (Agar Scientific).

DF-STEM and STEM-EDS: DF-STEM images and STEM-EDS mappings in Figures 5.6a, 5.10 and 5.14 were acquired by Dr James T. Griffiths and Tiesheng Wang using an FEI Osiris operating at 200 keV fitted with BF and annular dark field (ADF) detectors. Energy dispersive spectra were simultaneously recorded on four Bruker silicon drift detectors. STEM-EDS mappings in Figures 5.6 b and c were collected by Dr Lijun Gao from a JEOL F200 microscope operated at an accelerating voltage of 200 kV. Energy dispersive spectra were simultaneously recorded on a JEOL EDS detector. STEM samples were dispersed in ethanol and prepared by drop-casting 100 µl of sample suspension on carbon grids.

XPS: XPS results were collected by Dr Weiwei Li using a XPS with a monochromatic Al *Kα1* x-ray source (*hv* =1486.6 eV) and a SPECS PHOIBOS 150 electron energy analyzer with a total energy resolution of 500 meV. To remove charging effects during the measurements, a low-energy electron flood gun with proper energy was applied to compensate the charge. All spectra were aligned to the C 1s at 284.8 eV. For analysis of the Ru $2p_{3/2}$ spectrum, a linear background was subtracted. The samples were immobilised on the substrate by carbon tape.

XAS: XAS results were collected by Dr Lijun Gao and Mr Jinhu Dong. X-ray absorption spectra measurements were conducted at the BL14W1 beamline of the Shanghai Synchrotron Radiation Facility (SSRF). The spectra at Ru K-edge (around 22,120 eV) were recorded in transmission mode. The samples were loaded in plastic sample bag for characterisation.

Inductively coupled plasma optical emission spectrometry (ICP-OES): The Ru content was measured by inductively coupled plasma optical emission spectroscopy (7300DV, Perkin Elmer). The catalysts (5-10 mg) were digested by microwave dissolution in aqua regia and HF solution.

LC-MS: LC-MS results were collected by Dr Jingwei Hou and Ms Song Gao. Accurate mass measurements of the BMP oxidization products were performed by coupling an Accela LC system with a Waters 50 mm BEH C18 column interfaced to a Q-Exactive Plus mass spectrometer. For each test, 100 µL of sample was analysed using a 20 min gradient of water (A) versus acetonitrile (B) both with 0.1% formic acid. The mobile phase flow rate was 400 µm/min. After 1 min isocratic conditions at 90 % A, the gradient was operated from 90 % to 5 % A for 10 min., kept at 5 % for another 2 min and then back to the initial conditions in 2 min, which was then kept for another 5 min for the column regeneration. Ionisation was performed in positive and negative polarities for both electrospray and atmospheric pressure ionisation. The nebulized gas flow was 70 L/hr and drying gas flow was 450 L/hr at a temperature of 350 °C. Xcalibur version 2.0 software FROM Thermo Scientific was applied for data acquisition and analysis.

5.3.8 Investigating CO/O Interactions with RuO_2 for Both RuO_2@MOF-808-P and RuO_2/SiO_2

Note that, in this section, unless stated the experiments were performed by Dr Lijun Gao.

CO temperature-programmed reduction (CO-TPR): The CO-TPR was carried out with a micromeritics chemisorption analyzer (Auto Chem 2910) equipped with a mass spectrometer (MS, Omnistar). The sample (30 mg) was pretreated in 20 vol% O2 + 80 vol% Ar at 150 °C for 10 min (RuO_2@MOF-808-P) or 250 °C for 1 hr (RuO_2/SiO_2) and then switched to He gas. After cooling down to 45 °C in He, the treated sample was exposed to 5 vol% CO + 95 vol% He and held for 30 min. The sample was heated from 45 to 800 °C with a ramping rate of 10 °C. The products were analysed using an on-line mass spectrometry.

***In situ* XAS:** The XAS characterisation was performed by both Dr Lijun Gao and Mr Jinhu Dong. *In situ* XAS measurements were carried out at the BL14W1 beamline of SSRF. The spectra were recorded in transmission mode. Self-supporting pellets were prepared from RuO_2@MOF-808-P and Ru/SiO_2 samples. The pellets were loaded in a quartz cell. A heating element was wrapped around the cell to alter the sample temperature. The temperature was measured by a K-type thermocouple in contact with the cell. Prior to the XAS measurements the samples were activated by 20 vol% O_2 + 80 vol% He at 150 °C for 10 min (RuO_2@MOF-808-P) or 250 °C for 1 hr (RuO_2/SiO_2) and cooling down to 30 °C in Ar. The spectra were collected for the O_2-activated samples first. The comparison spectra were collected by treating the O2-activated samples with flow of 5 vol% CO + 95 vol% He at 30 °C for 30 min.

***In situ* DRIFTS:** *In situ* DRIFTS spectra were recorded on a BRUKER TENSOR 27 spectrometer equipped with a diffuse reflectance accessory (the Praying Mantis) and a reaction chamber (operation temperature from -150 °C to 600 °C). The powder sample was loaded into a sample cup. The sample temperature was controlled by a heater and measured by two thermocouples. One of them was placed in the sample cup; the other one was immobilized on the sampling stage. The flow rate passing through the reaction chamber was controlled by the mass flow controllers. The DRIFT spectra were recorded using a spectral resolution of 4 cm^{-1} and accumulating 32 scans. Before the DRIFTS acquisition, the samples were pre-treated in 20 vol% O_2 + 80 vol% Ar at 150 °C for 10 min (RuO_2@MOF-808-P) or 250 °C for 1 hr (RuO_2/SiO_2) and cooled down to room temperature in Ar.

For temperature-dependent CO desorption characterization, 5 vol% CO + 95 vol% He was used. The sample was exposed to 5% CO at room temperature first and then decreased to -50 °C by liquid nitrogen and kept for 2 hrs (RuO_2@MOF-808-P) or 1 hr (RuO_2/SiO_2) until no change was observed in the real-time spectra (*i.e.* CO adsorption in equilibrium). Then the gas flow was switched to Ar gas at room temperature and increased the sample temperature to the targeted one. After each targeted temperature was reached for 10 min, the corresponding DRIFTS spectra were collected.

Under reaction conditions, the O_2-activated samples were exposed to the reaction gas (1 vol% CO + 20 vol% O2 + 79 vol% He) at room temperature for 30 min first. It was heated to the target temperatures (*i.e.* 30 °C, 100 °C, and 150 °C) in Ar and held for 10 min, and then the DRIFTS spectra were collected.

5.3.9 Catalysed CO Oxidation Tests

Note that, in this section, unless stated the experiments were performed by Dr Lijun Gao.

The catalysts were loaded into a fixed-bed micro-reactor. Before catalytic activity, the RuO_2@MOF-808-P and Ru/SiO_2 catalysts were exposed to O_2 (O_2-activated) or Ar (Ar-activated) gas at 150 ^{o}C for 10 min with a flow rate of 30 ml/min (to form activated RuO_2@MOF-808-P) and 250 ^{o}C for 1 hr (to form activated RuO_2/SiO_2), respectively. After cooling down to room temperature in Ar gas (30 ml/min), the gas stream was switched to a reaction gas (1 vol% CO, 20 vol% O_2, 1vol% N_2, and balanced with He) with a specific weight hourly space velocity (WHSV). The gas products were analysed with an on-line micro-gas chromatograph (Agilent GC-490) equipped with a 5 Å molecular sieve column and a thermal conductivity detector (TCD). For the apparent activation energy measurements, CO oxidation reactions were performed under a kinetic-limiting region in which the CO conversion was below 25% using a much higher WHSV.

Activation energy (E_a) was obtained based on the Arrhenius equation:

$$k = Ae^{\frac{-E_a}{RT}} \qquad \text{Equation (5.16)}$$

where, k is the reaction rate, A is the pre-exponential factor, R is the gas constant (~ 8.314 $J \cdot mol^{-1} \cdot K^{-1}$) and T is the temperature in K. Taking the natural logarithm of the Equation 5.16 yields:

$$\ln(k) = \ln(A) - \frac{E_a}{R}\frac{1}{T} \qquad \text{Equation (5.17)}$$

Since k values at different temperatures were obtained from the detection system, linear Arrhenius relation was plotted based on the Equation 5.17. E_a was therefore calculated based on the slope of the plot.

Turnover frequency (TOF, conversion per unit site per unit time) is defined as the average number of molecules reacted at each catalytic site per unit time. The number of catalytic sites per unit mass of catalyst (*i.e.* catalytic site density) was obtained from the CO pulse chemisorption (assuming that one CO molecule could occupy one site), which was performed using a micromeritics chemisorption analyser (Auto Chem 2920). The sample (30 mg) was pre-treated in 20 vol% O_2 + 80 vol% Ar at 150 °C for 10 min (RuO_2@MOF-808-P) or 250 °C for 1 h (RuO_2/SiO_2) and then switched to He gas. After cooling down to -50 °C in He, the treated samples were exposed to CO pulses consisting of 5 vol% CO balanced with He. All gas follow rate was set to 30 ml/min. The CO concentration was measured using a detector based on thermal conductivity. TOF was then calculated:

$$TOF = \frac{k}{\text{catalytic site density}} \qquad \text{Equation (5.18)}$$

For the water stability tests, the RuO_2@MOF-808-P catalysts were pre-treated by reaction gas (1 vol% CO and 20 vol% O_2 balanced with He) at 150 ^{o}C for 10 min. After cooling down to room temperature in Ar, the gas flow was switched to reaction gas with WHSV = 400 $Lg_{Ru}^{-1}h^{-1}$ for activity test. Then the catalysts were treated by 10 vol% water which was injected by a syringe pump (LEAD FLUID, TYD03) at 100 ^{o}C for 1 hr. The lines from the pump to the reactor were heated at a high temperature. After the water treated, the catalysts were exposed to Ar at 120 ^{o}C for 60 min. The activity test was carried out from 30 ^{o}C to 100 ^{o}C with a heating rate of 0.5 ^{o}C/min. The gas products were analyzed by an on-line gas chromatography (Agilent GC 6890) equipped with a packed column PQ200 and a TCD. Before the products analysis, the moisture was condensed by ice.

5.4 Results and Discussion

5.4.1 RuO$_2$@MOF-808-P Preparation

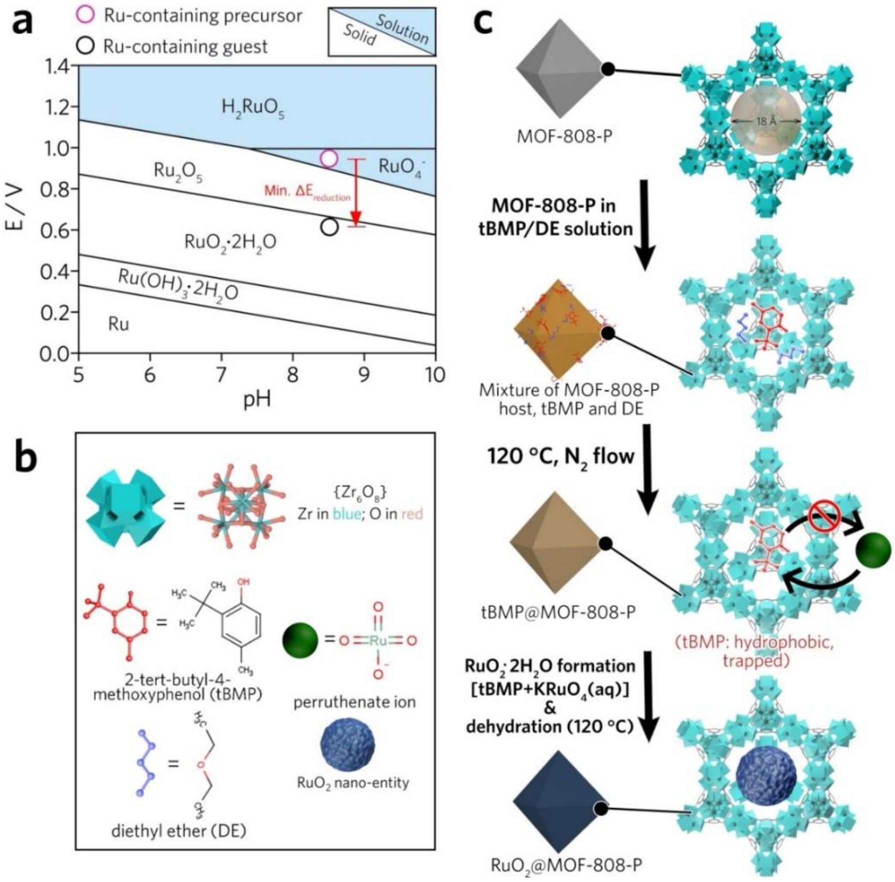

Figure 5.3 PEGS strategy for RuO$_2$@MOF-808-P: (a) The Pourbaix diagram for Ru-H$_2$O system (pH = 5-10; concentration of Ru-based solution = 20 mM) constructed based on previously available data versus standard hydrogen electrode (SHE).[238] (b) shows symbols for the scheme in (c), which describes RuO$_2$ synthesis inside the cavity of MOF-808-P using tBMP (hydrophobic reducing lipid). For clarity, (i) the schematics of MOF-808-P is simplified as standard MOF-808[249]; (ii) hydrogen atoms and carbon atoms for formates ($HCOO^-$) are omitted in the MOF cage. The schematic drawings were made by Dr Jingwei Hou and the author. The figure is reprinted under a Creative Commons Attribution 4.0 International Licence (CC BY 4.0) from ref. [260] (Copyright 2019 Nature Publishing Group).

The overview about RuO$_2$@MOF-808-P preparation is given in Figure 5.3. Since tBMP (Figure 5.2b) was solid at room temperature, DE (with low boiling temperature) was used as the solvent to prepare the tBMP solution for impregnation. Similar to the previous literature,[114,195] by HR-TGA characterisation (Figure 5.4) the author noticed that the temperature-controlled selective desorption could happen to the mixture of tBMP, DE and MOF-808-P (*i.e.* tBMP/DE@MOF-808-P). In the HR-TGA results, the stepwise drops in the top figure and the derived peaks in the bottom figure can be assigned to several desorption/decomposition events. Just below ~ 50 °C, DE can be mostly removed. There are two desorption temperatures for tBMP – a lower one at ~ 100 °C which is attributed to the tBMP outside the MOF (weaker tBMP-MOF interaction); the other one is just below 200 °C which can be due to tBMP entrapped inside the MOF. Above ~ 250 °C, there are two further weight-loss steps (at ~ 270 °C and ~ 570 °C) which can be assigned for the decomposition/pyrolysis of the MOF host (using the dried MOF-808-P as reference).

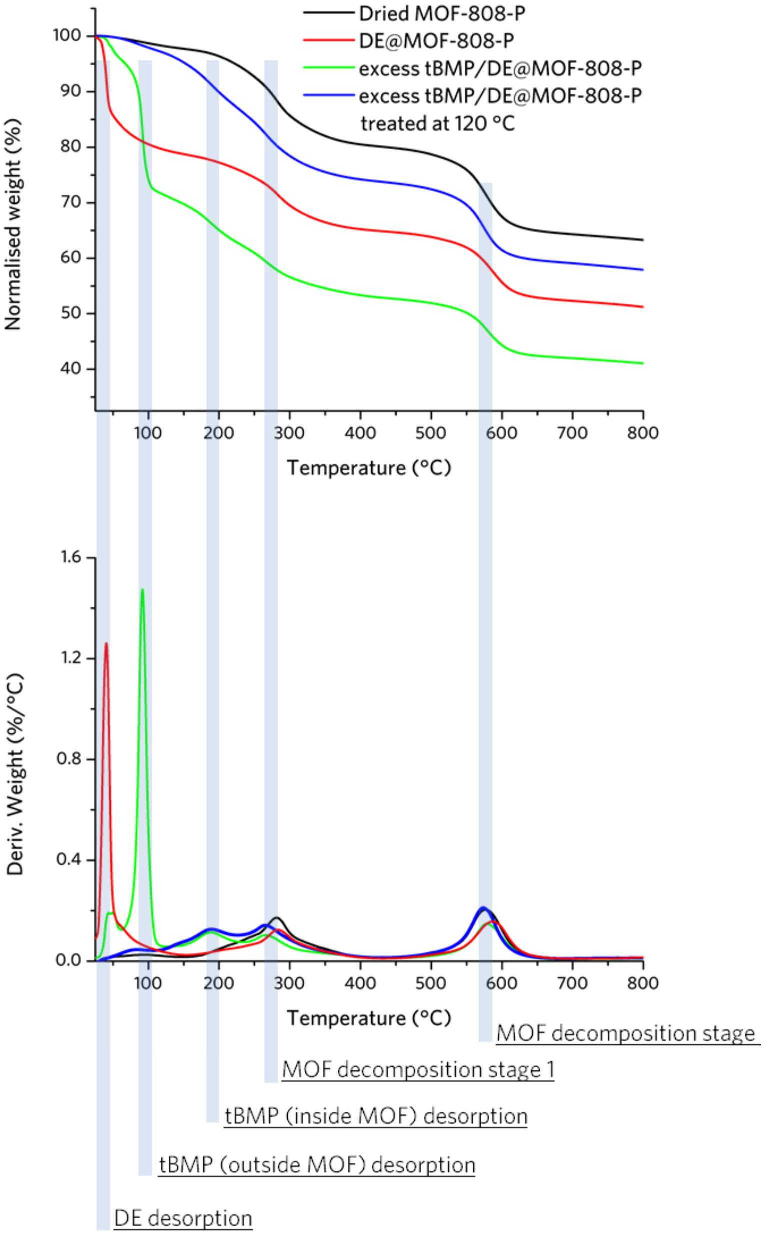

Figure 5.4 HR-TGA on dried MOF-808-P, DE@MOF-808-P, tBMP/DE@MOF-808-P (tBMP in excess) and tBMP/DE@MOF-808-P (tBMP in excess) after being treated at ~ 120 °C: normalized weight versus temperature (top) & derivative of weight loss (weight loss upon

incremental increase in temperature) versus temperature (bottom). The figure is reprinted under a Creative Commons Attribution 4.0 International Licence (CC BY 4.0) from ref. [260] (Copyright 2019 Nature Publishing Group).

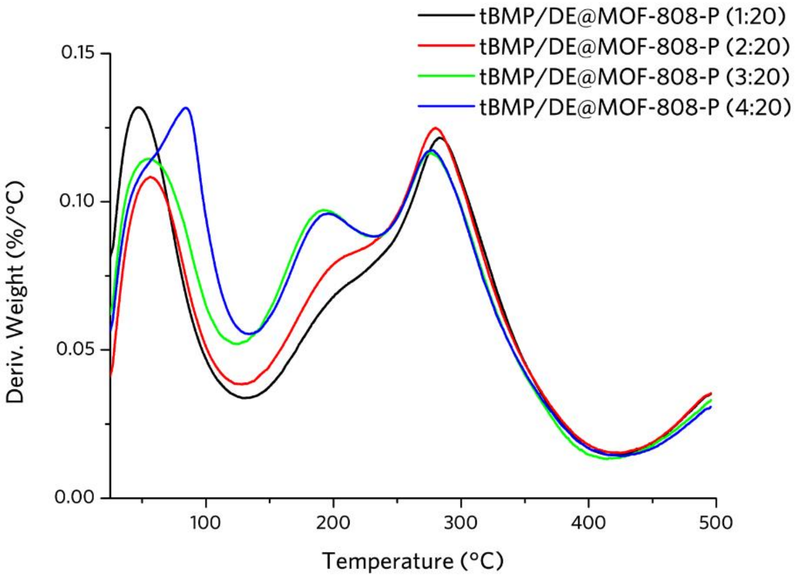

Figure 5.5 HR-TGA results (derivative of weight loss versus temperature) for tBMP/DE@MOF-808-P with different tBMP:MOF-808-P mass ratios. The figure is reprinted under a Creative Commons Attribution 4.0 International Licence (CC BY 4.0) from ref. [260] (Copyright 2019 Nature Publishing Group).

Hence, to remove both DE and tBMP (outside the MOF) tBMP/DE@MOF-808-P was treated at ~ 120 °C (Figure 5.3c). As a consequence, only tBMP inside the MOF host can remain after treatment, *i.e.* tBMP@MOF-808-P. In addition, by changing the tBMP:MOF-808-P mass ratio (retaining the tBMP-in-DE concentration), tBMP can be partially filled in the MOF's pore in a relatively controlled manner. The maximum tBMP loading has been reached when the tBMP:MOF-808-P mass ratio reaches 4:20 [*i.e.* tBMP/DE@MOF-808-P(4:20)]. A apparent peak can be found at ~ 100 °C revealing a significant amount of tBMP outside the MOF. Furthermore, peak height at ~ 200 °C (desorption of tBMP inside the MOF) is very similar (only marginally lower due to the change in relative ratio) to that of tBMP/DE@MOF-808-P(3:20) support the tBMP saturation inside the MOF using the impregnation method.

Hydrous RuO_2 can form inside the MOF by mixing tBMP@MOF-808-P with the $KRuO_4$ solution via the redox reaction between $KRuO_4$ and tBMP. Since tBMP is immiscible with the aqueous solution, when the $KRuO_4$ (aq) solution is about to infiltrate the MOF's pores tBMP molecules inside the MOF cannot escape from the cavity (Figure 5.3c). Upon contacting with tBMP, the RuO_4^- ion is reduced to hydrous RuO_2. During the reaction, $KRuO_4$ reduces to hydrous RuO_2 while tBMP can be oxidized to its oxidizing derivatives similar to the oxidation of BHT.[261,262] The LC-MS analysis of (i) filtrate solution after the reaction between tBMP@MOF-808-P and $KRuO_4$ (aq) and (ii) comparison reaction between pure tBMP and $KRuO_4$ (aq) confirms the presence of ketone derivatives as the oxidation products of tBMP. The reaction between tBMP@MOF-808-P and $KRuO_4$ solution was kept for ~ 4 hrs. In the case of using tBMP/DE@MOF-808-P(2:20), the pH was ~ pH8.5 and ~ pH6 before and after the reaction. To facilitate the $KRuO_4$ (aq) solution infiltration and the contact between tBMP and RuO_4^- partially filled tBMP@MOF-808-P [*e.g.* tBMP/DE@MOF-808-P(2:20)] were preferred in the experiments.

After the synthesis, the white MOF-808-P turned to almost black hydrous RuO_2@MOF-808-P. Additionally, no color change was found for both $KRuO_4$ solution and pure MOF-808-P upon mixing. This indicated that MOF-808-P could not react with $KRuO_4$, which was confirmed powder XRD detailed in the next section. The hydrous RuO_2@MOF-808-P was then dehydrated at ~ 140 °C to form RuO_2@MOF-808-P.

To demonstrate the loading position control, the redox reactions by adding $KRuO_4$ (aq) solution to tBMP/DE/MOF-808-P mixture with and without the temperature-controlled selective desorption (Figures 5.6a) were carried out. By deliberately avoid the temperature-controlled selective desorption, a significant material deposition was found on the outer surface of the MOF (Figures 5.6a, top) in the dehydrated product. Since the tBMP/DE mixture on the outer surface will form droplets in contact with the $KRuO_4$ (aq) solution to minimize the surface energy due to hydrophobic-hydrophilic repulsion, tBMP (outside the MOF) can only react with $KRuO_4$ at the droplet-water interface forming a solid shell of hydrated RuO_2. This is consistent with the core-shell nanostructures deposited outside the MOF.

The chemical composition of the core-shell structures was verified by STEM-EDS (Figures 5.6b). While both Zr and Ru signal were detected from the Zr-based MOF region after RuO_2 loading, only Ru signal can be collected for the core-shell nanostructures (highlighted in the yellow frame in Figures 5.6b). In contrast, the dehydrated product (*i.e.* RuO_2@MOF-808-P) from the reaction between $KRuO_4$ (aq) solution and tBMP@MOF-808-P (with the temperature-controlled selective desorption) shows quite clean MOF surface

(Figures 5.6a, bottom). Further, the Ru signal mapping overlaps well with that for Zr and the MOF DF-STEM image (Figures 5.6c). The significant outer surface disposition is therefore proved to be effectively inhibited by applying both temperature-controlled selective desorption and hydrophobic-hydrophilic repulsion.

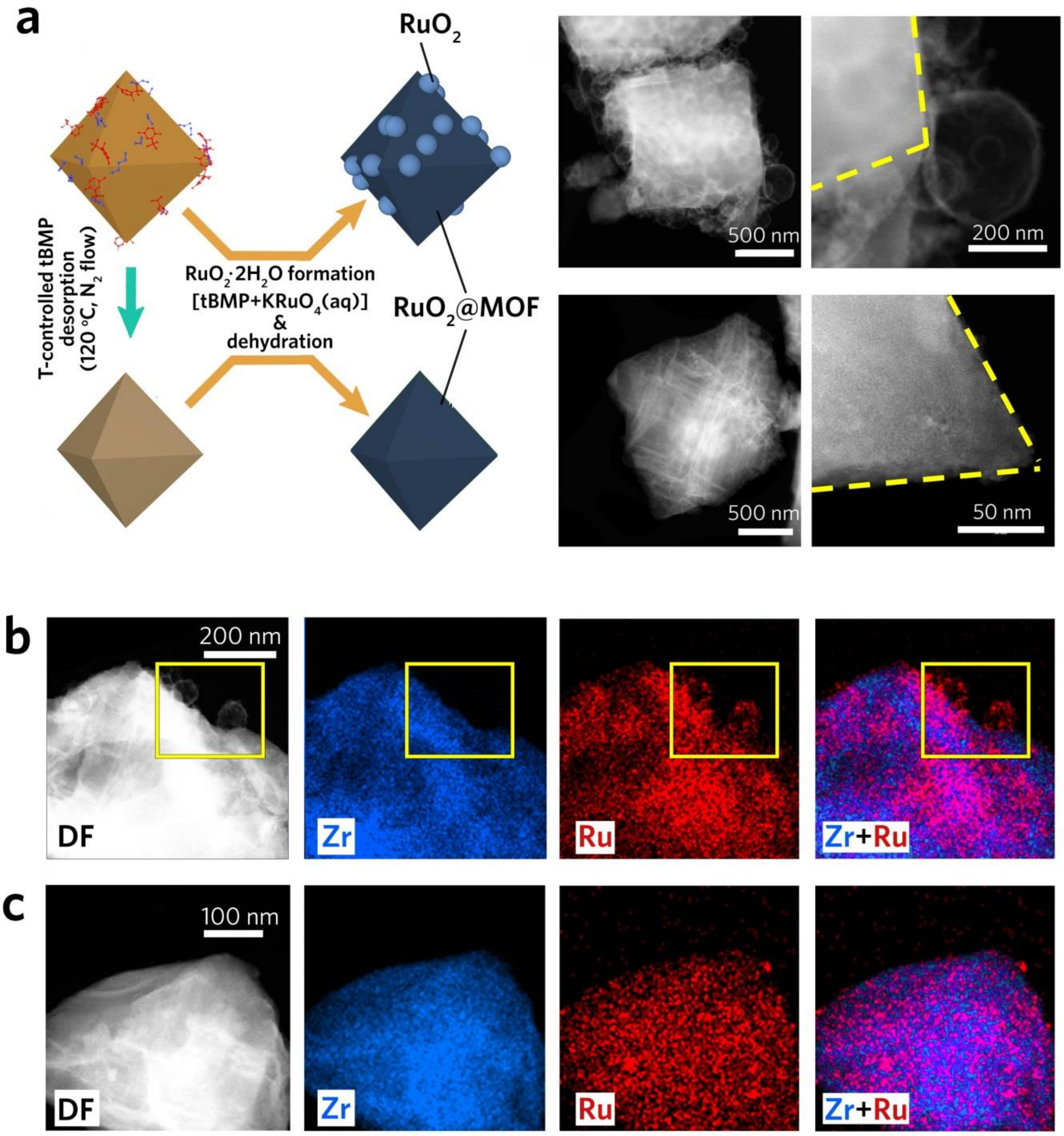

Figure 5.6 Controllable RuO$_2$ guest formation inside (or both inside and outside) the MOF-808-P: (a) RuO$_2$ can be formed both inside and outside the MOF, or only inside the MOF (i.e. RuO$_2$@MOF-808-P) via temperature-controlled selective desorption of the tBMP molecules outside the MOF. DF-STEM images to the right show core-shell structures on the outer surface of the MOF crystals (top, for RuO$_2$ formed inside and outside the MOF) vs. clean MOF crystal edges

(bottom, for RuO_2 loaded mostly inside the MOF). The deposition is further verified by STEM-EDS Zr and Ru mappings for (b) RuO_2 formed inside and outside the MOF and (c) RuO_2 loaded mostly inside the MOF. The yellow frames in (b) highlight the Ru-based core-shell structures. Raw images are provided as a Source Data file. The schematic drawing was prepared by Dr Jingwei Hou and the author. The DF-STEM was acquired by Dr James T. Griffiths and Tiesheng Wang. STEM-EDS was collected by Dr Lijun Gao. The figure is reprinted under a Creative Commons Attribution 4.0 International Licence (CC BY 4.0) from ref. [260] (Copyright 2019 Nature Publishing Group).

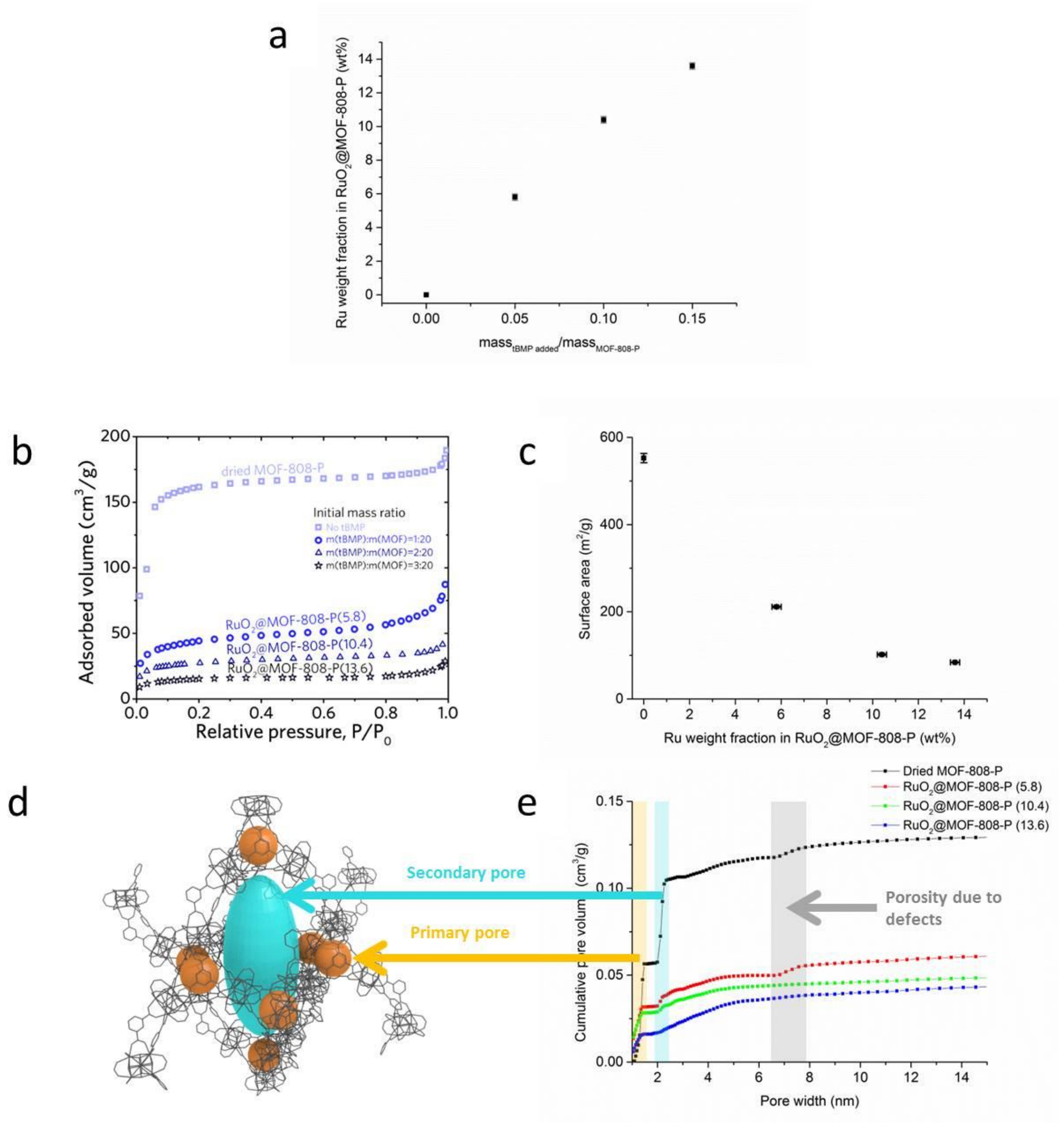

Figure 5.7 Tunable guest loading amount is confirmed by ICP-OES and N_2 adsorption measurements: (a) By varying tBMP amount loading in MOF-808-P [$n(KRuO_4)$: n(tBMP) kept to approx. 2:1], different RuO_2 guest loading was achived as revealed from the Ru-element weight

fraction measured by ICP-OES. (b) N_2 adsorption isotherms show the amount of guest (*i.e.* RuO_2, quantified by ICP-OES) loaded in the MOF is related to the amount of tBMP in the MOF. (c) BET surface area decreases when more guest (i.e. RuO_2) is incorporated (from ICP-OES). Similarly, the reduction in reduction in cumulative pore volume for both primary pore and secondary pore can be found in (d) and (e). The parentheses in samples' labels in (b) and (e) represent the Ru-element weight fraction measured by ICP-OES. Mr Servann J. A. Herou performed the N_2 adsorption measurements. The figure is reprinted under a Creative Commons Attribution 4.0 International Licence (CC BY 4.0) from ref. [260] (Copyright 2019 Nature Publishing Group).

Furthermore, tuneable loading amounts of the guest were achieved by adjusting the mass ratio between tBMP and the MOF (Figures 5.5 and 5.7). According to the N_2 adsorption results, the N_2 uptake decreases when more RuO_2 were loaded inside the MOF (Figure 5.7a). In the meantime, cumulative pore size distribution (Figure 5.7e) shows reduction in the pore volume of both primary pore and secondary pore when RuO_2 is loaded. This indicates that the RuO_2 guest can form in both pores. The pore volume for secondary pore, however, has larger drop meaning RuO_2 guest prefers to be placed inside the secondary pore due to their larger size. This observation was also supported by DF-STEM images of the RuO_2 guest in the next section. Additionally, compared with BET area for the dried MOF-808-P from the literature[249] (~ 550 cm^3/g at P/P_0 of 0.2), the dried MOF-808-P in this project has much lower BET area (~ 160 cm^3/g at P/P_0 of 0.2). This could be explained by the defect formation and partial amorphization during MOF synthesis, solvent exchange and thermal activation. An additional step at ~ 7 nm can be found in the cumulative pore size distribution for dried MOF-808-P (Figure 5.7e). This ca be associated with the defects generated. The volume reduction can be found for this defective pore when RuO_2 is formed, which indicates that RuO_2 can also form inside this type of empty space.

5.4.2 RuO_2@MOF-808-P Characterisations

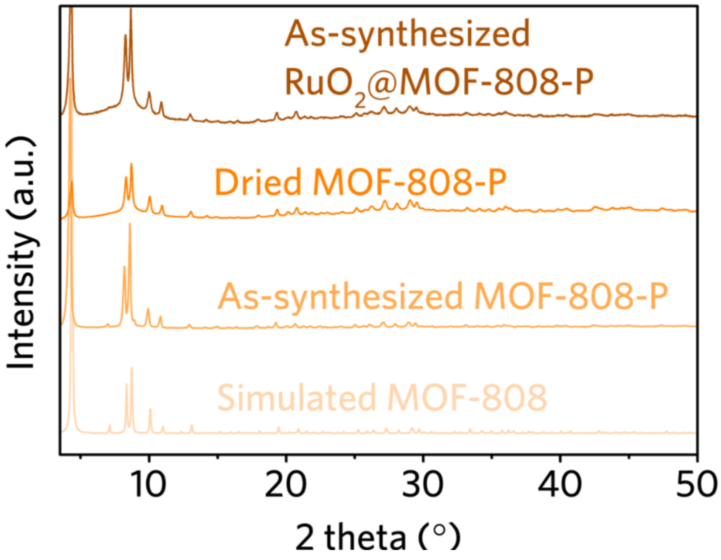

Figure 5.8 PXRD patterns for simulated MOF-808[249], as-synthesized MOF-808-P, dried MOF-808-P and as-synthesized RuO_2@MOF-808-P. The PXRD intensity is rescaled for better visualization. The figure is reprinted under a Creative Commons Attribution 4.0 International Licence (CC BY 4.0) from ref. [260] (Copyright 2019 Nature Publishing Group).

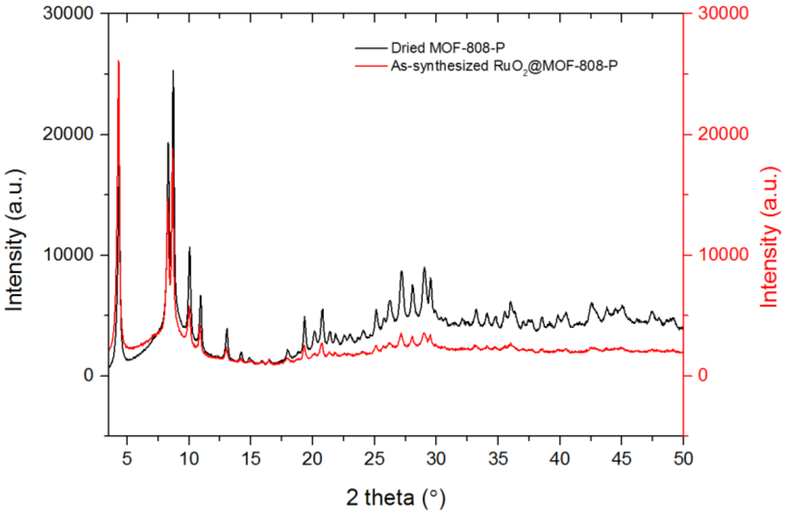

Figure 5.9. More detailed PXRD patterns for dried MOF-808-P and as-synthesized RuO_2@MOF-808-P. The figure is reprinted under a Creative Commons Attribution 4.0 International Licence (CC BY 4.0) from ref. [260] (Copyright 2019 Nature Publishing Group).

Since there is no significant change in the powder XRD peaks before and after loading RuO_2 (Figure 5.8), the MOF's structure was mostly preserved throughout the synthesis of RuO_2@MOF-808-P. No peak for RuO_2 crystal can be found in the powder XRD pattern for RuO_2@MOF-808-P, which indicates that if RuO_2 particles were there they would be very small (< 3 nm).[265] As shown in the more detailed PXRD patterns in Figure 5.9, peaks above 40° (2θ, related to long-range ordering features) can be hardly observed for as-prepared RuO_2@MOF-808-P (in red) as compared to dried MOF (in black). This indicates that further pore collapse and/or amorphization can take place during most-synthetic modification.[13,266,267] Note that the variation of intensity in peak below 5° (2 theta) can be largely influenced by the presence of guest compounds.[122]

The incorporation of Ru-based guest was characterised with a combination of (i) EDS mappings obtained from both SEM (Figure 5.10) and STEM (Figure 5.11), and (ii) XPS survey scan (Figure 5.12). The Ru signal distributions from SEM-EDS and STEM-EDS match well with those for Zr. Since MOF-808-P is a Zr-based MOF, the signal overlap confirms the successful loading of Ru-based guest. In the SEM-EDS spectrum, Ru Lα peak at ~ 2.6 keV can be seen. As a further verification, Ru 3p double peaks can be noticed at ~ 470 eV from the XPS survey scan. Note that no signal for potassium (K) residual can be found in the SEM-EDS spectrum (Figure 5.10, no peak at ~ 3.3 keV for Kα) or XPS survey spectrum (Figure 5.12, no peak at ~ 294 eV for K 2p). This is consistent with the further check by ICP-OES in the RuO_2@MOF-808-P.

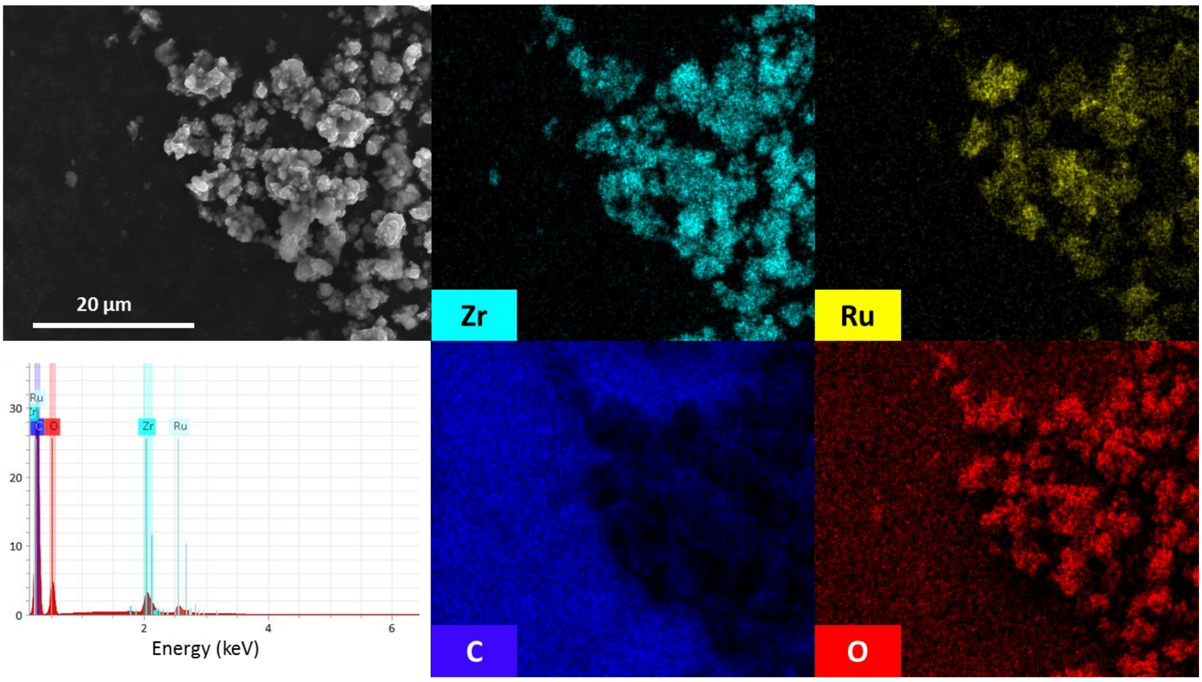

Figure 5.10 SEM-SE image (top left) and SEM-EDS overall spectrum and mappings (Zr, Ru, C and O) for RuO_2@MOF-808-P. Strong C signal in background can be found, as the sample powders are immobilized on the carbon tape. The figure is reprinted under a Creative Commons

Attribution 4.0 International Licence (CC BY 4.0) from ref. [260] (Copyright 2019 Nature Publishing Group).

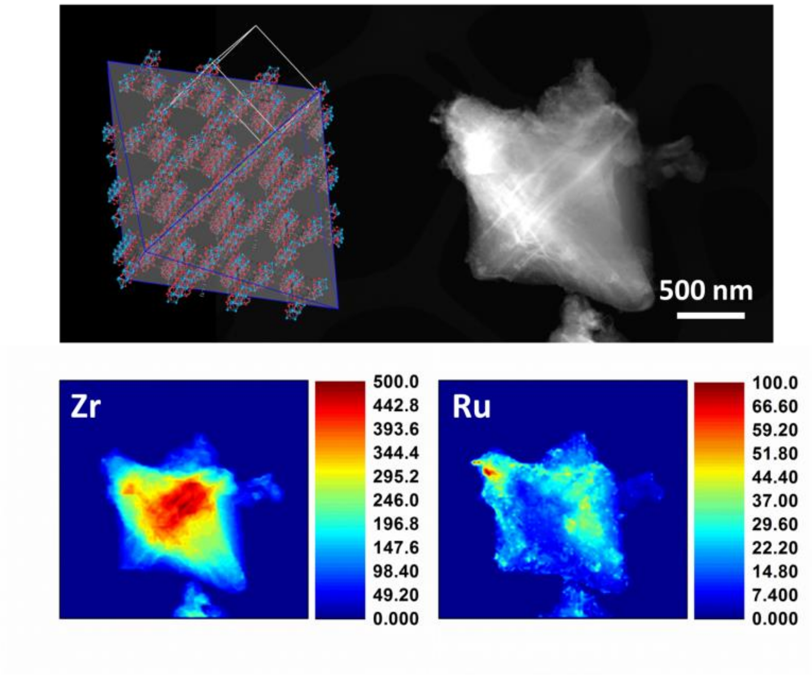

Figure 5.11 Simulated octahedron morphology of MOF-808 based on Ref. [250] by Mercury (https://www.ccdc.cam.ac.uk/solutions/csd-system/components/mercury/) (top left). DF-STEM image (top right) and its associated STEM-EDS mappings (Zr and Ru) for a RuO_2@MOF-808-P particle. Since Zr and Ru have similar atomic number, they interact similarly with the electrons. Therefore, the contrasts from the Zr-based host and Ru-based guest in the DF-STEM image are similar. The STEM results were collected by Dr James T. Griffiths and the author. The figure is reprinted under a Creative Commons Attribution 4.0 International Licence (CC BY 4.0) from ref. [260] (Copyright 2019 Nature Publishing Group).

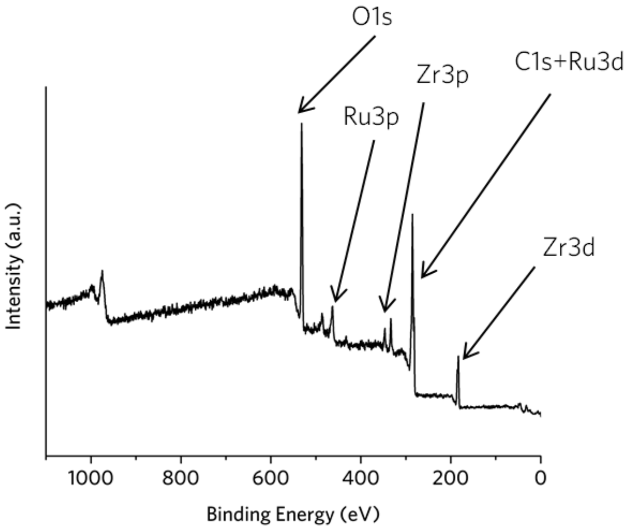

Figure 5.12 XPS survey spectrum for as-synthesized RuO_2@MOF-808-P. The presence of Ru (from the RuO_2 guest), Zr (from the MOF-808-P host), O (from both the guest and the host) and C (mostly from the host) is further verified. The XPS results were obtained by Dr Weiwei Li. The figure is reprinted under a Creative Commons Attribution 4.0 International Licence (CC BY 4.0) from ref. [260] (Copyright 2019 Nature Publishing Group).

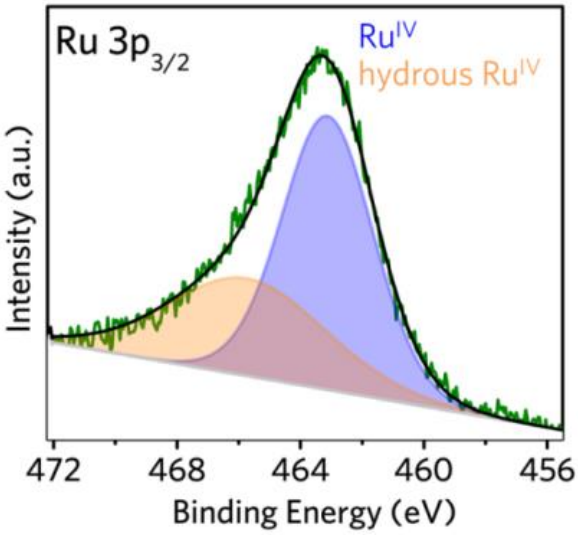

Figure 5.13 XPS Ru $3p_{3/2}$ spectrum for as-synthesized RuO_2@MOF-808-P. The Ru in as-synthesized RuO_2@MOF-808-P is dominated by Ru^{4+} at 463.2 eV.[268,269] The XPS results were obtained by Dr Weiwei Li. The figure is reprinted under a Creative Commons Attribution 4.0 International Licence (CC BY 4.0) from ref. [260] (Copyright 2019 Nature Publishing Group).

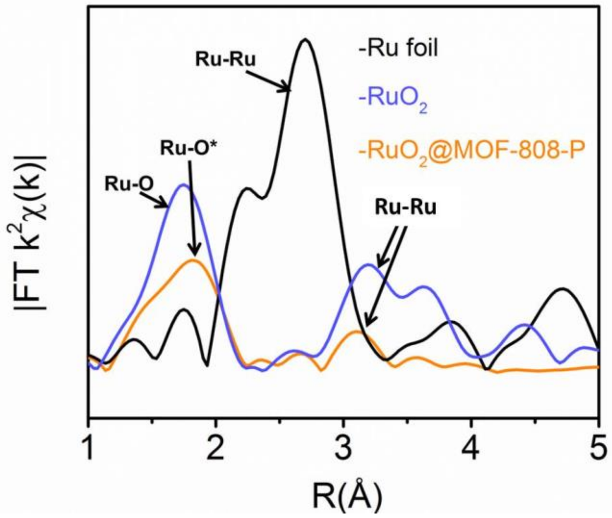

Figure 5.14 Fourier transformed (FT) k^2-weighted $\chi(k)$-function of the EXAFS results for Ru K-edge (~ 22.1 keV) for Ru foil, anhydrous RuO_2 and as-synthesized RuO_2@MOF-808-P obtained by XAS. The XAS results were obtained by Dr Lijun Gao and Mr Jinhu Dong. The

figure is reprinted under a Creative Commons Attribution 4.0 International Licence (CC BY 4.0) from ref. [260] (Copyright 2019 Nature Publishing Group).

XPS Ru $3p_{3/2}$ peak position (Figure 5.13) at ~ 463.2 eV confirmed the valence of Ru in the guest to be IV (*i.e.* Ru^{4+}).[268] A shoulder at higher binding energy was also observed which is likely to be the hydrous RuO_2 residual (in presence of –OH),[268,270] which can come from the uptake of moisture in the air. Extended x-ray absorption fine structure (EXAFS) measurements for Ru (Figure 5.14) identify the dominant Ru-O vector at ~ 1.78 Å[271]. Similar to the standard RuO_2 reference, the distance from a neighbouring Ru atom is ~ 3.1 Å (Figure 5.14), which matches reasonably well with the Ru-Ru distance in rutile RuO_2. Such Ru-Ru distance can be clearly distinguished from that for metallic Ru (*i.e.* Ru foil) (Figure 5.14). A marginal peak shift was noticed in RuO_2@MOF-808-P compared with the reference RuO_2. The presence of C (from the organic ligand of the MOF) in proximity to Ru might cause such small change.[271] Unlike the reference RuO_2 sample, there is no significant peaks for RuO_2@MOF-808-P beyond 4 Å (Figure 5.14). Since there is no indication for longer Ru-O or Ru-Ru inter-atomic distances, the particle size can be very small (*i.e.* from sub-nm to a few nm). Furthermore, high-resolution DF-STEM image (Figure 5.15) shows particles (~ 15 Å in diameter) with electron diffraction fringes. The space between two adjacent lines in the fringes is 2-2.5 Å (Figure 5.15b), which is consistent with the inter-planar spacing [$d_{(011)/(101)}$ or $d_{(200)/(020)}$)] expected for tetragonal RuO_2 (space group: $P4_2/mnm$). This, however, can also correspond to some inter-planar spacings for ZrO_2.

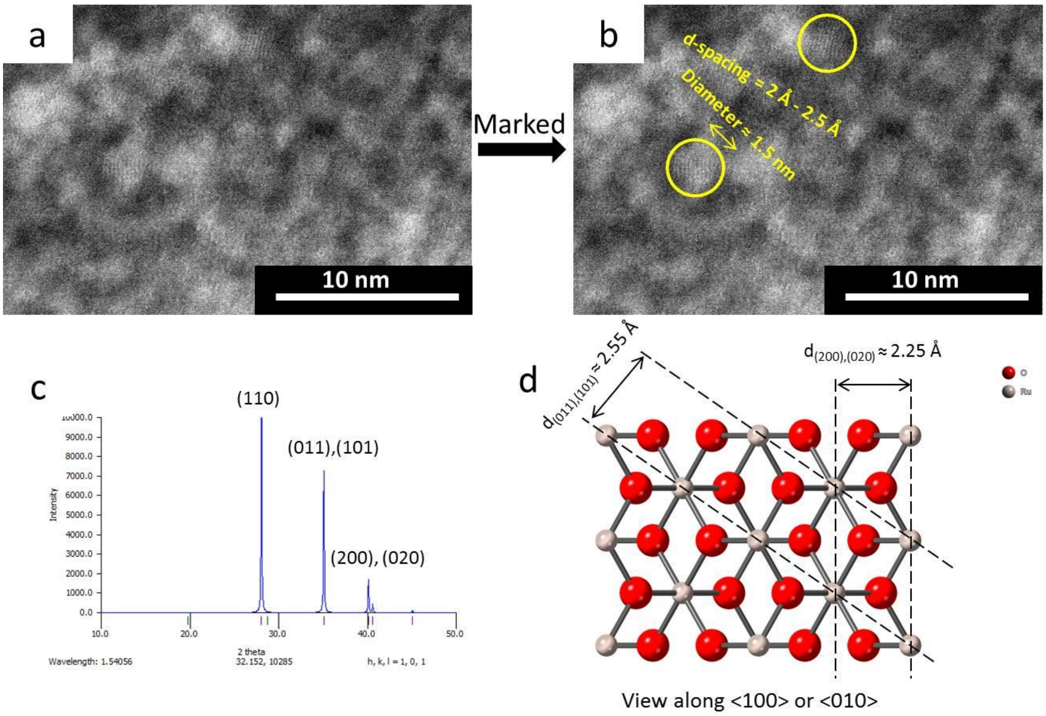

Figure 5.15 (a) DF-STEM image and (b) the same image highlighting the particles (~ 1.5 nm in diameter) with diffraction fringes of 2-2.5 Å. (c) Simulated RuO_2 (space group $P4_2/mnm$) XRD pattern. (d) Two potential diffraction planes in RuO_2 with d-spacing of 2-2.5 Å. The STEM results were obtained by Dr James T. Griffiths and the author. The figure is reprinted under a Creative Commons Attribution 4.0 International Licence (CC BY 4.0) from ref. [260] (Copyright 2019 Nature Publishing Group).

5.4.3 CO/O Interactions with RuO_2 for Both RuO_2@MOF-808-P and RuO_2/SiO_2

As mentioned in Section 5.2, the CO/O interactions with RuO_2 surface for RuO_2@MOF-808-P and the conventionally made RuO_2/SiO_2 were investigated. The preparation method and sample characterisations for RuO_2/SiO_2 are detailed in the Appendix for Chapter 5. Note that the Ru contents for both RuO_2@MOF-808-P and RuO_2/SiO_2 mentioned in this section are 10 wt%.

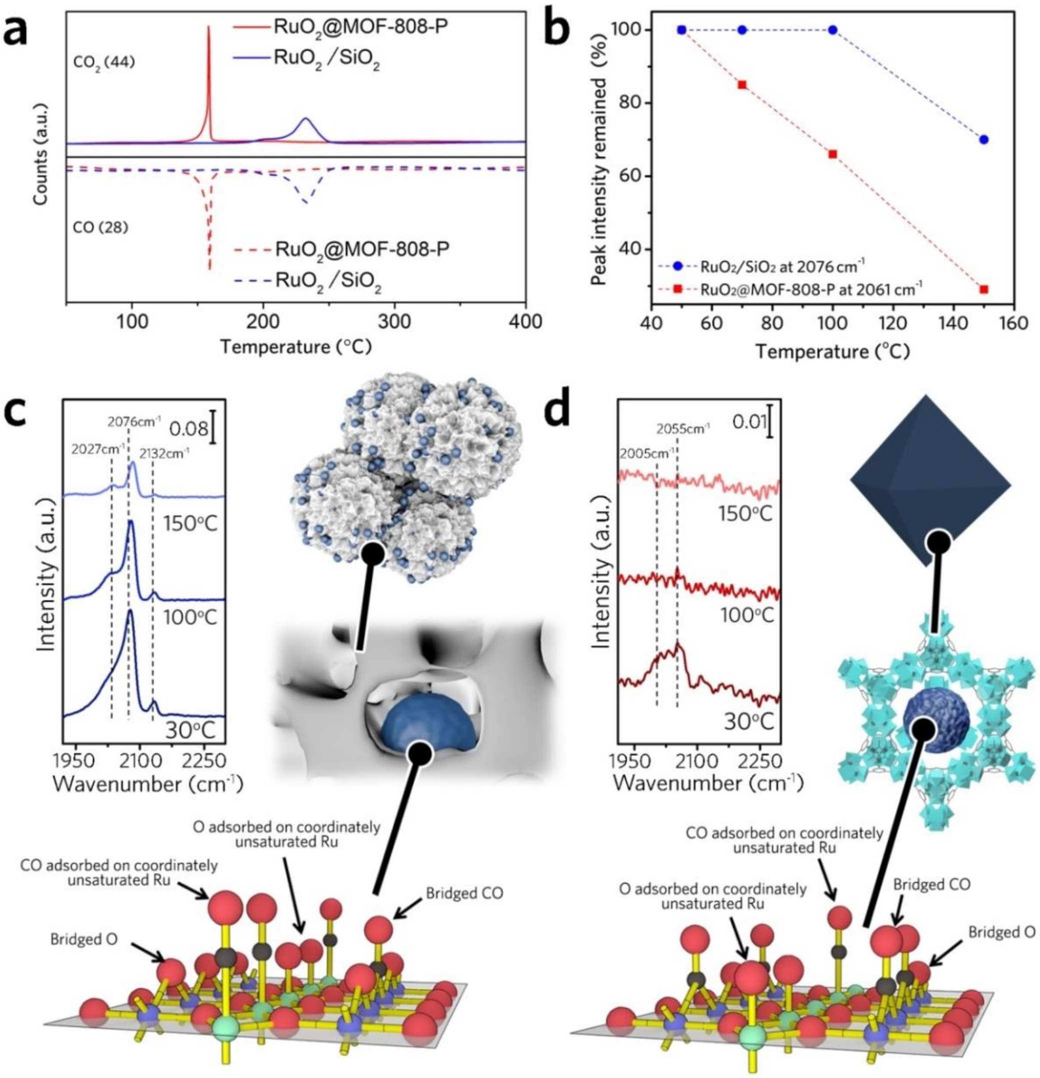

Figure 5.16 CO and O interactions with RuO_2 guest within the MOF as compared to RuO_2 supported on mesoporous SiO_2: (a) CO-TPR in flowing CO and (b) temperature-dependent DRIFTS peak intensity reduction (due to CO desorption) for samples with only surface-adsorbed CO in flowing Ar. (c) for RuO_2/SiO_2 and (d) for RuO_2@MOF-808-P show DRIFTS spectra with both surface-adsorbed CO and O in flowing Ar. The RuO_2 (110) surface is taken as an example to assist the interpretation of the DRIFTS results (O in red, C in black, and green and blue for alternating rows of Ru with different $\{RuO_6\}$ octahedral orientation). The CO-TPR and DRIFTS were done by Dr Lijun Gao. The schematic drawings were made by Dr Jingwei Hou and the author. The figure is reprinted under a Creative Commons Attribution 4.0 International Licence (CC BY 4.0) from ref. [260] (Copyright 2019 Nature Publishing Group).

Ru-O interactions within the RuO_2 were tested by CO-TPR, which were gradually heated in CO flow to find the minimum temperature for lattice Ru can be reduced (Figure 5.16a). The reduction peak for RuO_2@MOF-808-P emerged at a much lower temperature

(~ 160 °C) than that for RuO_2/SiO_2 (~ 240 °C). The results indicate that RuO_2 within the MOF has higher reducibility (*i.e.* weaker Ru-O bonding), which may be due to electronic confinement leading to bonding orbital distortion.[9] This is consistent with the *in situ* X-ray absorption near edge structure (XANES) spectra showing that RuO_2@MOF-808-P is susceptible to CO for reduction (Figure 5.17). The changes of slope in near-edge region of the spectra (highlighted in grey) reveal partial reduction in both RuO_2/SiO_2 and RuO_2@MOF-808-P upon CO exposure. From the weaker Ru-O bonding, the interaction of dissociated O with RuO_2 surface in RuO_2@MOF-808-P could also be weaker can be deduced.

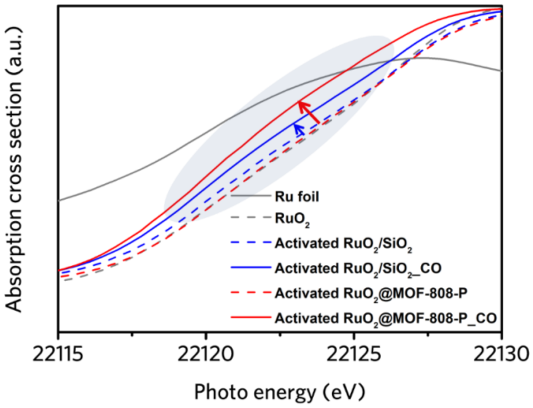

Figure 5.17 XANES spectra obtained from in situ XAS results for RuO_2/SiO_2 (in blue) and RuO_2@MOF-808-P (in red) before and after the CO adsorption at 30 °C (Ru foil and RuO_2 as reference samples in grey). The XAS results were obtained by Dr Lijun Gao and Mr Jinhu Dong. The figure is reprinted under a Creative Commons Attribution 4.0 International Licence (CC BY 4.0) from ref. [260] (Copyright 2019 Nature Publishing Group).

By comparing the results obtained from temperature-dependent CO desorption characterization (Figure 5.16b), the interaction of CO with MOF-confined RuO_2 surface was found to be weaker. Both samples were pre-treated in 5 vol% CO + 95 vol% He gas at room temperature and then heated up to 150 °C in flowing Ar. The peak intensity for on-top CO molecules (CO absorbed on coordinately unsaturated Ru) at the RuO_2@MOF-808-P surface (at 2061 cm^{-1}) is ready to decrease from room temperature and disappears at 150 °C whereas a similar peak for RuO_2/SiO_2 only start dropping from 100 °C and keeps 70% at 150 °C.

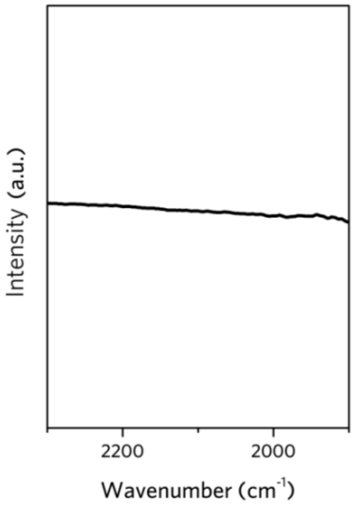

Figure 5.18 DRIFTS spectrum for MOF-808-P treated in the reaction gas and then in Ar at 30 °C. The treatment condition is the same as those mentioned in Figure 5.15. No signal for CO/O adsorption can be observed which provide a good background to study CO/O adsorption on RuO_2. The DRIFTS was done by Dr Lijun Gao. The figure is reprinted under a Creative Commons Attribution 4.0 International Licence (CC BY 4.0) from ref. [260] (Copyright 2019 Nature Publishing Group).

Table 5.1 DRIFTS absorption bands for RuO_2/SiO_2 and RuO_2@MOF-808-P and their interpretations.[254,255] The table is reprinted under a Creative Commons Attribution 4.0 International Licence (CC BY 4.0) from ref. [260] (Copyright 2019 Nature Publishing Group).

Sample	DRIFTS band (cm^{-1})	CO ads. type	Indication
RuO_2/SiO_2	2132	on-top	
	2076	on-top	presence of densely packed CO domains resisting CO oxidation at low temperatures
	2027	bridging	
RuO_2@ MOF-808-P	2055	on-top	loosely packed state of CO
	2005	bridging	with even fewer adsorbed O neighbors nearby

DRIFTS bands for samples pre-treated with gas for reaction also reveal the packing state of the adsorbed species, with densely packed CO adsorption domains observed on RuO_2/SiO_2 but not on RuO_2@MOF-808-P (Figures 5.16c&d). In this experiment, DRIFTS spectra of both samples were collected by adsorbing 1 vol% CO, 20 vol% O_2, and 79 vol% He at room temperature and then heating up in Ar. The DRIFTS bands are summarized in Table 5.1 with data interpretation,[254,255] which support the conclusions about weaker interactions of CO/O with RuO_2 within the MOF. As a control experiment (Figures 5.18) no similar peak feature was found in the spectra for the pure MOF-808-P.

Overall by forming RuO_2@MOF-808-P, (i) the interactions between O/CO and the catalyst (*i.e.* RuO_2) surface are weakened, which (ii) further inhibit the formation of densely packed CO domains. Therefore, in RuO_2@MOF-808-P, the adsorbed CO is more ready to react with adsorbed O and detach from the RuO_2 surface. This is further confirmed by the DRIFTS results in Figures 5.16c&d: at 100 ^{o}C, surface CO has been completely reacted and removed on the RuO_2@MOF-808-P catalysts whereas most CO molecules still stay on RuO_2/SiO_2. The ability to enhance the surface CO and O species desorption (*i.e.* modulation) by forming the RuO_2@MOF-808-P motivated us to check the performance of both catalysts for CO oxidation.[243,272–275]

5.4.4 RuO_2@MOF-808-P and RuO_2/SiO_2 as Catalysts for CO Oxidation

The oxidation tests demonstrate that RuO_2@MOF-808-P is a better catalyst than RuO_2/SiO_2 (~ 5% vs. no CO conversion at 30 °C; 100% at 65 °C vs. 100% at 150 °C). Note that the Ru contents for both RuO_2@MOF-808-P and RuO_2/SiO_2 mentioned in this section are 10 wt%. Both catalysts are more active after O_2 activation than after Ar activation (Figure 5.19a). This suggest that oxygen-rich Ru oxide is the active species low temperature CO oxidation.[276] The apparent E_a from the MOF-confined and SiO_2-supported RuO_2 was calculated to be E_a = 86 kJ/mol and E_a = 145 kJ/mol, respectively (Figure 5.19b). The activation energy of the RuO_2@MOF-808-P falls onto the lower boundary of the known RuO_2 activation energies.[244] Meanwhile, the TOF for RuO_2@MOF-808-P (Figure 5.19c) was found to be higher than that for RuO_2/SiO_2 and other similar catalysts in Table 5.2. The high TOF could be duo to the lack of densely packed CO domains. To confirm that the MOF has no influence on the catalysis, MOF-808-P and tBMP@MOF-808-P were tested for catalytic CO oxidation (Figure 5.20). Both reference samples were activated by Ar gas at 120 ^{o}C for 1h (catalysts mass: 25.8 mg, WHSV= 120 $L\cdot g_{Ru}^{-1}\cdot h^{-1}$). Both MOF-808-P and tBMP@MOF-808-P were inactive for CO oxidation. The negative conversion observed for tBMP@MOF-808-P could be caused by tBMP desorption from the MOF.

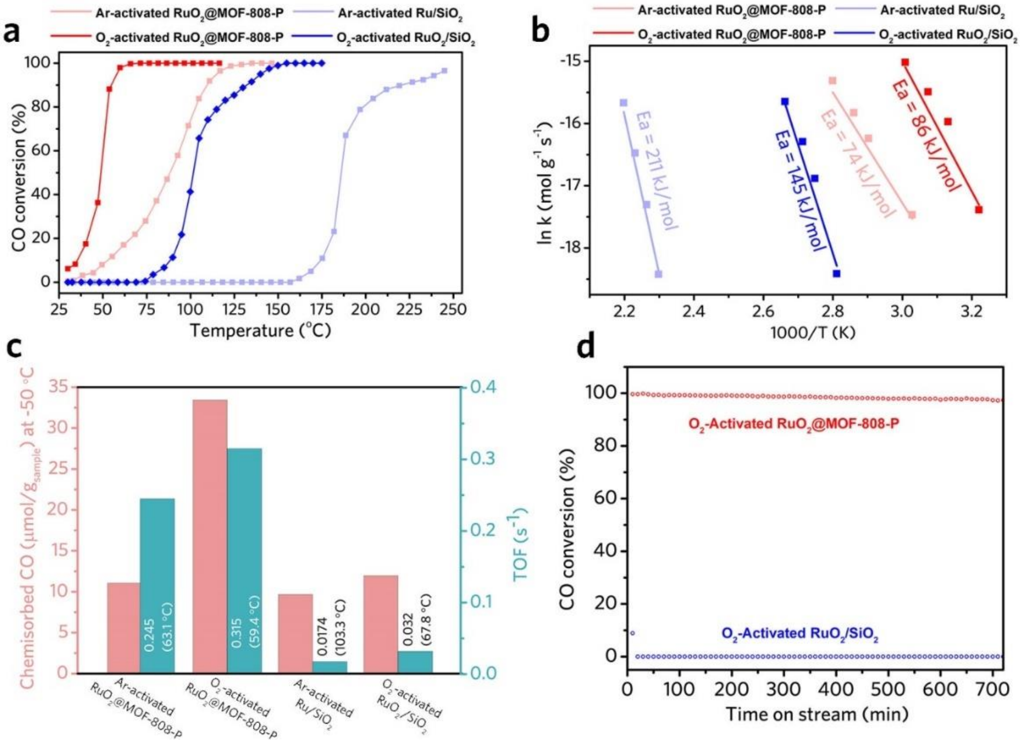

Figure 5.19 CO oxidation tests for RuO_2/SiO_2 and RuO_2@MOF-808-P catalysts: (a) CO conversion profiles at WHSV of 2000 $L\cdot g_{Ru}^{-1}\cdot h^{-1}$ with 15 mg catalysts; (b) Arrhenius plots and apparent E_a; (c) chemisorbed CO at -50 °C and calculated TOF. (d) Stability test at 100 °C using O_2-activated RuO_2/SiO_2 and RuO_2@MOF-808-P catalysts (2000 $L\cdot g_{Ru}^{-1}\cdot h^{-1}$, 15 mg catalysts). The CO oxidation tests were done by Dr Lijun Gao. The figure is reprinted under a Creative Commons Attribution 4.0 International Licence (CC BY 4.0) from ref. [260] (Copyright 2019 Nature Publishing Group).

Table 5.2 CO oxidation with other guest@MOF or Ru-based systems from the literature. The table is reprinted under a Creative Commons Attribution 4.0 International Licence (CC BY 4.0) from ref.[260] (Copyright 2019 Nature Publishing Group).

catalysts	CO/O_2 ratio	catalysts mass (mg)	WHSV (1×10^4 $ml\cdot g_{cat}^{-1}\cdot h^{-1}$)	particle size (nm)	T of 100 %CO conversion (°C)	T of 50 %CO conversion (°C)	Ea ($kJ\cdot mol^{-1}$)	TOF (s^{-1})	reference
10 % RuO_2@MOF-808-P	1/20	15	20	1-2	65	–	86	0.32	This work
10 % RuO_2/SiO_2	1/20	15	20	3-5	155	–	145	0.03	This work
5 % Au@ZIF-8	1/21	100	6	4.2	225	170	–		[265]
15 % Co_3O_4@ZIF-8	1/20	100	3	16.4	80	58	–		[277]
m-$5RuO_210CuO/CeO_2$	1/21	100	3	–	95		–		[278]
0.2 % RuO_2/Al_2O_3-ALD	1/21	2000	0.03	10	110		–	0.01	[279]
2 % Pt/ZIF-8 (encapsulation)	1/5	100	2	3.3	200		–		[280]
RuO_2	1/5	100	3	6	90		–		[281]
meso-RuO_2-O_2	1/2.8	60	5.2	6.2	29				[276]
3 % Ru/CeO_2	1/5	100	3	nanochain	140	127	–		[282]
5 % RuO_2/SnO_2-11	1/1	25	7	–	150	125	–		[283]
$Ru_{0.5}Cu_{0.5}/\gamma$-Al_2O_3	1/1	150	2	9.2	–	122	–		[284]
fcc-1% Ru/γ-Al_2O_3	1/1	150	2	5.9	–	141	–		[285]
2.92 Ru/SiO_2	2/1	15	Plug-flow condition	1.8	150 (CO conversion 90%)	–	–	0.0132 (CO_2 formation rate)	[286]

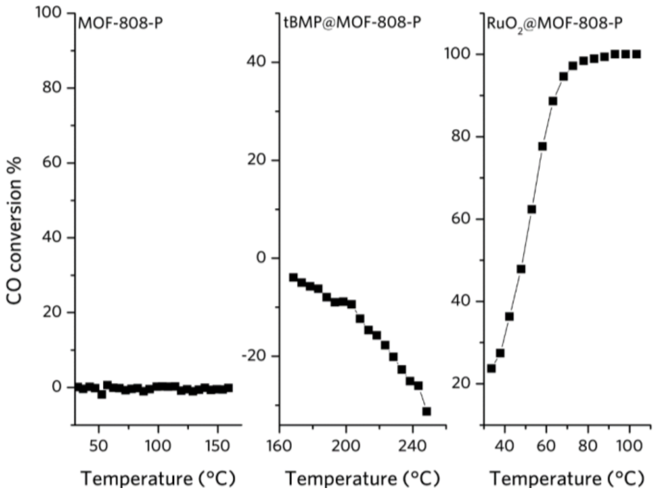

Figure 5.20 CO oxidation tests for MOF-808-P, tBMP@MOF-808-P and RuO_2@MOF-808-P. The CO oxidation tests were done by Dr Lijun Gao. The figure is reprinted under a Creative Commons Attribution 4.0 International Licence (CC BY 4.0) from ref. [260] (Copyright 2019 Nature Publishing Group).

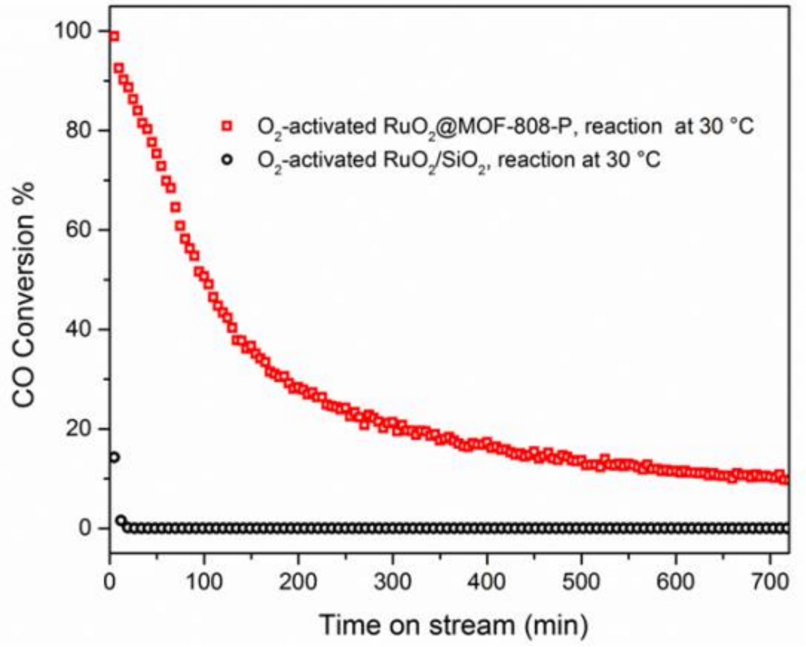

Figure 5.21 Stability test using O_2-activated RuO_2/SiO_2 and RuO_2@MOF-808-P (tests condition: 400 $L \cdot g_{Ru}^{-1} \cdot h^{-1}$, 30 mg catalysts) at 30 °C. The CO oxidation tests were done by Dr Lijun Gao. The figure is reprinted under a Creative Commons Attribution 4.0 International Licence (CC BY 4.0) from ref. [260] (Copyright 2019 Nature Publishing Group).

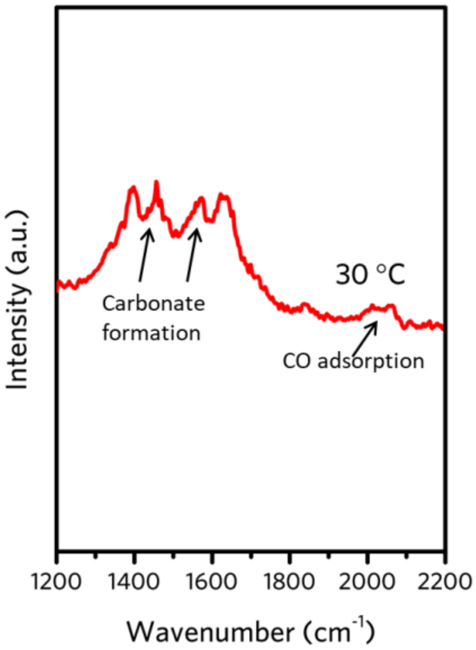

Figure 5.22 DRIFTS result for RuO_2@MOF-808-P in the reaction conditions as mentioned in Figure 5.21. At 30 °C, the peak features indicating the formation of carbonates can be noticed.[276] The DRIFTS was done by Dr Lijun Gao. The figure is reprinted under a Creative Commons Attribution 4.0 International Licence (CC BY 4.0) from ref. [260] (Copyright 2019 Nature Publishing Group).

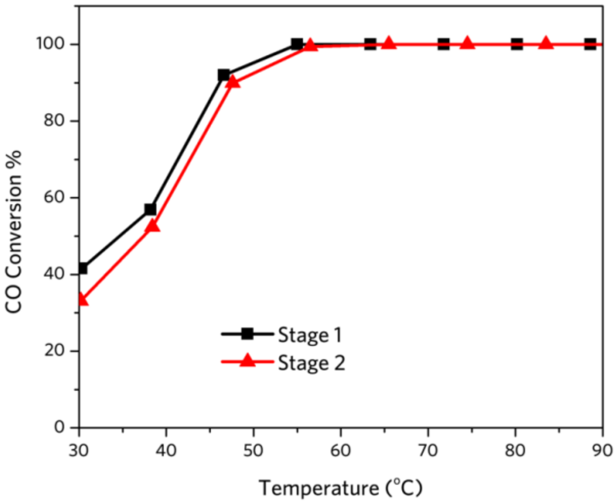

Figure 5.23 CO oxidation tests for RuO_2@MOF-808-P which was tested after the standard O_2-activation mentioned in this work (stage 1) and tested again after being treated with 10 vol% water vapour at 100 °C for 60 minutes (stage 2). Catalysts mass: 30 mg, WHSV = 400 $L \cdot g_{Ru}^{-1} \cdot h^{-1}$. The CO oxidation tests were done by Dr Lijun Gao. The figure is reprinted under a Creative Commons Attribution 4.0 International Licence (CC BY 4.0) from ref. [260] (Copyright 2019 Nature Publishing Group).

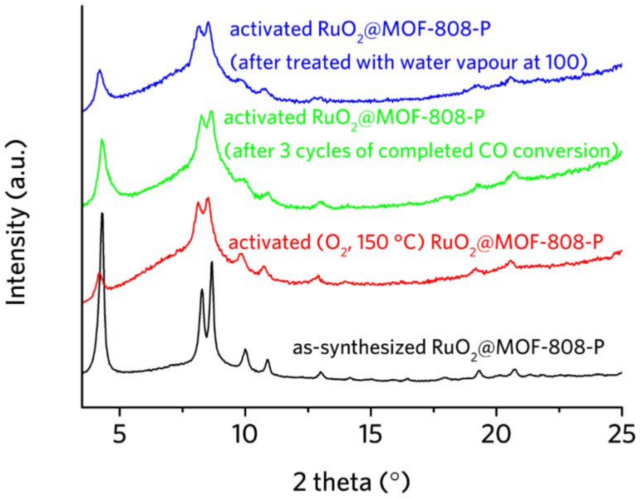

Figure 5.24 Powder XRD patterns for RuO_2@MOF-808-P after treatments/tests as labelled. The figure is reprinted under a Creative Commons Attribution 4.0 International Licence (CC BY 4.0) from ref. [260] (Copyright 2019 Nature Publishing Group).

At 100 °C and 2000 $L \cdot g_{Ru}^{-1} \cdot h^{-1}$ CO flow rate, RuO_2@MOF-808-P could still keep the conversion capability to be over 97% after 12 hrs (Figure 5.19d). In contrast, RuO_2/SiO_2 deactivated soon after the initiation of the test under the same conditions (within 20 min). This is consistent with the CO/O interactions with the RuO_2 surface found in Section 5.4.3 - at low temperatures, the densely-packed surface CO and O domains could form on the RuO_2 surface in RuO_2/SiO_2 thus prevent the CO-O reaction (*i.e.* deactivation). As for RuO_2@MOF-808-P, at low temperature, weakened CO/ O interactions with the RuO_2 surface allow adsorbed CO to react with adsorbed O more easily. At temperature close to room temperature (e.g. 30 °C) similar CO conversion performances (Figure 5.21) for RuO_2/SiO_2 and RuO_2@MOF-808-P were noticed, *i.e.* RuO_2/SiO_2 was fully deactivated after 12 min whereas RuO_2@MOF-808-P could maintain > 40% conversion after 2 hrs and can be easily regenerated. The gradual deactivation of RuO_2@MOF-808-P at 30 °C could be due to the surface carbonates formed on the surface as indicated by DRIFTS (Figure 5.22).[244] The low-temperature CO tests further promise the applications related to CO removal close to ambient conditions, when thermal stability is no longer the primary issue. Additionally, to address the concern about using RuO_2@MOF-808-P in moisture conditions,[59] RuO_2@MOF-808-P retaining high activity (Figure 5.23) was confirmed treating RuO_2@MOF-808-P with water vapour at 100 °C. Although some degree of structural degradation can be found from the PXRD patterns (Figure 5.24) after the tests, the major peaks can still be observed.

5.4.5 Preliminary Results for Other Guest@Nanoporous-Host Systems Achieved Using Pourbaix Enabled Guest Synthesis (PEGS)

The author have extended the PEGS method to other guests and nanoporous hosts,[13,287] such as MnO_x in different MOFs (MOF-808-P and DUT-67[67]) and RuO_2 inside zeolite Y[234] (Figure 5.25). They were prepared using similar method mentioned in Sections 5.3.5 and 5.3.6. The precursor for MnO_x was 20 mM $KMnO_4$ (aq); tBMP was used as the reducing agent for all the samples. As shown in the powder XRD patterns in Figure 5.25, the structures of hosts were stable throughout the syntheses. Meanwhile, the SEM-EDS mappings for Mn or Ru support the loading of Mn or Ru-based guests inside these host.

5.5 Summary

In this work, the PEGS strategy was introduced to predict the reagents and conditions for the ship-in-a-bottle synthesis. As a prototypical system for PEGS method RuO_2@MOF-808-P was prepared and characterised. CO/O interactions with the RuO_2 surface within the MOF were also found to be weaker than that for conventionally made RuO_2/SiO_2. Such modulation achieved by preparing RuO_2@MOF-808-P makes the RuO_2-based catalyst more active in catalysing low-temperature CO oxidation.

The PEGS approach could be applicable to insoluble compounds such as metals, oxides, hydroxides and sulfides[288]. Benefiting from the recent development of materials genome project and the continuous growth of Pourbaix diagrams databases (*e.g.* Materials Project[289–292]), other guests with more diverse chemistries (*e.g.* nitrides, phosphides and multi-element compounds) could also be prepared.

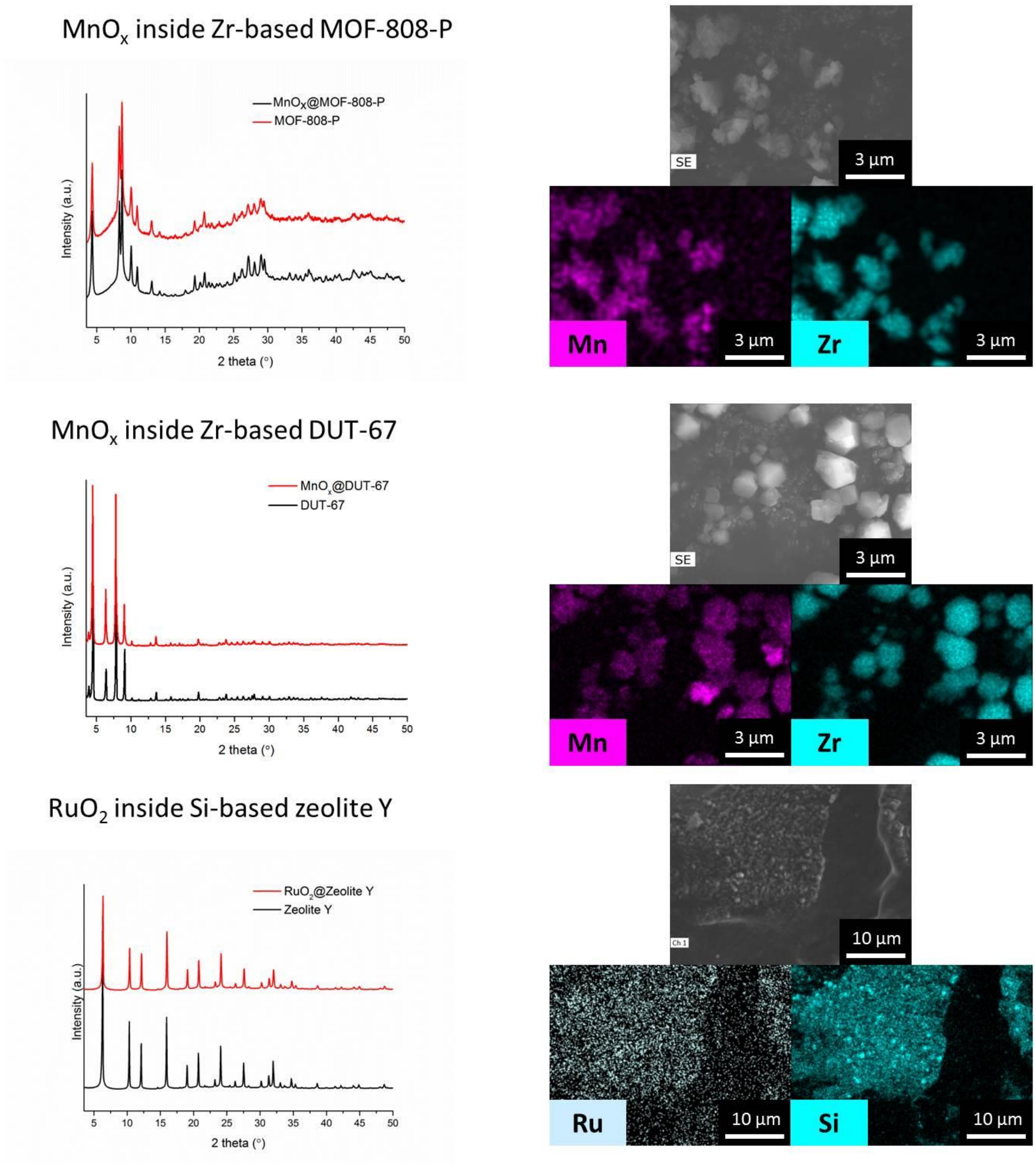

Figure 5.25 Powder XRD and SEM-EDS results for manganese oxide (MnO_x) in MOF-808-P (top) and another Zr-based MOF (i.e. DUT-67[67]) (middle) and RuO_2 in a commercially available zeolite Y[234] (bottom). The figure is reprinted under a Creative Commons Attribution 4.0 International Licence (CC BY 4.0) from ref. [260] (Copyright 2019 Nature Publishing Group).

Chapter 6

Growing Carbon-Based Structures with Multilevel Hierarchy from MOF–Guest Systems

Chapter 6: Growing Carbon-Based Structures with Multilevel Hierarchy from MOF–Guest Systems

6.1 Initiations, Collaborations, Outcomes, Research Funding

In early March 2017, Prof. Anthony K. Cheetham, Dr Stoyan K. Smoukov and the author had a meeting to summarise the publication in Materials Horizons (Chapter 4). Prof. Cheetham suggested that one of the future candidates for the guest is MoS_2, as it was heavily developed as the electrocatalyst for water splitting. Since the edge of this 2D catalyst had been identified as the active sites for H_2 production from the water,[293,294] creating small MoS_2 to expose more edges was a good project. The geometric confinement provided by the MOF host may enable to small MoS_2 formation. After browsing the literature, the author found that thiomolybdates ($Mo_xS_y^{z-}$) can decompose to MoS_x after heating.[295,296] Although the thermal treatment might decompose the MOF, Prof. Cheetham and Dr Smoukov encouraged the author to explore this direction. At that time, they were very curious about whether the thermally treated MOF can still confine the decomposed solid product(s) of the thiomolybdates. In the late March 2017 after the trip to Bulgaria, the author heated the thiomolybdates @MOF to 900 °C in Ar to check the carbonised product(s). He was surprised by the fibre assemblies he observed from SEM-BSE and told the discovery to Prof. Cheetham and Dr Smoukov on the next day. The author double-checked the results and properly started the project a few days after the discovery. The project was supervised by Dr Stoyan K. Smoukov and Prof. R. Vasant Kumar and advised by Prof. Anthony K. Cheetham.

As close collaborations, the author worked with Dr Hyun-Kyung Kim from Prof. R. Vasant Kumar's group in Cambridge for lithium-ion battery (LiB) anode tests. Dr Weiwei Li (University of Cambridge) performed XPS characterisations. Dr James T. Griffiths (University of Cambridge) and the author worked on TEM characterisation. Dr Yue Wu (University of Cambridge) performed single-crystal XRD experiments and analysed the results. Mr Chao Yun (University of Cambridge) and the author measured samples' electrical conductivity. Ms Kara D. Fong (University of Cambridge) and the author prepared schemes for Li^+ interaction with the LiB anode material. Prof. Judith L. MacManus-Driscoll, Ms Sue Gymer, and Mr Simon J. Griggs and Mr Robert Cornell are also acknowledged here for the kind support in using XPS, tube furnace, SEM and thermogravimetric analysis (TGA).

Unless stated in the experimental and results otherwise the work was accomplished by me.

A patent application related to the work covered in the chapter has been lodged (GB1801331.8). Meanwhile, the work was published in Journal of the American Chemical Society in 2018:

Tiesheng Wang, Hyun-Kyung Kim, Yingjun Liu, Weiwei Li, James T. Griffiths, Yue Wu, Sourav Laha, Kara D. Fong, Filip Podjaski, Chao Yun, R. Vasant Kumar, Bettina V. Lotsch, Anthony K. Cheetham, Stoyan K. Smoukov*, ***Bottom-up Formation of Carbon-Based Structures with Multilevel Hierarchy from MOF–Guest Polyhedra***, doi: 10.1021/jacs.8b02411, **Journal of the American Chemical Society**, 2018, 140 (19), pp 6130–6136

This project is funded through the European Research Council (ERC) grant (grant number: EMATTER 280078). In the period of the project, the author was funded by the China Scholarship Council (CSC) and supported by the Engineering and Physical Sciences Research Council (EPSRC) Centre for Doctoral Training in Sensor Technologies and Applications (EP/L015889/1 and 1566990). Prof. Anthony K. Cheetham was supported by the Ras Al Khaimah Centre for Advanced Materials (RAK-CAM). Dr Weiwei Li was supported by the EPSRC grants (EP/L011700/1 and EP/N004272/1). Ms Kara D. Fong was funded by the Winston Churchill Foundation of the United States; Mr Chao Yun was supported by the Cambridge Commonwealth, European and International Trust.

6.2 Introduction

Since MOFs have regular arrangement of organic ligands and metal-based clusters at molecular level, the carbonised MOF products often can retain the well-dispersed metal-based species within the carbon matrix. While the carbon structures can conduct electron transfer, the incorporated metal-based derivatives add extra functionality onto the carbon-based composites, which enhance the performance of carbon-based electrodes in batteries and catalysts. Relevant investigations have been carried out since the late 2000s.[82–84,297–302]

Apart from the normal non-catalytic pyrolytic processes (including decomposition, gasification, shrinkage and bond reformation of organic precursors),[303] filamentous growth of carbon (Figure 6.1), which has been known for over half a century, can also occur in presence of catalytically active species (*e.g.* Ni, Co and Fe).[304–307] briefly, the carbon-based feedstocks which are generated via organic decomposition can migrate onto the metal-based catalysts and further break down into atomised carbons. The carbons diffuse through the catalyst and make bond together again pushing the catalyst to move to the opposite direction. Sometimes, carbon-based fibres and/or tubes can also grow from the MOF polyhedral with catalytically active metal centres during the carbonisation.[133,308–314] Although MOF-guest systems [*e.g.* Mo-based polyoxometalate@HKUST-1(Cu)[315], W-based metal-carbonyl@MAF-6(Zn)[316], Ti-oxo-clusters@HKUST-1(Cu)[317] and dicyandiamide/$FeCl_3$@MIL-101-NH_2(Al)[318]] have also been carbonised to achieve more desired or tuneable chemical compositions, to the author's best knowledge carbon-based nanostructures with multilevel hierarchy formed by the catalysed fibre/tube growth had not been reported at the time the work was published.

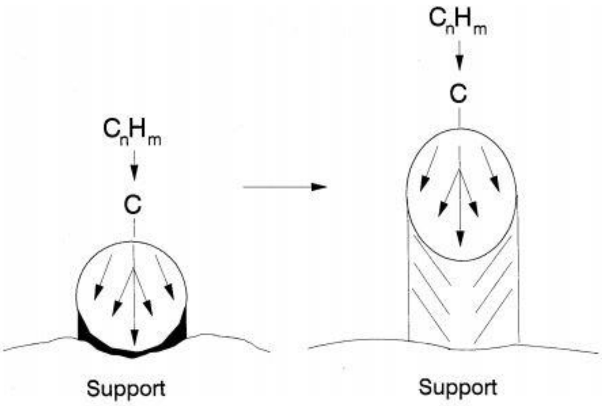

Figure 6.1 Schematic drawings about metal-catalysed filamentous growth of carbon. The circle represents the metal-based catalyst. The figure is reproduced from the work by Snoeck *et al.* with permission from ref. [319] (Copyright 1997 Elsevier B.V.).

In this chapter, the preparation and characterisation of carbon-based multilevel hierarchical nanostructures via the carbonisation of MOF-guest systems will be introduced. Since these carbon-based structures have morphological similarities with the diatomaceous species existed in nature, they were named as nano-diatoms. Considering the potential applications, HKUST-1 [*e.g.* HKUST-1(Cu)[320–322] and HKUST-1(Zn)[321,323]] was chosen as the MOF host, as it [particularly for HKUST-1(Cu)] is easy-to-obtain and easy-to-handle.

HKUST-1 [$Cu_3(BTC)_2$ for HKUST-1(Cu) and $Zn_3(BTC)_2{\cdot}(DMF)_3$ for HKUST-1(Zn)] is in cubic space group $Fm\overline{3}m$. Note that unlike HKUST-1(Cu), the presence of DMF is important for HKUST-1(Zn) to prevent the structural collapse.[321,323] The metal-based guests impregnated at room temperature were ammonium tetrathiomolybdate [$(NH_4)_2MoS_4$ or ATM] or ammonium tetrathiotungstate [$(NH_4)_2WS_4$ or ATT] which can produce molybdenum sulphides (MoS_x) or tungsten sulphides (WS_x) upon thermal decomposition.[295,296,324]

As a detailed demonstration, the case for ATM/DMF@HKUST-1(Cu) will be focused. By characterising the products at various temperatures, the current understanding on the nano-diatom formation will be presented. Meanwhile, by replacing the guest and the MOF host the morphology of these nano-diatoms depending on both MOF host and guest was found. Furthermore, the nano-diatoms made from ATM/DMF@HKUST-1(Cu) was used to demonstrate the potential application as a fast-charging LiB anode.

6.3 Experimental

6.3.1 Sample Overview

Table 6.1 Information about samples mentioned in the work. The table is reprinted under a Creative Commons Attribution 4.0 International Licence (CC BY 4.0) from ref. 122 (Copyright 2018 American Chemical Society).

	1 (precursors)	**2** (after washing)
A	Thermally activated HKUST-1(Cu)	Pyrolyzed **A1** at 800 °C under Ar, then washed with $FeCl_3$ (aq), HCl (aq), and deionized water
B	Thermally activated HKUST-1(Cu) impregnated with a solution of ATM in DMF, ATM/DMF@HKUST-1(Cu)	Pyrolyzed **B1** at 800 °C under Ar, then washed with $FeCl_3$ (aq), HCl (aq), and deionized water
C	Thermally activated HKUST-1(Cu) impregnated DMF	Pyrolyzed **C1** at 800 °C under Ar, then washed with $FeCl_3$ (aq), HCl (aq), and deionized water
D	Thermally activated HKUST-1(Cu) impregnated with a solution of ATT in DMF, ATT/DMF@HKUST-1(Cu)	Pyrolyzed **D1** at 800 °C under Ar, then washed with $FeCl_3$ (aq), HCl (aq), and deionized water
E	Thermally activated HKUST-1(Zn)	Pyrolyzed **E1** at 800 °C under Ar, then washed with HCl (aq) and deionized water
F	Thermally activated HKUST-1(Zn) impregnated with a solution of ATM in DMF, ATM/DMF@HKUST-1(Zn)	Pyrolyzed **F1** at 800 °C under Ar, then washed with HCl (aq) and deionized water

6.3.2 Materials

The following items were used as received: H_3BTC (ACROS Organics™, 98%), copper(II) nitrate trihydrate [$Cu(NO)_2 \cdot 3H_2O$, ACROS Organics™, 99%], $Zn(NO)_2 \cdot 6H_2O$ (ACROS Organics™, 98%), Milli-Q water (17 MΩ), ethanol absolute (Fisher Scientific, 99.8+%), DMF (Fisher Scientific, 99+%), ATM (ACROS Organics™, 99.98%), ATT (Alfa Aesar, 99.9+%), anhydrous $FeCl_3$ (Sigma-Aldrich, 98+%), HCl (Sigma-Aldrich, aq, 37wt%), and Whatman® polyamide membrane filters (pore size ~0.2 μm).

6.3.3 HKUST-1 Synthesis

HKUST-1(Cu) was synthesized using the methods reported by Yang *et al.*[322]. 5 g $Cu(NO)_2 \cdot 3H_2O$ was dissolved in 60 ml Milli-Q water and 1.36 g H_3BTC was dissolved in 60 ml ethanol. Both solutions were ultrasonicated for a few mins to achieve the complete dissolution. The two as-prepared solutions were mixed together in a borosilicate glass bottle (with screw cap). 4 ml DMF was then added to the mixture quickly. The mixed solution was kept at 80 °C in an oil bath for 20 hours. The as-synthesized HKUST-1(Cu) crystals were collected by filtration and rinsed with ethanol three times. It was then activated at 130 °C under nitrogen flow overnight to remove the solvent molecules (*e.g.* water and ethanol) to achieve **A1**.

HKUST-1(Zn) was prepared using the protocols from Feldblyum *et al.*[321] and Bhunia *et al.*[323]. 2.55 g $Zn(NO)_2 \cdot 6H_2O$ and 0.6 g H_3BTC were dissolved in 150 ml DMF, which was then kept at 88 °C for 16 hours in an oil bath. The as-synthesized HKUST-1(Zn) crystals were collected by filtration and rinsed with DMF three times. It was then activated at 130 °C under nitrogen flow overnight to obtain **E1**. The prepared MOFs were stored in a vacuum desiccator.

6.3.4 Guest@HKUST-1 (*i.e.* Carbonisation Precursors) Preparation

Sample B1: **A1** was immersed in ATM/DMF solution (1 g ATM per 100 ml DMF) for 2 hours at room temperature (22 °C, Cambridge, UK) with gentle stirring. The quantity of ATM added was chosen to keep the molar ratio of Mo:Cu to approximately 1:2 during the impregnation (based on the assumed chemical formula of **A1** as $Cu_3(BTC)_2$, or $Cu_3C_{18}H_6O_{12}$). The resultant solids were collected by filtration and then rinsed with DMF until the liquid filtrate was almost colourless. The solid (*i.e.* **B1**) was dried at room temperature under nitrogen flow overnight.

Sample C1: As a control sample, **A1** was immersed in DMF for 2 hours at room temperature with gentle stirring. The solid (*i.e.* **C1**) was collected by filtration and dried at room temperature under nitrogen flow overnight.

Sample D1: **A1** was immersed in ATT/DMF solution (1 g ATT per 100 ml DMF) for 2 hours at room temperature with gentle stirring. The quantity of ATT added was chosen to keep the molar ratio of Mo:Cu to approximately 1:2 during the impregnation (based on the assumed chemical formula of **A1** as $Cu_3(BTC)_2$, or $Cu_3C_{18}H_6O_{12}$). The resultant solids were collected by filtration and then washed with DMF until the liquid filtrate was almost colourless. The solid (*i.e.* **D1**) was dried at room temperature under nitrogen flow overnight.

Sample F1: E1 was immersed in ATM/DMF solution (1 g ATM per 100 ml DMF) for 2 hours at room temperature with gentle stirring. The quantity of ATM added was chosen to keep the molar ratio of Mo:Zn to approximately 1:2 during the impregnation (based on the assumed chemical formula of **E1** as $Zn_3(BTC)_2{\cdot}(DMF)_3$ or $Zn_3C_{27}N_3H_{27}O_{15}$). The resultant solids were collected by filtration and then rinsed with DMF until the liquid filtrate was almost colourless. The solid (*i.e.* **F1**) was dried at room temperature under nitrogen flow overnight.

6.3.5 Carbonisation and Washing

Samples **A1-F1** were all thermally carbonised by following the same procedure (Figure 6.2) in flow of Ar: A sample was loaded in an alumina combustion boat. It was then put into a Carbolite STF 15/450 tube furnace. To minimize carbon oxidation with air (as impurity) at elevated temperatures, the tube was vacuumed and refilled with Ar before heating for three times. To prevent overstress on the tube from thermal expansion upon heating, the heating power was initially set to be 30% of its maximum output power. After 60 min, when the furnace reached above 600 °C, the power was increased to 50%. The sample was heated to 800 °C, kept at 800 °C for 120 min and cooled down naturally in Ar (99.99+%). During the heating stage, the temperature increased at an average rate of ~ 10 °C/min (detailed profile is given in Figure 6.2c). This process produced carbonized **A1-F1**.

Carbonised **A1-D1** was washed with excess amounts of 0.5 M $FeCl_3$ (aq, good etchant for metallic Cu) followed by excess amounts of 10% (v/v) HCl (aq) and plenty of Milli-Q water to remove most of the Cu-containing by-products. Carbonised **E1** and **F1** were washed with excess amounts of 1 M HCl (aq) followed by plenty of MilliQ water to remove most of the Zn-containing by-products. The products obtained after the washing process and drying (100 °C) are **A2-F2**.

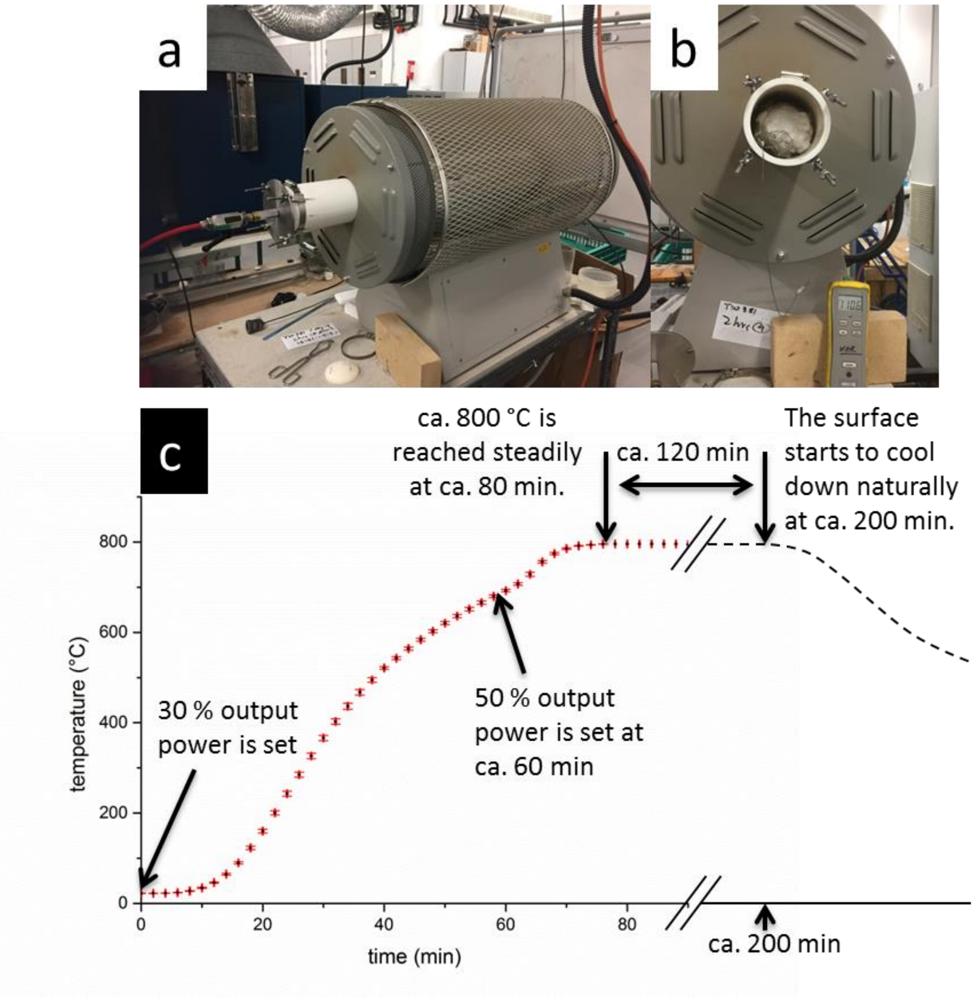

Figure 6.2 (a) Photograph of the thermal treatment (*i.e.* carbonisation) setup with a Carbolite STF 15/450 tube furnace; (b) photograph of the temperature calibration with a thermocouple; and (c) the temperature profile measured for the thermal treatment. Error bars give the standard error from the triplicate measurements. The figure is reprinted under a Creative Commons Attribution 4.0 International Licence (CC BY 4.0) from ref. 122 (Copyright 2018 American Chemical Society).

6.3.6 Materials Characterisations

SEM-SE and SEM-EDS: SEM-SE images and SEM-EDS mappings were obtained using a FEI Nova NanoSEM™ with a field emission gun, a SE detector and an EDS detector. The SEM-SE images were collected at the acceleration voltage of 5 kV; the SEM-EDS mappings were acquired at the acceleration voltage of 15 kV. Powder samples were immobilised on the carbon tapes, which were adhered to the standard aluminium stubs (Agar Scientific).

SEM-BSE: SEM-BSE images were acquired using a Phenom ProX Desktop microscope at an accelerating voltage of 15 kV. Powder samples were immobilised on the carbon tapes, which were adhered to the standard aluminium stubs (Agar Scientific).

Table 6.2 Experimental parameters for single-crystal XRD. The table is reprinted under a Creative Commons Attribution 4.0 International Licence (CC BY 4.0) from ref. 122 (Copyright 2018 American Chemical Society).

Sample	**B1**	**C1**
Empirical formula	$Cu_3C_{18}H_6O_{15}$	$Cu_3C_{18}H_6O_{15}$
Temperature/K	299.0(9)	298.3(4)
Crystal system	cubic	cubic
Space group	$Fm\bar{3}m$	$Fm\bar{3}m$
a/Å	26.3531(8)	26.3032(6)
α/°	90	90
Volume/Å^3	18301.8(16)	18198.2(11)
ρ_{calc}g/cm^3	0.948	0.949
μ/mm^{-1}	1.420	1.423
F(000)	5136.0	5184.0
Crystal size/mm^3	0.18 × 0.12 × 0.1	0.23 × 0.144 × 0.09
Radiation	MoKα (λ = 0.71073)	MoKα (λ = 0.71073)
2Θ range for data collection/°	3.09 to 56.574	4.38 to 56.49
Reflections collected	4078	4026
Independent reflections	1106 [R_{int} = 0.0931, R_{sigma} = 0.0731]	1091 [R_{int} = 0.0926, R_{sigma} = 0.0582]
Data/restraints/parameters	1106/0/36	1091/0/36
Goodness-of-fit on F^2	1.084	1.174
Final R indexes [I>=2σ (I)]	R_1 = 0.0932, wR_2 = 0.2702	R_1 = 0.0878, wR_2 = 0.2529
Final R indexes [all data]	R_1 = 0.1404, wR_2 = 0.3063	R_1 = 0.1062, wR_2 = 0.2795

Single-crystal XRD: Single-crystal XRD was done by Dr Yue Wu. Crystal structure determination was carried out using an Oxford Gemini E Ultra diffractometer, Mo Kα radiation (λ = 0.71073 Å), equipped with an Eos CCD detector. Data collection and reduction were conducted using CrysAliPro (Agilent Technologies). An empirical absorption correction was applied with the Olex2 platform.[325] The structure was solved using ShelXT[326] and refined by ShelXL[327].

Powder XRD： Powder XRD patterns were collected on a Bruker D8 ADVANCE with a Ni 0.012 filter between the X-ray source and the sample (2θ from 3.5° to 80° and a step size of 0.04°). Samples were uniformly distributed on a silicon disc supported by a round holder. The holder and the disc were rotated (30 rpm) during the measurement. The illumination slit length was fixed so that the exposure area forms a circle (16 mm in diameter) with the rotation.

DF-STEM and STEM-EDS: DF-STEM images and STEM-EDS mappings were acquired by Dr James T. Griffiths and Tiesheng Wang using an FEI Osiris operating at 200 keV fitted with BF and ADF detectors. Energy dispersive spectra were simultaneously recorded on four Bruker silicon drift detectors. STEM samples were dispersed in ethanol and prepared by drop-casting 100 µl of sample suspension on carbon grids.

XPS: XPS results were collected by Dr Weiwei Li using a XPS with a monochromatic Al *Kα1* x-ray source (*hv* =1486.6 eV) and a SPECS PHOIBOS 150 electron energy analyzer with a total energy resolution of 500 meV. To remove charging effects during the measurements, a low-energy electron flood gun with proper energy was applied to compensate the charge. All spectra were aligned to the C 1s at 284.8 eV. For analysis of the C 1s, Mo 3d, and S 2p spectra, a Shirley background was subtracted. The samples were immobilised on the substrate by carbon tape.

Thermogravimetric analysis with Fourier-transform infrared spectroscopy (TGA-FTIR): TGA-FTIR was performed with a TA Instruments Q500 thermogravimetric analyser connected to a Thermo Scientific™ Nicolet™ iS™10 FTIR spectrometer. Samples were heated from room temperature up to 1000 ºC at a constant rate of 10 ºC/min. Thermal decomposition was carried out in Ar, whereas combustion was performed in air. Gaseous products were passed to the Thermo Scientific™ Nicolet™ iS™10 FTIR spectrometer for analysis. A spectrum was acquired every 40 sec. The FTIR sampling chamber was kept at 400 ºC. The FTIR optical path length was 100 mm.

Nitrogen adsorption measurements: Nitrogen adsorption measurements were performed at 77 K (-196 ºC) using a MicroMeritics TriStar 3000 Porosimeter. Prior to the measurements, samples were quickly taken out from the vacuum desiccator and evacuated for 1 hour at 120 ºC under nitrogen flow.

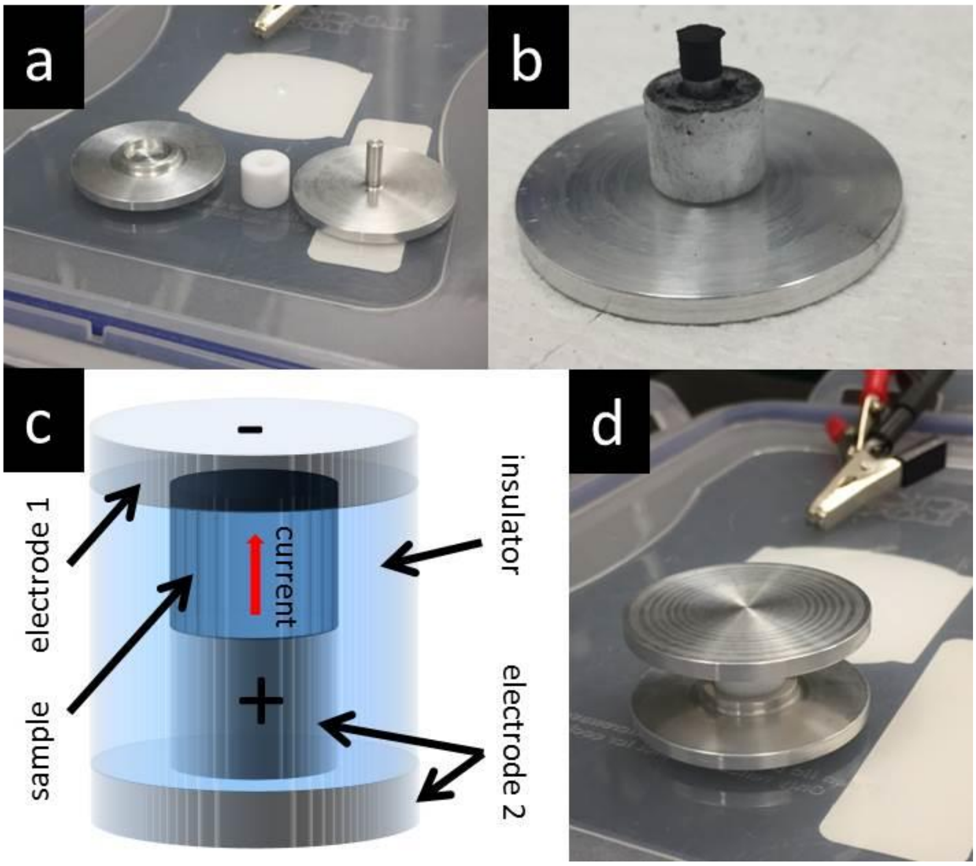

Figure 6.3 Two-probe current-voltage (I-V) measurement setup: (a) components used, (b) a cylindrical sample (formed from powder-like **B2**), (c) schematic drawing for a measurement, and (d) components assembled for measurement. The figure is reprinted under a Creative Commons Attribution 4.0 International Licence (CC BY 4.0) from ref. 122 (Copyright 2018 American Chemical Society).

Two-probe electric current-voltage (I-V) measurement: Electrical measurements were conducted by Chao Yun and Tiesheng Wang using a combination of a Keithley 2182 nanovoltmeter to apply voltage and a Keithley 2440 5A source meter to read current. The method used to obtain the conductivities and current-voltage plots of **A2** and **B2** was adapted from those reported previously for carbon black powder[328] and metal powder[329] (Figure 6.3). Briefly, sample powder was confined in a mold and shaped under pressure to be a cylinder with defined radius, r, and height, h. The top and bottom of the sample cylinder were in contact with the aluminum electrodes separately whereas the rest of the cylinder was surrounded by an electrically insulating Teflon mold. A voltage (V) was applied across the sample and the current (I) travelling through the cylinder was measured. The voltage was varied from +5 V to -5 V and then back to +5 V, with a step size of 0.5 V. The electrical conductivities, σ, were determined by fitting a line on the data from -2 V to 2 V. The slope (I/V) is 1/R, where R is resistance:

$$\sigma = \frac{1}{\rho} = \frac{h}{RA} = \frac{h}{\left(\frac{V}{I}\right)\pi r^2} \qquad \text{Equation (6.1)}$$

where, ρ is resistivity and A is contact area with the measurement electrodes.

Cyclic voltammetry (CV) and LiB half-cell tests: The electrochemical properties were investigated by Dr Hyun-Kyung Kim using 2032-type coin cells with a lithium foil counter electrode and 1 M $LiPF_6$ in ethylene carbonate/dimethyl carbonate (EC/DMC) (1:1 v/v) as the electrolyte. The working electrode was prepared using a mixture of 90 wt% **B2** and 10 wt% polyvinylidene fluoride (PVDF, as a binder); the mixture was deposited on a Cu foil. Each working electrode had a surface area of 1.13 cm^2, and the density of active material in the electrode was approximately 1 mg/cm^2. For comparison, electrodes were also prepared using **A2** or commercial graphite mixed with 10 wt% PVDF binder. The specific capacities of all the electrodes were calculated based on the masses of active materials. The relevant cyclic voltammetry (CV) scans and charge-discharge curves were collected with a potentiostat/galvanostat (IVIUM/ LAND) within a 0.01–3 V range against Li^+/Li potential. Coulombic efficiency is defined as the ratio of capacity discharged over capacity charged on the same cycle.

6.4 Results and Discussion

6.4.1 B1: ATM/DMF@HKUST-1(Cu)

After thermal activation, HKUST-1(Cu) turned from light blue in colour to dark blue or purple (Figure 6.4). The activated HKUST-1(Cu) is **A1**. The colour change could be due to the reduction in Cu coordination number – solvent molecules detached from Cu leaving unsaturated sites behind.[330,331] After soaking the ATM/DMF solution into the activated HKUST-1(Cu), the particles became green in colour (Figure 6.5), which is consistent with a similar system [*i.e.* Mo-based polyoxometalate@HKUST-1(Cu)] reported by Wu *et al.*[315]. Compared with the activated HKUST-1(Cu), the drastic decrease in N_2 uptake (Figure 6.5a) indicates that ATM and/or DMF molecules in **A1** [*i.e.* ATM/DMF@ HKUST-1(Cu)] could occupy the empty space within the MOF host preventing any further N_2 incorporation. As for the control sample, **C1**, it restored the light blue colour after the DMF impregnation.

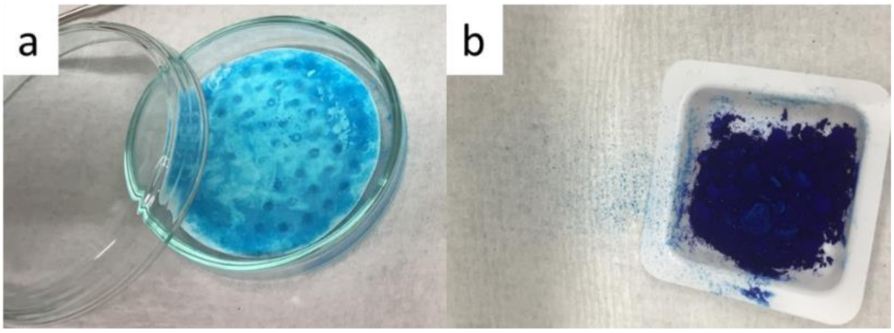

Figure 6.4 Photographs of (a) as-synthesized HKUST-1(Cu) and (b) thermally activated HKUST-1(Cu). The figure is reprinted under a Creative Commons Attribution 4.0 International Licence (CC BY 4.0) from ref. 122 (Copyright 2018 American Chemical Society).

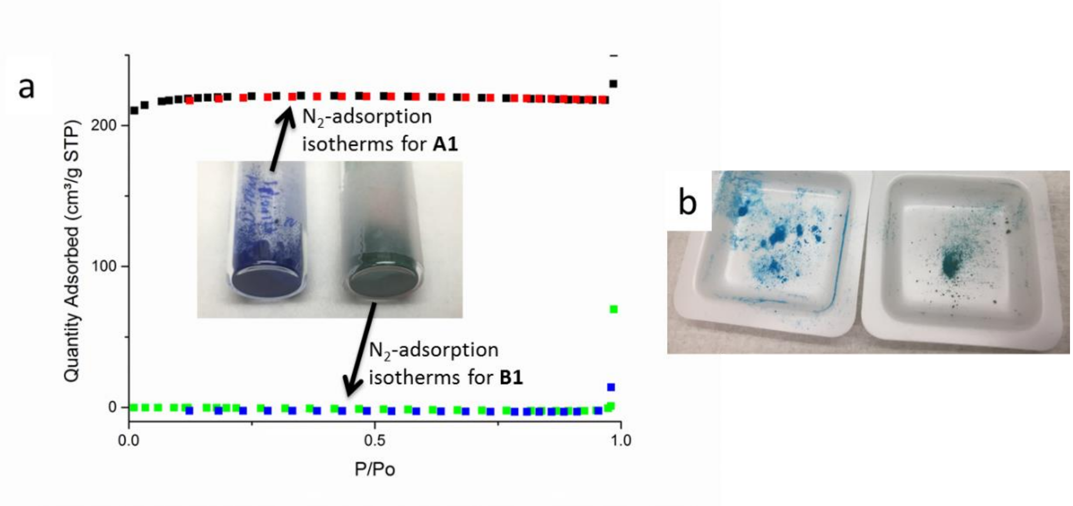

Figure 6.5 (a) N_2 adsorption isotherms and images for A1 (adsorption in black and desorption in red) and B1 (adsorption in green and desorption in blue); and (b) photographs for C1 (left) and B1 (right). The figure is reprinted under a Creative Commons Attribution 4.0 International Licence (CC BY 4.0) from ref. 122 (Copyright 2018 American Chemical Society).

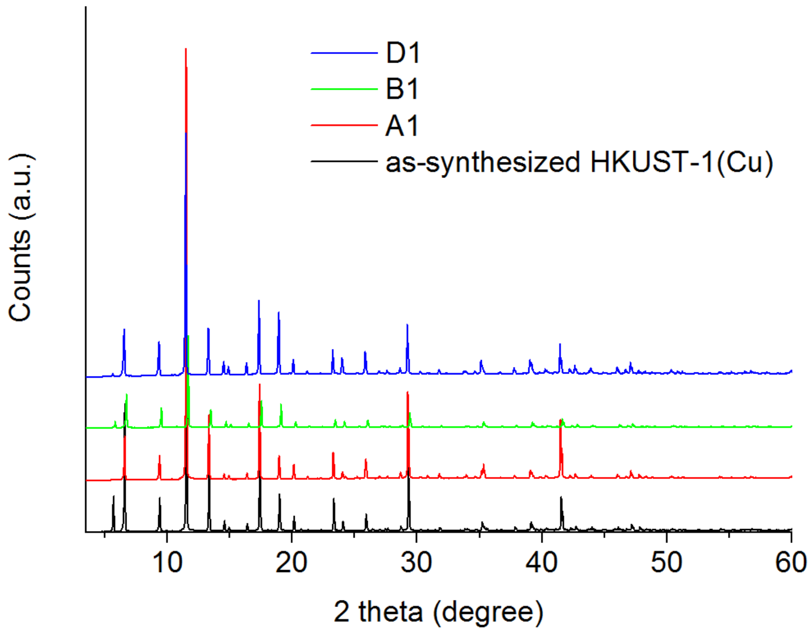

Figure 6.6 Powder XRD patterns for as-synthesized HKUST-1(Cu), A1, B1 and D1. The figure is reprinted under a Creative Commons Attribution 4.0 International Licence (CC BY 4.0) from ref. 122 (Copyright 2018 American Chemical Society).

The powder XRD peaks for **B1** match well with those for as-synthesized HKUST-1(Cu) and **A1** (Figure 6.6). The HKUST-1(Cu) host structure is, therefore, confirmed to be retained throughout the thermal activation and guest impregnation processes. Furthermore, there is a peak at ~ 6° (2θ) in the pattern for the as-synthesised HKUST-1(Cu) whereas the peak disappears in that for **A1** due to desorption of solvent guests. This is supported by the restoration of the peak in **B1**, when guests were reloaded into the host.

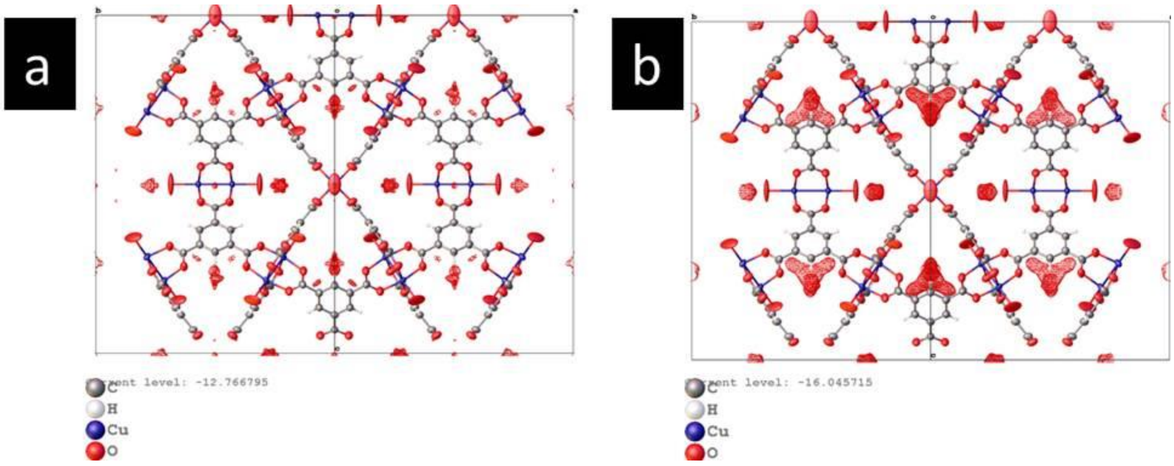

Figure 6.7 Fourier difference maps obtained from single-crystal XRD for (a) **B1** and (b) **C1** revealing the electron density (red contours) distributed in the void of the HKUST-1(Cu)

framework ([1 1 0] direction). The single-crystal XRD was done by Dr Yue Wu. The figure is reprinted under a Creative Commons Attribution 4.0 International Licence (CC BY 4.0) from ref. 122 (Copyright 2018 American Chemical Society).

By characterising **B1** and **C1** with single-crystal XRD (Figure 6.7), the electron density is found to be more localized in **B1** than in **C1**, which could be due to the heavier elements presented in **B1**'s guests [*i.e.* ATM (*e.g.* Mo and S) and DMF] compared to **C1**'s guests (*i.e.* DMF). Note that the electron density represented by the contours in these two figures is different; the smaller contour area indicates a more localised electron distribution. For B1, there are 2608 in-void electrons per unit cell; in contrast, for C1, there are 2231 in-void electrons (equivalent to ~ 56 DMF molecules) per unit cell. By assuming that the number of DMF molecules is unchanged and the additional electrons (*i.e.* 2608 – 2231 = 337 electrons) come from ATM, the number of ATM in a unit cell is 3. Therefore, the ATM concentration is 53.6 parts per thousand DMF molecules, which is ~ 18 times higher than the concentration of the as-prepared solution (2.98 parts per thousand DMF molecules for 1 g ATM per 100 ml DMF at room temperature). From the single-crystal XRD analysis, not only the incorporation of ATM was verified but also the accumulation of ATM inside the MOF host was found. This is likely to be caused by the strong binding interaction between the unsaturated copper sites with thiomolybdates, which is well-investigated by bioinorganic chemists. It is regarded as a health issue for ruminants in Mo-rich land, as they suffer from a Cu deficiency due to such interaction (known as Cu-Mo antagonism).[324]

6.4.2 Carbonisation of B1

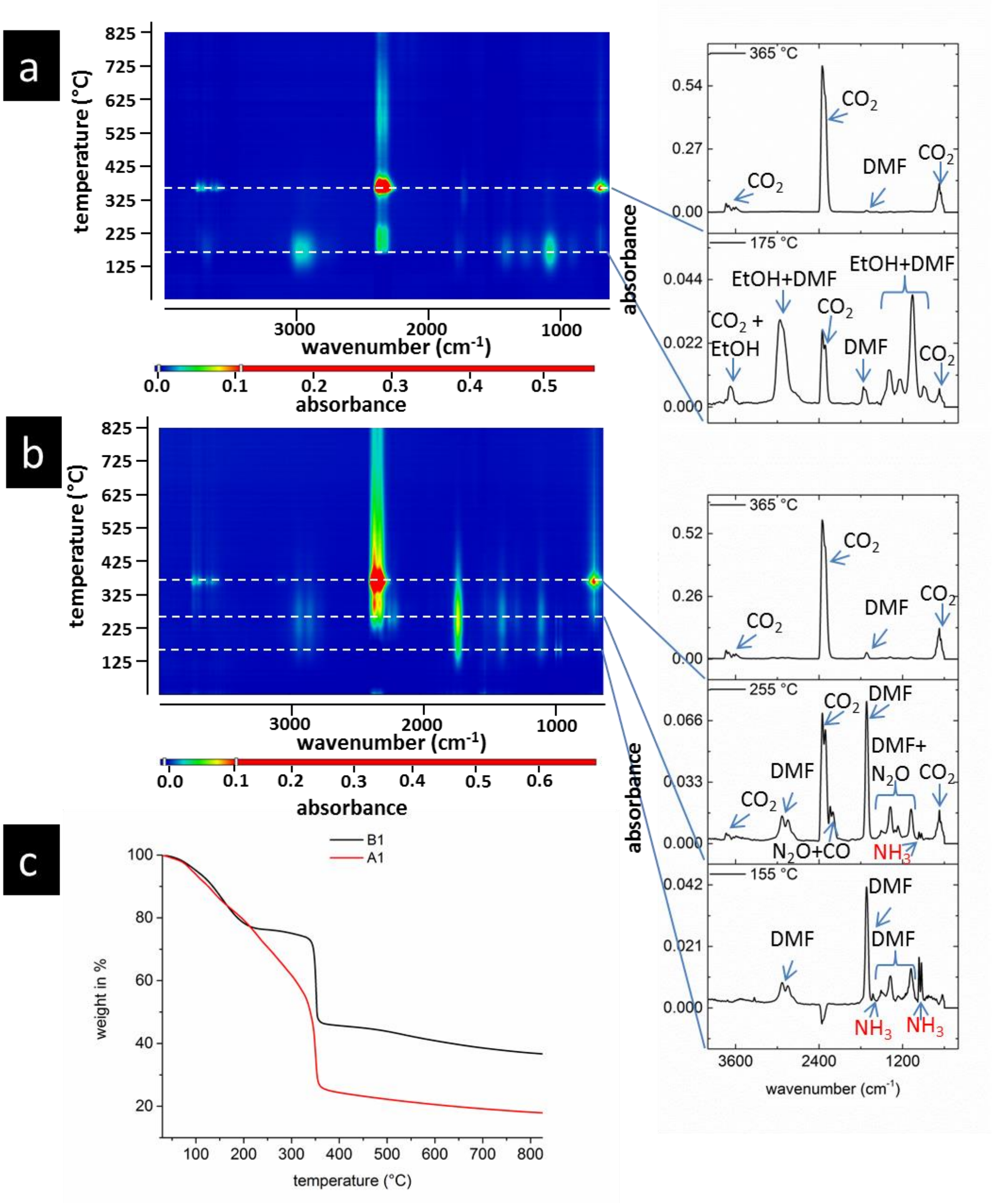

Figure 6.8 TGA-FTIR results for heating A1 and B1 in Ar (thermal decomposition): (**a**) FTIR mapping of the emitted gas species from **A1** upon heating**;** (**b**) FTIR mapping of the emitted gas species from **B1** upon heating; (**c**) TGA profiles for **A1** and **B1**. The peaks in FTIR spectra were matched with the spectra of standard gaseous compounds in the database provided by Thermo Scientific. The figure is reprinted under a Creative Commons Attribution 4.0 International Licence (CC BY 4.0) from ref. 122 (Copyright 2018 American Chemical Society).

To reveal the elementary processes of **B1** carbonisation**,** systematic characterizations on samples heated to various temperatures were performed. When a sample reached the target temperature, it was kept at this temperature for 10 min to reach equilibrium, unless mentioned specifically.

Below 300 °C, DMF desorption and ammonia formation were detected by TGA-FTIR (Figure 6.8). Note that there is an inevitable retard in the DMF detection, as DMF can easily condense. The presence of ammonia indicates ATM decomposition.[295] The Mo 3d XPS peaks (Figure 6.9) also shifts to higher binding energy (from ~ 228 eV to ~ 232 eV for Mo $3d_{5/2}$ and from ~ 231 eV to ~ 235 eV for Mo $3d_{3/2}$) during ATM decomposition indicating significant change in Mo's valence.[295,296] Instead of forming MoS_2[296] (Mo $3d_{5/2}$ at 229.1 eV and $3d_{3/2}$ at 232.3 eV), Mo 3d in Figure 6.9 peaks are at higher binding energy (Mo $3d_{5/2}$ at ~ 232 eV and $3d_{3/2}$ at ~ 235 eV), which is likely to arise from the strong interaction with HKUST-1(Cu). In the similar temperature regime, from powder XRD patterns (Figure 6.10) the crystalline structure of the MOF host was found to collapse due to the significant overall peak mismatch.

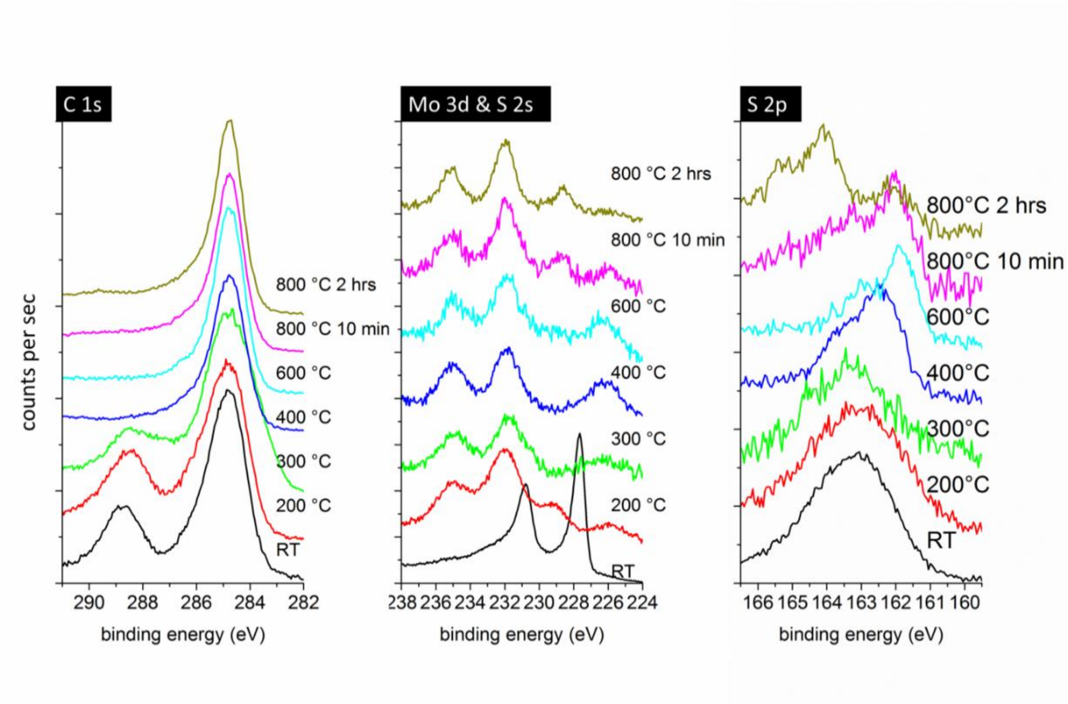

Figure 6.9 C 1*s*, Mo 3d, S 2s and S 2p XPS spectra for B1 treated up to various temperatures. The Mo 3d + S 2s spectrum for B1 has a doublet at 227.7 eV and 230.8 eV, matching amorphous MoS_3[332] with a slight shift to lower binding energy overlapping with the S 2s peak. The XPS results were obtained by Dr Weiwei Li. The figure is reprinted under a Creative Commons Attribution 4.0 International Licence (CC BY 4.0) from ref. 122 (Copyright 2018 American Chemical Society).

Pyrolysis (*i.e.* a carbonisation process) takes place between 300 °C and 400 °C. The BTC ligand in HKUST-1(Cu) decomposes to carbon-based molecules through dissociation of carboxylate group. This is discerned by CO_2 production collected by TGA-FTIR (Figure 6.8) and further supported by the disappearance of O-C=O bonding as revealed in XPS C 1s spectra (at ~ 288.8 eV in Figure 6.9). Meanwhile, peaks for metallic Cu can be noticed from powder XRD patterns in this temperature regime (Figure 6.10). Since metallic Cu is known to have poor interaction with C,[333] Cu tends to form particles which are shown in SEM images for samples at 400 °C (Figure 6.11). The carboxylate dissociation could lead to the Cu^{2+} [from HKUST-1(Cu)] reduction to maintain the charge neutrality. Meanwhile, strong interaction between Mo and the pyrolyzed MOF host stays valid in the range of 300 °C to over 600 °C – no significant change in Mo 3d peak positions. The interaction is likely the reason why Mo compounds stay in the pyrolyzed matrix.

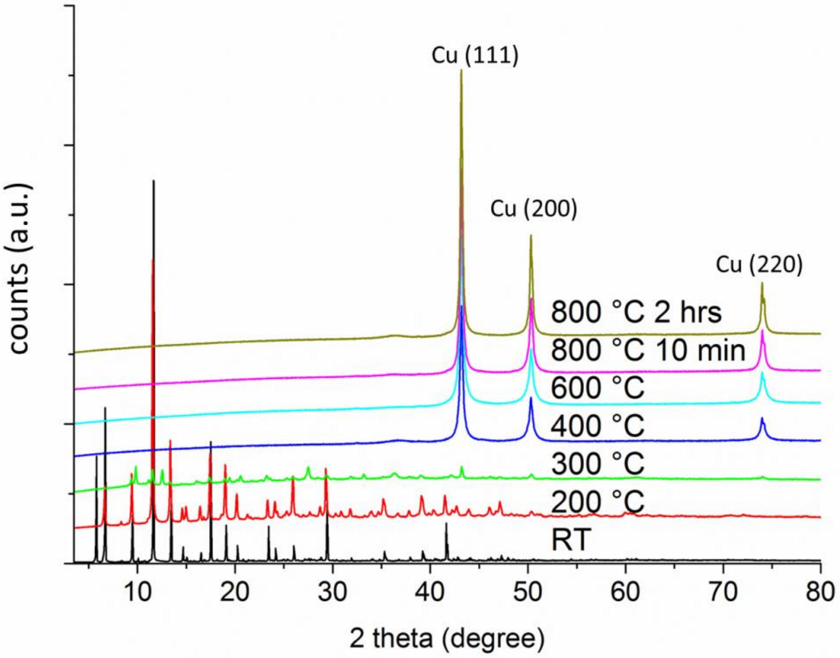

Figure 6.10 Powder XRD results for B1 treated up to various temperatures. The figure is reprinted under a Creative Commons Attribution 4.0 International Licence (CC BY 4.0) from ref. 122 (Copyright 2018 American Chemical Society).

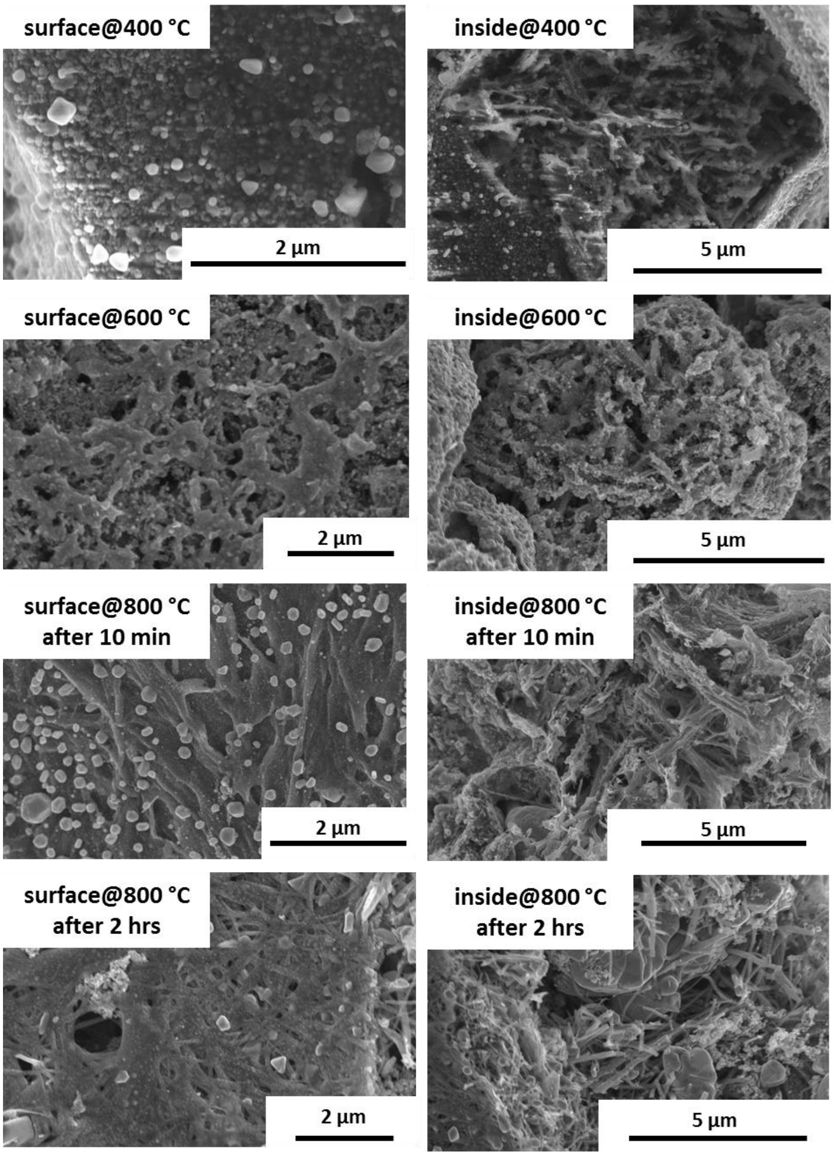

Figure 6.11 SE-SEM images of B1 treated up to 400 °C, 600 °C and 800 °C (800 °C for 10 min and 2 hrs). The figure is reprinted under a Creative Commons Attribution 4.0 International Licence (CC BY 4.0) from ref. 122 (Copyright 2018 American Chemical Society).

Above 600 °C **B1** starts to form fibrous carbon-based nanostructures (SEM images, Figure 6.11). Dendrite-like surface features are present in a macroporous interior network. As the temperature increases to 800 °C, the fibre/web-like features become more developed. The unique hierarchical structure could form through a hybrid reaction-diffusion process combining both pyrolysis and metal-based catalysis.[334] Similar filamentous carbon formations have been observed using organic molecules as carbonisation precursors and Fe, Ni and Co-based catalysts.[334,335] In the case of systems containing Cu ad Mo, the author hypothesised that both Cu and Mo species could be important in the catalysed carbon fibre formation. Both metallic Cu particles (from PXRD patterns in Figure 6.10) and Mo-C guest derivatives (from Mo 3d XPS spectra in Figure 6.9) were found after heating **B1** to 800 °C. The Mo-C compound is revealed by the peak at 228.7 eV for Mo^0, which is consistent with the MoC_x study carried out by Wan *et al.*[336].

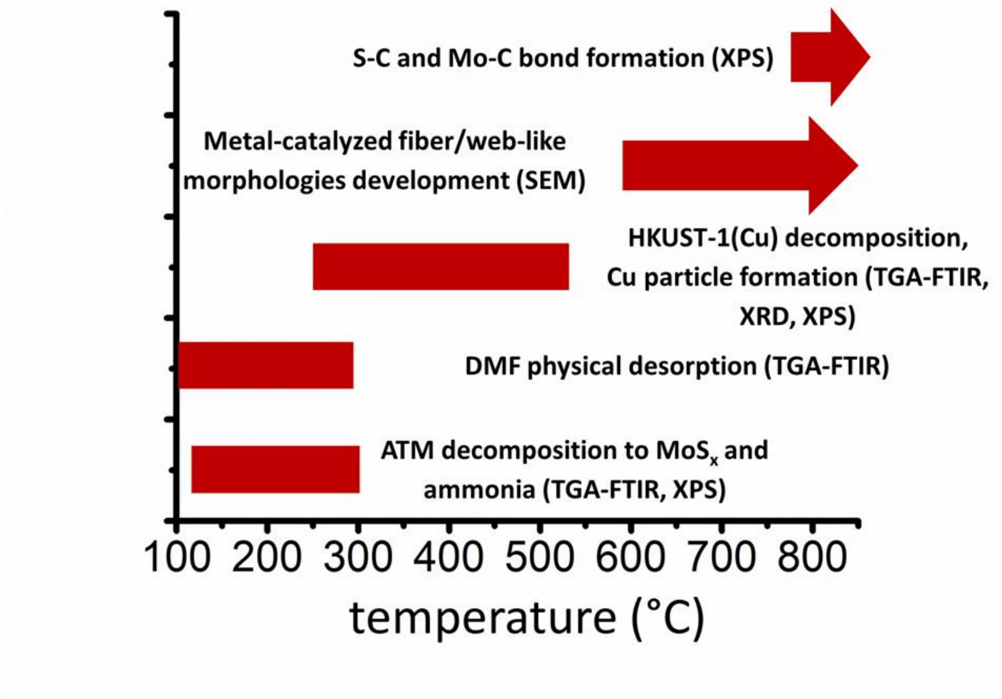

ATM decomposition:

$$(NH_4)_2MoS_4 \rightarrow MoS_x + NH_3 + C - S\ species\ (incoporated\ in\ MOF)\ or\ H_2S$$

HKUST-1(Cu) decomposition:

$$C_6H_3(COO)_3{}^{3-} + Cu^{2+} \rightarrow non - vaporised\ C - based\ species + Cu + CO_2$$

Note: $C_6H_3(COO)_3{}^{3-}$ (*i.e.* BTC) is the organic ligand for HKUST-1(Cu). Non-vaporised C-based species are the feedstock for the C-based nanostructure development.

S-C and Mo-C bond formation:

$$MoS_x\ in\ C - based\ matrix \rightarrow Mo - C\ \&\ S - C\ in\ C - based\ matrix$$

Figure 6.12 A summary of the section: steps for B1 carbonisation in different estimated temperature ranges and the associated characterisation techniques used to identify them. The figure is reprinted under a Creative Commons Attribution 4.0 International Licence (CC BY 4.0) from ref. 122 (Copyright 2018 American Chemical Society).

Metallic Cu by itself is often inactive for catalysing carbon fibre growth;[337,338] Mo by itself has very strong binding interaction with C yielding molybdenum carbides.[315,333] Metallic Cu in the presence of Mo, however, can catalyse the growth of fibre-like carbon-based nanostructures as investigated previously by Holmes *et al.*[338,339]. At high temperatures, Mo-C derivatives can assist in cracking the C-C bond in organic ligands.[340,341] According to Holmes' DFT calculations, metallic Cu particle in proximity to a Mo particle could have sufficient binding energy to stabilize the formation of carbon-based nanostructures (*e.g.* nanotubes). Therefore, for **B1**, the carbon fragment remnants of BTC produced via pyrolysis reform into carbon nanofibers catalysed by metallic Cu particles and Mo-C compounds. The Cu particles within the pyrolyzed matrix act as growth locations for the fibres.

Meanwhile, the growth of the carbon-based fibres is confined inside the original MOF-guest polyhedra (Figure 6.11). Due to weak Cu-C interactions[337] a significant amount of metallic Cu accumulates on the surface of the original polyhedral (Figure 6.11), which disrupts the Cu/Mo ratio necessary for catalysis and inhibits outward growth of the fibres.[338] Although the same metal compound in different environments can exhibit very different reactivity, nanostructure correlations and presence of the same metals in the current system yield the working hypothesis. In addition, the S 2p peak shift towards higher binding energy at around 800 °C indicates the formation of S-C bonding.[342]

As a summary (Figure 6.12), the decomposed to Mo/S-based guest derivatives interact with the pyrolyzed organic ligands strongly at temperatures exceeding 600 °C. While the majority of the metallic Cu originally from the MOF hosts condenses on the outside of the pyrolyzed matrix (*i.e.* polyhedra), while a small portion of it, together with the Mo-containing compounds, catalyses the formation of fibre-like carbon-based structures.

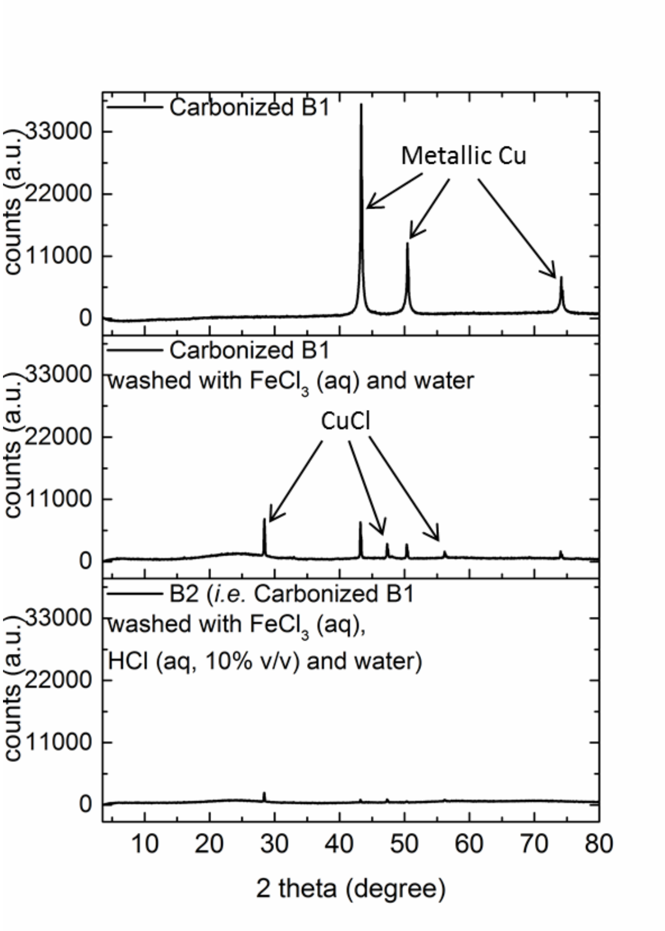

Figure 6.13 Powder XRD patterns of carbonised B1, carbonised B1 washed with $FeCl_3$ (aq) and water and B2 (carbonised B1 washed with $FeCl_3$ (aq), HCl (aq) and water). The figure is reprinted under a Creative Commons Attribution 4.0 International Licence (CC BY 4.0) from ref. 122 (Copyright 2018 American Chemical Society).

After **B1** carbonisation, Cu particles were removed chemically to reveal the carbon-based hierarchical nanostructure (*i.e.* nano-diatom) more clearly. Meanwhile, as suggested by Dr Hyun-Kyung Kim, the presence of Cu (an electrochemical active element) could deteriorate the performance of the nano-diatom as an anode material for LiB (Section 6.4.4). $FeCl_3$ was used first to convert Cu particles to CuCl (Figure 6.13). CuCl was then dissolved by HCl (aq, 10% v/v) followed by washing with deionised water to neutralise the pH. The dried product became the carbon-based nano-diatom, **B2**.

6.4.3 B2: Nano-Diatom Made from ATM/DMF@HKUST-1(Cu)

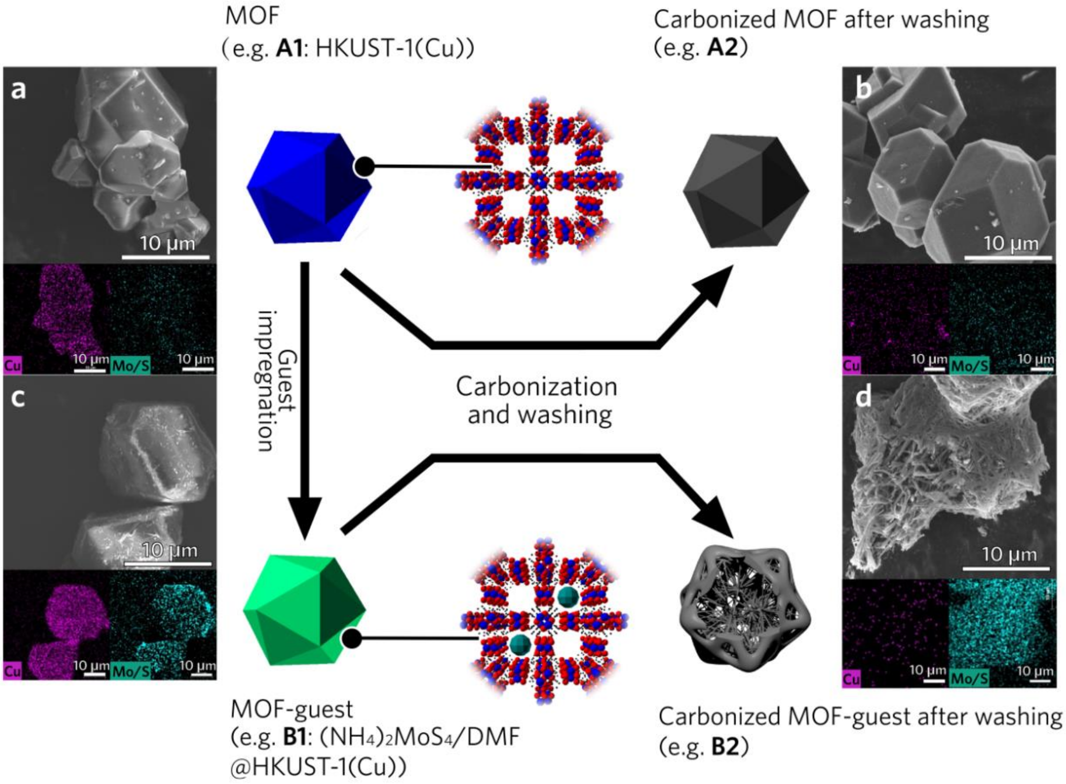

Figure 6.14 SEM-SE images and SEM-EDS mappings (Cu and Mo/S) for (a) **A1**, (b) **A2**, (c) **B1**, and (d) **B2**. Note that for EDS Mo Lα emission overlaps with S Kα emission. The figure is reprinted under a Creative Commons Attribution 4.0 International Licence (CC BY 4.0) from ref. 122 (Copyright 2018 American Chemical Society).

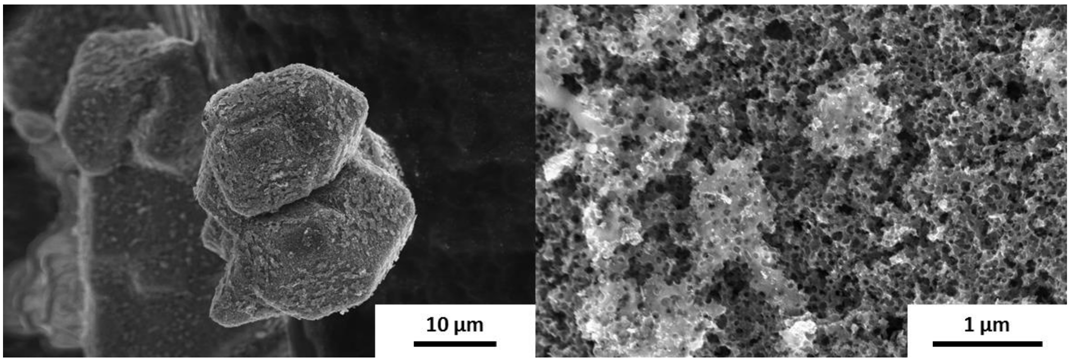

Figure 6.15 SEM-SE images of C2: an image at lower magnification (left) showing the overall shape retention from its precursor (**C1**) and an image at higher magnification (right) revealing the surface of **C2**. The figure is reprinted under a Creative Commons Attribution 4.0 International Licence (CC BY 4.0) from ref. 122 (Copyright 2018 American Chemical Society).

As a control sample, the HKUST(Cu) itself, **A1**, only retains the polyhedral particle-like morphology after carbonisation and washing (*i.e.* **A2**). Similarly, the DMF@ HKUST(Cu), **C1**, can also preserve the initial polyhedron shape. The rougher surface in **C1**could be caused by the DMF desorption (*i.e.* gasification) during the heat treatment. Overall, without the incorporation of ATM, the carbonisation is governed by the non-catalytic pyrolytic processes (including decomposition, gasification, shrinkage and bond reformation of organic precursors).[303]

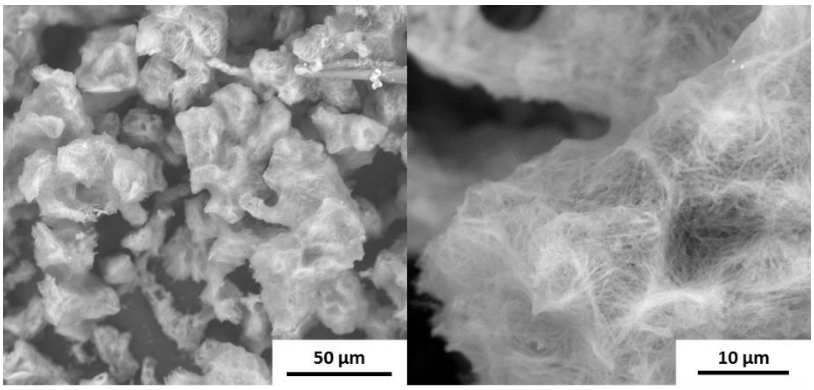

Figure 6.16 15 keV SEM-BSE of B2: (left) a low magnification image showing the overall **B2** morphology and (right) image at higher magnification shows the fibre-like building blocks underneath the surface. The figure is reprinted under a Creative Commons Attribution 4.0 International Licence (CC BY 4.0) from ref. 122 (Copyright 2018 American Chemical Society).

In contrast, after the identical carbonization treatments the host-guest precursor, **B1**, yields the hierarchically structured nano-diatom (*i.e.* **B2**). Detailed characterisations show four levels of hierarchy over a wide range of length scales. At the outermost level (i) the shape retention from the original MOF-guest polyhedra can be observed (*i.e.* cage, typically 15 µm, Figure 6.16 left). These cages are formed by (ii) webs (typically 0.5-1 µm in width, shown in Figures 6.17a-e). Inside the cages, (iii) assemblies of fibres are visible (typically 100 nm in diameter and a few µm in length, shown in Figure 6.16 and Figures 6.17f-g). Additionally, on both the webs and fibers there are (iv) mesopores (typically 20 nm in diameter Figures 6.17c&h). These mesopores could be created during the Cu-particle removal. **B2** was further confirmed to have no long-range order shown as diffuse rings in the electron diffraction pattern (Figure 6.18), which is consistent with the powder XRD results in Figure 6.13.

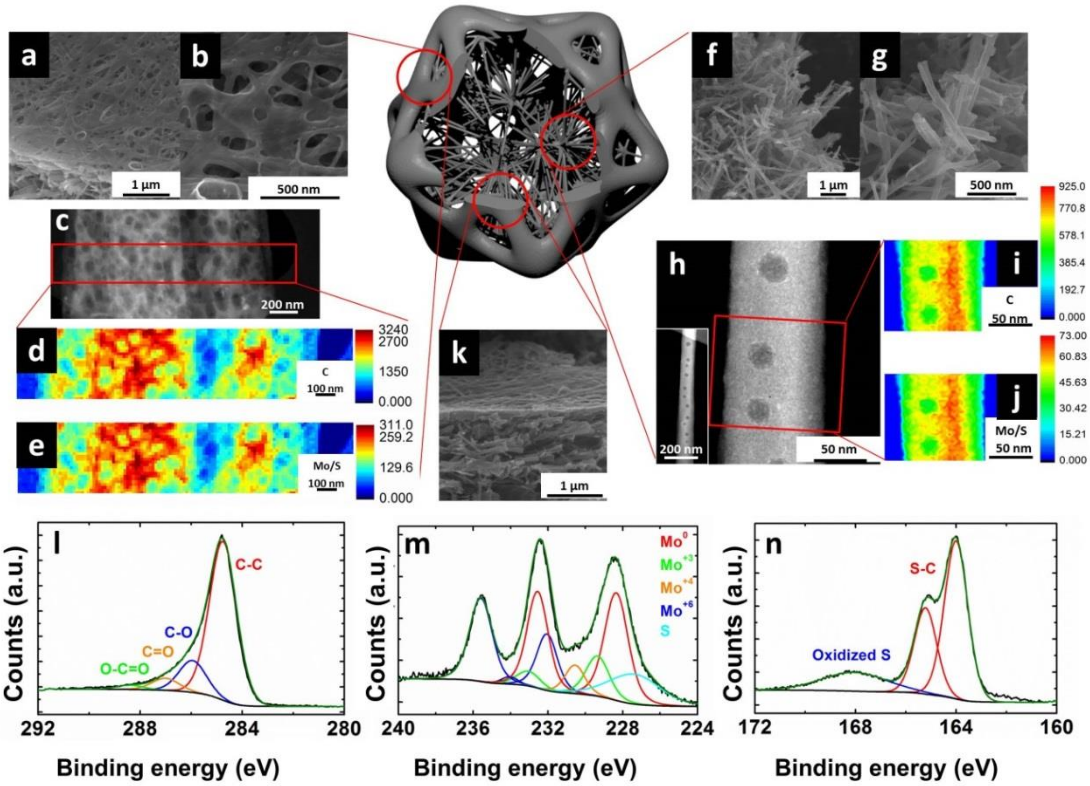

Figure 6.17 Characterization of B2. For the web-like surface, (a) and (b) SEM-SE images; (c) DF-STEM images; and (d) and (e) STEM-EDS mappings of C and Mo/S. For fibre-like structure, (f) and (g) SEM-SE images; (h), DF-STEM images; and (i) and (j) STEM-EDS elemental maps of C and Mo/S. SEM-SE image, (k), reveals the conjunction between the web-like surface and the fibre-like structure. XPS spectra are also shown: (l) C 1s; (m) Mo 3d + S 2s; and (n) S 2p. DF-STEM images and STEM-EDS mappings were acquired by Dr James T. Griffiths and the author; XPS results were obtained and analysed by Dr Weiwei Li. The figure is reprinted under a Creative Commons Attribution 4.0 International Licence (CC BY 4.0) from ref. 122 (Copyright 2018 American Chemical Society).

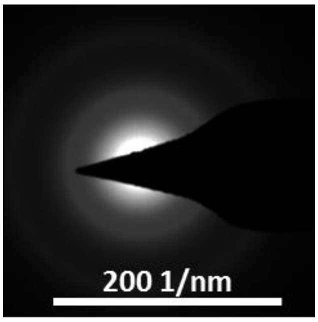

Figure 6.18 Electron-diffraction pattern of B2. The pattern was obtained by Dr James T. Griffiths and the author. The figure is reprinted under a Creative Commons Attribution 4.0 International Licence (CC BY 4.0) from ref. 122 (Copyright 2018 American Chemical Society).

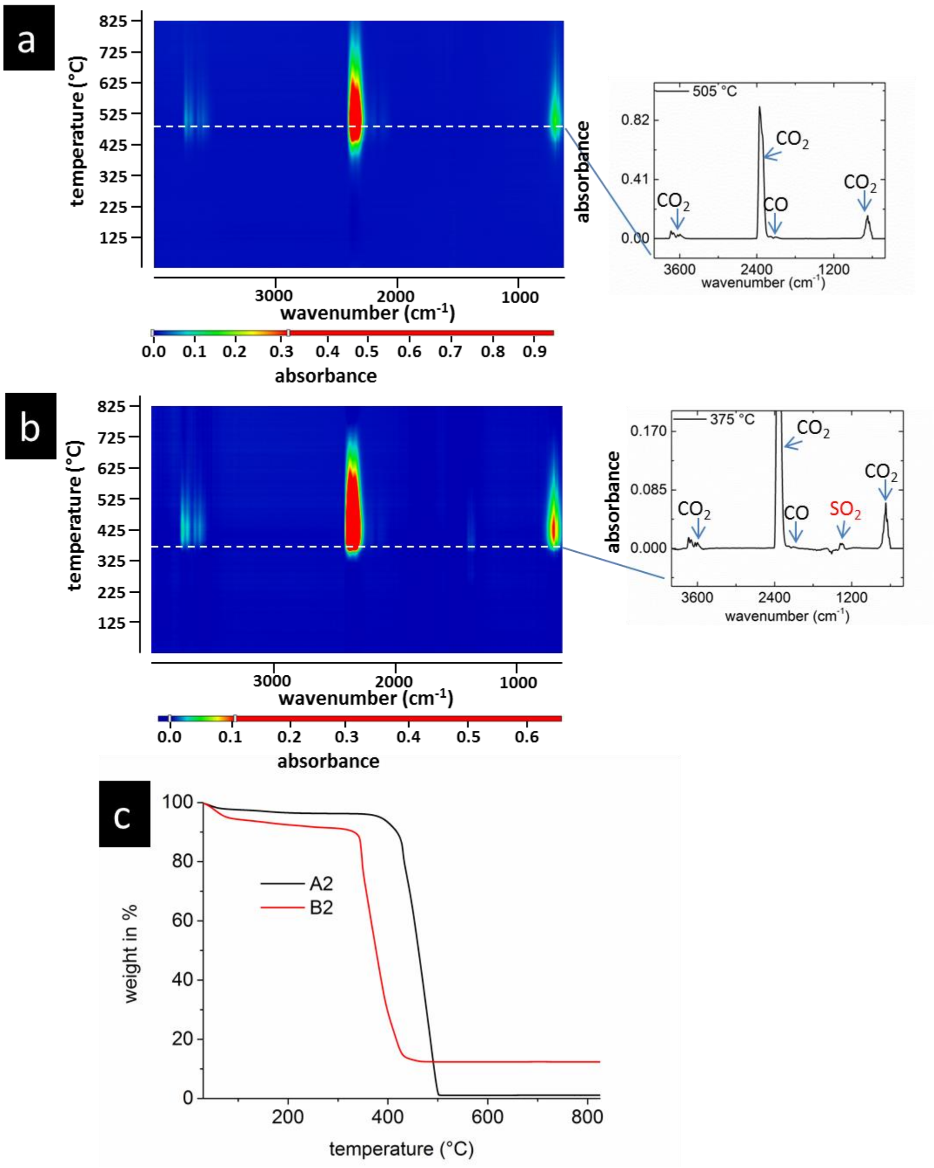

Figure 6.19 TGA-FTIR results for heating A2 and B2 in air (combustion): (**a**) FTIR mapping of the emitted gas products upon burning **A2;** (**b**) FTIR mapping of the emitted gas products upon burning **B2**; (**c**) combustion TGA profiles for **A2** and **B2**. The peaks in FTIR spectra were matched with the spectra of standard gaseous compounds in the database provided by Thermo Scientific. The figure is reprinted under a Creative Commons Attribution 4.0 International Licence (CC BY 4.0) from ref. 122 (Copyright 2018 American Chemical Society).

STEM-EDS elemental mappings (Figures 6.17d&i) and XPS C 1s spectrum (Figure 6.17l, dominated by a C-C peak at around 284.8 eV) reveal an abundance of C. Meanwhile, **B2** also have a small amount of Mo and S dispersed in them as shown in EDS mappings in Figures 6.17e&j. The more details about Mo and S in **B2** are provided by XPS Mo 3d and S 2p spectra (Figures 6.17m&n). The Mo 3d peak at 228.7 eV (for Mo^0)[336] suggests Mo-C bond formation. The S 2p doublets at ~ 164 eV (S $2p_{3/2}$) and ~ 165 eV (S $2p_{1/2}$) indicates the formation of S-C bonding.[342] These spectra are reasonably consistent with the XPS results in Figure 6.9 suggesting that the washing has insignificant influence on the chemistry of Mo and S within **B2**. Nonetheless, oxidised organic S was found from the XPS spectrum, which could be due to the interactions with entrapped O from the MOF host during carbonisation and/or oxidation during the washing step with $FeCl_3$ (aq) to remove Cu. By combusting **B2** in air using the TGA-FTIR, SO_2 emission was detected which further confirms the incorporation of S. Unlike **A2** remaining nothing after burning, **B2** has ~ 11 wt% solid product (likely to be MoO_3) remaining after combustion at ~ 500 °C. Therefore, a 7.4 wt% Mo incorporation in **B2** was estimated. The maximum S incorporation is ~ 9.8 wt% if all the S from MoS_4^{2-} were entrapped in **B2**.

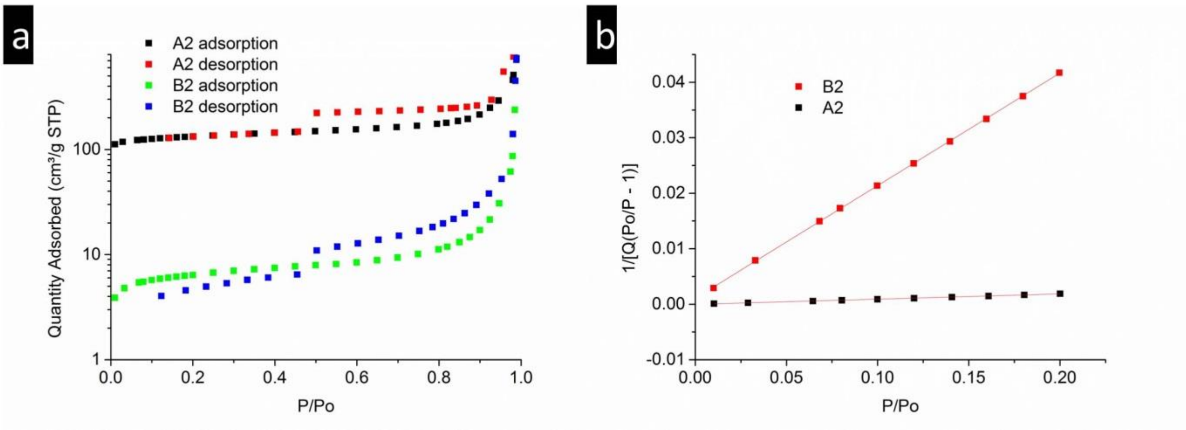

Figure 6.20 (a) Nitrogen adsorption isotherms for A2 and B2. (b) BET plots for A2 and B2. The figure is reprinted under a Creative Commons Attribution 4.0 International Licence (CC BY 4.0) from ref. 122 (Copyright 2018 American Chemical Society).

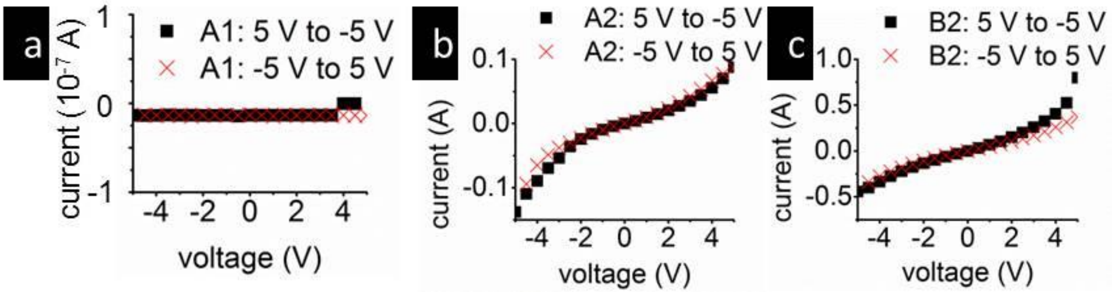

Figure 6.21 I-V plots for (a) A1, (b) A2 and (c) B2 respectively. These measurements were performed by Mr Chao Yun and the author. The figure is reprinted under a Creative Commons Attribution 4.0 International Licence (CC BY 4.0) from ref. 122 (Copyright 2018 American Chemical Society).

Unlike **A2** retaining reasonably large surface area (~ 460 m^2/g, calculated with the BET theory mentioned in Section 3.4) from the open-porous MOF, a significant reduction in surface area was found for **B2** (~ 21 m^2/g, similar to carbon nanofibre[343]) (Figure 6.20). This indicates that **B2** has experienced a significant structural rearrangement which further rationalise the formation of the nano-diatom. Furthermore, the electrical conductivities have been significantly improved after the carbonisation. Based on the I-V plots in Figure 6.21 and the method detailed in Section 6.3.6, the conductivities of **A2** and **B2** are ~ 0.39 S/m and ~ 0. 1 S/m, respectively.

6.4.4 B2 as an Anode Material for LiB

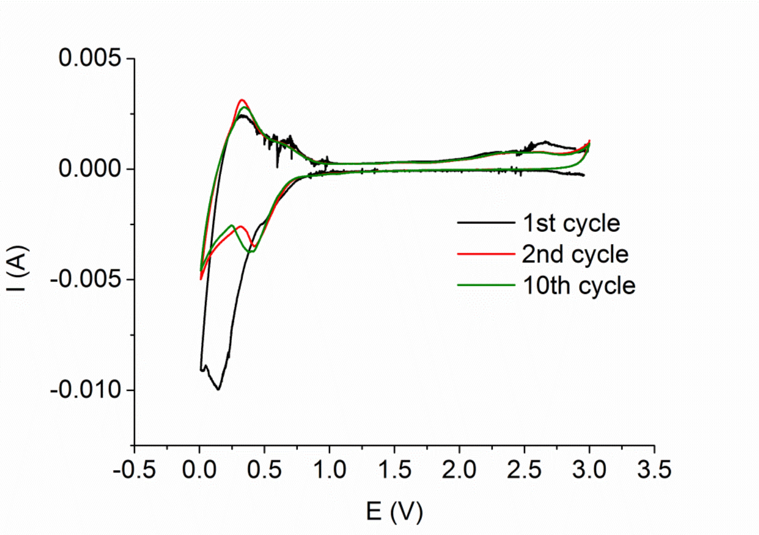

Figure 6.22 CV test for B2 at a scan rate of 0.2 mV/s. The sample was prepared the same way as those for LiB half-cell tests mentioned in Section 6.3.6. The test was performed by Dr Hyun-Kyung Kim. The figure is reprinted under a Creative Commons Attribution 4.0 International Licence (CC BY 4.0) from ref. 122 (Copyright 2018 American Chemical Society).

Fluctuation was found in the first cycle of CV for **B2** (Figure 6.22), which is likely due to some irreversible side reactions during first lithiation/delithiation. The side reactions could relate to the incorporation of Mo and S. In the second cycle, negligible fluctuation was noticed, which suggests the termination of the side reaction and the stabilization of the electrode's chemistry. The cathodic peak at around 0.4 V could be contributed by the reversible redox reactions of Mo-contained compounds. *e.g.* MoS_x[344,345] and MoO_x[346] could have cathodic peaks near 0.4- 0.6 V (Li_xMoS_x) and 0.4-0.5 V (Li_xMoO_x) during lithiation, respectively.

The open architecture of **B2** could facilitate electrolyte infiltration thus enabling fast ion storage.[347] Meanwhile, the mesoporosity could contribute to relatively high electrochemical utilization and storage capacity by increasing the ion-accessible surface area.[347] Based on these structural advantages (Figure 6.23a), **B2** was investigated as a LiB anode material. The relevant experimental is detailed in Section 6.3.6. Overall, its performance is among the best achieved for carbon-based materials (Figure 6.23).[343,347] The storage capacity is 830 mAh/g at 0.2 A/g (10th cycle, Figures 6.23b&c). The anode also has robust cycling performance during fast charge/discharge at 2 A/g (Figure 6.23d) with less than 25% decrease (from ~ 400 mAh/g to ~ 300 mAh/g) after 500 cycles and consistently high coulombic efficiency.

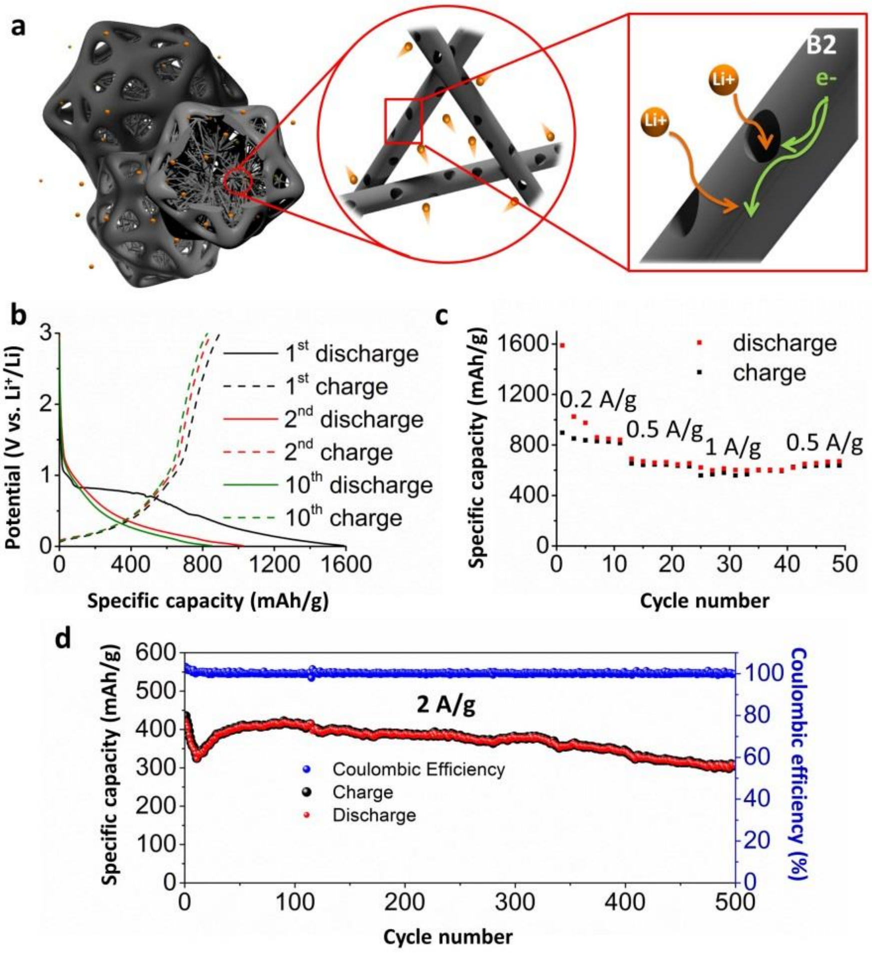

Figure 6.23 B2 works as an anode material for LiB: (a) Proposed schematic drawings to illustrate Li$^+$ interaction with **B2** during charging; (b) charge−discharge curves at 0.2 A/g; (c) rate capability test; and (d) cyclic stability tests at 2 A/g. The LiB tests were carried out by Dr Hyun-Kyung Kim. The schematic drawings were prepared by Ms Kara D. Fong and the author. The

figure is reprinted under a Creative Commons Attribution 4.0 International Licence (CC BY 4.0) from ref. 122 (Copyright 2018 American Chemical Society).

Additionaly, the incorporation of Mo, S (Figure 6.17) (< 10 wt% each obtained by TGA in Figure 6.19) and perhaps some O could also lead to the high storage capacity. This is supported by the cathodic peak in CV (Figure 6.22) at around 0.4 V for the reversible electrochemical reaction of Mo-containing compounds.

6.4.5 Other Nano-Diatoms

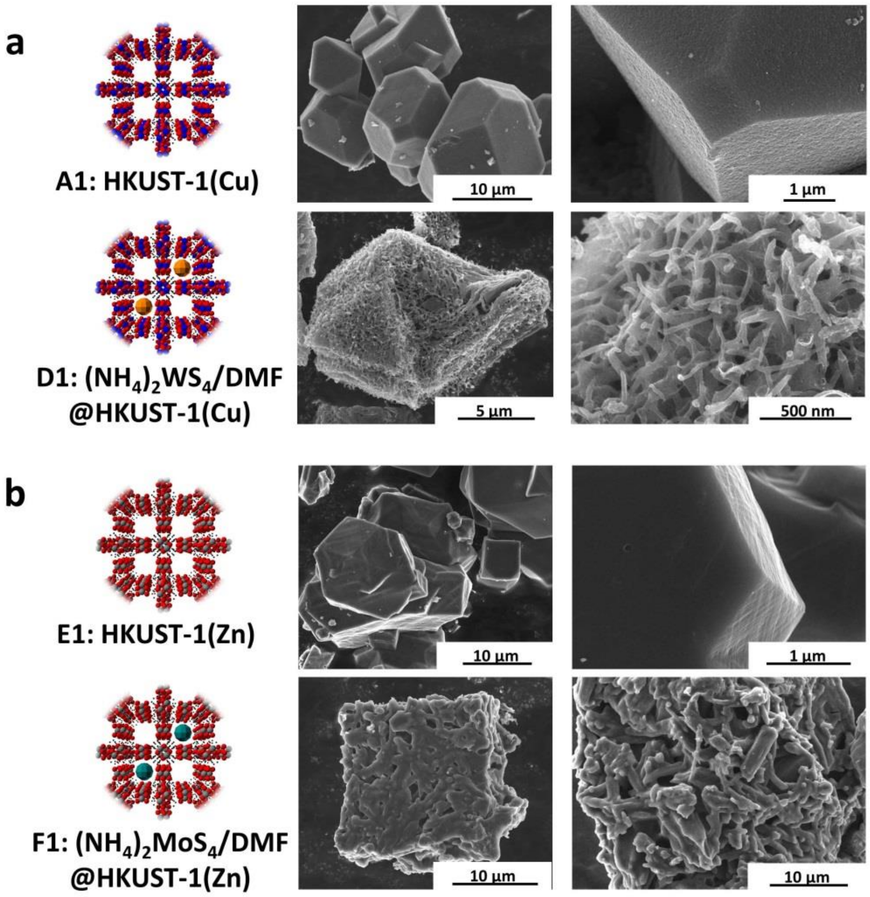

Figure 6.24 Summary for other nano-diatoms and their precursors. Schematic illustrations of precursors (left column) and SEM-SE images of products (two columns on the right hand side) after carbonization and washing for (a) **A1** (top) and **D1** (bottom); and (b) **E1** (top) and **F1** (bottom). The figure is reprinted under a Creative Commons Attribution 4.0 International Licence (CC BY 4.0) from ref. 122 (Copyright 2018 American Chemical Society).

To verify the hypotheses mentioned in Section 6.4.3 about nano-diatom formation, other MOF-guest combinations were investigated by replacing the guest or the MOF host with a homologous guest [*i.e.* $(NH_4)_2WS_4$ or ATT] or MOF host [*i.e.* HKUST-1(Zn)].

Mo was first replaced with W, which is another group VI element predicted to have similar reactivity[333,339] to form ATT/DMF@HKUST-1(Cu) (*i.e.* **D1**). After thermal carbonization and washing, the product (*i.e.* **D2**) also showed carbon-based filamentous growth similar to **B2** (Figure 6.24a). The metal-catalysed fibres in **D2**, however, grew outwards from the precursor surface, which is indicates that even small amounts of W in the Cu-rich surface would still catalyse the carbon-based filamentous growth. This is consistent with the work by Holmes *et al.*[339], *i.e.* W has stronger interaction with C than Mo thus enhances catalysed carbon-based filamentous growth. Furthermore, the higher activity of W could lead to higher nucleation density thus shorter fibres (assuming the same amount of carbon-based feedstock as that for Mo).

The original guest (*i.e.* ATM) but replaced the MOF host with HKUST-1(Zn) (*i.e.* **E1**) was also investigated. HKUST-1(Zn) has a similar crystal structure to HKUST-1(Cu).[321] The carbonised product (*i.e.* **E2**) can also retain the MOF polyhedral shape (Figure 6.24b) similar to **A2**. After carbonising and washing the host-guest precursor [i.e. ATM/DMF@HKUST-1(Zn), **F1**] some micron-sized rods were observed. There was no carbon-based nano-fibre like those found in **B2** and **D2**. The high-temperature Zn-based product (*e.g.* ZnO) could be inactive for catalysed carbon-based filamentous growth even in presence of Mo. The micron rods in **F2** are likely the result of collapse and reconfiguration of the MOF structures assisted by Mo-containing derivatives, as they can interact strongly with C and facilitate the scissoring of the carbon structures formed (*i.e.* cracking the C-C bond of organic compounds).[340,341]

The means to creating a broad range of carbon-based structures with multiple levels of hierarchy (i.e. nano-diatoms) could be generalised. While the transformations are observed in all of these MOF-guest systems (**B**, **D** and **F**), the resulting morphologies depend on the interactions between pyrolyzed carbon-based products and the metal-based derivatives from both guests and hosts.

6.5 Summary

I have found an approach to produce carbon-based structures with multiple levels of hierarchy (*i.e.* nano-diatoms) via a simple, bottom-up thermal carbonisation and washing process using MOF-guest systems as precursors. During high-temperature carbonisation, the guest derivatives and metal-containing derivatives from the MOF host can interact vigorously with the pyrolyzed carbon-based products thus result in dramatic morphological transformations to form guest/host-dependent nano-diatoms. To the author's best knowledge, this is one of the initial works studying MOF-guest interactions at elevated temperatures. In this chapter, the carbonisation process is focus.

So far only some Cu/Zn-MOF hosts with some Mo/W-based guests have been explored as prototypical demonstration. The author, however, is aware of (i) the abundance of MOF-guest systems (thousands of MOFs exist[52]) available for the process, and (ii) the highly diversified guest/host-dependent products could be obtained. The applicability of **B2** has also been demonstrated as a high-performance LiB anode material with fast charging capability (*i.e.* 2 A/g). The continued development of cheap, commercially available or easy-to-obtain, and easy-to-handle MOFs (*e.g.* HKUST-1(Cu) in this work) will enhance the potential for industrial-scale manufacturing of these hierarchical structures. On a more general level, the nano-diatoms derived from the MOF-guest systems with diverse carbon-based morphologies and chemistries incorporated in carbon matrix could be used for a variety of future applications, such as energy storage, energy conversion, and sensing.

Chapter 7

Concluding Remarks and Future Work

Chapter 7: Concluding Remarks and Future Work

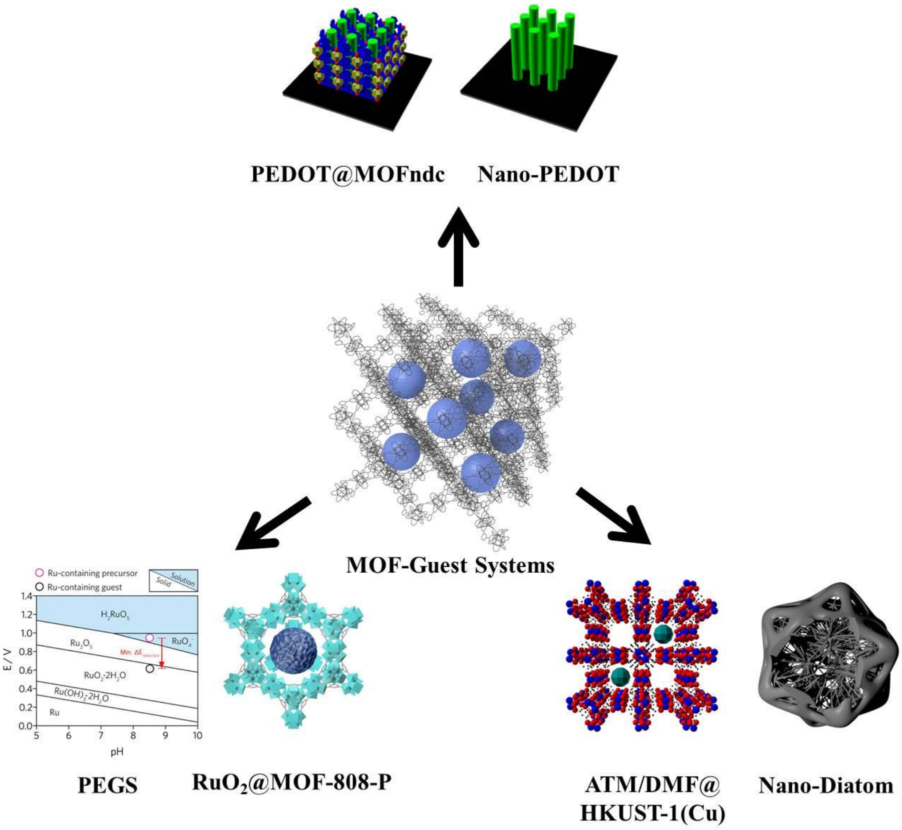

Figure 7.1 An overview of the thesis. The figure is reproduced from ref. 114 under a Creative Commons Attribution 3.0 Unported Licence (CC BY 3.0) (Copyright 2017 The Royal Society of Chemistry), ref. 122 under a Creative Commons Attribution 4.0 International Licence (CC BY 4.0) (Copyright 2018 American Chemical Society), and ref. [260] under a Creative Commons Attribution 4.0 International Licence (CC BY 4.0) (Copyright 2019 Nature Publishing Group).

The thesis has covered three projects related to the host-guest systems based on MOF (Figure 7.1). In the first project (Chapter 4), conducting polymer PEDOT has been successfully polymerised inside the 1-dimentional channels of MOFndc, which was grown on the PPy-coated steel substrate. The incorporated PEDOT turned the electrically insulating MOF into a conducting composite. Nanostructured PEDOT (*i.e.* nano-PEDOT) with anisotropic morphology was obtained after removing the MOF host. The nano-PEDOT is significantly softer than the standard PEDOT. PEGS approach was introduced in the second project (Chapter 5) to guide ship-in-a-bottle synthesis inside the MOF host. As a working example, RuO_2 was produced inside MOF-808-P which showed weaker surface interactions with CO and dissociated O than those for conventionally made RuO_2/SiO_2. Such interaction modulation led RuO_2@MOF-808-P to be more active for catalysing CO oxidation particularly at low temperatures (100 ^{o}C or lower). Furthermore, another guest (*e.g.* MnO_x) and other hosts (e.g. DUT-67 and Zeolite Y) have been confirmed to be compatible with the PEGS method. Unlike the former two projects which focus on the preparation of the MOF-guest systems, the third project (Chapter 6) treated the MOF-guest system (*e.g.* ATM/DMF@HKUST-1) as the precursor to produce carbon-based hierarchical nano-diatoms). At elevated temperatures (*e.g.* 800 ^{o}C) the guest derivatives could interact with the pyrolyzed MOF host vigorously thus trigger metal-catalysed carbon fibre growth. Nonetheless, the high temperature interactions and the morphology of the carbonised products depend on the guests and the MOF hosts used. Additionally, one of the nano-diatoms has been demonstrated as a competitive anode material for fast-charging LiB.

To highlight the novelty and significance of the PhD work, the author provides a main point summary as following:

(i) This PhD work includes the first attempt to incorporate the PEDOT into MOF and to use MOF as template to form nanostructured PEDOT.
(ii) By introducing the PEGS strategy, the author initiated the systemic approach to prepare the MOF-guest systems, which could bring the research field to a more advanced level.
(iii) This PhD work contains the first study to report the carbon-based nanostructures with controlled multilevel hierarchy made from the carbonised MOF-guest systems. Indeed, it could be the one of the initial attempts to seriously investigate the MOF-guest interactions at elevated temperatures (*e.g.* thermal carbonisation).

After the PhD study, the author will join Professor Deanna D’Alessandro’s group in The University of Sydney as a postdoctoral research associate. He also plans to obtain a faculty position and establish his group in China in a few years. In the future, the author would like to carry out some studies along two directions based on the work coved in the thesis:

(i) To gain more systematic understanding about the MOF-guest thermal carbonisation process. Some functional carbon-based materials can therefore be designed and prepared, which may benefit catalysis, energy storage and chemical sensing.
(ii) To expend the application of PEGS strategy for ship-in-a-bottle synthesis. In this way, the author can further explore or consolidate confinement effects and host-guest interactions based on the experimentally prepared systems.

Appendix for Chapter 5

RuO2/SiO2 Preparation and Characterisation

Appendix for Chapter 5: RuO_2/SiO_2 Preparation and Characterisation

A1: RuO_2/SiO_2 Preparation

RuO_2 particles supported on commercial silica (Qingdao Ocean Chemical Company) were prepared by an impregnation method using $RuCl_3$ (Tianjin Kemiou Chemical Reagent, China) as the precursor. The nominal loading of Ru in catalysts were maintained at 10 wt. %. The fresh catalysts were dried in an oven at 63 ^oC overnight, and then reduced by H_2 (70 ml/min) at 250 ^oC for 2 hrs (donated as Ru/SiO_2). Before catalytic activity test, the catalysts were oxidized by O_2 (30 ml/min) at 250 ^oC for 1 hrs (donated as RuO_2/SiO_2). After H_2 reduction, the samples were washed by Milli-Q water thoroughly at room temperature to remove K.

A2: RuO_2/SiO_2 Characterisation

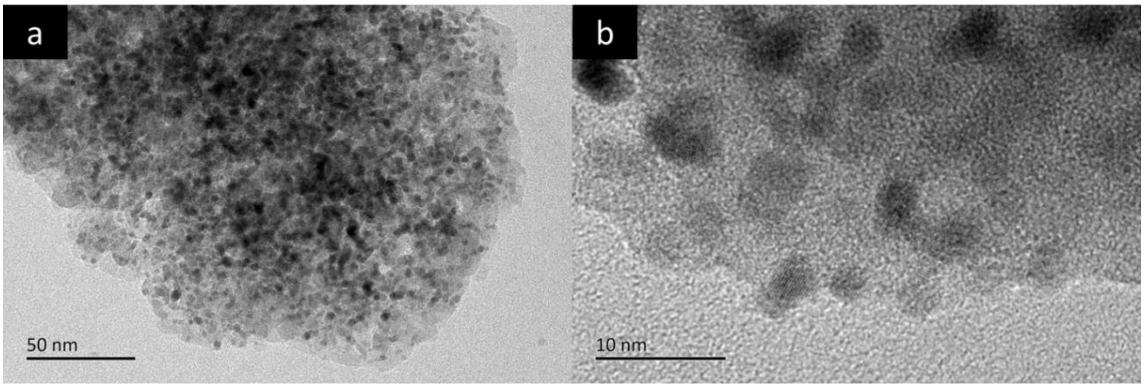

Figure A2.1 TEM images about the Ru/SiO_2. The Ru nanoparticles distributed uniformly on the SiO_2 supports with an average diameter between ~ 3 nm and ~ 5 nm. The TEM images for RuO_2/SiO_2 were acquired on the JEM-2100 microscope operated at an accelerating voltage of 200 kV. TEM samples were prepared by drop-casting 100 µl of sample suspension (ground sample powder dispersed in ethanol) on copper grids. The figure is reprinted under a Creative Commons Attribution 4.0 International Licence (CC BY 4.0) from ref. [260] (Copyright 2019 Nature Publishing Group).

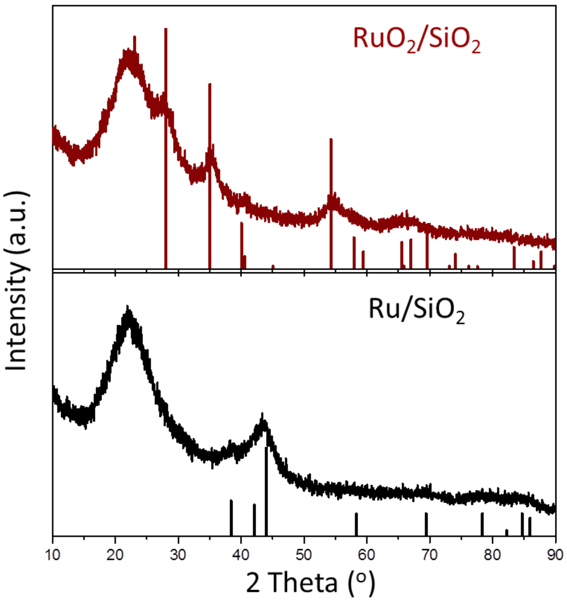

Figure A2.2 Powder XRD patterns for Ru/SiO_2 (bottom, with simulated Ru peaks provided) and its oxidized form (RuO_2/SiO_2) (top, with simulated RuO_2 peaks provided). The results illustrate that the metallic Ru was oxidized to RuO_2 after O_2 oxidation at 250 °C. The peak loaded at 23° was attributed to amorphous SiO_2. Powder XRD patterns for RuO_2/SiO_2 were collected on an Empyrean diffractometer using a Cu Ka (λ = 1.5406 Å) radiation source at 40 kV and 40 mA and scanning rate of 12° per min. The figure is reprinted under a Creative Commons Attribution 4.0 International Licence (CC BY 4.0) from ref. [260] (Copyright 2019 Nature Publishing Group).

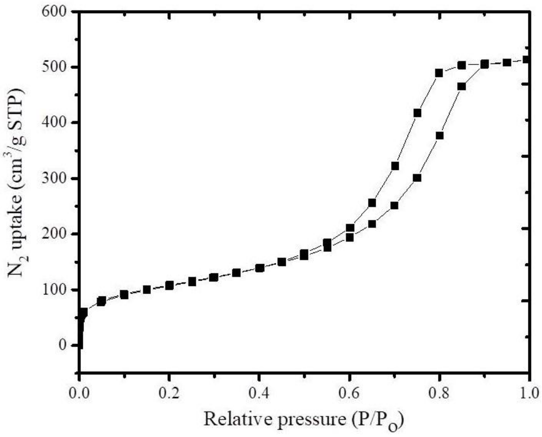

Figure A2.3 Nitrogen physisorption isotherm of the SiO_2 support, which has typical Type IV isotherm shape[149] showing the mesoporous SiO_2 with 356.1 m^2/g BET area. Further analysis shows the pore diameter is 5-10 nm. The mesoporous SiO_2 was analysed by N_2 adsorption/desorption at 77 K using Quantachrome Autosorb iQ2 equipment. The samples were degassed at 300 °C for 6 h under vacuum. The figure is reprinted under a Creative Commons Attribution 4.0 International Licence (CC BY 4.0) from ref. [260] (Copyright 2019 Nature Publishing Group).

References

References

(1) Wenz, G. An Overview of Host-Guest Chemistry and Its Application to Nonsteroidal Anti-Inflammatory Drugs. *Clin. Drug Investig.* **2000**, *19* (Supplement 2), 21–25. https://doi.org/10.2165/00044011-200019002-00003.

(2) *Inclusion Chemistry with Zeolites: Nanoscale Materials by Design*; Herron, N., Corbin, D. R., Eds.; Topics in Inclusion Science; Kluwer Academic Publishers: Dordrecht, 1995; Vol. 6. https://doi.org/10.1007/978-94-011-0119-6.

(3) *Host-Guest-Systems Based on Nanoporous Crystals*; Laeri, F., Schüth, F., Simon, U., Wark, M., Eds.; Wiley-VCH Verlag GmbH & Co. KGaA: Weinheim, FRG, 2003. https://doi.org/10.1002/3527602674.

(4) Corma, A.; Garcia, H. Supramolecular Host-Guest Systems in Zeolites Prepared by Ship-in-a-Bottle Synthesis. *Eur. J. Inorg. Chem.* **2004**, No. 6, 1143–1164. https://doi.org/10.1002/ejic.200300831.

(5) Corma, A.; Garcia, H. Zeolite-Based Photocatalysts. *Chem. Commun.* **2004**, No. 13, 1443. https://doi.org/10.1039/b400147h.

(6) Ichikawa, M. “Ship-in-Bottle” Catalyst Technology: Novel Templating Fabrication of Platinum Group Metals Nanoparticles and Wires in Micro/Mesopores. *Platin. Met. Rev.* **2000**, *44* (1), 3–14.

(7) García-García, P.; Müller, M.; Corma, A. MOF Catalysis in Relation to Their Homogeneous Counterparts and Conventional Solid Catalysts. *Chem. Sci.* **2014**, *5* (8), 2979. https://doi.org/10.1039/c4sc00265b.

(8) Chen, L.; Luque, R.; Li, Y. Controllable Design of Tunable Nanostructures inside Metal–Organic Frameworks. *Chem. Soc. Rev.* **2017**, *46* (15), 4614–4630. https://doi.org/10.1039/C6CS00537C.

(9) Corma, A.; García, H.; Llabrés i Xamena, F. X. Engineering Metal Organic Frameworks for Heterogeneous Catalysis. *Chem. Rev.* **2010**, *110* (8), 4606–4655. https://doi.org/10.1021/cr9003924.

(10) *Functional Metal-Organic Frameworks: Gas Storage, Separation and Catalysis*; Schröder, M., Ed.; Topics in Current Chemistry; Springer Berlin Heidelberg: Berlin,

Heidelberg, 2010; Vol. 293. https://doi.org/10.1007/978-3-642-14613-8.

(11) Li, M.; Li, D.; O'Keeffe, M.; Yaghi, O. M. Topological Analysis of Metal-Organic Frameworks with Polytopic Linkers and/or Multiple Building Units and the Minimal Transitivity Principle. *Chem. Rev.* **2014**, *114* (2), 1343–1370. https://doi.org/10.1021/cr400392k.

(12) Furukawa, H.; Cordova, K. E.; O'Keeffe, M.; Yaghi, O. M. The Chemistry and Applications of Metal-Organic Frameworks. *Science (80-.).* **2013**, *341* (6149), 1230444–1230444. https://doi.org/10.1126/science.1230444.

(13) Howarth, A. J.; Liu, Y.; Li, P.; Li, Z.; Wang, T. C.; Hupp, J. T.; Farha, O. K. Chemical, Thermal and Mechanical Stabilities of Metal–Organic Frameworks. *Nat. Rev. Mater.* **2016**, *1* (3), 15018. https://doi.org/10.1038/natrevmats.2015.18.

(14) Kitagawa, S.; Kitaura, R.; Noro, S. Functional Porous Coordination Polymers. *Angew. Chemie Int. Ed.* **2004**, *43* (18), 2334–2375. https://doi.org/10.1002/anie.200300610.

(15) Férey, G. Hybrid Porous Solids: Past, Present, Future. *Chem. Soc. Rev.* **2008**, *37* (1), 191–214. https://doi.org/10.1039/B618320B.

(16) O'Keeffe, M.; Yaghi, O. M. Deconstructing the Crystal Structures of Metal-Organic Frameworks and Related Materials into Their Underlying Nets. *Chem. Rev.* **2012**, *112* (2), 675–702. https://doi.org/10.1021/cr200205j.

(17) Conflig. Why is the black pearl in a bottle? http://blenderartists.org/t/why-is-the-black-pearl-in-a-bottle/693909 (accessed Oct 15, 2018).

(18) Moller, K.; Bein, T. Inclusion Chemistry in Periodic Mesoporous Hosts. *Chem. Mater.* **1998**, *10* (10), 2950–2963. https://doi.org/10.1021/cm980243e.

(19) Fujita, M.; Oguro, D.; Miyazawa, M.; Oka, H.; Yamaguchi, K.; Ogura, K. Self-Assembly of Ten Molecules into Nanometre-Sized Organic Host Frameworks. *Nature* **1995**, *378* (6556), 469–471. https://doi.org/10.1038/378469a0.

(20) Lee, J.; Farha, O. K.; Roberts, J.; Scheidt, K. A.; Nguyen, S. T.; Hupp, J. T. Metal–Organic Framework Materials as Catalysts. *Chem. Soc. Rev.* **2009**, *38* (5), 1450. https://doi.org/10.1039/b807080f.

(21) Meilikhov, M.; Yusenko, K.; Esken, D.; Turner, S.; Van Tendeloo, G.; Fischer, R. A. Metals@MOFs - Loading MOFs with Metal Nanoparticles for Hybrid Functions. *Eur. J. Inorg. Chem.* **2010**, *2010* (24), 3701–3714. https://doi.org/10.1002/ejic.201000473.

(22) Juan-Alcañiz, J.; Gascon, J.; Kapteijn, F. Metal–Organic Frameworks as Scaffolds for the Encapsulation of Active Species: State of the Art and Future Perspectives. *J. Mater. Chem.* **2012**, *22* (20), 10102. https://doi.org/10.1039/c2jm15563j.

(23) Pan, X.; Bao, X. The Effects of Confinement inside Carbon Nanotubes on Catalysis. *Acc. Chem. Res.* **2011**, *44* (8), 553–562. https://doi.org/10.1021/ar100160t.

(24) Zhao, M.; Yuan, K.; Wang, Y.; Li, G.; Guo, J.; Gu, L.; Hu, W.; Zhao, H.; Tang, Z. Metal–Organic Frameworks as Selectivity Regulators for Hydrogenation Reactions. *Nature* **2016**, *539* (7627), 76–80. https://doi.org/10.1038/nature19763.

(25) An, B.; Zhang, J.; Cheng, K.; Ji, P.; Wang, C.; Lin, W. Confinement of Ultrasmall Cu/ZnO x Nanoparticles in Metal–Organic Frameworks for Selective Methanol Synthesis from Catalytic Hydrogenation of CO 2. *J. Am. Chem. Soc.* **2017**, *139* (10), 3834–3840. https://doi.org/10.1021/jacs.7b00058.

(26) Yang, Y.; Chen, J.-S.; Liu, J.-Y.; Zhao, G.-J.; Liu, L.; Han, K.-L.; Cook, T. R.; Stang, P. J. Photophysical Properties of a Post-Self-Assembly Host/Guest Coordination Cage: Visible Light Driven Core-to-Cage Charge Transfer. *J. Phys. Chem. Lett.* **2015**, *6* (10), 1942–1947. https://doi.org/10.1021/acs.jpclett.5b00783.

(27) Allendorf, M. D.; Foster, M. E.; Léonard, F.; Stavila, V.; Feng, P. L.; Doty, F. P.; Leong, K.; Ma, E. Y.; Johnston, S. R.; Talin, A. A. Guest-Induced Emergent Properties in Metal–Organic Frameworks. *J. Phys. Chem. Lett.* **2015**, *6* (7), 1182–1195. https://doi.org/10.1021/jz5026883.

(28) Stucky, G. D.; Mac Dougall, J. E. Quantum Confinement and Host/Guest Chemistry: Probing a New Dimension. *Science (80-.).* **1990**, *247* (4943), 669–678. https://doi.org/10.1126/science.247.4943.669.

(29) Rosi, N. L.; Eckert, J.; Eddaoudi, M.; Vodak, D. T.; Kim, J.; O'Keeffe, M.; Yaghi, O. M. Hydrogen Storage in Microporous Metal-Organic Frameworks. *Science (80-.).* **2003**, *300* (5622), 1127–1129. https://doi.org/10.1126/science.1083440.

(30) Rowsell, J. L. C.; Yaghi, O. M. Strategies for Hydrogen Storage in Metal-Organic Frameworks. *Angew. Chemie Int. Ed.* **2005**, *44* (30), 4670–4679. https://doi.org/10.1002/anie.200462786.

(31) Li, J.-R.; Kuppler, R. J.; Zhou, H.-C. Selective Gas Adsorption and Separation in Metal–Organic Frameworks. *Chem. Soc. Rev.* **2009**, *38* (5), 1477. https://doi.org/10.1039/b802426j.

(32) Li, J.-R.; Sculley, J.; Zhou, H.-C. Metal–Organic Frameworks for Separations. *Chem. Rev.* **2012**, *112* (2), 869–932. https://doi.org/10.1021/cr200190s.

(33) Achmann, S.; Hagen, G.; Kita, J.; Malkowsky, I.; Kiener, C.; Moos, R. Metal-Organic Frameworks for Sensing Applications in the Gas Phase. *Sensors* **2009**, *9* (3), 1574–1589. https://doi.org/10.3390/s90301574.

(34) Kreno, L. E.; Leong, K.; Farha, O. K.; Allendorf, M.; Van Duyne, R. P.; Hupp, J. T. Metal-Organic Framework Materials as Chemical Sensors. *Chem. Rev.* **2012**, *112* (2), 1105–1125. https://doi.org/10.1021/cr200324t.

(35) Huxford, R. C.; Della Rocca, J.; Lin, W. Metal–Organic Frameworks as Potential Drug Carriers. *Curr. Opin. Chem. Biol.* **2010**, *14* (2), 262–268. https://doi.org/10.1016/j.cbpa.2009.12.012.

(36) McKinlay, A. C.; Morris, R. E.; Horcajada, P.; Férey, G.; Gref, R.; Couvreur, P.; Serre, C. BioMOFs: Metal-Organic Frameworks for Biological and Medical Applications. *Angew. Chemie - Int. Ed.* **2010**, *49* (36), 6260–6266. https://doi.org/10.1002/anie.201000048.

(37) Horcajada, P.; Gref, R.; Baati, T.; Allan, P. K.; Maurin, G.; Couvreur, P.; Férey, G.; Morris, R. E.; Serre, C. Metal–Organic Frameworks in Biomedicine. *Chem. Rev.* **2012**, *112* (2), 1232–1268. https://doi.org/10.1021/cr200256v.

(38) Teplensky, M. H.; Fantham, M.; Li, P.; Wang, T. C.; Mehta, J. P.; Young, L. J.; Moghadam, P. Z.; Hupp, J. T.; Farha, O. K.; Kaminski, C. F.; et al. Temperature Treatment of Highly Porous Zirconium-Containing Metal–Organic Frameworks Extends Drug Delivery Release. *J. Am. Chem. Soc.* **2017**, *139* (22), 7522–7532. https://doi.org/10.1021/jacs.7b01451.

(39) Cheetham, A. K.; Férey, G.; Loiseau, T. Open-Framework Inorganic Materials. *Angew. Chemie Int. Ed.* **1999**, *38* (22), 3268–3292. https://doi.org/10.1002/(SICI)1521-3773(19991115)38:22<3268::AID-ANIE3268>3.0.CO;2-U.

(40) Weitkamp, J. Zeolites and Catalysis. *Solid State Ionics* **2000**, *131* (1–2), 175–188. https://doi.org/10.1016/S0167-2738(00)00632-9.

(41) Thomas, J. M.; Thomas, W. J. *Principles and Practice of Heterogeneous Catalysis*, 1st ed.; Wiley-VCH Verlag GmbH & Co. KGaA: Weinheim, FRG, 1996.

(42) Kinoshita, Y.; Matsubara, I.; Higuchi, T.; Saito, Y. The Crystal Structure of Bis(Adiponitrilo)Copper(I) Nitrate. *Bull. Chem. Soc. Jpn.* **1959**, *32* (11), 1221–1226. https://doi.org/10.1246/bcsj.32.1221.

(43) Hoskins, B. F.; Robson, R. Design and Construction of a New Class of Scaffolding-like Materials Comprising Infinite Polymeric Frameworks of 3D-Linked Molecular Rods. A Reappraisal of the Zinc Cyanide and Cadmium Cyanide Structures and the Synthesis and Structure of the Diamond-Rela. *J. Am. Chem. Soc.* **1990**, *112* (4), 1546–1554. https://doi.org/10.1021/ja00160a038.

(44) Abrahams, B. F.; Hoskins, B. F.; Robson, R. A New Type of Infinite 3D Polymeric Network Containing 4-Connected, Peripherally-Linked Metalloporphyrin Building Blocks. *J. Am. Chem. Soc.* **1991**, *113* (9), 3606–3607. https://doi.org/10.1021/ja00009a065.

(45) Fujita, M.; Kwon, Y. J.; Washizu, S.; Ogura, K. Preparation, Clathration Ability, and Catalysis of a Two-Dimensional Square Network Material Composed of Cadmium(II) and 4,4’-Bipyridine. *J. Am. Chem. Soc.* **1994**, *116* (3), 1151–1152. https://doi.org/10.1021/ja00082a055.

(46) Yaghi, O. M.; Sun, Z.; Richardson, D. A.; Groy, T. L. Directed Transformation of Molecules to Solids: Synthesis of a Microporous Sulfide from Molecular Germanium Sulfide Cages. *J. Am. Chem. Soc.* **1994**, *116* (2), 807–808. https://doi.org/10.1021/ja00081a067.

(47) Macgillivray, L. R.; Subramanian, S.; Zaworotko, M. J. Interwoven 2-Dimensional and 3-Dimensional Coordination Polymers Through Self-Assembly of Cut Cations

With Linear Bidentate Ligands. *J. Chem. Soc. Commun.* **1994**, No. 11, 1325–1326. https://doi.org/10.1039/c39940001325.

(48) Abrahams, B. F.; Hoskins, B. F.; Michail, D. M.; Robson, R. Assembly of Porphyrin Building Blocks into Network Structures with Large Channels. *Nature* **1994**, *369* (6483), 727–729. https://doi.org/10.1038/369727a0.

(49) Dietrich-Buchecker, C. .; Sauvage, J. .; Kintzinger, J. . Une Nouvelle Famille de Molecules : Les Metallo-Catenanes. *Tetrahedron Lett.* **1983**, *24* (46), 5095–5098. https://doi.org/10.1016/S0040-4039(00)94050-4.

(50) Fujita, M.; Yazaki, J.; Ogura, K. Preparation of a Macrocyclic Polynuclear Complex, [(En)Pd(4,4’-Bpy)]4(NO3)8 (En = Ethylenediamine, Bpy = Bipyridine), Which Recognizes an Organic Molecule in Aqueous Media. *J. Am. Chem. Soc.* **1990**, *112* (14), 5645–5647. https://doi.org/10.1021/ja00170a042.

(51) Kim, D.; Liu, X.; Lah, M. S. Topology Analysis of Metal-Organic Frameworks Based on Metal-Organic Polyhedra as Secondary or Tertiary Building Units. *Inorg. Chem. Front.* **2015**, *2* (4), 336–360. https://doi.org/10.1039/c4qi00236a.

(52) Moghadam, P. Z.; Li, A.; Wiggin, S. B.; Tao, A.; Maloney, A. G. P.; Wood, P. A.; Ward, S. C.; Fairen-Jimenez, D. Development of a Cambridge Structural Database Subset: A Collection of Metal–Organic Frameworks for Past, Present, and Future. *Chem. Mater.* **2017**, *29* (7), 2618–2625. https://doi.org/10.1021/acs.chemmater.7b00441.

(53) Yaghi, O. M.; Li, H.; Eddaoudi, M.; O’Keeffe, M. Design and Synthesis of an Exceptionally Stable and Highly Porous Metal-Organic Framework. *Nature* **1999**, *402* (6759), 276–279. https://doi.org/10.1038/46248.

(54) Huang, X.; Zhang, J.; Chen, X. [Zn(Bim)2] · (H2O)1.67: A Metal-Organic Open-Framework with Sodalite Topology. *Chinese Sci. Bull.* **2003**, *48* (15), 1531–1534. https://doi.org/10.1007/BF03183954.

(55) Chui, S. S.-Y.; Lo, S. M.-F.; Charmant, J. P. H.; Orpen, A. G.; Williams, I. D. A Chemically Functionalizable Nanoporous Material [Cu3(TMA)2(H2O)3]N. *Science (80-.).* **1999**, *283* (5405), 1148–1150. https://doi.org/10.1126/science.283.5405.1148.

(56) Cavka, J. H.; Jakobsen, S.; Olsbye, U.; Guillou, N.; Lamberti, C.; Bordiga, S.; Lillerud, K. P. A New Zirconium Inorganic Building Brick Forming Metal Organic Frameworks with Exceptional Stability. *J. Am. Chem. Soc.* **2008**, *130* (42), 13850–13851. https://doi.org/10.1021/ja8057953.

(57) Mondloch, J. E.; Bury, W.; Fairen-Jimenez, D.; Kwon, S.; Demarco, E. J.; Weston, M. H.; Sarjeant, A. A.; Nguyen, S. T.; Stair, P. C.; Snurr, R. Q.; et al. Vapor-Phase Metalation by Atomic Layer Deposition in a Metal-Organic Framework. *J. Am. Chem. Soc.* **2013**, *135* (28), 10294–10297. https://doi.org/10.1021/ja4050828.

(58) Tian, T.; Zeng, Z.; Vulpe, D.; Casco, M. E.; Divitini, G.; Midgley, P. A.; Silvestre-Albero, J.; Tan, J. C.; Moghadam, P. Z.; Fairen-Jimenez, D. A Sol-Gel Monolithic Metal-Organic Framework with Enhanced Methane Uptake. *Nat. Mater.* **2018**, *17* (2), 174–179. https://doi.org/10.1038/NMAT5050.

(59) Gascon, J.; Corma, A.; Kapteijn, F.; Llabrés i Xamena, F. X. Metal Organic Framework Catalysis: Quo Vadis ? *ACS Catal.* **2014**, *4* (2), 361–378. https://doi.org/10.1021/cs400959k.

(60) Zeng, L.; Guo, X.; He, C.; Duan, C. Metal–Organic Frameworks: Versatile Materials for Heterogeneous Photocatalysis. *ACS Catal.* **2016**, *6* (11), 7935–7947. https://doi.org/10.1021/acscatal.6b02228.

(61) Hu, Z.; Deibert, B. J.; Li, J. Luminescent Metal–Organic Frameworks for Chemical Sensing and Explosive Detection. *Chem. Soc. Rev.* **2014**, *43* (16), 5815–5840. https://doi.org/10.1039/C4CS00010B.

(62) Horcajada, P.; Chalati, T.; Serre, C.; Gillet, B.; Sebrie, C.; Baati, T.; Eubank, J. F.; Heurtaux, D.; Clayette, P.; Kreuz, C.; et al. Porous Metal–Organic-Framework Nanoscale Carriers as a Potential Platform for Drug Delivery and Imaging. *Nat. Mater.* **2010**, *9* (2), 172–178. https://doi.org/10.1038/nmat2608.

(63) Horike, S.; Shimomura, S.; Kitagawa, S. Soft Porous Crystals. *Nat. Chem.* **2009**, *1* (9), 695–704. https://doi.org/10.1038/nchem.444.

(64) Yang, F.; Xu, G.; Dou, Y.; Wang, B.; Zhang, H.; Wu, H.; Zhou, W.; Li, J. R.; Chen, B. A Flexible Metal-Organic Framework with a High Density of Sulfonic Acid Sites for Proton Conduction. *Nat. Energy* **2017**, *2* (11), 877–883.

https://doi.org/10.1038/s41560-017-0018-7.

(65) Ban, Y.; Li, Z.; Li, Y.; Peng, Y.; Jin, H.; Jiao, W.; Guo, A.; Wang, P.; Yang, Q.; Zhong, C.; et al. Confinement of Ionic Liquids in Nanocages: Tailoring the Molecular Sieving Properties of ZIF-8 for Membrane-Based CO2Capture. *Angew. Chemie - Int. Ed.* **2015**, *54* (51), 15483–15487. https://doi.org/10.1002/anie.201505508.

(66) Coghlan, C. J.; Sumby, C. J.; Doonan, C. J. Utilising Hinged Ligands in MOF Synthesis: A Covalent Linking Strategy for Forming 3D MOFs. *CrystEngComm* **2014**, *16* (28), 6364–6371. https://doi.org/10.1039/c4ce00181h.

(67) Bon, V.; Senkovska, I.; Baburin, I. a; Kaskel, S. Zr- and Hf-Based Metal–Organic Frameworks: Tracking Down the Polymorphism. *Cryst. Growth Des.* **2013**, *13* (3), 1231–1237. https://doi.org/10.1021/cg301691d.

(68) Furukawa, H.; Gándara, F.; Zhang, Y.-B.; Jiang, J.; Queen, W. L.; Hudson, M. R.; Yaghi, O. M. Water Adsorption in Porous Metal–Organic Frameworks and Related Materials. *J. Am. Chem. Soc.* **2014**, *136* (11), 4369–4381. https://doi.org/10.1021/ja500330a.

(69) Lollar, C. T.; Qin, J.-S.; Pang, J.; Yuan, S.; Becker, B.; Zhou, H.-C. Interior Decoration of Stable Metal–Organic Frameworks. *Langmuir* **2018**, No. May, acs.langmuir.8b00823. https://doi.org/10.1021/acs.langmuir.8b00823.

(70) Burtch, N. C.; Jasuja, H.; Walton, K. S. Water Stability and Adsorption in Metal-Organic Frameworks. *Chem. Rev.* **2014**, *114* (20), 10575–10612. https://doi.org/10.1021/cr5002589.

(71) Yuan, S.; Feng, L.; Wang, K.; Pang, J.; Bosch, M.; Lollar, C.; Sun, Y.; Qin, J.; Yang, X.; Zhang, P.; et al. Stable Metal-Organic Frameworks: Design, Synthesis, and Applications. *Adv. Mater.* **2018**, *1704303*, 1704303. https://doi.org/10.1002/adma.201704303.

(72) Hassanzadeh Fard, Z.; Wong, N. E.; Malliakas, C. D.; Ramaswamy, P.; Taylor, J. M.; Otsubo, K.; Shimizu, G. K. H. Superprotonic Phase Change to a Robust Phosphonate Metal-Organic Framework. *Chem. Mater.* **2018**, *30* (2), 314–318. https://doi.org/10.1021/acs.chemmater.7b04467.

(73) Bennett, T. D.; Goodwin, A. L.; Dove, M. T.; Keen, D. A.; Tucker, M. G.; Barney, E. R.; Soper, A. K.; Bithell, E. G.; Tan, J. C.; Cheetham, A. K. Structure and Properties of an Amorphous Metal-Organic Framework. *Phys. Rev. Lett.* **2010**, *104* (11), 2–5. https://doi.org/10.1103/PhysRevLett.104.115503.

(74) Umeyama, D.; Horike, S.; Inukai, M.; Itakura, T.; Kitagawa, S. Reversible Solid-to-Liquid Phase Transition of Coordination Polymer Crystals. *J. Am. Chem. Soc.* **2015**, *137* (2), 864–870. https://doi.org/10.1021/ja511019u.

(75) Valenzano, L.; Civalleri, B.; Chavan, S.; Bordiga, S.; Nilsen, M. H.; Jakobsen, S.; Lillerud, K. P.; Lamberti, C. Disclosing the Complex Structure of UiO-66 Metal Organic Framework: A Synergic Combination of Experiment and Theory. *Chem. Mater.* **2011**, *23* (7), 1700–1718. https://doi.org/10.1021/cm1022882.

(76) Sun, J.-K.; Xu, Q. Functional Materials Derived from Open Framework Templates/Precursors: Synthesis and Applications. *Energy Environ. Sci.* **2014**, *7* (7), 2071. https://doi.org/10.1039/c4ee00517a.

(77) Easun, T. L.; Moreau, F.; Yan, Y.; Yang, S.; Schröder, M. Structural and Dynamic Studies of Substrate Binding in Porous Metal–Organic Frameworks. *Chem. Soc. Rev.* **2017**, *46* (1), 239–274. https://doi.org/10.1039/C6CS00603E.

(78) Wang, R.; Jin, D.; Zhang, Y.; Wang, S.; Lang, J.; Yan, X.; Zhang, L. Engineering Metal Organic Framework Derived 3D Nanostructures for High Performance Hybrid Supercapacitors. *J. Mater. Chem. A* **2017**, *5* (1), 292–302. https://doi.org/10.1039/C6TA09143A.

(79) Lu, G.; Li, S.; Guo, Z.; Farha, O. K.; Hauser, B. G.; Qi, X.; Wang, Y.; Wang, X.; Han, S.; Liu, X.; et al. Imparting Functionality to a Metal–Organic Framework Material by Controlled Nanoparticle Encapsulation. *Nat. Chem.* **2012**, *4* (4), 310–316. https://doi.org/10.1038/nchem.1272.

(80) Masoomi, M. Y.; Morsali, A. Applications of Metal–Organic Coordination Polymers as Precursors for Preparation of Nano-Materials. *Coord. Chem. Rev.* **2012**, *256* (23–24), 2921–2943. https://doi.org/10.1016/j.ccr.2012.05.032.

(81) Zhang, F.; Jiang, D.; Zhang, X. Porous NiO Materials Prepared by Solid-State Thermolysis of a Ni-MOF Crystal for Lithium-Ion Battery Anode. *Nano-Structures*

& Nano-Objects **2016**, *5*, 1–6. https://doi.org/10.1016/j.nanoso.2015.12.002.

(82) Shen, K.; Chen, X.; Chen, J.; Li, Y. Development of MOF-Derived Carbon-Based Nanomaterials for Efficient Catalysis. *ACS Catal.* **2016**, *6* (9), 5887–5903. https://doi.org/10.1021/acscatal.6b01222.

(83) Hu, M.; Reboul, J.; Furukawa, S.; Torad, N. L.; Ji, Q.; Srinivasu, P.; Ariga, K.; Kitagawa, S.; Yamauchi, Y. Direct Carbonization of Al-Based Porous Coordination Polymer for Synthesis of Nanoporous Carbon. *J. Am. Chem. Soc.* **2012**, *134* (6), 2864–2867. https://doi.org/10.1021/ja208940u.

(84) Liu, B.; Shioyama, H.; Akita, T.; Xu, Q. Metal-Organic Framework as a Template for Porous Carbon Synthesis. *J. Am. Chem. Soc.* **2008**, *130* (16), 5390–5391. https://doi.org/10.1021/ja7106146.

(85) Tan, J. C.; Cheetham, A. K. Mechanical Properties of Hybrid Inorganic–Organic Framework Materials: Establishing Fundamental Structure–Property Relationships. *Chem. Soc. Rev.* **2011**, *40* (2), 1059. https://doi.org/10.1039/c0cs00163e.

(86) Tan, J. C.; Merrill, C. A.; Orton, J. B.; Cheetham, A. K. Anisotropic Mechanical Properties of Polymorphic Hybrid Inorganic–Organic Framework Materials with Different Dimensionalities. *Acta Mater.* **2009**, *57* (12), 3481–3496. https://doi.org/10.1016/j.actamat.2009.04.004.

(87) Rogge, S. M. J.; Waroquier, M.; Van Speybroeck, V. Reliably Modeling the Mechanical Stability of Rigid and Flexible Metal–Organic Frameworks. *Acc. Chem. Res.* **2017**, acs.accounts.7b00404. https://doi.org/10.1021/acs.accounts.7b00404.

(88) Zhu, Q.-L.; Xu, Q. Metal–Organic Framework Composites. *Chem. Soc. Rev.* **2014**, *43* (16), 5468–5512. https://doi.org/10.1039/C3CS60472A.

(89) Li, S.; Huo, F. Metal–Organic Framework Composites: From Fundamentals to Applications. *Nanoscale* **2015**, *7* (17), 7482–7501. https://doi.org/10.1039/C5NR00518C.

(90) Majewski, M. B.; Howarth, A. J.; Li, P.; Wasielewski, M. R.; Hupp, J. T.; Farha, O. K. Enzyme Encapsulation in Metal–Organic Frameworks for Applications in Catalysis. *CrystEngComm* **2017**, *19* (29), 4082–4091.

https://doi.org/10.1039/C7CE00022G.

(91) Yu, J.; Mu, C.; Yan, B.; Qin, X.; Shen, C.; Xue, H.; Pang, H. Nanoparticle/MOF Composites: Preparations and Applications. *Mater. Horizons* **2017**, *4* (4), 557–569. https://doi.org/10.1039/C6MH00586A.

(92) Kitao, T.; Zhang, Y.; Kitagawa, S.; Wang, B.; Uemura, T. Hybridization of MOFs and Polymers. *Chem. Soc. Rev.* **2017**, *46* (11), 3108–3133. https://doi.org/10.1039/C7CS00041C.

(93) Li, G.; Zhao, S.; Zhang, Y.; Tang, Z. Metal-Organic Frameworks Encapsulating Active Nanoparticles as Emerging Composites for Catalysis: Recent Progress and Perspectives. *Adv. Mater.* **2018**, *1800702,* 1800702. https://doi.org/10.1002/adma.201800702.

(94) Lisovskii, A. F. Thermodynamics of the Formation of Gradient Structures in Nanodispersed Composite Materials. *J. Superhard Mater.* **2009**, *31* (4), 226–231. https://doi.org/10.3103/S1063457609040030.

(95) Web of Science http://apps.webofknowledge.com (accessed Sep 14, 2018).

(96) Hermes, S.; Schröter, M.-K.; Schmid, R.; Khodeir, L.; Muhler, M.; Tissler, A.; Fischer, R. W.; Fischer, R. A. Metal@MOF: Loading of Highly Porous Coordination Polymers Host Lattices by Metal Organic Chemical Vapor Deposition. *Angew. Chemie Int. Ed.* **2005**, *44* (38), 6237–6241. https://doi.org/10.1002/anie.200462515.

(97) Müller, M.; Hermes, S.; Kähler, K.; van den Berg, M. W. E.; Muhler, M.; Fischer, R. a. Loading of MOF-5 with Cu and ZnO Nanoparticles by Gas-Phase Infiltration with Organometallic Precursors: Properties of Cu/ZnO@MOF-5 as Catalyst for Methanol Synthesis. *Chem. Mater.* **2008**, *20* (14), 4576–4587. https://doi.org/10.1021/cm703339h.

(98) Hermes, S.; Schröder, F.; Amirjalayer, S.; Schmid, R.; Fischer, R. A. Loading of Porous Metal–Organic Open Frameworks with Organometallic CVD Precursors: Inclusion Compounds of the Type [L n M] a @MOF-5. *J. Mater. Chem.* **2006**, *16* (25), 2464–2472. https://doi.org/10.1039/B603664C.

(99) Müller, M.; Zhang, X.; Wang, Y.; Fischer, R. A. Nanometer-Sized Titania Hosted inside MOF-5. *Chem. Commun.* **2009**, *5* (1), 119–121. https://doi.org/10.1039/B814241F.

(100) Kim, C. R.; Uemura, T.; Kitagawa, S. Inorganic Nanoparticles in Porous Coordination Polymers. *Chem. Soc. Rev.* **2016**, *45* (14), 3828–3845. https://doi.org/10.1039/c5cs00940e.

(101) Uemura, T.; Yanai, N.; Kitagawa, S. Polymerization Reactions in Porous Coordination Polymers. *Chem. Soc. Rev.* **2009**, *38* (5), 1228–1236. https://doi.org/10.1039/b802583p.

(102) Yu, R.; Kuang, X. F.; Wu, X. Y.; Lu, C. Z.; Donahue, J. P. Stabilization and Immobilization of Polyoxometalates in Porous Coordination Polymers through Host-Guest Interactions. *Coord. Chem. Rev.* **2009**, *253* (23–24), 2872–2890. https://doi.org/10.1016/j.ccr.2009.07.003.

(103) Alkordi, M. H.; Liu, Y.; Larsen, R. W.; Eubank, J. F.; Eddaoudi, M. Zeolite- like Metal−Organic Frameworks as Platforms for Applications: On Metalloporphyrin-Based Catalysts. *J. Am. Chem. Soc.* **2008**, *130* (38), 12639–12641. https://doi.org/10.1021/ja804703w.

(104) Li, Y.; Xu, H.; Ouyang, S.; Ye, J. Metal–Organic Frameworks for Photocatalysis. *Phys. Chem. Chem. Phys.* **2016**, *18* (11), 7563–7572. https://doi.org/10.1039/C5CP05885F.

(105) Allendorf, M. D.; Bauer, C. A.; Bhakta, R. K.; Houk, R. J. T. Luminescent Metal-Organic Frameworks. *Chem. Soc. Rev.* **2009**, *38* (5), 1330–1352. https://doi.org/10.1039/b802352m.

(106) Medishetty, R.; Zaręba, J. K.; Mayer, D.; Samoć, M.; Fischer, R. A. Nonlinear Optical Properties, Upconversion and Lasing in Metal-Organic Frameworks. *Chem. Soc. Rev.* **2017**, *46* (16), 4976–5004. https://doi.org/10.1039/c7cs00162b.

(107) Cui, Y.; Yue, Y.; Qian, G.; Chen, B. Luminescent Functional Metal–Organic Frameworks. *Chem. Rev.* **2012**, *112* (2), 1126–1162. https://doi.org/10.1021/cr200101d.

(108) Stassen, I.; Burtch, N.; Talin, A.; Falcaro, P.; Allendorf, M.; Ameloot, R. An Updated Roadmap for the Integration of Metal–Organic Frameworks with Electronic Devices and Chemical Sensors. *Chem. Soc. Rev.* **2017**, *46* (11), 3185–3241. https://doi.org/10.1039/C7CS00122C.

(109) Uemura, T.; Horike, S.; Kitagawa, S. Polymerization in Coordination Nanospaces. *Chem. - An Asian J.* **2006**, *1* (1–2), 36–44. https://doi.org/10.1002/asia.200600074.

(110) Mochizuki, S.; Ogiwara, N.; Takayanagi, M.; Nagaoka, M.; Kitagawa, S.; Uemura, T. Sequence-Regulated Copolymerization Based on Periodic Covalent Positioning of Monomers along One-Dimensional Nanochannels. *Nat. Commun.* **2018**, *9* (1). https://doi.org/10.1038/s41467-017-02736-1.

(111) Uemura, T.; Ono, Y.; Kitagawa, K.; Kitagawa, S. Radical Polymerization of Vinyl Monomers in Porous Coordination Polymers: Nanochannel Size Effects on Reactivity, Molecular Weight, and Stereostructure. *Macromolecules* **2008**, *41* (1), 87–94. https://doi.org/10.1021/ma7022217.

(112) Malonzo, C. D.; Wang, Z.; Duan, J.; Zhao, W.; Webber, T. E.; Li, Z.; Kim, I. S.; Kumar, A.; Bhan, A.; Platero-Prats, A. E.; et al. Application and Limitations of Nanocasting in Metal–Organic Frameworks. *Inorg. Chem.* **2018**, *57* (5), 2782–2790. https://doi.org/10.1021/acs.inorgchem.7b03181.

(113) Malonzo, C. D.; Shaker, S. M.; Ren, L.; Prinslow, S. D.; Platero-Prats, A. E.; Gallington, L. C.; Borycz, J.; Thompson, A. B.; Wang, T. C.; Farha, O. K.; et al. Thermal Stabilization of Metal–Organic Framework-Derived Single-Site Catalytic Clusters through Nanocasting. *J. Am. Chem. Soc.* **2016**, *138* (8), 2739–2748. https://doi.org/10.1021/jacs.5b12688.

(114) Wang, T.; Farajollahi, M.; Henke, S.; Zhu, T.; Bajpe, S. R.; Sun, S.; Barnard, J. S.; Lee, J. S.; Madden, J. D. W.; Cheetham, A. K.; et al. Functional Conductive Nanomaterials via Polymerisation in Nano-Channels: PEDOT in a MOF. *Mater. Horizons* **2017**, *4* (1), 64–71. https://doi.org/10.1039/C6MH00230G.

(115) Kobayashi, Y.; Honjo, K.; Kitagawa, S.; Uemura, T. Preparation of Porous Polysaccharides Templated by Coordination Polymer with Three-Dimensional Nanochannels. *ACS Appl. Mater. Interfaces* **2017**, *9* (13), 11373–11379.

https://doi.org/10.1021/acsami.6b15936.

(116) Kitao, T.; MacLean, M. W. A.; Le Ouay, B.; Sasaki, Y.; Tsujimoto, M.; Kitagawa, S.; Uemura, T. Preparation of Polythiophene Microrods with Ordered Chain Alignment Using Nanoporous Coordination Template. *Polym. Chem.* **2017**, *8* (34), 5077–5081. https://doi.org/10.1039/C7PY00309A.

(117) Sun, J.-K.; Xu, Q. Functional Materials Derived from Open Framework Templates/Precursors: Synthesis and Applications. *Energy Environ. Sci.* **2014**, *7* (7), 2071–2100. https://doi.org/10.1039/c4ee00517a.

(118) Yang, Y.; Yang, F.; Sun, C.-J.; Zhao, H.; Hao, S.; Brown, D. E.; Zhang, J.; Ren, Y. Ru–Fe Alloy Mediated α-Fe 2 O 3 Particles on Mesoporous Carbon Nanofibers as Electrode Materials with Superior Capacitive Performance. *RSC Adv.* **2017**, *7* (12), 6818–6826. https://doi.org/10.1039/C6RA27324F.

(119) Salunkhe, R. R.; Kamachi, Y.; Torad, N. L.; Hwang, S. M.; Sun, Z.; Dou, S. X.; Kim, J. H.; Yamauchi, Y. Fabrication of Symmetric Supercapacitors Based on MOF-Derived Nanoporous Carbons. *J. Mater. Chem. A* **2014**, *2* (46), 19848–19854. https://doi.org/10.1039/C4TA04277H.

(120) Yang, S. J.; Kim, T.; Im, J. H.; Kim, Y. S.; Lee, K.; Jung, H.; Park, C. R. MOF-Derived Hierarchically Porous Carbon with Exceptional Porosity and Hydrogen Storage Capacity. *Chem. Mater.* **2012**, *24* (3), 464–470. https://doi.org/10.1021/cm202554j.

(121) Salunkhe, R. R.; Kaneti, Y. V.; Kim, J.; Kim, J. H.; Yamauchi, Y. Nanoarchitectures for Metal–Organic Framework-Derived Nanoporous Carbons toward Supercapacitor Applications. *Acc. Chem. Res.* **2016**, *49* (12), 2796–2806. https://doi.org/10.1021/acs.accounts.6b00460.

(122) Wang, T.; Kim, H.; Liu, Y.; Li, W.; Griffiths, J. T.; Wu, Y.; Laha, S.; Fong, K. D.; Podjaski, F.; Yun, C.; et al. Bottom-up Formation of Carbon-Based Structures with Multilevel Hierarchy from MOF–Guest Polyhedra. *J. Am. Chem. Soc.* **2018**, *140* (19), 6130–6136. https://doi.org/10.1021/jacs.8b02411.

(123) Chen, L.; Luque, R.; Li, Y. Encapsulation of Metal Nanostructures into Metal–Organic Frameworks. *Dalt. Trans.* **2018**, *47* (11), 3663–3668.

https://doi.org/10.1039/C8DT00092A.

(124) Chen, L.; Chen, H.; Luque, R.; Li, Y. Metal−organic Framework Encapsulated Pd Nanoparticles: Towards Advanced Heterogeneous Catalysts. *Chem. Sci.* **2014**, *5* (10), 3708–3714. https://doi.org/10.1039/C4SC01847H.

(125) Rimoldi, M.; Bernales, V.; Borycz, J.; Vjunov, A.; Gallington, L. C.; Platero-Prats, A. E.; Kim, I. S.; Fulton, J. L.; Martinson, A. B. F.; Lercher, J. A.; et al. Atomic Layer Deposition in a Metal-Organic Framework: Synthesis, Characterization, and Performance of a Solid Acid. *Chem. Mater.* **2017**, *29* (3), 1058–1068. https://doi.org/10.1021/acs.chemmater.6b03880.

(126) Li, Z.; Rayder, T. M.; Luo, L.; Byers, J. A.; Tsung, C.-K. Aperture-Opening Encapsulation of a Transition Metal Catalyst in a Metal–Organic Framework for CO $_2$ Hydrogenation. *J. Am. Chem. Soc.* **2018**, *140* (26), 8082–8085. https://doi.org/10.1021/jacs.8b04047.

(127) Morabito, J. V.; Chou, L. Y.; Li, Z.; Manna, C. M.; Petroff, C. A.; Kyada, R. J.; Palomba, J. M.; Byers, J. A.; Tsung, C. K. Molecular Encapsulation beyond the Aperture Size Limit through Dissociative Linker Exchange in Metal-Organic Framework Crystals. *J. Am. Chem. Soc.* **2014**, *136* (36), 12540–12543. https://doi.org/10.1021/ja5054779.

(128) Szilágyi, P. Á.; Rogers, D. M.; Zaiser, I.; Callini, E.; Turner, S.; Borgschulte, A.; Züttel, A.; Geerlings, H.; Hirscher, M.; Dam, B. Functionalised Metal–Organic Frameworks: A Novel Approach to Stabilising Single Metal Atoms. *J. Mater. Chem. A* **2017**, *5* (30), 15559–15566. https://doi.org/10.1039/C7TA03134C.

(129) Hwang, Y. K.; Hong, D.-Y.; Chang, J.-S.; Jhung, S. H.; Seo, Y.-K.; Kim, J.; Vimont, A.; Daturi, M.; Serre, C.; Férey, G. Amine Grafting on Coordinatively Unsaturated Metal Centers of MOFs: Consequences for Catalysis and Metal Encapsulation. *Angew. Chemie Int. Ed.* **2008**, *47* (22), 4144–4148. https://doi.org/10.1002/anie.200705998.

(130) Wei, Y.; Han, S.; Walker, D. A.; Fuller, P. E.; Grzybowski, B. A. Nanoparticle Core/Shell Architectures within MOF Crystals Synthesized by Reaction Diffusion. *Angew. Chemie Int. Ed.* **2012**, *51* (30), 7435–7439.

https://doi.org/10.1002/anie.201202549.

(131) Fortea-Pérez, F. R.; Mon, M.; Ferrando-Soria, J.; Boronat, M.; Leyva-Pérez, A.; Corma, A.; Herrera, J. M.; Osadchii, D.; Gascon, J.; Armentano, D.; et al. The MOF-Driven Synthesis of Supported Palladium Clusters with Catalytic Activity for Carbene-Mediated Chemistry. *Nat. Mater.* **2017**, *16* (7), 760–766. https://doi.org/10.1038/nmat4910.

(132) Sun, C.; Liu, S.; Liang, D.; Shao, K.; Ren, Y.; Su, Z. Highly Stable Crystalline Catalysts Based on a Microporous Metal−Organic Framework and Polyoxometalates. *J. Am. Chem. Soc.* **2009**, *131* (5), 1883–1888. https://doi.org/10.1021/ja807357r.

(133) Xia, B. Y.; Yan, Y.; Li, N.; Wu, H. Bin; Lou, X. W. D.; Wang, X. A Metal–Organic Framework-Derived Bifunctional Oxygen Electrocatalyst. *Nat. Energy* **2016**, *1* (1), 15006. https://doi.org/10.1038/nenergy.2015.6.

(134) Turner, S.; Lebedev, O. I.; Schröder, F.; Esken, D.; Fischer, R. A.; Tendeloo, G. Van. Direct Imaging of Loaded Metal−Organic Framework Materials (Metal@MOF-5). *Chem. Mater.* **2008**, *20* (17), 5622–5627. https://doi.org/10.1021/cm801165s.

(135) Stock, N.; Biswas, S. Synthesis of Metal-Organic Frameworks (MOFs): Routes to Various MOF Topologies, Morphologies, and Composites. *Chem. Rev.* **2012**, *112* (2), 933–969. https://doi.org/10.1021/cr200304e.

(136) Choi, E.-Y.; Park, K.; Yang, C.-M.; Kim, H.; Son, J.-H.; Lee, S. W.; Lee, Y. H.; Min, D.; Kwon, Y.-U. Benzene-Templated Hydrothermal Synthesis of Metal-Organic Frameworks with Selective Sorption Properties. *Chem. - A Eur. J.* **2004**, *10* (21), 5535–5540. https://doi.org/10.1002/chem.200400178.

(137) Liu, Y.; Kravtsov, V. C.; Larsen, R.; Eddaoudi, M. Molecular Building Blocks Approach to the Assembly of Zeolite-like Metal–Organic Frameworks (ZMOFs) with Extra-Large Cavities. *Chem. Commun.* **2006**, No. 14, 1488. https://doi.org/10.1039/b600188m.

(138) Uemura, T.; Hoshino, Y.; Kitagawa, S.; Yoshida, K.; Isoda, S. Effect of Organic Polymer Additive on Crystallization of Porous Coordination Polymer. *Chem. Mater.*

2006, *18* (4), 992–995. https://doi.org/10.1021/cm052427g.

(139) Tsuruoka, T.; Furukawa, S.; Takashima, Y.; Yoshida, K.; Isoda, S.; Kitagawa, S. Nanoporous Nanorods Fabricated by Coordination Modulation and Oriented Attachment Growth. *Angew. Chemie Int. Ed.* **2009**, *48* (26), 4739–4743. https://doi.org/10.1002/anie.200901177.

(140) Tranchemontagne, D. J.; Hunt, J. R.; Yaghi, O. M. Room Temperature Synthesis of Metal-Organic Frameworks: MOF-5, MOF-74, MOF-177, MOF-199, and IRMOF-0. *Tetrahedron* **2008**, *64* (36), 8553–8557. https://doi.org/10.1016/j.tet.2008.06.036.

(141) Huang, L. Synthesis, Morphology Control, and Properties of Porous Metal–Organic Coordination Polymers. *Microporous Mesoporous Mater.* **2003**, *58* (2), 105–114. https://doi.org/10.1016/S1387-1811(02)00609-1.

(142) Cravillon, J.; Münzer, S.; Lohmeier, S.-J.; Feldhoff, A.; Huber, K.; Wiebcke, M. Rapid Room-Temperature Synthesis and Characterization of Nanocrystals of a Prototypical Zeolitic Imidazolate Framework. *Chem. Mater.* **2009**, *21* (8), 1410–1412. https://doi.org/10.1021/cm900166h.

(143) Mondloch, J. E.; Karagiaridi, O.; Farha, O. K.; Hupp, J. T. Activation of Metal-Organic Framework Materials. *CrystEngComm* **2013**, *15* (45), 9258–9264. https://doi.org/10.1039/c3ce41232f.

(144) DoITPoMS. X-ray Diffraction Techniques https://www.doitpoms.ac.uk/tlplib/xray-diffraction/index.php (accessed May 2, 2019).

(145) Cullity, B. D. *Elements of X-Ray Diffraction*, Second edi.; Addison-Wesley Publishing Company, Inc.: Reading, MA, 1978.

(146) Vickers, M. E. Introduction to X-Ray Diffraction. Cambridge, United Kingdom 2018.

(147) Clegg, W.; Blake, A. J.; Cole, J. M.; Evans, J. S. O.; Main, P.; Parsons, S.; Watkin, D. J. *Crystal Structure Analysis*; Clegg, W., Blake, A. J., Cole, J. M., Evans, J. S. O., Main, P., Parsons, S., Watkin, D. J., Eds.; Oxford University Press: Oxford, 2009. https://doi.org/10.1093/acprof:oso/9780199219469.001.0001.

(148) Coats, A. W.; Redfern, J. P. Thermogravimetric Analysis. A Review. *Analyst* **1963**,

88 (1053), 906. https://doi.org/10.1039/an9638800906.

(149) Anovitz, L. M.; Cole, D. R. Characterization and Analysis of Porosity and Pore Structures. *Rev. Mineral. Geochemistry* **2015**, *80* (1), 61–164. https://doi.org/10.2138/rmg.2015.80.04.

(150) Sing, K. S. W.; Everett, D. H.; Haul, R. A. W.; Moscou, L.; Pierotti, R. A.; Rouquerol, J.; Siemieniewska, T. Reporting Physisorption Data for Gas/Solid Systems with Special Reference to the Determination of Surface Area and Porosity (Recommendations 1984). *Pure Appl. Chem.* **1985**, *57* (4), 603–619. https://doi.org/10.1351/pac198557040603.

(151) Kruk, M.; Jaroniec, M. Gas Adsorption Characterization of Ordered Organic−Inorganic Nanocomposite Materials. *Chem. Mater.* **2001**, *13* (10), 3169–3183. https://doi.org/10.1021/cm0101069.

(152) Brunauer, S.; Emmett, P. H.; Teller, E. Adsorption of Gases in Multimolecular Layers. *J. Am. Chem. Soc.* **1938**, *60* (2), 309–319. https://doi.org/10.1021/ja01269a023.

(153) Ismail, I. M. K. Cross-Sectional Areas of Adsorbed N2 , Ar , Kr , and 0 2 on Carbons and Fumed Silicas at Liquid Nitrogen Temperature. *Langmuir* **1992**, *8* (2), 360–365. https://doi.org/10.1021/la00038a006.

(154) Barrett, E. P.; Joyner, L. G.; Halenda, P. P. The Determination of Pore Volume and Area Distributions in Porous Substances. I. Computations from Nitrogen Isotherms. *J. Am. Chem. Soc.* **1951**, *73* (1), 373–380. https://doi.org/10.1021/ja01145a126.

(155) Do, D. D.; Do, H. D. Pore Characterization of Carbonaceous Materials by DFT and GCMC Simulations: A Review. *Adsorpt. Sci. Technol.* **2003**, *21* (5), 389–423. https://doi.org/10.1260/026361703769645753.

(156) Siegbahn, K. Electron Spectroscopy for Chemical Analysis (E.S.C.A.). *Philos. Trans. R. Soc. A Math. Phys. Eng. Sci.* **1970**, *268* (1184), 33–57. https://doi.org/10.1098/rsta.1970.0060.

(157) Hollander, J. M.; Jolly, W. L. X-Ray Photoelectron Spectroscopy. *Acc. Chem. Res.* **1970**, *3* (6), 193–200. https://doi.org/10.1021/ar50030a003.

(158) Guo, T. More Power to X-Rays: New Developments in X-Ray Spectroscopy. *Laser Photonics Rev.* **2009**, *3* (6), 591–622. https://doi.org/10.1002/lpor.200810028.

(159) Goodhew, P. J.; Humphreys, J.; Beanland, R. *Electron Microscopy and Analysis*, Third Edit.; Taylor & Francis: London and New York, 2001.

(160) Urban, K. W. Studying Atomic Structures by Aberration-Corrected Transmission Electron Microscopy. *Science (80-.).* **2008**, *321* (5888), 506–510. https://doi.org/10.1126/science.1152800.

(161) Hagendorfer, H. New Analytical Methods for Size Fractionated, Quantitative, and Element Specific Analysis of Metallic Engineered Nanoparticles in Aerosols and Dispersions, École Polytechnique Fédérale de Lausanne, 2011. https://doi.org/10.5075/epfl-thesis-5202.

(162) Cazaux, J. Recent Developments and New Strategies in Scanning Electron Microscopy. *J. Microsc.* **2005**, *217* (1), 16–35. https://doi.org/10.1111/j.0022-2720.2005.01414.x.

(163) Muller, D. A. Structure and Bonding at the Atomic Scale by Scanning Transmission Electron Microscopy. *Nat. Mater.* **2009**, *8* (4), 263–270. https://doi.org/10.1038/nmat2380.

(164) Zięba, P. Recent Progress in the Energy-Dispersive X-Ray Spectroscopy Microanalysis of the Discontinuous Precipitation and Discontinuous Dissolution Reactions. *Mater. Chem. Phys.* **2000**, *62* (3), 183–213. https://doi.org/10.1016/S0254-0584(99)00179-0.

(165) Thomas, J. M.; Williams, B. G.; Sparrow, T. G. Electron-Energy-Loss Spectroscopy and the Study of Solids. *Acc. Chem. Res.* **1985**, *18* (11), 324–330. https://doi.org/10.1021/ar00119a001.

(166) Joy, D. C.; Maher, D. M. Electron Energy-Loss Spectroscopy. *J. Phys. E.* **1980**, *13* (3), 260–270. https://doi.org/10.1088/0022-3735/13/3/001.

(167) Richardson, N. V. High Resolution Electron Energy Loss Spectroscopy. *Curr. Opin. Solid State Mater. Sci.* **1997**, *2* (5), 517–524. https://doi.org/10.1016/S1359-0286(97)80039-3.

(168) Erskine, J. L. High-Resolution Electron Energy Loss Spectroscopy. *Crit. Rev. Solid State Mater. Sci.* **1987**, *13* (4), 311–379. https://doi.org/10.1080/10408438708242181.

(169) Egerton, R. F. Electron Energy-Loss Spectroscopy in the TEM. *Reports Prog. Phys.* **2009**, *72* (1), 016502. https://doi.org/10.1088/0034-4885/72/1/016502.

(170) García De Abajo, F. J. Optical Excitations in Electron Microscopy. *Rev. Mod. Phys.* **2010**, *82* (1), 209–275. https://doi.org/10.1103/RevModPhys.82.209.

(171) Uemura, T.; Kaseda, T.; Sasaki, Y.; Inukai, M.; Toriyama, T.; Takahara, A.; Jinnai, H.; Kitagawa, S. Mixing of Immiscible Polymers Using Nanoporous Coordination Templates. *Nat. Commun.* **2015**, *6* (May), 7473. https://doi.org/10.1038/ncomms8473.

(172) Uemura, T. Polymer Synthesis in Coordination Nanospaces. *Bull. Chem. Soc. Jpn.* **2011**, *84* (11), 1169–1177. https://doi.org/10.1246/bcsj.20110211.

(173) Uemura, T.; Yanai, N.; Watanabe, S.; Tanaka, H.; Numaguchi, R.; Miyahara, M. T.; Ohta, Y.; Nagaoka, M.; Kitagawa, S. Unveiling Thermal Transitions of Polymers in Subnanometre Pores. *Nat. Commun.* **2010**, *1* (7), 1–8. https://doi.org/10.1038/ncomms1091.

(174) MacLean, M. W. A.; Kitao, T.; Suga, T.; Mizuno, M.; Seki, S.; Uemura, T.; Kitagawa, S. Unraveling Inter- and Intrachain Electronics in Polythiophene Assemblies Mediated by Coordination Nanospaces. *Angew. Chemie Int. Ed.* **2016**, *55* (2), 708–713. https://doi.org/10.1002/anie.201510084.

(175) Uemura, T.; Kitagawa, K.; Horike, S.; Kawamura, T.; Kitagawa, S.; Mizuno, M.; Endo, K. Radical Polymerisation of Styrene in Porous Coordination Polymers. *Chem. Commun. (Camb).* **2005**, No. 48, 5968–5970. https://doi.org/10.1039/b508588h.

(176) Uemura, T.; Hiramatsu, D.; Kubota, Y.; Takata, M.; Kitagawa, S. Topotactic Linear Radical Polymerization of Divinylbenzenes in Porous Coordination Polymers. *Angew. Chemie Int. Ed.* **2007**, *46* (26), 4987–4990. https://doi.org/10.1002/anie.200700242.

(177) Uemura, T.; Ono, Y.; Kitagawa, S. Radical Copolymerizations of Vinyl Monomers in a Porous Coordination Polymer. *Chem. Lett.* **2008**, *37* (6), 616–617. https://doi.org/10.1246/cl.2008.616.

(178) Uemura, T.; Horike, S.; Kitagawa, K.; Mizuno, M.; Endo, K.; Bracco, S.; Comotti, A.; Sozzani, P.; Nagaoka, M.; Kitagawa, S. Conformation and Molecular Dynamics of Single Polystyrene Chain Confined in Coordination Nanospace. *J. Am. Chem. Soc.* **2008**, *130*, 6781–6788. https://doi.org/10.1021/ja800087s.

(179) Uemura, T.; Ono, Y.; Hijikata, Y.; Kitagawa, S. Functionalization of Coordination Nanochannels for Controlling Tacticity in Radical Vinyl Polymerization. *J. Am. Chem. Soc.* **2010**, *132* (13), 4917–4924. https://doi.org/10.1021/ja100406k.

(180) Comotti, A.; Bracco, S.; Mauri, M.; Mottadelli, S.; Ben, T.; Qiu, S.; Sozzani, P. Confined Polymerization in Porous Organic Frameworks with an Ultrahigh Surface Area. *Angew. Chemie Int. Ed.* **2012**, *51* (40), 10136–10140. https://doi.org/10.1002/anie.201205618.

(181) Yanai, N.; Uemura, T.; Ohba, M.; Kadowaki, Y.; Maesato, M.; Takenaka, M.; Nishitsuji, S.; Hasegawa, H.; Kitagawa, S. Fabrication of Two-Dimensional Polymer Arrays: Template Synthesis of Polypyrrole between Redox-Active Coordination Nanoslits. *Angew. Chemie Int. Ed.* **2008**, *47* (51), 9883–9886. https://doi.org/10.1002/anie.200803846.

(182) Uemura, T.; Kadowaki, Y.; Yanai, N.; Kitagawa, S. Template Synthesis of Porous Polypyrrole in 3D Coordination Nanochannels. *Chem. Mater.* **2009**, *21* (18), 4096–4098. https://doi.org/10.1021/cm901361m.

(183) Uemura, T.; Uchida, N.; Asano, A.; Saeki, A.; Seki, S.; Tsujimoto, M.; Isoda, S.; Kitagawa, S. Highly Photoconducting π-Stacked Polymer Accommodated in Coordination Nanochannels. *J. Am. Chem. Soc.* **2012**, *134* (20), 8360–8363. https://doi.org/10.1021/ja301903x.

(184) Lu, C.; Ben, T.; Xu, S.; Qiu, S. Electrochemical Synthesis of a Microporous Conductive Polymer Based on a Metal-Organic Framework Thin Film. *Angew. Chemie Int. Ed.* **2014**, *53* (25), 6454–6458. https://doi.org/10.1002/anie.201402950.

(185) Kitao, T.; Bracco, S.; Comotti, A.; Sozzani, P.; Naito, M.; Seki, S.; Uemura, T.;

Kitagawa, S. Confinement of Single Polysilane Chains in Coordination Nanospaces. *J. Am. Chem. Soc.* **2015**, *137* (15), 5231–5238. https://doi.org/10.1021/jacs.5b02215.

(186) Bossi, A.; Piletsky, S. A.; Piletska, E. V; Righetti, P. G.; Turner, A. P. An Assay for Ascorbic Acid Based on Polyaniline-Coated Microplates. *Anal. Chem.* **2000**, *72* (18), 4296–4300. https://doi.org/10.1021/ac000185s.

(187) Mei, G.; Liming, D.; Gordon, G. W. Biosensors Based on Aligned Carbon Nanotubes Coated with Inherently Conducting Polymers. *Electroanalysis* **2003**, *15* (13), 1089–1094.

(188) Simon, P.; Gogotsi, Y. Materials for Electrochemical Capacitors. *Nat. Mater.* **2008**, *7* (11), 845–854. https://doi.org/10.1038/nmat2297.

(189) Winther-Jensen, B.; Winther-Jensen, O.; Forsyth, M.; MacFarlane, D. R. High Rates of Oxygen Reduction over a Vapor Phase-Polymerized PEDOT Electrode. *Science (80-.).* **2008**, *321* (5889), 671–674. https://doi.org/10.1126/science.1159267.

(190) Im, S. G.; Gleason, K. K. Systematic Control of the Electrical Conductivity of Poly (3, 4-Ethylenedioxythiophene) via Oxidative Chemical Vapor Deposition. *Macromolecules* **2007**, *40* (18), 6552–6556. https://doi.org/10.1021/ma0628477.

(191) Fong, K. D.; Wang, T.; Smoukov, S. K. Multidimensional Performance Optimization of Conducting Polymer-Based Supercapacitor Electrodes. *Sustain. Energy Fuels* **2017**, *1* (9), 1857–1874. https://doi.org/10.1039/C7SE00339K.

(192) Heywang, G.; Jonas, F.; Heinze, J.; Dietrich, M. New Polythiophene, Process for Their Production and Their Use. DE 3843412 A1, 1988.

(193) Fu, D.; Zhou, H.; Zhang, X.; Han, G.; Chang, Y. Flexible Solid–State Supercapacitor of Metal–Organic Framework Coated on Carbon Nanotube Film Interconnected by Electrochemically -Codeposited PEDOT-GO. *ChemistrySelect* **2016**, *1* (2), 285–289. https://doi.org/10.1002/slct.201600084.

(194) Yamada, M.; Ohnishi, N.; Watanabe, M.; Hino, Y. Prussian Blue Nanoparticles Protected by the Water-Soluble π-Conjugated Polymer PEDOT-S: Synthesis and Multiple-Color PH-Sensing with a Redox Reaction. *Chem. Commun.* **2009**, No. 46,

7203. https://doi.org/10.1039/b917552k.

(195) Le Ouay, B.; Boudot, M.; Kitao, T.; Yanagida, T.; Kitagawa, S.; Uemura, T. Nanostructuration of PEDOT in Porous Coordination Polymers for Tunable Porosity and Conductivity. *J. Am. Chem. Soc.* **2016**, *138* (32), 10088–10091. https://doi.org/10.1021/jacs.6b05552.

(196) Jonas, F.; Schrader, L. Conductive Modifications of Polymers with Polypyrroles and Polythiophenes. *Synth. Met.* **1991**, *41* (3), 831–836. https://doi.org/10.1016/0379-6779(91)91506-6.

(197) Corradi, R.; Armes, S. P. Chemical Synthesis of Poly(3,4-Ethylenedioxythiophene). *Synth. Met.* **1997**, *84* (1–3), 453–454. https://doi.org/10.1016/S0379-6779(97)80828-4.

(198) Niu, L.; Kvarnström, C.; Fröberg, K.; Ivaska, A. Electrochemically Controlled Surface Morphology and Crystallinity in Poly(3,4-Ethylenedioxythiophene) Films. *Synth. Met.* **2001**, *122* (2), 425–429. https://doi.org/10.1016/S0379-6779(00)00562-2.

(199) Nguyen, V.-Q.; Schaming, D.; Martin, P.; Lacroix, J.-C. Highly Resolved Nanostructured PEDOT on Large Areas by Nanosphere Lithography and Electrodeposition. *ACS Appl. Mater. Interfaces* **2015**, *7* (39), 21673–21681. https://doi.org/10.1021/acsami.5b06699.

(200) Fabretto, M.; Zuber, K.; Hall, C.; Murphy, P.; Griesser, H. J. The Role of Water in the Synthesis and Performance of Vapour Phase Polymerised PEDOT Electrochromic Devices. *J. Mater. Chem.* **2009**, *19* (42), 7871. https://doi.org/10.1039/b912324e.

(201) Yamamoto, T.; Abla, M. Synthesis of Non-Doped Poly(3,4-Ethylenedioxythiophene) and Its Spectroscopic Data. *Synth. Met.* **1999**, *100* (2), 237–239. https://doi.org/10.1016/S0379-6779(99)00005-3.

(202) Chun, H.; Dybtsev, D. N.; Kim, H.; Kim, K. Synthesis, X-Ray Crystal Structures, and Gas Sorption Properties of Pillared Square Grid Nets Based on Paddle-Wheel Motifs: Implications for Hydrogen Storage in Porous Materials. *Chem. - A Eur. J.* **2005**, *11* (12), 3521–3529. https://doi.org/10.1002/chem.200401201.

(203) Yanai, N.; Uemura, T.; Kosaka, W.; Matsuda, R.; Kodani, T.; Koh, M.; Kanemura, T.; Kitagawa, S. End-Functionalization of a Vinylidene Fluoride Oligomer in Coordination Nanochannels. *Dalt. Trans.* **2012**, *41* (14), 4195. https://doi.org/10.1039/c2dt11891b.

(204) Dybtsev, D. N.; Chun, H.; Kim, K. Rigid and Flexible: A Highly Porous Metal-Organic Framework with Unusual Guest-Dependent Dynamic Behavior. *Angew. Chemie - Int. Ed.* **2004**, *43* (38), 5033–5036. https://doi.org/10.1002/anie.200460712.

(205) Uemura, K.; Yamasaki, Y.; Komagawa, Y.; Tanaka, K.; Kita, H. Two-Step Adsorption/Desorption on a Jungle-Gym-Type Porous Coordination Polymer. *Angew. Chemie Int. Ed.* **2007**, *46* (35), 6662–6665. https://doi.org/10.1002/anie.200702390.

(206) Henke, S.; Li, W.; Cheetham, A. K. Guest-Dependent Mechanical Anisotropy in Pillared-Layered Soft Porous Crystals – a Nanoindentation Study. *Chem. Sci.* **2014**, 2392–2397. https://doi.org/10.1039/c4sc00497c.

(207) Sun, S.; Henke, S.; Wharmby, M. T.; Yeung, H. H. M.; Li, W.; Cheetham, A. K. Mechanical Properties of a Calcium Dietary Supplement, Calcium Fumarate Trihydrate. *Inorg. Chem.* **2015**, *54* (23), 11186–11192. https://doi.org/10.1021/acs.inorgchem.5b01466.

(208) Oliver, W. C.; Pharr, G. M. An Improved Technique for Determining Hardness and Elastic Modulus Using Load and Displacement Sensing Indentation Experiments. *J. Mater. Res.* **1992**, *7* (06), 1564–1583. https://doi.org/10.1557/JMR.1992.1564.

(209) Yamaura, M.; Hagiwara, T.; Iwata, K. Enhancement of Electrical Conductivity of Polypyrrole Film by Stretching: Counter Ion Effect. *Synth. Met.* **1988**, *26* (3), 209–224. https://doi.org/10.1016/0379-6779(88)90238-X.

(210) Shoa, T.; Madden, J. D. W.; Mirfakhrai, T.; Alici, G.; Spinks, G. M.; Wallace, G. G. Electromechanical Coupling in Polypyrrole Sensors and Actuators. *Sensors Actuators A Phys.* **2010**, *161* (1–2), 127–133. https://doi.org/10.1016/j.sna.2010.04.024.

(211) Han, G.; Liu, Y.; Kan, E.; Tang, J.; Zhang, L.; Wang, H.; Tang, W. Sandwich-

Structured MnO2/Polypyrrole/Reduced Graphene Oxide Hybrid Composites for High-Performance Supercapacitors. *RSC Adv.* **2014**, *4* (20), 9898–9904. https://doi.org/10.1039/c3ra47764a.

(212) Henke, S.; Schneemann, A.; Wütscher, A.; Fischer, R. A. Directing the Breathing Behavior of Pillared-Layered Metal–Organic Frameworks via a Systematic Library of Functionalized Linkers Bearing Flexible Substituents. *J. Am. Chem. Soc.* **2012**, *134* (22), 9464–9474. https://doi.org/10.1021/ja302991b.

(213) Tan, K.; Nijem, N.; Canepa, P.; Gong, Q.; Li, J.; Thonhauser, T.; Chabal, Y. J. Stability and Hydrolyzation of Metal Organic Frameworks with Paddle-Wheel SBUs upon Hydration. *Chem. Mater.* **2012**, *24* (16), 3153–3167. https://doi.org/10.1021/cm301427w.

(214) Arenas, J. F.; Marcos, J. I. Infrared and Raman Spectra of Phtalate, Isophtalate and Terephtalate Ions. *Spectrochim. Acta Part A Mol. Spectrosc.* **1979**, *35* (4), 355–363. https://doi.org/10.1016/0584-8539(79)80191-9.

(215) Selvaganesh, S. V.; Mathiyarasu, J.; Phani, K. L. N.; Yegnaraman, V. Chemical Synthesis of PEDOT–Au Nanocomposite. *Nanoscale Res. Lett.* **2007**, *2* (11), 546–549. https://doi.org/10.1007/s11671-007-9100-6.

(216) Lisowska-Oleksiak, A.; Nowak, A. P.; Wilamowska, M.; Sikora, M.; Szczerba, W.; Kapusta, C. Ex Situ XANES, XPS and Raman Studies of Poly(3,4-Ethylenedioxythiophene) Modified by Iron Hexacyanoferrate. *Synth. Met.* **2010**, *160* (11–12), 1234–1240. https://doi.org/10.1016/j.synthmet.2010.03.015.

(217) Guzonas, D. A.; Irish, D. E. A Raman and Infrared Spectroscopic Study of Triethylenediamine (DABCO) and Its Protonated Forms. *Can. J. Chem.* **1988**, *66* (5), 1249–1257. https://doi.org/10.1139/v88-203.

(218) Uemura, T.; Kaseda, T.; Kitagawa, S. Controlled Synthesis of Anisotropic Polymer Particles Templated by Porous Coordination Polymers. *Chem. Mater.* **2013**, *25* (18), 3772–3776. https://doi.org/10.1021/cm4025843.

(219) Distefano, G.; Suzuki, H.; Tsujimoto, M.; Isoda, S.; Bracco, S.; Comotti, A.; Sozzani, P.; Uemura, T.; Kitagawa, S. Highly Ordered Alignment of a Vinyl Polymer by Host-Guest Cross-Polymerization. *Nat. Chem.* **2013**, *5* (4), 335–341.

https://doi.org/10.1038/nchem.1576.

(220) Guo, J.; Xu, Y.; Jin, S.; Chen, L.; Kaji, T.; Honsho, Y.; Addicoat, M. A.; Kim, J.; Saeki, A.; Ihee, H.; et al. Conjugated Organic Framework with Three-Dimensionally Ordered Stable Structure and Delocalized π Clouds. *Nat. Commun.* **2013**, *4* (1), 2736. https://doi.org/10.1038/ncomms3736.

(221) Winther-Jensen, B.; West, K. Vapor-Phase Polymerization of 3,4-Ethylenedioxythiophene: A Route to Highly Conducting Polymer Surface Layers. *Macromolecules* **2004**, *37* (12), 4538–4543. https://doi.org/10.1021/ma049864l.

(222) Sun, L.; Miyakai, T.; Seki, S.; Dincă, M. Mn2(2,5-Disulfhydrylbenzene-1,4-Dicarboxylate): A Microporous Metal-Organic Framework with Infinite (-Mn-S-)∞ Chains and High Intrinsic Charge Mobility. *J. Am. Chem. Soc.* **2013**, *135* (22), 8185–8188. https://doi.org/10.1021/ja4037516.

(223) Sheberla, D.; Sun, L.; Blood-Forsythe, M. A.; Er, S.; Wade, C. R.; Brozek, C. K.; Aspuru-Guzik, A.; Dincă, M. High Electrical Conductivity in Ni3(2,3,6,7,10,11-Hexaiminotriphenylene)2, a Semiconducting Metal-Organic Graphene Analogue. *J. Am. Chem. Soc.* **2014**, *136* (25), 8859–8862. https://doi.org/10.1021/ja502765n.

(224) Talin, A. A.; Centrone, A.; Ford, A. C.; Foster, M. E.; Stavila, V.; Haney, P.; Kinney, R. A.; Szalai, V.; El Gabaly, F.; Yoon, H. P.; et al. Tunable Electrical Conductivity in Metal-Organic Framework Thin-Film Devices. *Science (80-.).* **2014**, *343* (6166), 66–69. https://doi.org/10.1126/science.1246738.

(225) Nie, X.; Kulkarni, A.; Sholl, D. S. Computational Prediction of Metal Organic Frameworks Suitable for Molecular Infiltration as a Route to Development of Conductive Materials. *J. Phys. Chem. Lett.* **2015**, *6* (9), 1586–1591. https://doi.org/10.1021/acs.jpclett.5b00298.

(226) Aubrey, M. L.; Wiers, B. M.; Andrews, S. C.; Sakurai, T.; Reyes-Lillo, S. E.; Hamed, S. M.; Yu, C. J.; Darago, L. E.; Mason, J. A.; Baeg, J. O.; et al. Electron Delocalization and Charge Mobility as a Function of Reduction in a Metal-Organic Framework. *Nat. Mater.* **2018**, *17* (7), 625–632. https://doi.org/10.1038/s41563-018-0098-1.

(227) Petrov, V. I. Cathodoluminescence Scanning Microscopy. *Phys. Status Solidi* **1992**,

133 (2), 189–230. https://doi.org/10.1002/pssa.2211330202.

(228) Valeur, B. *Molecular Fluorescence*, 1st ed.; Wiley-VCH Verlag GmbH: Weinheim, FRG, 2001. https://doi.org/10.1002/3527600248.

(229) Bischak, C. G.; Hetherington, C. L.; Wang, Z.; Precht, J. T.; Kaz, D. M.; Schlom, D. G.; Ginsberg, N. S. Cathodoluminescence-Activated Nanoimaging: Noninvasive Near-Field Optical Microscopy in an Electron Microscope. *Nano Lett.* **2015**, *15* (5), 3383–3390. https://doi.org/10.1021/acs.nanolett.5b00716.

(230) Houk, R. J. T.; Jacobs, B. W.; Gabaly, F. El; Chang, N. N.; Talin, A. A.; Graham, D. D.; House, S. D.; Robertson, I. M.; Allendorf, M. D. Silver Cluster Formation, Dynamics, and Chemistry in Metal−Organic Frameworks. *Nano Lett.* **2009**, *9* (10), 3413–3418. https://doi.org/10.1021/nl901397k.

(231) Martin, D. C.; Wu, J.; Shaw, C. M.; King, Z.; Spanninga, S. A.; Richardson-Burns, S.; Hendricks, J.; Yang, J. The Morphology of Poly(3,4-Ethylenedioxythiophene). *Polym. Rev.* **2010**, *50* (3), 340–384. https://doi.org/10.1080/15583724.2010.495440.

(232) Szilágyi, P. A.; Callini, E.; Anastasopol, A.; Kwakernaak, C.; Sachdeva, S.; Van De Krol, R.; Geerlings, H.; Borgschulte, A.; Züttel, A.; Dam, B. Probing Hydrogen Spillover in Pd@MIL-101(Cr) with a Focus on Hydrogen Chemisorption. *Phys. Chem. Chem. Phys.* **2014**, *16* (12), 5803–5809. https://doi.org/10.1039/c3cp54898h.

(233) Liu, R.; Duay, J.; Lee, S. B. Redox Exchange Induced MnO 2 Electrochemical Energy Storage. *ACS Nano* **2010**, *4* (7), 4299–4307. https://doi.org/10.1021/nn1010182.

(234) Herron, N. A Cobalt Oxygen Carrier in Zeolite Y. A Molecular “Ship in a Bottle.” *Inorg. Chem.* **1986**, *25* (26), 4714–4717. https://doi.org/10.1021/ic00246a025.

(235) Revie, R. W.; Uhlig, H. H. *Corrosion and Corrosion Control: An Introduction to Corrosion Science and Engineering*; John Wiley & Sons, Inc.: Hoboken New Jersey, 2008. https://doi.org/10.1002/9780470277270.

(236) Pourbaix, M. *Atlas of Electrochemical Equilibria in Aqueous Solutions*, 1st Englis.; Pergamon Press: Oxford, United Kingdom, 1966.

(237) Campbell, J. A.; Whiteker, R. A. A Periodic Table Based on Potential-PH

Diagrams. *J. Chem. Educ.* **1969**, *46* (2), 90. https://doi.org/10.1021/ed046p90.

(238) Povar, I.; Spinu, O. Ruthenium Redox Equilibria: 3. Pourbaix Diagrams for the Systems Ru-H2O and Ru-Cl--H2O. *J. Electrochem. Sci. Eng.* **2016**, *6* (1), 145. https://doi.org/10.5599/jese.229.

(239) Wills, L. A.; Qu, X.; Chang, I.-Y.; Mustard, T. J. L.; Keszler, D. A.; Persson, K. A.; Cheong, P. H.-Y. Group Additivity-Pourbaix Diagrams Advocate Thermodynamically Stable Nanoscale Clusters in Aqueous Environments. *Nat. Commun.* **2017**, *8* (May), 15852. https://doi.org/10.1038/ncomms15852.

(240) Exner, K. S.; Over, H. Kinetics of Electrocatalytic Reactions from First-Principles: A Critical Comparison with the Ab Initio Thermodynamics Approach. *Acc. Chem. Res.* **2017**, *50* (5), 1240–1247. https://doi.org/10.1021/acs.accounts.7b00077.

(241) Polarz, S.; Kuschel, A. Chemistry in Confining Reaction Fields with Special Emphasis on Nanoporous Materials. *Chem. - A Eur. J.* **2008**, *14* (32), 9816–9829. https://doi.org/10.1002/chem.200800674.

(242) Gardeniers, H. J. G. E. Chemistry in Nanochannel Confinement. *Anal. Bioanal. Chem.* **2009**, *394* (2), 385–397. https://doi.org/10.1007/s00216-009-2672-5.

(243) Sun, M.; Fu, Q.; Gao, L.; Zheng, Y.; Li, Y.; Chen, M.; Bao, X. Catalysis under Shell: Improved CO Oxidation Reaction Confined in Pt@h-BN Core–Shell Nanoreactors. *Nano Res.* **2017**, *10* (4), 1403–1412. https://doi.org/10.1007/s12274-017-1512-8.

(244) Over, H. Surface Chemistry of Ruthenium Dioxide in Heterogeneous Catalysis and Electrocatalysis: From Fundamental to Applied Research. *Chem. Rev.* **2012**, *112* (6), 3356–3426. https://doi.org/10.1021/cr200247n.

(245) Royer, S.; Duprez, D. Catalytic Oxidation of Carbon Monoxide over Transition Metal Oxides. *ChemCatChem* **2011**, *3* (1), 24–65. https://doi.org/10.1002/cctc.201000378.

(246) Ertl, G. Reactions at Surfaces: From Atoms to Complexity (Nobel Lecture). *Angew. Chemie Int. Ed.* **2008**, *47* (19), 3524–3535. https://doi.org/10.1002/anie.200800480.

(247) Freund, H. J.; Meijer, G.; Scheffler, M.; Schlögl, R.; Wolf, M. CO Oxidation as a

Prototypical Reaction for Heterogeneous Processes. *Angew. Chemie - Int. Ed.* **2011**, *50* (43), 10064–10094. https://doi.org/10.1002/anie.201101378.

(248) Lamberti, C.; Zecchina, A.; Groppo, E.; Bordiga, S. Probing the Surfaces of Heterogeneous Catalysts by in Situ IR Spectroscopy. *Chem. Soc. Rev.* **2010**, *39* (12), 4951–5001. https://doi.org/10.1039/c0cs00117a.

(249) Jiang, J.; Gándara, F.; Zhang, Y.; Na, K.; Yaghi, O. M.; Klemperer, W. G. Superacidity in Sulfated Metal–Organic Framework-808. *J. Am. Chem. Soc.* **2014**, *136* (37), 12844–12847. https://doi.org/10.1021/ja507119n.

(250) Furukawa, H.; Gándara, F.; Zhang, Y.-B.; Jiang, J.; Queen, W. L.; Hudson, M. R.; Yaghi, O. M. Water Adsorption in Porous Metal–Organic Frameworks and Related Materials. *J. Am. Chem. Soc.* **2014**, *136* (11), 4369–4381. https://doi.org/10.1021/ja500330a.

(251) Zheng, H.-Q.; Liu, C.-Y.; Zeng, X.-Y.; Chen, J.; Lü, J.; Lin, R.-G.; Cao, R.; Lin, Z.-J.; Su, J.-W. MOF-808: A Metal–Organic Framework with Intrinsic Peroxidase-Like Catalytic Activity at Neutral PH for Colorimetric Biosensing. *Inorg. Chem.* **2018**, *57* (15), 9096–9104. https://doi.org/10.1021/acs.inorgchem.8b01097.

(252) Coupry, D. E.; Butson, J.; Petkov, P. S.; Saunders, M.; O'Donnell, K.; Kim, H.; Buckley, C.; Addicoat, M.; Heine, T.; Szilágyi, P. Á. Controlling Embedment and Surface Chemistry of Nanoclusters in Metal–Organic Frameworks. *Chem. Commun.* **2016**, *52* (29), 5175–5178. https://doi.org/10.1039/C6CC00659K.

(253) Joo, S. H.; Park, J. Y.; Renzas, J. R.; Butcher, D. R.; Huang, W.; Somorjai, G. A. Size Effect of Ruthenium Nanoparticles in Catalytic Carbon Monoxide Oxidation. *Nano Lett.* **2010**, *10* (7), 2709–2713. https://doi.org/10.1021/nl101700j.

(254) Aßmann, J.; Löffler, E.; Birkner, A.; Muhler, M. Ruthenium as Oxidation Catalyst: Bridging the Pressure and Material Gaps between Ideal and Real Systems in Heterogeneous Catalysis by Applying DRIFT Spectroscopy and the TAP Reactor. *Catal. Today* **2003**, *85* (2–4), 235–249. https://doi.org/10.1016/S0920-5861(03)00391-2.

(255) Farkas, A.; Mellau, G. C.; Over, H. Novel Insight in the CO Oxidation on RuO 2 (110) by in Situ Reflection−Absorption Infrared Spectroscopy. *J. Phys. Chem. C*

2009, *113* (32), 14341–14355. https://doi.org/10.1021/jp902138q.

(256) Assmann, J.; Narkhede, V.; Breuer, N. A.; Muhler, M.; Seitsonen, A. P.; Knapp, M.; Crihan, D.; Farkas, A.; Mellau, G.; Over, H. Heterogeneous Oxidation Catalysis on Ruthenium: Bridging the Pressure and Materials Gaps and Beyond. *J. Phys. Condens. Matter* **2008**, *20* (18), 184017. https://doi.org/10.1088/0953-8984/20/18/184017.

(257) Spinacé, E. V.; Vaz, J. M. Liquid-Phase Hydrogenation of Benzene to Cyclohexene Catalyzed by Ru/SiO2 in the Presence of Water–Organic Mixtures. *Catal. Commun.* **2003**, *4* (3), 91–96. https://doi.org/10.1016/S1566-7367(02)00270-4.

(258) Povar, I.; Spinu, O. Ruthenium Redox Equilibria: 1. Thermodynamic Stability of Ru(III) and Ru(IV) Hydroxides. *J. Electrochem. Sci. Eng.* **2016**, *6* (1), 123. https://doi.org/10.5599/jese.226.

(259) Povar, I.; Spinu, O. Ruthenium Redox Equilibria: 2. Thermodynamic Analysis of Disproportionation and Comproportionation Conditions. *J. Electrochem. Sci. Eng.* **2016**, *6* (1), 135. https://doi.org/10.5599/jese.228.

(260) Wang, T.; Gao, L.; Hou, J.; Herou, S. J. A.; Griffiths, J. T.; Li, W.; Dong, J.; Gao, S.; Titirici, M.; Kumar, R. V.; et al. Rational Approach to Guest Confinement inside MOF Cavities for Low-Temperature Catalysis. *Nat. Commun.* **2019**, *10* (1), 1340. https://doi.org/10.1038/s41467-019-08972-x.

(261) Yohe, G. R.; Dunbar, J. E.; Pedrotti, R. L.; Scheidt, F. M.; Lee, F. G. H.; Smith, E. C. The Oxidation of 2,6-Di- Tert -Butyl-4-Methylphenol. *J. Org. Chem.* **1956**, *21* (11), 1289–1292. https://doi.org/10.1021/jo01117a020.

(262) Richards, J. A.; Evans, D. H. Electrochemical Oxidation of 2,6-Di-Tert-Butyl-4-Isopropylphenol. *J. Electroanal. Chem. Interfacial Electrochem.* **1977**, *81* (1), 171–187. https://doi.org/10.1016/S0022-0728(77)80369-0.

(263) Keattch, C. J.; Redfern, J. P. The Preparation and Properties of a Hydrous Ruthenium Oxide. *J. Less Common Met.* **1962**, *4* (5), 460–465. https://doi.org/10.1016/0022-5088(62)90031-0.

(264) Sauerbrunn, S.; Gill, P. *Decomposition Kinetics Using TGA*; TA-075; New Castle.

(265) Jiang, H.; Liu, B.; Akita, T.; Haruta, M.; Sakurai, H.; V, K. U.; Ku, N.; Sciences, E. V; Metropolitan, T.; Uni, V. Au @ ZIF-8 : CO Oxidation over Gold Nanoparticles Deposited to Metal - Organic Framework. *J. Am. Chem. Soc.* **2009**, *2*, 11302–11303. https://doi.org/10.1021/ja9047653.

(266) Fang, Z.; Bueken, B.; De Vos, D. E.; Fischer, R. A. Defect-Engineered Metal-Organic Frameworks. *Angew. Chemie Int. Ed.* **2015**, *54* (25), 7234–7254. https://doi.org/10.1002/anie.201411540.

(267) Cheetham, A. K.; Bennett, T. D.; Coudert, F. X.; Goodwin, A. L. Defects and Disorder in Metal Organic Frameworks. *Dalt. Trans.* **2016**, *45* (10), 4113–4126. https://doi.org/10.1039/c5dt04392a.

(268) Velázquez-Palenzuela, A.; Centellas, F.; Garrido, J. A.; Arias, C.; María Rodríguez, R.; Brillas, E.; Cabot, P.-L. Structural Properties of Unsupported Pt−Ru Nanoparticles as Anodic Catalyst for Proton Exchange Membrane Fuel Cells. *J. Phys. Chem. C* **2010**, *114* (10), 4399–4407. https://doi.org/10.1021/jp9119815.

(269) Zhang, X.; Chan, K. Y. Water-in-Oil Microemulsion Synthesis of Platinum-Ruthenium Nanoparticles, Their Characterization and Electrocatalytic Properties. *Chem. Mater.* **2003**, *15* (2), 451–459. https://doi.org/10.1021/cm0203868.

(270) Rolison, D. R.; Hagans, P. L.; Swider, K. E.; Long, J. W. Role of Hydrous Ruthenium Oxide in Pt−Ru Direct Methanol Fuel Cell Anode Electrocatalysts: The Importance of Mixed Electron/Proton Conductivity. *Langmuir* **1999**, *15* (3), 774–779. https://doi.org/10.1021/la9807863.

(271) Wang, X.; Chen, W.; Zhang, L.; Yao, T.; Liu, W.; Lin, Y.; Ju, H.; Dong, J.; Zheng, L.; Yan, W.; et al. Uncoordinated Amine Groups of Metal–Organic Frameworks to Anchor Single Ru Sites as Chemoselective Catalysts toward the Hydrogenation of Quinoline. *J. Am. Chem. Soc.* **2017**, *139* (28), 9419–9422. https://doi.org/10.1021/jacs.7b01686.

(272) Li, H.; Xiao, J.; Fu, Q.; Bao, X. Confined Catalysis under Two-Dimensional Materials. *Proc. Natl. Acad. Sci.* **2017**, *114* (23), 5930–5934. https://doi.org/10.1073/pnas.1701280114.

(273) Jiang, H.; Liu, B.; Akita, T.; Haruta, M.; Sakurai, H.; Xu, Q. Au@ZIF-8: CO

Oxidation over Gold Nanoparticles Deposited to Metal−Organic Framework. *J. Am. Chem. Soc.* **2009**, *131* (32), 11302–11303. https://doi.org/10.1021/ja9047653.

(274) Fu, Q.; Bao, X. Surface Chemistry and Catalysis Confined under Two-Dimensional Materials. *Chem. Soc. Rev.* **2017**, *46* (7), 1842–1874. https://doi.org/10.1039/C6CS00424E.

(275) Janda, A.; Vlaisavljevich, B.; Lin, L.-C.; Smit, B.; Bell, A. T. Effects of Zeolite Structural Confinement on Adsorption Thermodynamics and Reaction Kinetics for Monomolecular Cracking and Dehydrogenation of n -Butane. *J. Am. Chem. Soc.* **2016**, *138* (14), 4739–4756. https://doi.org/10.1021/jacs.5b11355.

(276) Park, J.-N.; Shon, J. K.; Jin, M.; Kong, S. S.; Moon, K.; Park, G. O.; Boo, J.-H.; Kim, J. M. Room-Temperature CO Oxidation over a Highly Ordered Mesoporous RuO2 Catalyst. *React. Kinet. Mech. Catal.* **2011**, *103* (1), 87–99. https://doi.org/10.1007/s11144-011-0284-5.

(277) Wang, W.; Li, Y.; Zhang, R.; He, D.; Liu, H.; Liao, S. Metal-Organic Framework as a Host for Synthesis of Nanoscale Co3O4 as an Active Catalyst for CO Oxidation. *Catal. Commun.* **2011**, *12* (10), 875–879. https://doi.org/10.1016/j.catcom.2011.02.001.

(278) Cui, X.; Wang, Y.; Chen, L.; Shi, J. Synergetic Catalytic Effects in Tri-Component Mesostructured Ru-Cu-Ce Oxide Nanocomposite in CO Oxidation. *ChemCatChem* **2014**, *6* (10), 2860–2871. https://doi.org/10.1002/cctc.201402392.

(279) Kim, I. H.; Jeong, M. G.; Han, S. W.; Park, E. J.; Hwang, Y. K.; Kim, Y. D. CO Oxidation Catalyzed by RuO2nanoparticles Supported on Mesoporous Al2O3prepared via Atomic Layer Deposition. *Curr. Appl. Phys.* **2016**, *16* (10), 1407–1412. https://doi.org/10.1016/j.cap.2016.07.015.

(280) Lu, G.; Li, S.; Guo, Z.; Farha, O. K.; Hauser, B. G.; Qi, X.; Wang, Y.; Wang, X.; Han, S.; Liu, X.; et al. Imparting Functionality to a Metal-Organic Framework Material by Controlled Nanoparticle Encapsulation. *Nat. Chem.* **2012**, *4* (4), 310–316. https://doi.org/10.1038/nchem.1272.

(281) Shen, W.; Shi, J.; Chen, H.; Gu, J.; Zhu, Y.; Dong, X. Synthesis and CO Oxidation Catalytic Character of High Surface Area Ruthenium Dioxide Replicated by Cubic

Mesoporous Silica. *Chem. Lett.* **2005**, *34* (3), 390–391. https://doi.org/10.1246/cl.2005.390.

(282) Sreedhala, S.; Vinod, C. P. Surfactant Assisted Formation of Ruthenium Nanochains under Mild Conditions and Their Catalytic CO Oxidation Activity. *Chem. Commun.* **2015**, *51* (50), 10178–10181. https://doi.org/10.1039/C4CC09430A.

(283) Yu, J.; Zhao, D.; Xu, X.; Wang, X.; Zhang, N. Study on RuO_2/SnO_2: Novel and Active Catalysts for CO and CH_4 Oxidation. *ChemCatChem* **2012**, *4* (8), 1122–1132. https://doi.org/10.1002/cctc.201200038.

(284) Huang, B.; Kobayashi, H.; Yamamoto, T.; Matsumura, S.; Nishida, Y.; Sato, K.; Nagaoka, K.; Kawaguchi, S.; Kubota, Y.; Kitagawa, H. Solid-Solution Alloying of Immiscible Ru and Cu with Enhanced CO Oxidation Activity. *J. Am. Chem. Soc.* **2017**, *139* (13), 4643–4646. https://doi.org/10.1021/jacs.7b01186.

(285) Kusada, K.; Kobayashi, H.; Yamamoto, T.; Matsumura, S.; Sumi, N.; Sato, K.; Nagaoka, K.; Kubota, Y.; Kitagawa, H. Discovery of Face-Centered-Cubic Ruthenium Nanoparticles: Facile Size-Controlled Synthesis Using the Chemical Reduction Method. *J. Am. Chem. Soc.* **2013**, *135* (15), 5493–5496. https://doi.org/10.1021/ja311261s.

(286) Liang, C.; Narkhede, V.; Aßmann, J.; Muhler, M. Controlled Synthesis of Supported Ruthenium Catalysts for CO Oxidation by Organometallic Chemical Vapor Deposition. *Stud. Surf. Sci. Catal.* **2006**, *162*, 473–480. https://doi.org/10.1016/S0167-2991(06)80942-0.

(287) Prodinger, S.; Shi, H.; Eckstein, S.; Hu, J. Z.; Olarte, M. V.; Camaioni, D. M.; Derewinski, M. A.; Lercher, J. A. Stability of Zeolites in Aqueous Phase Reactions. *Chem. Mater.* **2017**, *29* (17), 7255–7262. https://doi.org/10.1021/acs.chemmater.7b01847.

(288) Ning, J.; Zheng, Y.; Young, D.; Brown, B.; Nešić, S. Thermodynamic Study of Hydrogen Sulfide Corrosion of Mild Steel. *CORROSION* **2014**, *70* (4), 375–389. https://doi.org/10.5006/0951.

(289) Materials Project http://materialsproject.org (accessed Sep 6, 2018).

(290) Jain, A.; Ong, S. P.; Hautier, G.; Chen, W.; Richards, W. D.; Dacek, S.; Cholia, S.; Gunter, D.; Skinner, D.; Ceder, G.; et al. Commentary: The Materials Project: A Materials Genome Approach to Accelerating Materials Innovation. *APL Mater.* **2013**, *1* (1), 011002. https://doi.org/10.1063/1.4812323.

(291) Singh, A. K.; Zhou, L.; Shinde, A.; Suram, S. K.; Montoya, J. H.; Winston, D.; Gregoire, J. M.; Persson, K. A. Electrochemical Stability of Metastable Materials. *Chem. Mater.* **2017**, *29* (23), 10159–10167. https://doi.org/10.1021/acs.chemmater.7b03980.

(292) Persson, K. A.; Waldwick, B.; Lazic, P.; Ceder, G. Prediction of Solid-Aqueous Equilibria: Scheme to Combine First-Principles Calculations of Solids with Experimental Aqueous States. *Phys. Rev. B* **2012**, *85* (23), 235438. https://doi.org/10.1103/PhysRevB.85.235438.

(293) Jaramillo, T. F.; Jorgensen, K. P.; Bonde, J.; Nielsen, J. H.; Horch, S.; Chorkendorff, I. Identification of Active Edge Sites for Electrochemical H2 Evolution from MoS2 Nanocatalysts. *Science (80-.).* **2007**, *317* (5834), 100–102. https://doi.org/10.1126/science.1141483.

(294) Karunadasa, H. I.; Montalvo, E.; Sun, Y.; Majda, M.; Long, J. R.; Chang, C. J. A Molecular MoS2 Edge Site Mimic for Catalytic Hydrogen Generation. *Science (80-.).* **2012**, *335* (6069), 698–702. https://doi.org/10.1126/science.1215868.

(295) Prasad, T. P.; Diemann, E.; Müller, A. Thermal Decomposition of (NH4)2MoO2S2, (NH4)2MoS4, (NH4)2WO2S2 and (NH4)2WS4. *J. Inorg. Nucl. Chem.* **1973**, *35* (6), 1895–1904. https://doi.org/10.1016/0022-1902(73)80124-1.

(296) Wang, H. W.; Skeldon, P.; Thompson, G. E. Thermogravimetric-Differential Thermal Analysis of the Solid-State Decomposition of Ammonium Tetrathiomolybdate during Heating in Argon. *J. Mater. Sci.* **1998**, *33* (12), 3079–3083. https://doi.org/10.1023/A:1004335604327.

(297) Pachfule, P.; Shinde, D.; Majumder, M.; Xu, Q. Fabrication of Carbon Nanorods and Graphene Nanoribbons from a Metal–Organic Framework. *Nat. Chem.* **2016**, *8* (7), 718–724. https://doi.org/10.1038/NCHEM.2515.

(298) Guan, C.; Zhao, W.; Hu, Y.; Lai, Z.; Li, X.; Sun, S.; Zhang, H.; Cheetham, A. K.;

Wang, J. Cobalt Oxide and N-Doped Carbon Nanosheets Derived from a Single Two-Dimensional Metal–Organic Framework Precursor and Their Application in Flexible Asymmetric Supercapacitors. *Nanoscale Horizons* **2017**, *2* (2), 99–105. https://doi.org/10.1039/C6NH00224B.

(299) Kaneti, Y. V.; Tang, J.; Salunkhe, R. R.; Jiang, X.; Yu, A.; Wu, K. C. W.; Yamauchi, Y. Nanoarchitectured Design of Porous Materials and Nanocomposites from Metal-Organic Frameworks. *Adv. Mater.* **2017**, *29* (12), 1604898. https://doi.org/10.1002/adma.201604898.

(300) Xi, K.; Cao, S.; Peng, X.; Ducati, C.; Vasant Kumar, R.; Cheetham, A. K. Carbon with Hierarchical Pores from Carbonized Metal–Organic Frameworks for Lithium Sulphur Batteries. *Chem. Commun.* **2013**, *49* (22), 2192. https://doi.org/10.1039/c3cc38009b.

(301) Chaikittisilp, W.; Ariga, K.; Yamauchi, Y. A New Family of Carbon Materials: Synthesis of MOF-Derived Nanoporous Carbons and Their Promising Applications. *J. Mater. Chem. A* **2013**, *1* (1), 14–19. https://doi.org/10.1039/C2TA00278G.

(302) Kongpatpanich, K.; Horike, S.; Fujiwara, Y.; Ogiwara, N.; Nishihara, H.; Kitagawa, S. Formation of Foam-like Microstructural Carbon Material by Carbonization of Porous Coordination Polymers through a Ligand-Assisted Foaming Process. *Chem. - A Eur. J.* **2015**, *21* (38), 13278–13283. https://doi.org/10.1002/chem.201501988.

(303) Rahaman, M. S. A.; Ismail, A. F.; Mustafa, A. A Review of Heat Treatment on Polyacrylonitrile Fiber. *Polym. Degrad. Stab.* **2007**, *92* (8), 1421–1432. https://doi.org/10.1016/j.polymdegradstab.2007.03.023.

(304) Gibson, J.; Riley, H. L.; Taylor, J. Filamentous Carbon. *Nature* **1944**, *154* (3913), 544–544. https://doi.org/10.1038/154544a0.

(305) Oberlin, A.; Endo, M.; Koyama, T. Filamentous Growth of Carbon through Benzene Decomposition. *J. Cryst. Growth* **1976**, *32* (3), 335–349. https://doi.org/10.1016/0022-0248(76)90115-9.

(306) De Jong, K. P.; Geus, J. W. Carbon Nanofibers: Catalytic Synthesis and Applications. *Catal. Rev.* **2000**, *42* (4), 481–510. https://doi.org/10.1081/CR-100101954.

(307) Davis, W. R.; Slawson, R. J.; Rigby, G. R. An Unusual Form of Carbon. *Nature* **1953**, *171* (4356), 756–756. https://doi.org/10.1038/171756a0.

(308) Li, H.; Yue, F.; Yang, C.; Xue, P.; Li, N.; Zhang, Y.; Wang, J. Structural Evolution of a Metal–Organic Framework and Derived Hybrids Composed of Metallic Cobalt and Copper Encapsulated in Nitrogen-Doped Porous Carbon Cubes with High Catalytic Performance. *CrystEngComm* **2017**, *19* (1), 64–71. https://doi.org/10.1039/C6CE01995A.

(309) Zou, F.; Chao, S. L.; Wang, Y. X.; Wang, Y. L.; Guan, Q. X.; Li, W. Controllable Self-Catalytic Fabrication of Carbon Nanomaterials Mediated by a Nickel Metal Organic Framework. *Environ. Sci. Nano* **2017**, *4* (1), 46–51. https://doi.org/10.1039/C6EN00441E.

(310) Meng, J.; Niu, C.; Xu, L.; Li, J.; Liu, X.; Wang, X.; Wu, Y.; Xu, X.; Chen, W.; Li, Q.; et al. General Oriented Formation of Carbon Nanotubes from Metal-Organic Frameworks. *J. Am. Chem. Soc.* **2017**, *139* (24), 8212–8221. https://doi.org/10.1021/jacs.7b01942.

(311) Guan, B. Y.; Yu, X. Y.; Wu, H. Bin; Lou, X. W. D. Complex Nanostructures from Materials Based on Metal-Organic Frameworks for Electrochemical Energy Storage and Conversion. *Adv. Mater.* **2017**, *29* (47), 1703614. https://doi.org/10.1002/adma.201703614.

(312) Zhang, W.; Jiang, X.; Wang, X.; Kaneti, Y. V.; Chen, Y.; Liu, J.; Jiang, J.-S.; Yamauchi, Y.; Hu, M. Spontaneous Weaving of Graphitic Carbon Networks Synthesized by Pyrolysis of ZIF-67 Crystals. *Angew. Chemie Int. Ed.* **2017**, *56* (29), 8435–8440. https://doi.org/10.1002/anie.201701252.

(313) Jia, G.; Zhang, W.; Fan, G.; Li, Z.; Fu, D.; Hao, W.; Yuan, C.; Zou, Z. Three-Dimensional Hierarchical Architectures Derived from Surface-Mounted Metal-Organic Framework Membranes for Enhanced Electrocatalysis. *Angew. Chemie Int. Ed.* **2017**, *56* (44), 13781–13785. https://doi.org/10.1002/anie.201708385.

(314) Su, P.; Xiao, H.; Zhao, J.; Yao, Y.; Shao, Z.; Li, C.; Yang, Q. Nitrogen-Doped Carbon Nanotubes Derived from Zn–Fe-ZIF Nanospheres and Their Application as Efficient Oxygen Reduction Electrocatalysts with in Situ Generated Iron Species.

Chem. Sci. **2013**, *4* (7), 2941. https://doi.org/10.1039/c3sc51052b.

(315) Wu, H. Bin; Xia, B. Y.; Yu, L.; Yu, X.-Y.; Lou, X. W. (David). Porous Molybdenum Carbide Nano-Octahedrons Synthesized via Confined Carburization in Metal-Organic Frameworks for Efficient Hydrogen Production. *Nat. Commun.* **2015**, *6*, 6512. https://doi.org/10.1038/ncomms7512.

(316) Xu, Y.-T.; Xiao, X.; Ye, Z.-M.; Zhao, S.; Shen, R.; He, C.-T.; Zhang, J.-P.; Li, Y.; Chen, X.-M. Cage-Confinement Pyrolysis Route to Ultrasmall Tungsten Carbide Nanoparticles for Efficient Electrocatalytic Hydrogen Evolution. *J. Am. Chem. Soc.* **2017**, *139* (15), 5285–5288. https://doi.org/10.1021/jacs.7b00165.

(317) Gu, Z.-G.; Zhang, D.-X.; Fu, W.-Q.; Fu, Z.-H.; Vohra, M. I.; Zhang, L.; Wöll, C.; Zhang, J. Facile Synthesis of Metal-Loaded Porous Carbon Thin Films via Carbonization of Surface-Mounted Metal–Organic Frameworks. *Inorg. Chem.* **2017**, *56* (6), 3526–3531. https://doi.org/10.1021/acs.inorgchem.6b03140.

(318) Zhu, Q.-L.; Xia, W.; Zheng, L.-R.; Zou, R.; Liu, Z.; Xu, Q. Atomically Dispersed Fe/N-Doped Hierarchical Carbon Architectures Derived from a Metal–Organic Framework Composite for Extremely Efficient Electrocatalysis. *ACS Energy Lett.* **2017**, *2* (2), 504–511. https://doi.org/10.1021/acsenergylett.6b00686.

(319) Snoeck, J. W.; Froment, G. F.; Fowles, M. Filamentous Carbon Formation and Gasification: Thermodynamics, Driving Force, Nucleation, and Steady-State Growth. *J. Catal.* **1997**, *169* (1), 240–249. https://doi.org/10.1006/jcat.1997.1634.

(320) S-Y Chui, S.; M-F Lo, S.; H Charmant, J. P.; Guy Orpen, A.; Williams, I. D. A Chemically Functionalizable Nanoporous Material [Cu 3 (TMA) 2 (H 2 O) 3] N. *Science (80-.).* **1999**, *283*, 1148–1150. https://doi.org/10.1126/science.283.5405.1148.

(321) Feldblyum, J. I.; Liu, M.; Gidley, D. W.; Matzger, A. J. Reconciling the Discrepancies between Crystallographic Porosity and Guest Access As Exemplified by Zn-HKUST-1. *J. Am. Chem. Soc.* **2011**, *133* (45), 18257–18263. https://doi.org/10.1021/ja2055935.

(322) Peng, Y.; Krungleviciute, V.; Eryazici, I.; Hupp, J. T.; Farha, O. K.; Yildirim, T. Methane Storage in Metal-Organic Frameworks: Current Records, Surprise

Findings, and Challenges. *J. Am. Chem. Soc.* **2013**, *135* (32), 11887–11894. https://doi.org/10.1021/ja4045289.

(323) Bhunia, M. K.; Hughes, J. T.; Fettinger, J. C.; Navrotsky, A. Thermochemistry of Paddle Wheel MOFs: Cu-HKUST-1 and Zn-HKUST-1. *Langmuir* **2013**, *29* (25), 8140–8145. https://doi.org/10.1021/la4012839.

(324) Müller, A.; Diemann, E.; Jostes, R.; Bögge, H. Transition Metal Thiometalates: Properties and Significance in Complex and Bioinorganic Chemistry. *Angew. Chemie Int. Ed. English* **1981**, *20* (11), 934–955. https://doi.org/10.1002/anie.198109341.

(325) Dolomanov, O. V.; Bourhis, L. J.; Gildea, R. J.; Howard, J. A. K.; Puschmann, H. OLEX2 : A Complete Structure Solution, Refinement and Analysis Program. *J. Appl. Crystallogr.* **2009**, *42* (2), 339–341. https://doi.org/10.1107/S0021889808042726.

(326) Sheldrick, G. M. SHELXT - Integrated Space-Group and Crystal-Structure Determination. *Acta Crystallogr. Sect. A Found. Crystallogr.* **2015**, *71* (1), 3–8. https://doi.org/10.1107/S2053273314026370.

(327) Sheldrick, G. M. A Short History of SHELX. *Acta Crystallogr. Sect. A Found. Crystallogr.* **2008**, *64* (1), 112–122. https://doi.org/10.1107/S0108767307043930.

(328) Benson, G.; Gluck, J.; Kaufmann, C. Methods Used for the Measurement of the Electrical Conductivity of Carbon Black Are Described . The Results Obtained When the Black Is Compressed to a Standard Apparent Density Are Shown to Be More in Accordance with Performance of the Black in Dry Cells. *J. Electrochem. Soc.* **1946**, *90* (1), 441–447. https://doi.org/10.1149/1.3071758.

(329) Montes, J. M.; Cuevas, F. G.; Cintas, J.; Urban, P. Electrical Conductivity of Metal Powders under Pressure. *Appl. Phys. A* **2011**, *105* (4), 935–947. https://doi.org/10.1007/s00339-011-6515-9.

(330) Cheng, Y.; Rondo, A.; Noguchi, H.; Kajiro, H.; Urita, K.; Ohba, T.; Kaneko, K.; Kanoh, H. Reversible Structural Change of Cu-MOF on Exposure to Water and Its CO2adsorptivity. *Langmuir* **2009**, *25* (8), 4510–4513. https://doi.org/10.1021/la803818p.

(331) Al-Janabi, N.; Hill, P.; Torrente-Murciano, L.; Garforth, A.; Gorgojo, P.; Siperstein, F.; Fan, X. Mapping the Cu-BTC Metal-Organic Framework (HKUST-1) Stability Envelope in the Presence of Water Vapour for CO<inf>2</Inf> Adsorption from Flue Gases. *Chem. Eng. J.* **2015**, *281*, 669–677. https://doi.org/10.1016/j.cej.2015.07.020.

(332) Vrubel, H.; Merki, D.; Hu, X. Hydrogen Evolution Catalyzed by MoS3 and MoS2 Particles. *Energy Environ. Sci.* **2012**, *5* (3), 6136. https://doi.org/10.1039/c2ee02835b.

(333) Simoes, J. A. M.; Beauchamp, J. L. Transition Metal-Hydrogen and Metal-Carbon Bond Strengths: The Keys to Catalysis. *Chem. Rev.* **1990**, *90* (4), 629–688. https://doi.org/10.1021/cr00102a004.

(334) Lobo, L. S. Catalytic Carbon Formation: Clarifying the Alternative Kinetic Routes and Defining a Kinetic Linearity for Sustained Growth Concept. *React. Kinet. Mech. Catal.* **2016**, *118* (2), 393–414. https://doi.org/10.1007/s11144-016-0993-x.

(335) Terrones, M.; Grobert, N.; Olivares, J.; Zhang, J. P.; Terrones, H.; Kordatos, K.; Hsu, W. K.; Hare, J. P.; Townsend, P. D.; Prassides, K.; et al. Controlled Production of Aligned-Nanotube Bundles. *Nature* **1997**, *388* (6637), 52–55. https://doi.org/10.1038/40369.

(336) Wan, C.; Regmi, Y. N.; Leonard, B. M. Multiple Phases of Molybdenum Carbide as Electrocatalysts for the Hydrogen Evolution Reaction. *Angew. Chemie* **2014**, *126* (25), 6525–6528. https://doi.org/10.1002/ange.201402998.

(337) Li, J.; Croiset, E.; Ricardez-Sandoval, L. Effects of Metal Elements in Catalytic Growth of Carbon Nanotubes/Graphene: A First Principles DFT Study. *Appl. Surf. Sci.* **2014**, *317*, 923–928. https://doi.org/10.1016/j.apsusc.2014.09.008.

(338) Li, Z.; Larsson, J. A.; Larsson, P.; Ahuja, R.; Tobin, J. M.; O’Byrne, J.; Morris, M. A.; Attard, G.; Holmes, J. D. Copper/Molybdenum Nanocomposite Particles as Catalysts for the Growth of Bamboo-Structured Carbon Nanotubes. *J. Phys. Chem. C* **2008**, *112* (32), 12201–12206. https://doi.org/10.1021/jp8023556.

(339) O’Byrne, J. P.; Li, Z.; Tobin, J. M.; Larsson, J. A.; Larsson, P.; Ahuja, R.; Holmes, J. D. Growth of Carbon Nanotubes from Heterometallic Palladium and Copper

Catalysts. *J. Phys. Chem. C* **2010**, *114* (18), 8115–8119. https://doi.org/10.1021/jp909309t.

(340) Bridgewater, A. J.; Burch, R.; Mitchell, P. C. H. Molybdenum/Carbon Catalysts for Reforming Reactions. *J. Chem. Soc. Faraday Trans. 1 Phys. Chem. Condens. Phases* **1980**, *76* (Iv), 1811. https://doi.org/10.1039/f19807601811.

(341) He, K.; Zhang, S.; Mi, J.; Chen, J.; Cheng, L. Mechanism of Catalytic Hydropyrolysis of Sedimentary Organic Matter with MoS2. *Pet. Sci.* **2011**, *8* (2), 134–142. https://doi.org/10.1007/s12182-011-0126-0.

(342) Quan, B.; Yu, S.-H.; Chung, D. Y.; Jin, A.; Park, J. H.; Sung, Y.-E.; Piao, Y. Single Source Precursor-Based Solvothermal Synthesis of Heteroatom-Doped Graphene and Its Energy Storage and Conversion Applications. *Sci. Rep.* **2015**, *4* (1), 5639. https://doi.org/10.1038/srep05639.

(343) Su, D. S.; Schlögl, R. Nanostructured Carbon and Carbon Nanocomposites for Electrochemical Energy Storage Applications. *ChemSusChem* **2010**, *3* (2), 136–168. https://doi.org/10.1002/cssc.200900182.

(344) Dominko, R.; Arčon, D.; Mrzel, A.; Zorko, A.; Cevc, P.; Venturini, P.; Gaberscek, M.; Remskar, M.; Mihailovic, D. Dichalcogenide Nanotube Electrodes for Li-Ion Batteries. *Adv. Mater.* **2002**, *14* (21), 1531–1534. https://doi.org/10.1002/1521-4095(20021104)14:21<1531::AID-ADMA1531>3.0.CO;2-P.

(345) Xiao, J.; Choi, D.; Cosimbescu, L.; Koech, P.; Liu, J.; Lemmon, J. P. Exfoliated MoS2 Nanocomposite as an Anode Material for Lithium Ion Batteries. *Chem. Mater.* **2010**, *22* (16), 4522–4524. https://doi.org/10.1021/cm101254j.

(346) Sun, H.; Hanlon, D.; Dinh, D. A.; Boland, J. B.; Del Rio Castillo, A. E.; Di Giovanni, C.; Ansaldo, A.; Pellegrini, V.; Coleman, J. N.; Bonaccorso, F. Carbon Nanotubes-Bridged Molybdenum Trioxide Nanosheets as High Performance Anode for Lithium Ion Batteries. *2D Mater.* **2017**, *5* (1), 015024. https://doi.org/10.1088/2053-1583/aa9963.

(347) Nishihara, H.; Kyotani, T. Templated Nanocarbons for Energy Storage. *Adv. Mater.* **2012**, *24* (33), 4473–4498. https://doi.org/10.1002/adma.201201715.